NTNU

Norwegian University of
Science and Technology

Wet Chemical Synthesis of Materials for Intermediate Band Solar Cells

Øyvind Sunde Sortland

Chemical Engineering and Biotechnology
Submission date: June 2011
Supervisor: Fride Vullum, IMTE

Declaration

I declare that this Master thesis has been preformed independently and in accordance with the Examination regulations at the Norwegian University of Science and Technology (NTNU).

_____

Øvind Sunde Sortland
Trondheim, June 27, 2011

Abstract

The economical feasibility of commercial, single-junction solar cells is limited by high costs and limited efficiencies. New solar cell concepts and materials are sought to decrease the production costs and increase the efficiency. Intermediate band solar cells (IBSCs) show a promising concept for increased efficiency up to 46.77% as they employ three band gaps that can be matched to the solar spectrum to minimize fundamental losses. Doping of copper gallium disulphide ($CuGaS_2$) with transition metals like Fe and Ni to high concentrations can theoretically form an intermediate band (IB), which for Fe doping gives nearly optimal band gaps for IBSC applications. $CuGaS_2$ is synthesized in an environmentally friendly, inexpensive and simple hydrothermal synthesis which may contribute to decreased costs of solar cell production.

The hydrothermal synthesis is developed to produce $CuGaS_2$ from copper(I) chloride (CuCl), gallium(III) chloride ($GaCl_3$) and excess thiourea (Tu) ($SC(NH_2)_2$) in deionized water. The influence of varying synthesis parameters on product purity, yield and morphology has been investigated through X-ray diffraction (XRD) and scanning electron microscopy (SEM). Energy dispersive X-ray spectroscopy (EDS) is used to investigate doping of $CuGaS_2$ and identify particle morphologies formed by different phases. Formation of $CuGaS_2$ proceeds through slow decomposition of Tu, driven by an equilibrium shift due to hydrogen disulphide (H_2S) evolution and precipitation of sulphides like the intermediate phase digenite ($Cu_{2-\delta}S$) into which Ga^{3+} ions are incorporated. An additional impurity of copper(II) sulphide (CuS) is commonly formed, and gallium(III) hydroxyoxide (GaO(OH)) forms at pH > 0.5. Products of high purity and yield are obtained at 250 °C with concentrations above 0.060 M CuCl and $GaCl_3$ with the complexing agent 1-pentanethiol, and 0.319 M without 1-pentanethiol. Introducing nickel(II) chloride ($NiCl_2$) or iron(III) chloride ($FeCl_3$) in the hydrothermal synthesis forms vaesite (NiS_2) or iron pyrite (FeS_2) impurities, respectively, and $CuGaS_2$ is not doped to a desirable concentration for IB formation.

Color variations in the products reveal off-stoichiometries which contribute to a wide range of particle and crystallite morphologies within each product. Yellow, stoichiometric $CuGaS_2$ particles have been deposited on a Si(100) substrate and growth of a red, Ga-rich film was achieved with 1-pentanethiol. These products were subject to photoluminescence spectroscopy (PL) along with off-stoichiometric powders of doped and undoped products, but no luminescence was obtained, possibly due to high defect densities and non-radiative recombination. Dispersions of powders were also subject to absorption spectroscopy which indicate extensive scattering due to wide ranges of particle sizes. The morphology of powder products shows particularly large variations within and between the products. Nanoplate and pyramidal crystallites are produced through nucleation and growth to form network structures and polycrystalline spheres, rods and rose-like particles, which along with the crystallites have varying irregularities and sizes.

Keywords: IBSC, hydrothermal synthesis, $CuGaS_2$, doping, XRD, morphology.

Preface

The work presented here was carried out at the Norwegian University of Science and Technology at the Department for Materials Science and Engineering in the spring of 2011. It constitutes my Master Thesis as part of the Materials Chemistry and Energy Technology specialization in the Master's Degree Program in Chemical Engineering and Biotechnology. The Master Thesis is a continuation of my Specialization project during the fall of 2010, reported by Sortland [1]. The experimental work was predominately performed in the clean room for Chemical Methods at NTNU NanoLab.

I will here give my appreciation to the people that have contributed to the completion of this work. First of all I thank my supervisor Fride Vullum-Bruer for her guidance and answers, and co-supervisors Mari-Ann Einarsrud and Tor Grande. I will also express my thanks to Julian Tolchard for help with XRD equipment and analyses, Jerome Maria for conducting photoluminescence and absorption measurements and Tor Olav Løveng Sunde for pressing powders into pellets for photoluminescence measurements.

Contents

List of Tables

List of Figures

List of Symbols and Acronyms

A absorbance.

C concentration.

C_{min}^{nu} minimum concentration for nucleation.

C_s solubility concentration.

E_F Fermi level.

E_G band gap.

E_H the highest energy gap ending in the IB.

E_L the lowest energy gap ending in the IB.

E_C lower CB edge.

E_V upper VB edge.

G Gibb's free energy.

$\Delta_c G$ critical free energy of nucleation.

$\Delta_f G$ free energy of formation.

I ionic strength.

N_A Avogadro constant, $6.022 \cdot 10^{23}$ mol^{-1}.

T temperature.

V voltage.

$\Delta\mu$ difference in free energy between supersaturated solution and bulk precipitate.

Γ surface tension.

δ off-stoichiometry coefficient.

γ activity coefficient.

μ chemical potential.

θ angle.

ε_0 vacuum permittivity, $8.854 \cdot 10^{-12}$ C^{2}s^{2}kg^{-1}m^{-3}.

ε_r relative permittivity.

c speed of light in vacuum, $2.998 \cdot 10^8$ m/s.

c_p molar heat capacity at constant pressure.

e elementary charge, $1.602 \cdot 10^{-19}$ C.

h Plank constant, $6.626 \cdot 10^{-34}$ Js.

i radiant intensity.

k_B Boltzmann constant, $1.381 \cdot 10^{-23}$ J/K.

m mass.

r radius.

r_c critical radius of nucleation.

x molar fraction.

x   fraction of the lattice parameter a of a unit cell.

y   fraction of the lattice parameter b of a unit cell.

z charge number.

z   fraction of the lattice parameter c of a unit cell.

CB   conduction band.
CCP   closed packed cubic.
CIGS   chalcopyrite crystals of Cu, In and/or Ga and S or Se.

DOS   density of states.

EDS   energy dispersive X-ray spectroscopy.
En   ethylenediamine, $C_2H_4(NH_2)_2$.

IB   intermediate band.
IBSC   intermediate band solar cell.

NIR   near infrared.

PL   photoluminescence spectroscopy.

SEM   scanning electron microscope.
S(T)EM   scanning (transmission) electron microscope.

T_+, T_- types of tetrahedral voids in a crystal lattice.
Teflon   polytetrafluoroethylene (PTFE).
Tu   thiourea $(SC(NH_2)_2)$.

UV-Vis   ultraviolet-visible.

VB   valence band.

XRD   X-ray diffraction.

1   Introduction

The feasibility of conventional Si solar cells for large scale energy production is limited by the high costs relative to the electricity output [2]. One strategy to reduce the electricity costs from solar cells is to develop more efficient cells. The concept of intermediate band solar cells (IBSCs) can achieve this goal as IBSCs have a higher theoretical maximum efficiency compared to conventional single gap solar cells. For optimal cells, these efficiencies are 46,77% [3] for IBSCs and approaches 30% for single gap solar cells [4] when the sunlight is not concentrated. This improvement is due to an intermediate band (IB) within the band gap of a host semiconductor, as explained in Secion 2.1. The IBSC concept have a even higher efficiency limit than two-junction tandem cells while their structure of material layers is simpler, but their development is at a too early stage for surpassing the efficiency of even conventional single-gap solar cells [1].

Although most research has focused on quantum dot materials for formation of intermediate bands [5], bulk materials have principal advantages over quantum dot materials as explained in Section 2.1. Copper gallium disulphide ($CuGaS_2$) has a nearly optimal band gap for IBSC applications, and is an interesting candidate as host material for IB formation. High concentration doping is however necessary to form the IB. Calculations by Tablero and Fuertes Marrón [6] and Martí et al. [3] show that e.g. Fe and Ni dopants will have sufficient solubility and introduce an IB in $CuGaS_2$, of which the $CuGaS_2$:Fe system has a nearly optimal IB position. However, no experimental studies have to the author's knowledge investigated doping of $CuGaS_2$ for IBSC applications.

$CuGaS_2$ has traditionally been prepared by vacuum techniques for thin-film solar cell applications, but several simpler non-vacuum methods are now available for commercial production as described by Hibberd et al. [7]. Amongst these non-vacuum methods, hydrothermal synthesis is one of the most promising solution chemical methods for preparing $CuGaS_2$ as it allows control over particle sizes and size distribution as well as their morphology [8]. It is also a clean, environmentally friendly, simple and inexpensive method as the reactants are dissolved in an aqueous solution and the synthesis is performed at relatively low temperatures using inexpensive equipment that is easy to operate [1]. It is also appears suitable for up-scaling from laboratory scale to a continuous industrial process.

A hydrohermal synthesis is thus selected for preparation of $CuGaS_2$. Copper(I) chloride (CuCl), gallium(III) chloride ($GaCl_3$) and thiourea (Tu) ($SC(NH_2)_2$) are the selected precursors. These provide the right valency of Cu^+ and Ga^{3+} ions directly, and precipitation is controlled by a slow Tu decomposition to release S^{2-} ions [8]. Through development of a synthesis for producing pure $CuGaS_2$, which is a continuation of that reported by Sortland [1], the influence of reaction parameters on this hydrothermal system is reported with respect to product purity, yield, $CuGaS_2$ stoichiometry and morphology. Specifically, the influence of reactant concentrations and acidification through addition of hydrochloric acid (HCl), complexing of the cations by 1-pentanethiol ($CH_3(CH_2)_3CH_2SH$), heating time, temperature and changes in fill factor, explained in Section 2.4, is explored. Film formation on Si and silica (SiO_2) is also investigated. Thin films are desirable for $CuGaS_2$ solar cells due to high material costs [7] and it can lower the requirements for processing of the material relative to a powder which has to be densified and fashioned into wafers. Nickel(II) chloride ($NiCl_2$) or iron(III) chloride ($FeCl_3$) are introduced in a selected syn-

thesis to give different doping concentrations which are reported in Section 2.3 to provide an IB.

All products are characterized by X-ray diffraction (XRD) for identification of crystalline phases. The particles formed by commonly produced phases are identified by energy dispersive X-ray spectroscopy (EDS) and characterized by scanning electron microscopy (SEM). SEM is also used to analyze the overall morphology of the products in terms of the abundance of the characterized particles and how their morphology is affected by the changes in reaction parameters. Small particles are the desired morphology as this minimizes the risk of pore formation during powder processing into a completely dense material in a subsequent production step. Photoluminescence spectroscopy (PL) is used to investigate IB formation in doped products. Analysis of the results of these characterization techniques are further used to assess the reactions occurring, as in-situ measurements could not be performed during synthesis, as explained in Section 3.1. The work presented also give some information on the feasibility of a hydrothermal method for preparation of $CuGaS_2$, in terms of the compositional quality of the products as well as their morphologies.

2 Theory

2.1 IBSC Concept and Potentials for CuGaS$_2$ Cells

Regular, single gap solar cells suffer low utilization of the solar radiation energy as a consequence of their limitation to match the electronic structure to the photon energies in the solar spectrum. A single gap solar cell can only absorb photons with higher energy than its band gap, as depicted schematically in Figure 2.1(a). The Energy (E) is inverse proportional to the wavelength (λ) as shown in Equation (2.1) [9], in which h is the Plank constant of $6.626 \cdot 10^{-34}$ Js and c is the speed of light in vacuum of $2.998 \cdot 10^8$ m/s.

$$E = \frac{hc}{\lambda} \tag{2.1}$$

AM0 is the solar spectrum outside the atmosphere and AM1.5 is the spectrum at sea-level when the sun is at an angle of 48.2° from the vertical zenith. The IBSC concept has potential to utilize more of the energy from the Sun as it has a total of three band gaps that can be better matched to the solar spectrum [1]. Modification of the material in a single gap solar cell to introduce a narrow energy band, the IB, within the band gap give rise to two lower energy gaps, one between the valence band (VB) and the IB, and one between the IB and the conduction band (CB). Figure 2.1(b) show schematically how these energy gaps may absorb photons of low energy that would pass straight through a single gap solar cell based on the same material, as seen from a comparison with Figure 2.1(a).

IBSCs introduce an IB material in between the p- and n-type emitters as depicted in the upper part of Figure 2.2. The term n-type conductivity is used when the concentration
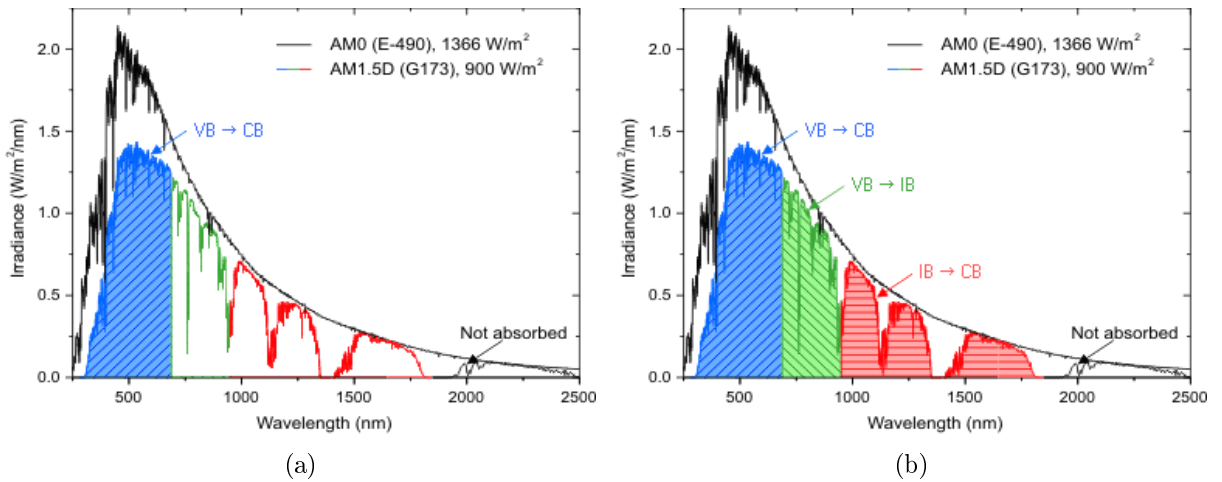
Figure 2.1: Schematic comparison of photon absorption of sunlight in single gap solar cells and IBSCs. The blue area in part (a) show the part of the AM1.5 spectrum that can be absorbed in a single gap solar cell with a band gap corresponding to the energy of photons with a wavelength of 690 nm. Additional absorption due to the two lower energy gaps in IBSCs is indicated by the green and red areas in part (b). The colored labels indicate the preferred electron transition upon photon absorption (adapted with modifications from SUNLab [10]).

of electrons in the CB is so low that it controls the conductivity. P-type conductivity is used for an equivalently low concentration of empty electron states in the VB which are called electron holes. The electron holes are for simplicity treated as positive charges that move opposite of the electrons that move into them, and they are said to transfer the charge in p-type conductivity [1]. The possibility of using CuGaS$_2$ also in the voltage generating emitters is demonstrated by the technology for manufacturing chalcopyrite crystals of Cu, In and/or Ga and S or Se (CIGS) for thin film pn-junction solar cells, in which the n- and p-type emitters are combined directly.

The IB layer is what differentiates IBSCs from single gap solar cells, and consequently the focus of this work is on IB materials. The formation of an IB in bulk materials is based on doping of a host semiconductor with impurity elements that introduce no more than a few energy levels within the band gap, and this concept have potential benefits over the quantum dot alternative. Bulk materials avoid residual strain due to lattice mismatch between the quantum dot and matrix materials, and this has proven to give experimental difficulties [5]. Also, the density of impurities might become higher than the density of quantum dots due to their relative sizes and the issue with residual stresses, provided the solubility of the impurity element in the bulk semiconductor is sufficient [1]. This will in principal allow a higher density of states (DOS) in bulk materials. A realistic dissolution of 5% impurities in bulk material and 10% quantum dot dilution produce a higher DOS in the IB in the bulk material and thus a higher absorption coefficient.
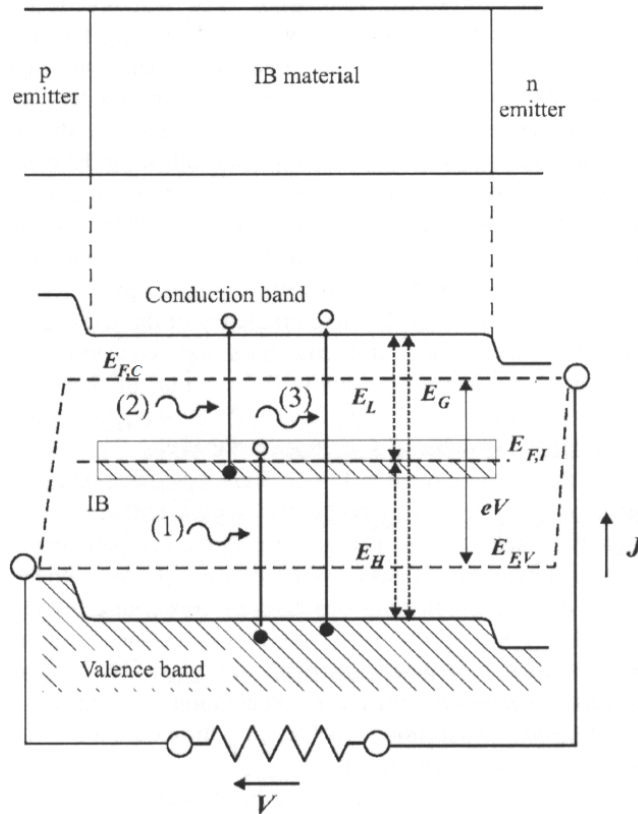
Figure 2.2: General structure of an IBSC showing the p-i-n junction in the upper part and important energy levels and gaps along with possible photon absorption processes in the band diagram below (adapted from Martí et al. [3]).

The IB splits the band gap (E_G) in two additional energy gaps (E_H and E_L) over which electrons can be excited by photon absorption. These energy gaps are shown as two-headed arrows with broken lines in Figure 2.2 and excitation across them from absorption of photons with increasing energy, (1), (2) and (3), are indicated by solid upward arrows in the band diagram. Electron excitation across E_H and E_L sum up to promote an electron to the CB, where it adds to the current of a corresponding single gap solar cell of the host material upon collection in the n-type emitter. The solar cell voltage is the difference between the Fermi level (E_F) in the p-type and n-type emitter and are depicted as the solid double-headed arrow in Figure 2.2, and it is ideally the same for a single gap solar cell without the IB layer. However, doping of the host may alter the upper VB edge (E_V) and/or the lower CB edge (E_C). Compared to an optimal single gap solar cell of a lower band gap material than the IBSC host, the IBSC convert more of the photon energy in the solar spectrum as photons of increasing energy can excite electrons over subsequently higher band gaps [1].

To allow electron excitation across both E_H and E_L without requiring simultaneous photon absorption, the IB is ideally half-filled. Then, the purpose of excitations from the VB to the IB is to refill the IB with electrons after excitations from the IB to the CB, which is the excitation that can contribute to the current [1]. Additional doping with electron donors or acceptors might be necessary to achieve this half-filling. Electron donors are elements that results in a release of electrons into energy bands when they are substitutionally dissolved and thus promote n-type conductivity, and acceptor doping promote p-type conductivity by removal of electrons from the band structure. Intrinsic crystal defects may also act as acceptors or donors so that stoichiometry control can provide adequate doping for the n- and p-type emitters and possibly also half filling of the IB, as described in Section 2.4.5.

The position of the dopant energy levels, and thus the IB they form, in the band gap of the host is important for the selection of material system in the IB layer as it determines the energy gaps E_H and E_L. These gaps must be sufficiently large to prevent thermalization across them [1]. Thermalization is a heat loss mechanism that very rapidly relaxes electrons or holes that are excited above the lower CB edge (E_C) or below the upper VB edge (E_V). Such rapid transitions between electron states are due to their small energy separation within bands, so that quantized lattice vibrations called phonons can take up energy from the electrons. Recombination across a band gap is a much slower process due to the larger energy separation between the electron states as phonons seldom have such high energies, and photon absorption can maintain thermal unbalance in the electron distribution between the bands so that E_F splits into quasi-Fermi levels. $E_{F,V}$, $E_{F,I}$ and $E_{F,C}$ are the quasi-Fermi levels for the VB, IB and CB, respectively, and they are indicated by broken lines in the band diagram of Figure 2.2. The energy difference between $E_{F,C}$ and $E_{F,V}$ can be utilized through the emitters and is depicted as a double-headed solid arrow labeled eV in Figure 2.2, where V is the output voltage and e the elementary charge. This is the part of the photon energy that each absorption across E_G and each pair of absorptions across E_H and E_L can contribute, so the more energy a photon has in excess of the gap it is absorbed across, the lower is the energy utilization. For the areas representing photon absorption in Figure 2.1 to show the energy flux presented on the y-axis as output from an IBSC, thermalization losses must be included, giving decreased utilization of the energy as the wavelengths of the

photons decrease below that corresponding to the energy gap related to the absorption. In this respect, IBSCs also has increased utilization of the photon energies compared to single gap cells with a lower band gap than the IBSC host material [1].

Detailed balance calculations have been carried out to determine the maximum theoretical efficiency from the energy gaps E_H, E_L and E_G. These calculations assume all electron transitions between bands to be radiative so that all excitations consume a photon and all recombinations produce a photon that may be absorbed before leaving the material. Thus, the only heat loss is through thermalization of electrons within the bands [1]. Furthermore, these calculations assume selective absorption where absorbed photons excite electrons across the highest energy gap below the photon energy, as in Figure 2.1(b). Such calculations give a radiative efficiency limit of 46.77% in un-concentrated black body radiation from the sun at 6000 K [3], which is a simplification of the AM0 spectrum in Figure 2.1, and 63.2% at maximum concentration in which sunlight comes from all angles in the hemisphere above the cell. These efficiencies relate to 30% [4] for a single gap solar cell in un-concentrated radiation and 40.7% at full concentration, and 55.4% for a two-junction tandem cell at full sunlight concentration. As the development of IBSCs with the chalcopyrite crystal structure is intended for incorporation with the existing CIGS thin film technology, they are predominantly intended for use in un-concentrated sunlight [3]. The assumption of selective photon absorption is not very realistic as photons with energy above E_H can excite electrons across E_L as well, and photons with energy above E_G can excite electrons across any energy gap. Such overlap between the absorption coefficients for the different band gaps results in increased thermalization losses. Cuadra et al. [11] showed that this heat loss can be minimized if the absorption coefficient increases with increasing photon energy, and by optimizing the cell thickness and employing light confinement techniques. These techniques include use of textured solar cell surface, back reflector and/or external mirrors creating a cavity above the cell, and they are described by Luque [12].

The radiative efficiency limit in un-concentrated sunlight is achieved at optimal band gaps of $E_G = 2.41$ eV, $E_H = 1,49$ eV and $E_L = 0.92$ eV. The band gap of 2.46 eV in $CuGaS_2$ is close to the optimal value and the radiative limit with a $CuGaS_2$ host material is 46.73% with an optimal IB position. Furthermore, $Cu(In,Ga)(S,Se)_2$ alloys can reduce the band gap to the optimal value. Such band gap manipulation is however more important for use in concentrated sunlight, because this reduces the optimal energy gaps to $E_G \approx 1.95$ eV, $E_H \approx 1.24$ eV and $E_L \approx 0.71$ eV [2]. Martí et al. [3] predicted that introduction of $Fe^{3+/2+}$ or $Ti^{4+/3+}$ in $CuGaS_2$ forms an IB around 1.54 eV above E_V, which give E_H and E_L values close to the optimal for un-concentrated sunlight. However, Palacios et al. [13] predicted Ti to be insoluble in $CuGaS_2$, although doping is expected to be possible through kinetic control in the synthesis. Thus, $CuGaS_2$:Fe remain the most promising chalcopyrite IBSC candidate. Its near optimal energy gaps give a radiative efficiency limit slightly above 46% as shown in Figure 2.3. $Ni^{4+/3+}$ and $Ni^{3+/2+}$ are expected to introduce an IB at around 1.24 eV and 2.06 eV above E_V, respectively, so the radiative limit for $CuGaS_2$:Ni is far below optimal as shown in Figure 2.3. Fe and Ni doping of $CuGaS_2$ and similar chalcopyrites are further described in Section 2.3. All IBs introduced by Fe and Ni are above the middle of the band gap, which is beneficial as it allows a second mode for promoting electrons into the CB, called energy transference [5]. In this mode, two electrons in the IB interact so that one is excited across E_L to
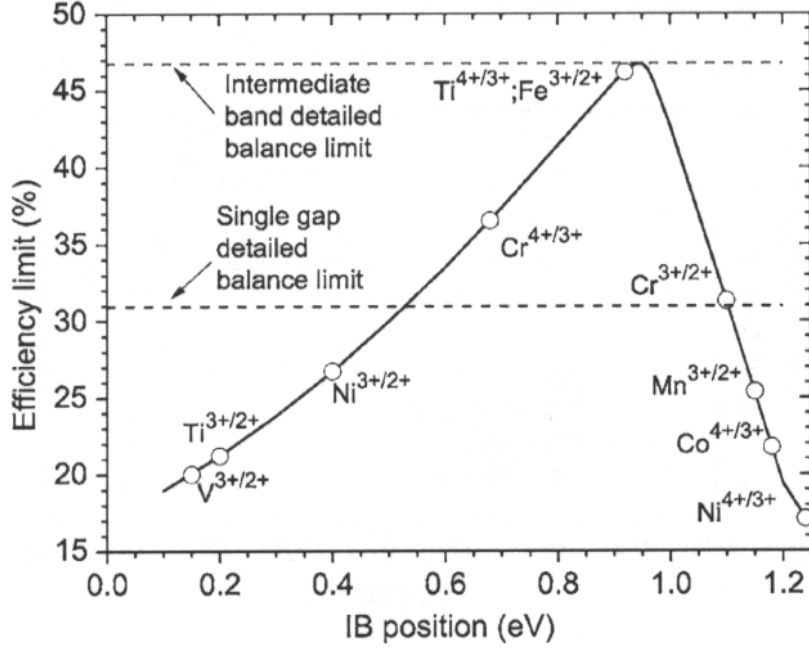
Figure 2.3: Radiative efficiency limits calculated from detailed balance calculations based on introduction of IBs at different energy levels in the CuGaS$_2$ band gap from transition metal doping (adapted from Martí et al. [3]).

the CB by the energy E_H as the other is relaxed to the VB. Thus, the current can be increased through IB operation without excitations from photon absorption across E_L. However, lower efficiency is expected for this mode as the energy difference between E_H and E_L is lost and photons of energies below E_H are not absorbed.

Impurity elements that introduce energy levels within the semiconductor band gap are detrimental to the performance of other p-n junction solar cells. This is because each electron state introduced is localized to the impurity element when the concentration is low. Localized electrons have different momentum compared to delocalized electrons in bands and recombinations to or from these energy levels require considerable momentum transfer from the electron to the crystal structure [1]. This process is called trapping and is a kind of non-radiative recombination and thereby represents heat loss. It is essential that the dopant have periodic distribution in the crystal structure and high enough concentration to make their electron states become delocalized and form the IB. Substitutional dissolution of the dopant might provide the necessary periodicity, but this might not be necessary at dopant concentrations above around $6 \cdot 10^{19}$ cm^{-3} according to Luque et al. [14]. Through a calculation of the concentration of CuGaS$_2$ formula units from the chalcopyrite unit cell shown in Figure 2.4 in Section 2.2 with the lattice parameters given in Table 2.1 in Section 2.2, this corresponds to substitution of 0.45% of the sites for one of the cations. The solubility of the dopant in the host crystal limits the combinations of host semiconductor and doping element in addition to their electronic structure. Other impurities as well as crystal defects that introduce localized electron states between the bands are also detrimental to the performance of IBCSs due to increased non-radiative recombination.

Grain boundaries tend to be particularly detrimental to photovoltaic materials as

crystal defects and impurities are concentrated, but polycrystalline copper indium dise-lenide (CuInSe$_2$) might even be a better electronic material than single-crystal CuInSe$_2$. This is because the grain boundaries have an energy barrier towards electron holes so that there are no empty states at grain boundaries that electrons in the CB can recombine to. Nevertheless, non-radiative recombination is expected to be significant in CuGaS$_2$ IB materials due to high defect densities within the grains, particularly in chalcopyrite materials with off-stoichiometry, as described in Sections 2.2 and 2.4.5. Furthermore, intrinsic defects can form localized energy levels within the band gap of CuGaS$_2$ [15], promoting non-radiative recombination. Thus, efficiencies far below the radiative limit is expected for any dopant introduced in CuGaS$_2$. In 2008, experimental CIGS solar cell showed current losses no less than 23%, which can only be a goal for the development of chalcopyrite IBSCs.

2.2 CuGaS$_2$ Crystal Structure and its Stability

The chalcopyrite crystal structure of CuGaS$_2$ incorporates two different cations in the cubic zinc blende lattice, in which all of either type of tetrahedral voids (T$_+$ or T$_-$) in a closed packed cubic (CCP) anion lattice are occupied. Thus the unit cell is approximately doubled along the c axis compared to the zinc blende unit cell, so that the chalcopyrite unit cell is tetragonal and the CuGaS$_2$ unit cell has a ratio of lattice parameters c to a of 1.95876. The lattice parameters for the tetragonal unit cell are reported by Abrahams and Bernstein [16] and reproduced in Table 2.1

The cations arrange so that two of each type, i.e. Cu$^+$ and Ga^{3+}, is the nearest neighbors to each sulphide anion, and the symmetry of chalcopyrite crystals is defined by the space group $I\bar{4}2d$ [16]. The atomic positions in the cell are given in Table 2.2, and it show that the sulphide anions are slightly distorted from their positions in zinc blende. This is seen from the value x being slightly above $\frac{1}{4}$. Based on the lattice parameters in Tables 2.1 and atom positions in Table 2.2, the CuGaS$_2$ unit cell is constructed in Figure 2.4.

Table 2.1: Lattice parameters for the CuGaS$_2$ unit cell, adopted from Abrahams and Bernstein [16].

a [Å]	b [Å]	c [Å]
5.34741 ± 0.00007	5.34741 ± 0.00007	10.47429 ± 0.00006

Table 2.2: Atom positions of the different elements in the CuGaS$_2$ unit cell, adapted from Abrahams and Bernstein [16]. The positions are given as fractions (x,y and z) of the lattice parameters a, b and c in Table 2.1.

Element	x	y	z
Cu	0	0	0
Ga	0	0	$\frac{1}{2}$
S	$0.25385 \pm 3.5 \cdot 10^{-4}$	$\frac{1}{4}$	$\frac{1}{8}$
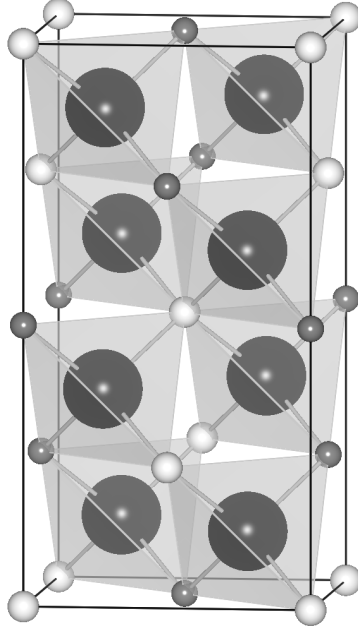
Figure 2.4: Unit cell of $CuGaS_2$ constructed in the VESTA software developed by Momma and Izumi [17] from the parameters in Tables 2.1 and 2.2 (adapted from Sortland [1]). ● S, ○ Cu, • Ga.

Defect formation in chalcopyrite crystals is important for their electronic structure as described in Section 2.1 and 2.4.5, and they may become high enough to create competing defect phases to the stoichiometric chalcopyrite crystal [1]. In respect to this, the Kröger-Vink defect notation is presented here through relevant examples:

Cu_{Cu}^{x} Cu^+ ion at a Cu site. This is not a defect, but part of the perfect crystal and thus has no charge compared to this reference.

$V_{Cu}^{'}$ A Cu site is vacant, and thus has a negative charge compared to the perfect crystal.

$Ga_{Cu}^{..}$ Ga^{3+} substitutes Cu^+, and the site get two positive charges.

$Cu_{i}^{.}$ Cu^+ introduce a positive elementary charge at an interstitial site.

The charge indication is sometimes omitted for simplicity.

Interaction between defects, for instance by charge transfer, allow very low formation energies. This is the observed for $(2V_{Cu}^{'}+In_{Cu}^{..})$ in copper indium diselenide ($CuInSe_2$), and similar pairing can also be expected in $CuGaS_2$. These defect pairs can further interact and form periodically to produce ordered defect compounds with different stoichiometries, like $Cu_3In_7Se_{12}$, $CuIn_3Se_5$ and $CuIn_5Se_8$ [18]. Similar competing phases of $CuIn_5S_8$ and $CuIn_{11}S_{17}$ to copper indium disulphide ($CuInS_2$) [19] help justifying drawing parallels between different I-II-VI chalcogenides.

Any phase consisting of Cu, Ga and/or S is a potential competing phase to formation of chalcopyrite $CuGaS_2$. $CuGaS_2$ is the only stable phase at some intermediate chemical potential ratios as shown in the stability diagrams in Figure 2.6. The chemical potential of each element must be negative to avoid precipitation of elemental Cu, Ga or S [6] provided elemental precursors or spontaneous reactions that may produce elemental Cu, Ga or S.

Furthermore the sum of the precursor chemical potentials must equal the free energy of formation of $CuGaS_2$ since the stability diagrams give chemical potentials at equilibrium. This gives the boundaries for the stability diagrams and the chemical potential of S can be found as the distance from the lower left boundary given by the $CuGaS_2$ formation energy, reaching half of the $CuGaS_2$ formation energy at the origin since its stoichiometric coefficient is two. The stability region at which $CuGaS_2$ is the only stable phase in the Cu-Ga-S system is seen between the CuS, Ga_2S_3 and GaS boundaries in Figures 2.6(a) and (b), which indicate that kinetic control is not required to form $CuGaS_2$.

At a high chemical potential of Cu and a low chemical potential of Ga, copper sulphides become stable, and vice versa for binary gallium sulphides. In these regions, kinetic control is necessary to obtain a pure product as all stable phases will form, but at different rates. A combination of two or more phases may also be more stable than either single phase. In such multiphase regions, kinetic control is necessary to achieve a pure product. The $CuGaS_2$ stoichiometry varies through defect formation, giving increasing Cu contents at increasing chemical potentials of Cu towards the stability region of copper sulphides and equivalently, Ga-rich $CuGaS_2$ is most stable at high chemical potential of Ga. Such off-stoichiometry can be identified through visual observation as stoichiometric $CuGaS_2$ is yellow, Cu-rich is black and Ga-rich $CuGaS_2$ is red [15]. The diagrams in Figures 2.6(a) and 2.6(b) are based on different calculations and show large differences. For instance, the formation energy of $CuGaS_2$ used in Figure 2.6(b) is -2.49 eV [20], while Bailey et al. [21] calculated the formation energy to be -1.58 eV for Figure 2.6(a).

Common impurities in previous development of the hydrothermal synthesis reported by Sortland [1] include copper(II) sulphide (CuS) and a off-stoichiometric digenite ($Cu_{2-\delta}S$) phase, both showing blue to black colors [22, 23], instead of Cu_2S used in the stability diagrams in Figure 2.6. The stability of this phase is shown in an excerpt of the Cu-S phase diagram in Figure 2.5. Abbreviations of the names for the different phases are used in this diagram, including Dg for digenite, Cv for covellite (CuS) and Ch for chalcocite (Cu_2S). Below 435 °C, digenite takes part in two-phase regions both with CuS at higher S contents and with Cu_2S at lower S contents, and the compositional range in which a single digenite phase is stable increases with increasing temperature below 490 °C.

Like $CuGaS_2$, digenite has a CCP lattice of S anions, but the distribution of Cu cations is complex [24], and it has been suggested that Cu occupy tetrahedral voids randomly like in a solid solution, but might also take distorted or completely other positions. The composition will also affect the number of Cu ions in the structure and this have shown to affect the XRD spectra [25], which can be due to different extents of expansion of the S sublattice and different extents of extinction of Bragg reflections from atomic planes of S by planes constituted by Cu. Bragg reflections are constructive interference of X-rays reflected from stacked atomic planes at an angle (Θ) to the incident beam, and is the origin of the peaks in a diffractogram. Digenite is stable for temperatures down to 73 °C at which it transforms to a metastable α-digenite polymorph, accommodating structural alterations in the stacking sequence of closed packed anion planes from cubic to hexagonal packing, which tend to accommodate stacking faults of the atomic planes. This transformation is found to take a few hours by rapid cooling to 0 °C, while the subsequent transformation to the stable phase of orthorhombic anilite (An) ($Cu_{1.75}S$) require several months at room temperature.
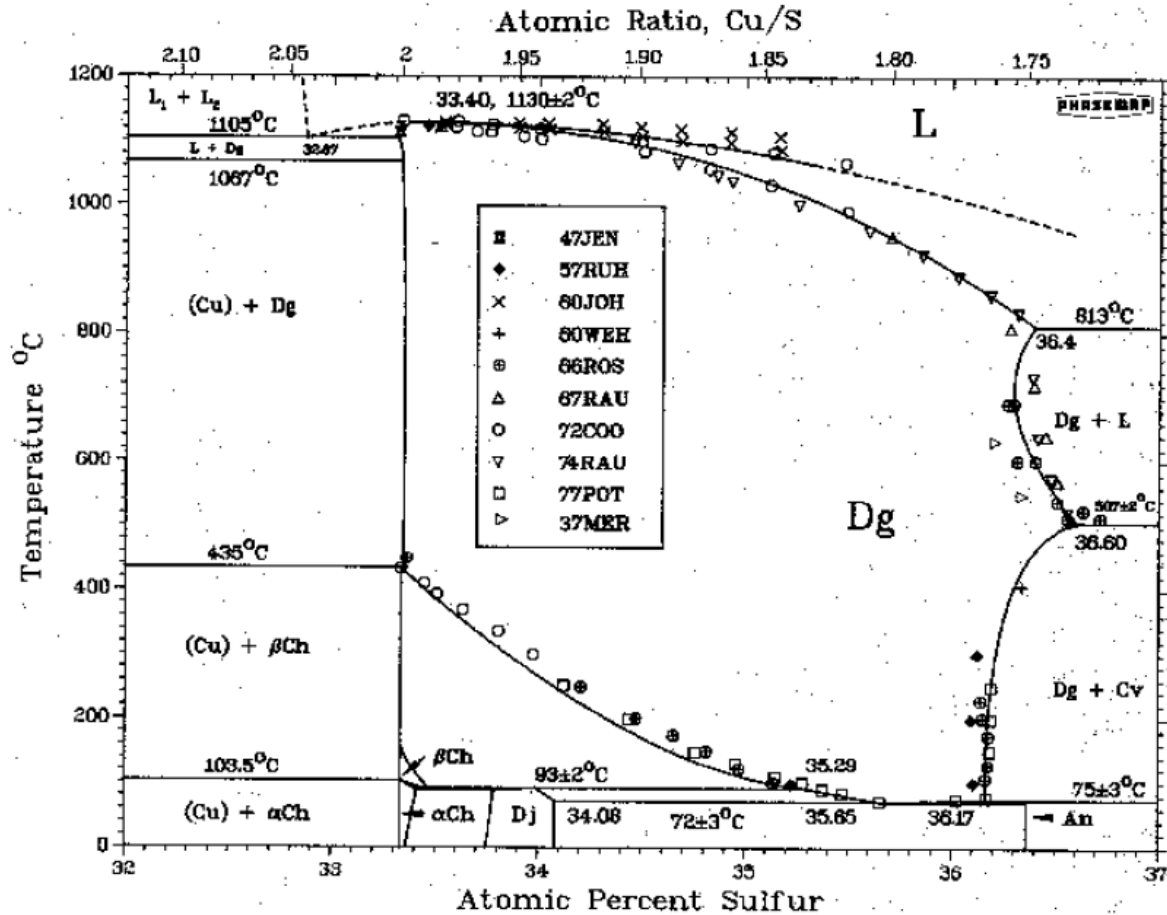
Figure 2.5: Phase diagram for the Cu-S binary system (adapted from Chakrabarti and Laughiln [25]).

For a complete analysis of competing phases in a given synthesis, all elements introduced must be included, and thus oxides, hydrides, chlorides and principally compounds of C and N from the Tu reactant can potentially form competing phases for the hydrothermal synthesis presented here. However, a low solubility in water is necessary for formation of impurity phases in hydrothermal syntheses, and this is the basis for selecting chloride precursors. For doping of $CuGaS_2$ with Fe and Ni, iron or nickel sulphides are probable competing phases due to their low solubility in water. Equilibrium chemical potential of S for formation of different nickel sulphides are shown as red lines in Figure 2.6(b) and their stability regions stretches to the diagram boundary at $\mu_S = 0$. The limiting case of $\mu_{Ni} = 0$, at which elemental Ni becomes stable, is used to calculate the minimum chemical potentials of S for formation of the different nickel sulphides [6]. NiS reduces the $CuGaS_2$ single-phase region to the shaded area of Figure 2.6(b) while Ni_3S_2 is a stable secondary phase in the entire $CuGaS_2$ stability region so that kinetic control may be required to prevent its formation. However, the formation of different impurity phases also requires spontaneous reactions to provide the proper oxidation states of the constituent elements, so utilizing a divalent nickel precursor may prevent formation of Ni_3S_2 as a spontaneous oxidation of nickel is required for its formation. Both NiS and NiS_2 contain divalent Ni, and vaesite (NiS_2) has the same cubic structure as iron pyrite (FeS_2), with S^- anions [26].

11
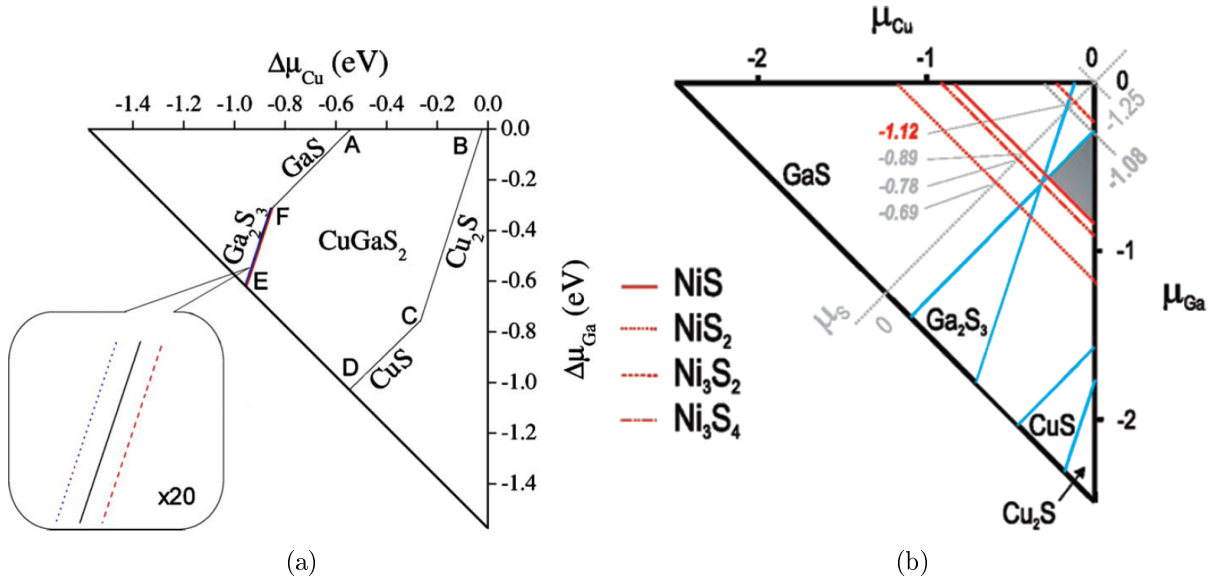
Figure 2.6: Calculated stability diagrams for the Cu-Ga-S system, adapted from Bailey et al. [21] (a) and Tablero and Fuertes Marrón [6] (b). Part 2.6(a) includes an inset showing the equilibrium conditions for the defect compounds $CuGa_3S_5$ (dotted blue line) and $CuGa_5S_8$ (dashed red line), while part(b) includes competing nickel sulphide phases .

The stability region of $CuGaS_2$ is expressed in terms of the stoichiometry of the constituent elements in the ternary phase diagram in Figure 2.7. This phase diagram shows which phase or combination of phases give the lowest free energy in a limited composition range from stoichiometric $CuGaS_2$ at room temperature. The darkest area is the stability region of chalcopyrite $CuGaS_2$. It accommodates the ordered defect compounds and show the stable off-stoichiometries of $CuGaS_2$. The stability region shows extensions toward high S contents and low Cu contents [1]. Stoichiometric $CuGaS_2$ is at the intersection between the $CuS - GaS$ and $Cu_2S - Ga_2S_3$ joins near the edge of the stability region towards the lower left corner, which indicate that highly Cu-rich chalcopyrite is not stable as a single phase. At slightly increased Cu content from stoichiometric $CuGaS_2$, a mixture with copper sulphide impurities become stable, while mixtures with Cu-Ga alloys become stable at reduced S content.

12
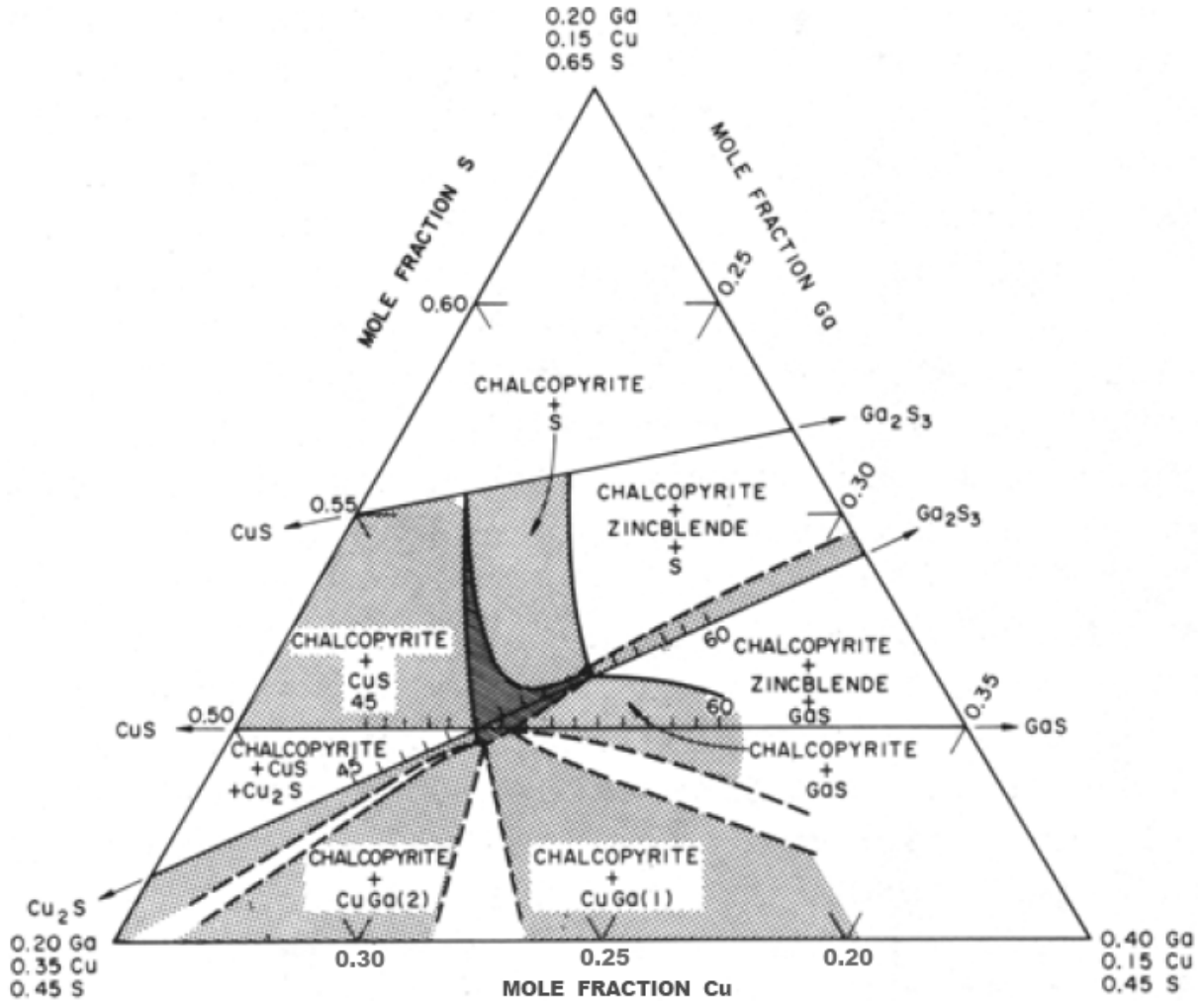
Figure 2.7: Phase diagram for the Cu-Ga-S ternary system in a limited composition range at room temperature. The darkest area show the stability region of pure $CuGaS_2$ (adapted with modifications from Kokta et al. [27]).

2.3   Doping of $CuGaS_2$

Modified $CuGaS_2$ for IBSC applications also requires a certain solubility so that the dopant can be introduced in high enough concentration to form the IB and reaction conditions where they do not form impurity phases with Cu, Ga and/or S can be found [1]. Stability calculations by Tablero and Fuertes Marrón [6] suggest that Fe and Ni, along with Co, Ge, Ir, Ni, Pd, Rh, Si and Sn, might have high enough solubility in $CuGaS_2$ for IBSC applications.

$CuGaS_2$:Fe is the most studied of the $CuGaS_2$ modifications investigated in this work, but as with Ni doping, no experimental studies are concerned with IB formation for solar cell applications. Fe is completely soluble in chalcopyrite $CuGaS_2$, accommodating a linear decrease in the a axis of the unit cell and an increase in the c axis up to a maximum at 25% Ga substitution [28]. The relaxation of the crystal structure described above only takes place for substitution at In sites in $CuInSe_2$, which correspond to Ga sites in $CuGaS_2$, and substitution at Cu sites does not lead to a considerable alteration of the

CuInSe$_2$ crystal. The site of substitution can be controlled by stoichiometry as Ga-rich crystals have Cu vacancies ready to accommodate Fe^{2+}, which is achieved at chalcopyrite growth conditions with low chemical potential of Cu [29], while Ga substitution is preferred in stoichiometric [6] and Cu-rich crystals [30].

According to Tanaka et al. [31], Fe^{3+} easily substitutes Ga where it is electrically inactive in a trivalent state. In their synthesis, Fe^{2+} in FeS substituted Ga by oxidation to Fe^{3+}, while theoretical studies [6, 29] suggest that Fe^{2+} also can substitute at Cu sites through a reduction to Fe$^+$. Fe$_{Cu}^{x}$ substitution requires a high concentration of Cu vacancies to be favorable, as the oxidation state of $+$I for Fe$^+$ is uncommon due to its low stability [1]. Raulot et al. [29] explained these oxidation states of Fe in CuInSe$_2$ by the fact that the electronegativity of Fe is between those of Cu and In. At In sites, Fe^{3+} can take up an electron from the VB as it is reduced to Fe^{2+} so that holes are created in the VB, making Fe$_{In}$ an acceptor defect [29]. However, at high enough doping for IB formation, the energy states related to Fe are delocalized as well, so electrons remain mobile upon excitation to or from these states. Actually, the desired half-filling of the IB gives metallic conductivity. Each Fe$_{Cu}$ substitution introduces a V$_{Cu}^{'}$ instead, indicating that the formation energy of V$_{Cu}^{'}$ is lower than E_G. A similar oxidation from monovalent to divalent Fe at Cu sites makes Fe$_{Cu}^{x}$ a donor defect at concentrations below those forming an IB.

Both sites of Fe substitution can give an IB according to Tablero and Fuertes Marrón [6], although Fe$_{Ga}$ provide an IB close to the middle of the band gap while the IB introduced by Fe$_{Cu}$ at 25% substitution is calculated to form near the CB. Thus, Fe$_{Ga}$ substitution can provide the highest IBSC efficiency according to Section 2.1. In the case of Ga substitution, the IB is empty in the ground state at 0 K and in the case of substitution of Cu, E_F is at the top of the IB for a doping concentration of 25% cation substitution. However, E_F can be adjusted to the middle of the IB by stoichiometry control described in Section 2.4.5, although at the expense of increased non-radiative recombination losses in off-stoichiometric crystals [1]. The calculated DOS shows two peaks in the IB for both substitutions. These correspond in both cases to absorption bands at 1.40 eV and 1.86 eV above the VB top in absorption spectra of CuGaS$_2$:Fe at impurity concentrations where the 3d states of Fe remain localized. These peaks originate from energy splitting of the Fe 3d orbital as Fe is situated in tetrahedral voids between neighboring S^{2-} anions in CuGaS$_2$. In such a tetrahedral crystal field, three of the d orbitals (d_{xy}, d_{xz} and d_{yz}) of transition metals like Fe and Ni, point towards the neighboring S^{2-} anions, causing an electrostatic repulsion between Fe and S electrons and thus an increase in energy. The remaining two d orbitals ($d_{x^2-y^2}$ and d_{z^2}) point between the neighboring S^{2-} anions as seen from Figure 2.8 and has a lower energy [32]. The three orbitals pointing towards the anions show a further energy splitting as they are combined with S orbitals pointing towards the tetrahedral void to form an antibonding electron state through hybridization. This results in three different energy states from Fe$_{Ga}$ substitution, of which one is within the valence band of CuGaS$_2$ and the remaining two are within the band gap [31]. The energy state within the band gap is responsible for a dark green coloration of Fe and Ni doped CuGaS$_2$, even at very low impurity concentrations.
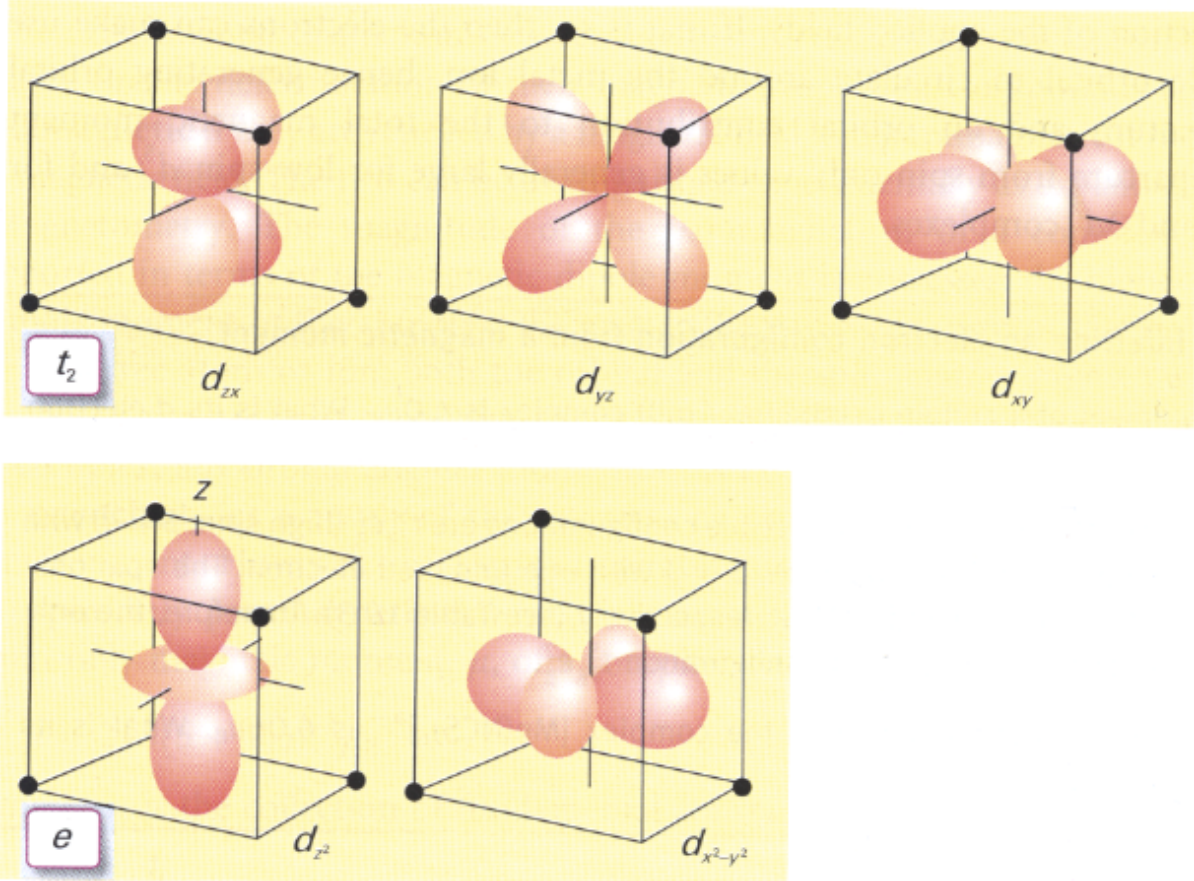
Figure 2.8: Geometry of 3d orbitals around the atom nucleus at origin. The black spheres represent S anions in tetrahedral coordination around the transition metal cation (adapted from Shriver et al. [32]).

These studies also reveal an increase in light absorption involving the energy levels in the band gap with increasing concentration of Fe. Similarly, an increase in the DOS of the IB at increasing dopant concentrations calculated by [6, 29] can cause increased light absorption [1]. Calculations by Tablero and Fuertes Marrón [6] show that Fe and Ni dopants introduce delocalized electron states in the band gap if they occupy 25% of Cu sites for Cu substitution or Ga sites for Ga substitution, along with 12.5% Fe_{Ga} substitution. Furthermore, half of this Fe concentration is sufficient for forming an IB the system $CuIn_15/16Fe_1/16Se_2$, and this dopant concentration is an order of magnitude larger than the required concentration suggested by Luque and Martí [5] and cited in Section 2.1. A difference in band structure between $CuGa_{7/8}Fe_{1/8}S_2$ and $CuGa_{15/16}Fe_{1/16}S_2$ suggests the dopant concentration to influence the range of available energy levels within the band gap, and Raulot et al. [29] calculated that an IB broadens to fill the band gap for Fe substituting 25% of the Cu or In sites of $CuInSe_2$. However, Tablero and Fuertes Marrón [6] calculated that the intermediate band is retained for this Fe concentration for both sites of substitution in $CuGaS_2$.

Which cation Ni substitutes is controversial, and both Ni^+ substitution at Cu sites and Ni^{3+} substitution at Ga sites have been reported [6, 33]. As with Fe^{2+}, the site of Ni substitution can be controlled by stoichiometry. The 3d orbitals of Ni^{3+} at Ga sites split

15

into the same three levels as for Fe^{3+}. Although these have slightly different energies from those at Fe^{3+}, the two highest remain in the $CuGaS_2$ band gap. For Ni^+ substitution at Cu sites, all degeneracy between the 3d orbitals is broken in the distorted tetrahedral crystal field as shown by Kaufmann [33], resulting in a total of five energy levels originating from the 3d orbitals. Polarized adsorption spectrum measured by Tanaka et al. [31] reveals a broad absorption band in Ni^+ doped $CuGaS_2$ similar to that from doping with Fe^{3+}, and its maximum at 1.84 eV also resembles that of $CuGaS_2$:Fe. Calculations by Tablero and Fuertes Marrón [6] show two close peaks in the total DOS of which the lower extends the VB and the higher energy peak make up an empty IB if Cu is substituted. Ni_{Ga} substitution does not produce an IB at all.

2.4   Hydrothermal Synthesis

The traditional method for synthesizing $CuGaS_2$ is by solid-state reactions that require high temperatures to overcome the energy barrier and provide sufficient interdiffusion of the solid reagents to keep the reaction time within days or hours [34]. In a hydrothermal synthesis, the crystals are grown from a solution of mobile reactants, so that high temperatures are not necessary for sufficient diffusion [1]. In addition, metastable phases can be prepared by hydrothermal synthesis through kinetic control while the high temperatures of solid-state reactions generally only form the thermodynamically stable product. Traditional precipitation from a homogeneous solution would require post-annealing at about 800 °C to obtain crystalline products [35], while hydro- and solvothermal methods have proven to form $CuGaS_2$ crystals at 160 °C [8], and the similar compound $CuInS_2$ can form at temperatures down to $120 - 150$ °C [36].

As water is the solvent in hydrothermal synthesis, it is considered an environmentally clean method preferable to large-scale, industrial production. It does not rely on expensive equipment and together with the use of aqueous solutions and comparably low temperatures, it is a also an inexpensive synthetic route [37]. Hu et al. [8] suggested a hydrothermal synthesis to be one of the most promising solution chemical methods for synthesis of $CuGaS_2$ as it allows for control of particle size and their distribution as well as morphology in addition to the crystallinity and stoichiometry of the product. Hydrothermal synthesis can be defined as reactions in aqueous solutions occurring at high temperatures and pressures, i.e. above the boiling point of water and above atmospheric pressure, in closed systems [37]. The only difference between hydrothermal and solvothermal synthesis is that pure water is the solvent in hydrothermal synthesis, while solvothermal synthesis uses any other solvent, even diluted with water.

Hydrothermal syntheses are carried out in autoclaves, which in general are sealed containers that can maintain pressure build-up. Autoclaves are often fitted with a cup and lid of polytetrafluoroethylene (Teflon) that prevents corrosion of the stainless steel container in strongly acidic and also alkaline solutions, but it will also delay heating due to its insulating properties [34]. Figure 2.9 show the different parts of an autoclave. Evaporated water in the autoclave increases the pressure, which in turn prevents complete evaporation as it shifts the evaporation equilibrium. The obtained pressure depends on the solvent used in solvothermal syntheses and principally also dissolved species giving boiling point elevation [1], but only up to a certain temperature and fill factor, which is the percentage of the autoclave filled with solution. This domain is shown as the part

16

of the curves with no or little slope in Figure 2.10 and as the evaporation equilibrium governs the pressure, the fill factor has principally no influence on the pressure in this domain. The break in the curve indicate the temperature at which thermal expansion causes the solution to completely fill the autoclave at a given initial fill factor. Further thermal expansion makes the liquid compressible as there is no more volume available, and this leads to a rapid increase in pressure with increasing temperature. This poses a risk to the pressure limitations of the autoclave. The temperature and pressure might approach the supercritical domain of water, although supercritical fluid is usually not utilized in hydrothermal synthesis, and have not been used in $CuGaS_2$ syntheses. Such hydrothermal conditions give drastically increased solubility compared to solutions at atmospheric pressure, and also more heat is provided to overcome the energy barrier of crystallization from the solution. Also, the viscosity of water decreases with increasing temperature, which is thought to increase the mobility of dissolved species [34].
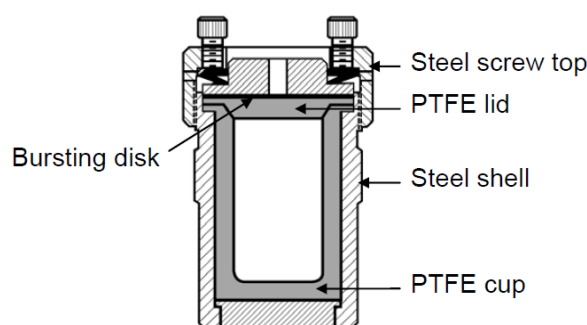
Figure 2.9: Schematic drawing of an autoclave (adapted from Rørvik [38]).
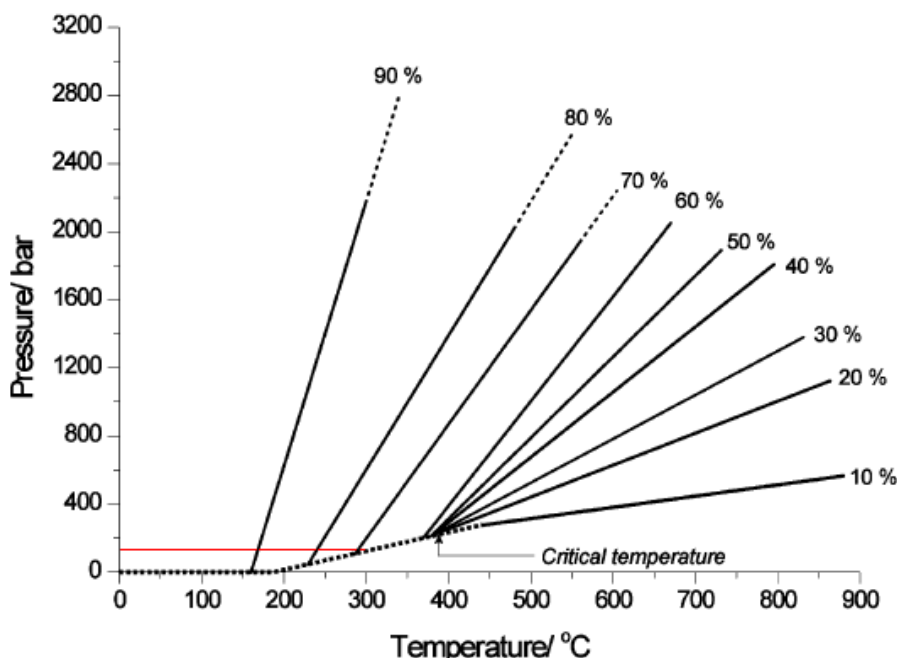
Figure 2.10: Pressure as function of temperature and fill percentage of water in a sealed vessel. The red line show the operating pressure limit for the autoclaves used in the syntheses (adapted with modifications from Walton [34]).

In the hydrothermal syntheses presented in this work, CuCl, GaCl$_3$ and Tu are dissolved in distilled water to make CuGaS$_2$. Ga^{3+} ions in aqueous solution has a very strong tendency to hydrolyze to GaOH^{2+} at low H$^+$ concentrations [39], and combined with Cl$^-$ ions, the reaction in Equation (2.2) can be constructed for the dissolution of GaCl$_3$ [1].

$$GaCl_3 \text{ (s)} + H_2O \text{ (l)} \rightarrow GaOH^{2+} \text{ (aq)} + HCl \text{ (aq)} + 2Cl^- \text{ (aq)} \qquad (2.2)$$
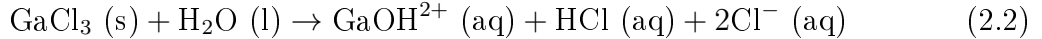
The HCl produced is corrosive, and along with dissolution and decomposition of Tu, it makes the reaction solution acidic. Although CuCl has high solubility in HCl solutions of high concentrations, it is only slightly soluble in neutral water [40]. CuCl has been reported to be insoluble in 1 M HCl, but soluble in 5 M HCl [41]. The need for hydrothermal conditions in the synthesis is thus represented by the low CuCl solubility. CuCl that is not dissolved reacts with water as monovalent copper ions are oxidized to a divalent state to form copper(II) hydroxychloride (Cu(OH)Cl). This is a slow reaction in air as Lampe-Önnerud et al. [42] found that significant oxidation of Cu$^+$ in CuCl to Cu^{2+} in Cu(OH)Cl requires days in air. Cu(OH)Cl has a bright green color while pure CuCl is white as a powder.

2.4.1 Debye-Hückel Theory

Debye-Hückel theory is used for calculation of chemical potential of single ions in solutions. An ion in solution interacts with a polar solvent to form a solvation sheath, in which solvent species like H$_2$O are attracted to and arrange around the central ion by electrostatic forces between the charged ions and aligned dipoles [43]. Such stabilization is the only ion interactions in an ideal solution, which thus is at infinite dilution. In real solutions, ions will also interact with each other, giving rise to non-ideality expressed through the activity coefficient (γ) in Equation (2.3). In this equation, μ_i is the chemical potential of the ionic specie denoted i, and μ_i^0 is the chemical potential of this specie in solution at the standard molality of 1 mol/kg. The molality expresses the amount of dissolved species per mass of solvent, and for dilute aqueous solutions it can be replaced by the concentration (C_i) as in Equation (2.3), since the density of water is approximately 1 kg/dm^3 [44] and dilute solutions will have a limited volume expansion upon dissolution. The standard molality is thus repaced by a standard concentration (C_i^0) of 1 mol/dm^3 in Equation (2.3), which also contain the Boltzmann constant (k_B) and the Avogadro constant (N_A).

$$\mu_i = \mu_i^0 + k_B N_A \ln \gamma_i \frac{C_i}{C_i^0} \qquad (2.3)$$

Debye-Hückel theory explained by Hamann et al. [43] allows for estimation of the activity coefficient in terms of the concentration of ions for dilute solutions for which the radius of the solvation sheet is very much larger than the diameter of the central ion. The relation in Equation (2.4) is the Debye-Hückel limiting law. It shows that the activity coefficient varies with ionic strength (I) of the solution, which has contributions from all ionic species according to the definition in Equation (2.5) using concentrations instead of molalities. The charge number (z) is the valency of the ionic specie, the relative permittivity (ε_r) is a solvent parameter, and the vacuum permittivity (ε_0) and elementary

charge (e) are constants.

$$\ln \gamma_i = -\frac{z_i^2 e^3 N_A^{\frac{1}{2}}}{4\pi(\varepsilon_0 \varepsilon_r k_B T)^{\frac{3}{2}}} \sqrt{\frac{I}{2}} \tag{2.4}$$

$$I = \frac{1}{2} \sum_i z_i \frac{C_i}{C^0} \tag{2.5}$$

Although the activity coefficient varies with temperature and also pressure through the relative permittivity of water as the solvent [45], it does not account for the dependence of chemical potential on temperature and pressure deviations from 25 °C in the standard state of 1 bar. The molar heat capacity at constant pressure (c_p) allows for a simple estimation of the temperature dependence shown in Equation (2.6), in which $\Delta_f G^0$ is the standard free energy of formation at 298.15 K. This estimation is made inaccurate by the linear approximation and the pressure is not constant during heating of the autoclaves.

$$\mu_i^0 = \Delta_f G^0 + c_{p,i}(T - 298.15 \text{ K}) \tag{2.6}$$

2.4.2 Proposed Mechanisms for Reactions in Water and Ethanol

Similar hydrothermal syntheses of $CuGaS_2$ and $CuInS_2$ to that presented here have been reported by Hu et al. [8], Das et al. [46] and Feng et al. [36]. Hu et al. [8] reacted CuCl, $GaCl_3$ and Tu in water at 160 °C for 5 h, while Feng et al. [36] and Das et al. [46] used a solvothermal method with ethanol in which indium(III) chloride ($InCl_3$) is used to form $CuInS_2$ at $120 - 200$ °C for $2 - 12$ h. Hu et al. [8] proposed a reaction mechanism in which dissolved CuCl and Tu form $[Cu(Tu)_x]^+$ complexes. Das et al. [46] reported on the formation of indium-thiourea complexes also in ethanol, and suggested that also complexes between Ga and Tu might form. These complexes are thought to decompose to release Tu molecules that slowly react with water or ethanol to form sulphide ions (S^{2-}) according to Equation (2.7) [47] in water and (2.10) in ethanol. In water, this complex decomposition leave behind dissociative Cu^+ ions, which finally can combine with Ga^{3+} and S^{2-} ions to grow $CuGaS_2$ crystals in an ion-by-ion mechanism. Direct decomposition of $[Cu(Tu)_x]^+$ complexes to a solid sulphide phase is also possible in a complex decomposition ion-by-ion mechanism [47], and whether such complexes dissociate or not before crystallization of the sulphide can usually not be confirmed in experiments. However, such a mechanism is complicated for $CuGaS_2$ precipitation without intermediate phases, like the one proposed by Hu et al. [8], as this requires Ga^{3+} to take part in the complex decomposition to form $CuGaS_2$.

Tu requires about 130 °C [48] to decompose in ethanol according to Feng et al. [36], which gives a lower limit to the reaction temperature, but it has been reportet to decompose at 90 °C and above in water [49]. Decomposition of Tu in acidified water in Equation (2.7) [47] and precipitation of $CuGaS_2$ in Equation (2.8) summarize the reaction mechanism proposed by Hu et al. [8]. Cyanamide (CN_2H_2) have been found as impurities along with its hydrolyzed compounds.

$$SC(NH_2)_2 \rightarrow S^{2-} + CN_2H_2 + 2H^+ \tag{2.7}$$

$$Cu^+ + Ga^{3+} + 2S^{2-} \rightarrow CuGaS_2 \tag{2.8}$$
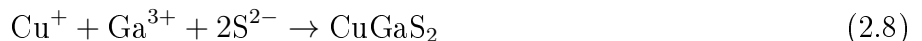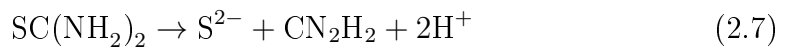
Tu decomposition is slow and often driven by a shift in the equilibrium due to sulphide precipitation in various sulphide chemical solution depositions [47]. Ideally, the sulphide with the lowest solubility product is preferentially formed as its precipitation limits the S^{2-} concentration below the limit for less stable sulfides [1]. Since the Tu decomposition proceeds towards equilibrium during syntheses and its rate decreases as the concentration of Tu decreases, precipitation can come to a halt before the precursors are depleted. An alternative Tu decomposition becomes possible in acidic solutions, given in Equation (2.9). This decomposition release thiocyanate (CNS^-) and can lead to deposition of thiocyanates instead of sulphides [47]. Furthermore, evolution of hydrogen sulphide (H_2S) gas is a potential competing reaction to the precipitation of sulphides in acidic solutions as H_2S has a pKa value of 7.02 [44], and protonation of S^{2-} to SH^- and H_2S is promoted by increasing acidity.

$$SC(NH_2)_2 \rightarrow NH_4^+ + CNS^- \tag{2.9}$$

Hydro- and solvothermal formation of $CuInS_2$ have been more extensively studied than the formation of $CuGaS_2$. However, the reports on formation of $CuGaS_2$ show similarity with those on $CuInS_2$ formation as indicated by a comparison of Hu et al. [8] and Feng et al. [36], so reports on $CuInS_2$ that show similarities with Hu et al. [8] are included to explore the reaction mechanism. It can also be mentioned that Lu et al. [35] showed that the formation of $CuInS_2$ and $CuGaS_2$ can follow the same mechanism, although one slightly different from that presented here as elemental In or Ga and S powders were reactants. Such similarities are also expected for syntheses of chalcopyrite selenides instead of sulphides, which is supported by the simultaneous treatment of both $CuInS_2$ and $CuInSe_2$ by Jiang et al. [50]. These similarities are principally due to In being in the same group of the periodic table as Ga, and also S and Se are both in group VI, which implies that their valence electrons have the same configuration so that their bonding characteristics are similar [1]. Due to these similarities, different chalcopyrite systems may in some regards be treated under the collective term I-III-VI chalcopyrites. Nevertheless, slight differences between the systems are to be expected, so comparisons can in general not be done with absolute certainty. For instance, Gurin [19] found the possibility of formation of $CuGaS_2$ from an aqueous solution lower than those for $CuInS_2$ and $CuInSe_2$, although this is in view of a colloidal synthesis and not under hydrothermal conditions.

Feng et al. [36] found CuS to form in ethanol at short reaction times of $2-4$ h, while 6 h was sufficient for crystallizing $CuInS_2$ as the only product, and they suggest that CuS as well as indium(III) sulphide (In_2S_3) form as steps in the reaction mechanism. Also Das et al. [46] reported on the formation of CuS and In_2S_3 byproducts from solutions of excess of CuCl and excess of $InCl_3$, respectively. The formation of CuS from solutions with CuCl indeed requires the Cu^+ from decomposition of copper-thiourea complexes to be oxidized to Cu^{2+} before combining with S^{2-} from decomposition of Tu [1]. Decomposition of indium-thiourea complexes require about 180 °C to form In_2S_3 with high crystallinity according to Das et al. [46]. In_2S_3 is proposed as an intermediate compound for formation of $CuInS_2$ also at lower temperatures. Feng et al. [36] achieved increased crystallinity of the $CuInS_2$ product at 180 °C, indicating that the crystallinity of the chalcopyrite product might depend on the crystallinity of the CuS and In_2S_3, or possibly Ga_2S_3, intermediate products. The reaction steps proposed by Feng et al. [36] for synthesis of $CuInS_2$ from CuCl, $InCl_3$ and Tu in ethanol are summarized in Equations (2.10)–(2.13). S^{2-} can form

from dissociation of the acid H_2S in Equation (2.10).

$$SC(NH_2)_2 + C_2H_5OH \rightarrow H_2S + CO_2 + NH_3 \tag{2.10}$$

$$Cu^{2+} + S^{2-} \rightarrow CuS \tag{2.11}$$

$$In^{3+} + S^{2-} \rightarrow In_2S_3 \tag{2.12}$$

$$2CuS + In_2S_3 \rightarrow 2CuInS_2 + S \tag{2.13}$$
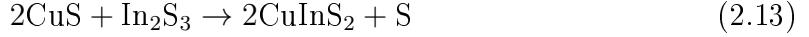
Equations (2.11)–(2.13) can be envisaged to occur also in aqueous solutions, based upon their similarities with the mechanism proposed by Hu et al. [8], as summarized in Equations (2.7) and (2.8). The decomposition of Tu has its equivalent in water as shown in (2.7), and the chalcopyrite crystals form through combination of dissociative ions in both water and ethanol. Furthermore, both CuS and In_2S_3 are insoluble also in water [1], so their formation as intermediate products can be considered a possibility in aqueous solutions as a competing mechanism to the direct crystallization of the chalcopyrite product proposed by Hu et al. [8]. In addition, the final solid state reaction proposed for the synthesis in ethanol does not involve the solvent and may equally well proceed in the precipitate of an aqueous solution. However, Ga_2S_3 does not form in aqueous solutions [44] as Ga^{3+} is easily hydrolyzed into hydroxide complexes, depending on pH. Gallium(III) hydroxide ($Ga(OH)_3$) precipitates fast from aqueous solutions at pH ≤ 5 as a step in the synthesis of gallium(III) hydroxyoxide ($GaO(OH)$) and quickly transform into this product [20]. Increasing acidity inhibit the hydration of Ga^{3+} ions, and at pH ≈ 4, $Ga(OH)_2^+$ has its maximum occurrence and $Ga(OH)^{2+}$ has its maximum at pH ≈ 3, but the pH must be decreased below 1 to prevent hydration of Ga^{3+} ions in water at ambient conditions. Accompanying the decomposition of urea ($OC(NH_2)_2$), pH = 2.8 is sufficient for precipitation of $GaO(OH)$.

2.4.3   Nucleation and Crystal Growth

The precipitation occurs as the S^{2-} ions released by decomposition of Tu cause a certain supersaturation of the solution. Any fluctuations in this supersaturated solution promote nucleation of the thermodynamically favored solid phase [51] through combinations of ions like in Equation (2.8) in Section 2.4.2. The main contributions to the free energy of nucleation is a bulk term representing the bulk free energy gain from formation of a solid phase from the supersaturated solution ($\Delta\mu$), which for a spherical nucleus of radius r is $-\frac{4}{3}\pi\Delta\mu r^3$, and the surface energy of $4\pi\Gamma r^2$, in which Γ is the surface tension. This relation is expressed in Equation (2.14) and plotted as a function of the radius in Figure 2.11. The critical free energy ($\Delta_c G$) of $\frac{16\pi\Gamma}{(3\Delta\mu)^2}$ required for formation of nuclei with a critical radius (r_c) of $-2\frac{\Gamma}{\Delta\mu}$ represents a barrier for precipitation and shows the necessity of supersaturation. The critical radius represents the minimum size of a nucleus required for spontaneous growth into a particle, as smaller nuclei dissolve spontaneously [52]. Thus, the critical size represents a lower limit to the particle sizes in the precipitate, and this can be reduced by increasing supersaturation giving a larger bulk energy gain ($\Delta\mu$) [53].

$$\Delta G(r) = -\frac{4}{3}\pi\Delta\mu r^3 + 4\pi\Gamma r^2 \tag{2.14}$$
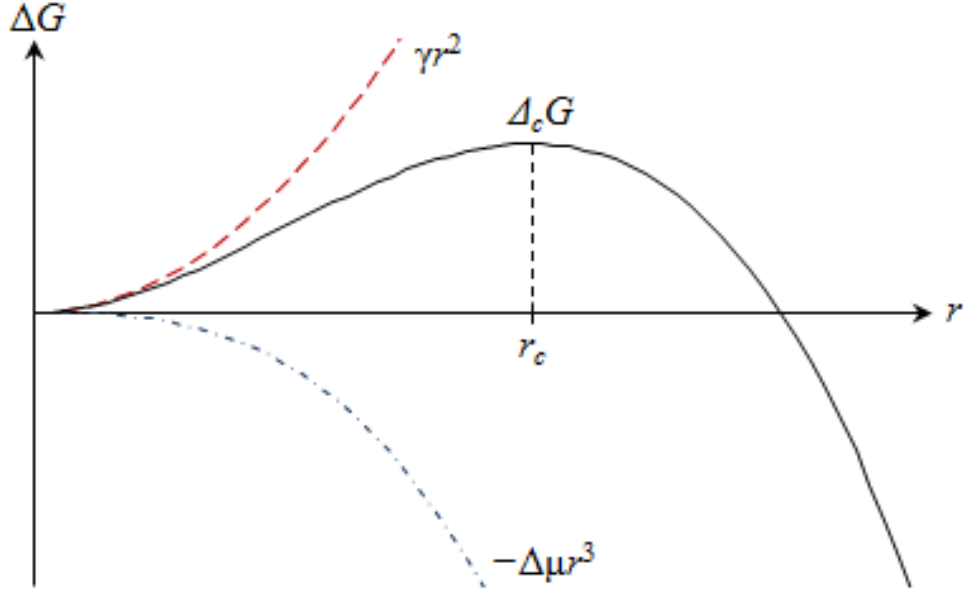
Figure 2.11: Plot of the contributions to the free energy for nucleation and the total free energy with its critical point.

Compared to homogeneous nucleation within the solution, heterogeneous nucleation at an existing interface, such as a substrate, container wall or a previously grown particle, can occur closer to equilibrium. Heterogeneous nucleation requires that the $CuGaS_2$ deposit wets the substrate, which represents a decrease in surface energy at the nucleus surface facing the substrate compared to that towards the solution. Heterogeneous nucleation thus results in a lower critical free energy of nucleation and also reduced critical nucleus size. The slow release of S^{2-} from Tu decomposition can for instance be utilized for film growth on a substrate if sufficient supersaturation for homogeneous precipitation in the solution is not reached, and only heterogeneous nucleation occurs [47]. If the ions interact more strongly with each other in $CuGaS_2$ than with the substrate species, the nucleation mode called island growth is predominant. In this mode, the ions in solution nucleate to small islands on the substrate due to limited wetting, and these coalesce to a film upon subsequent growth [53].

In case of complete wetting, in which the deposited ions show equally strong or stronger interactions with the substrate species compared to each other, the layer growth mode takes place. It is characterized by direct growth of a monolayer before subsequent atomic layers are grown. Layer growth may form single crystal films by strict control of growth conditions [53]. Single crystal films may be grown through either homoepitaxy, in which the substrate is the same crystalline material as the deposit, or heteroepitaxy, in which the substrate crystal is a close match to the film material. The diamond crystal structure of Si is similar to the chalcopyrite structure explained in Section 2.2 as the atomic positions are the same in diamond and zinc blende structures, so the only difference is that there are identical atoms in all positions in Si as well as the slight distortions of atomic positions and unit cell parameters in chalcopyrite compared to two stacked zinc blende unit cells. The cubic lattice parameter of Si of 5.43102 Å [54] does not match with the a and b parameters of $CuGaS_2$ of 5.34741 Å, and this mismatch is increased along the c axis of the unit cells. Such lattice mismatch can result in island-layer growth, which is

an intermediate combination of the aforementioned nucleation modes. Depositions following this mode start as layered growth, but the lattice mismatch cause stress and thus strain energy to build up during deposition. The strain energy eventually surpasses the surface energy and island growth takes over as nuclei start to form on the epitaxial film.

Figure 2.12(a) shows the process of nucleation and growth. Supersaturation is obtained as the concentration of S^{2-} builds up from initial Tu decomposition in stage I. At sufficient supersaturation to overcome the critical free energy of nucleation, represented by C_{min}^{nu}, nucleation starts and the nucleation rate increases rapidly as shown for stage II in Figure 2.12(b) [53]. After formation of a sufficiently large nucleus, it will grow by a diffusion controlled transport of ions to energetically favored sites on the crystal surface [55]. Crystal growth becomes a significant path for precipitation after a large number of stable nuclei are formed, since the growth rate is also high at the high supersaturation in stage II. Nucleation can continue as long as the supersaturation is sufficient for overcoming the critical free energy of nucleation, but due to this energy barrier, nucleation stops when the concentration of the ions in solution is reduced below the minimum supersaturation for nucleation. However, precipitation can continue in stage III through growth of the existing particles. Inhomogeneities like concentration and temperature gradients may give different rates of nucleation and growth, although the slow decomposition of Tu limits concentration gradients, and this helps to narrow the size distribution of nuclei and particle growth rates.

(a)   (b)
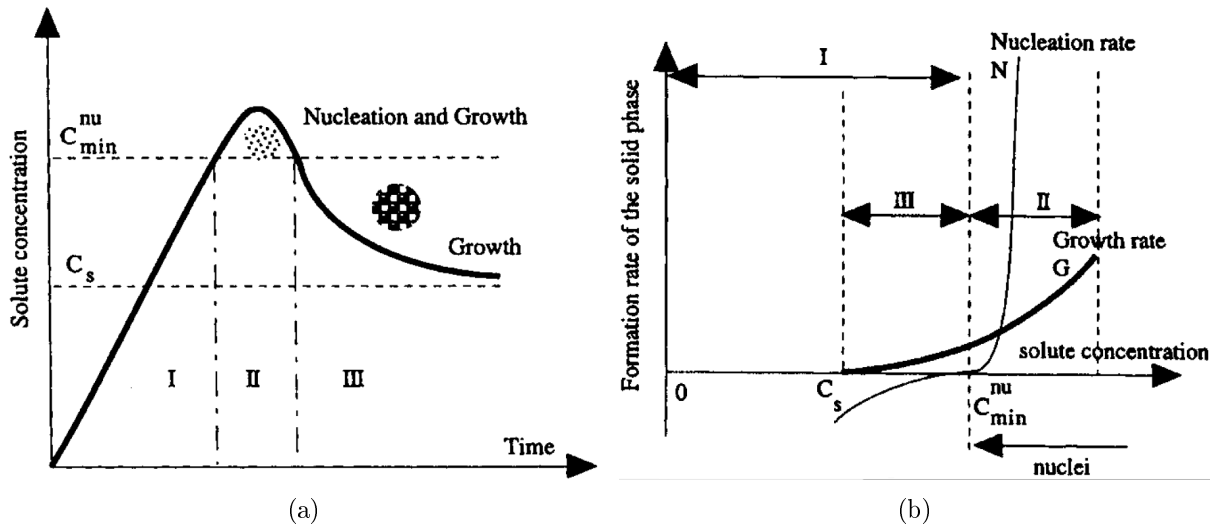
Figure 2.12: Schematic concentration evolution during different stages of nucleation and growth (a) and schematic nucleation and growth rates as a function of concentration in the different stages (b) (adapted with modifications from Cao [53]).

As supersaturation diminishes and the solubility concentration (C_s) at equilibrium is approached, further precipitation slows down. However, the morphology continues to evolve through dynamic dissolution and crystallization at equilibrium through recrystallization, aging and aggregation [1]. As larger particles are thermodynamically favored, this dissolution and recrystallization generally cause large particles to grow at the expense of smaller particles through Ostwald ripening, although this process becomes less important with reduced solubility [53]. During such aging, the size distribution of parti-

cles increases while their numbers decrease [55]. The small crystal dimensions that are commonly produced in hydro- and solvothermal syntheses have high specific surface areas and surface energies, which allow them to easily aggregate into polycrystalline particles [56]. Furthermore, particles can associate by weak bonds to form agglomerates, provided they are not separated by electrostatic repulsion due to adsorption of anions in solutions without surfactants [52].

Both ethanol and water are non-chelating solvents, meaning that they do not form complexes in which a ligand molecule is attached to the central ion, i.e. Cu^+, at two points [57]. Such non-chelating solvents can not direct the growth of crystals and mainly irregular particles and spheres are produced from random orientation of crystallites in polycrystalline particles [36, 58]. However, single crystals may form specific shapes due to differences in the number of bonds exposed to the solution for different crystallographic planes [59]. High-index planes expose more bonds that can bind to species in solution than low-index planes, and high-index planes can thus grow faster as dissolved species are more favorable attached to such a surface. This difference in growth rate for different crystallographic planes predominantly leaves the more slowly growing low-index planes exposed to the solution. This is also thermodynamically favored as the comparably few bonds exposed to the solution relates to a low surface energy and the crystal shape is unique to the crystal lattice at equilibrium conditions [60]. However, growth conditions are often far from equilibrium, in which case the crystal structure has little influence on the morphology. Particles can also attain more complex shapes as certain features can grow from previously formed crystals in what is called hierarchical growth [1].

2.4.4 Similar Reactions

Both water and ethanol participate in the formation of chalcopyrites through decomposition of Tu to release S^{2-} ions [8, 36]. $CuInS_2$ can also be formed in inert solvents such as benzene, indicating that the solvent participation is not necessary at all with proper selection of precursors, which Lu et al. [35] selected to CuCl, elemental In or Ga and S powders. Ethylenediamine (En), $C_2H_4(NH_2)_2$, is a chelating solvent that form $[Cu(En)_2]^+$ chelates more stable than the complexes formed by Tu. These chelates can self-organize with sulfur or selenium precursors such as Tu molecules or intermediate compounds such as $[InSe_2]^-$ to allow directional growth of the chalcopyrite crystals into rods, whiskers, sheets or plates, or spherical particles can form depending on reactant concentrations and reaction temperature [58]. En is an attractive solvent for the formation of CIGS also because it enhances diffusion, crystallization and solubility of precursors [56], although it is less environmentally friendly and more expensive than water [1].

Cu^+ usually form tetrahedral complexes, although coordination numbers lower than four are possible like in linear complexes [61], while Cu^{2+} usually form irregular complexes with coordination numbers ranging from four to six. Thiols (RSH) are reported to form strong complexes with copper ions in aqueous solutions, but their structure is unclear. Laglera and van den Berg [62] found the binding strength between copper ions to take two different values depending on the concentration of copper ions in estuarine waters. A transition between these binding strengths occurred at a saturation concentration of copper ions at pCu values of $13.7-14.4$, so that the copper ion can be bonded to two thiol ligands at lower copper ion concentrations. Klotz et al. [63] reported on the formation of

24

the complex Cu(II)[RS-Cu(I)]$_4$, in which RS$^-$ binds to both Cu$^+$ and Cu^{2+} ions, through reduction of Cu^{2+} ions by the thiols.

The earliest processes for depositing sulphides used thiosulphate (S$_2$O$_3^{2-}$) as S^{2-} precursor in weakly acidic solutions [47]. The reaction mechanisms for such depositions are not clear, although it has been suggested that thiosulphate decomposes to elemental S. Since thiosulphate is a reducing agent, remaining thiosulphate ions may then reduce the elemental S ions. Also Cu^{2+} can be reduced to Cu$^+$ in solutions with thiosulphate. Furthermore, thiosulphate stabilize certain metal ions through formation of strong complexes, although its stabilizing ability is usually reduced in acidic solutions, which also holds for Tu and other sulphide precursors.

2.4.5   Influence of Synthesis Parameters

The variable parameters for a hydrothermal synthesis is the concentration and stoichiometry of reactants as well as surfactants, structure-directing or complexing agents, pH-modifiers, temperature, reaction time, autoclave volume and fill factor [38]. For the solvothermal synthesis of CIGS, directional structures are achieved through the use of En as solvent or elemental In as reactant, and not through structure-directing additives [1].

The product stoichiometry follows the reactant stoichiometry amongst the cation precursors, but also the total cation/anion ratio is affected as well as the density of crystal defects as presented by Das et al. [46]. A stoichiometric product of CuInS$_2$ in ethanol is obtained when the ratio of the CuCl and InCl$_3$ reactant concentrations is 0.80. This deficiency of In and S in the product compared to the solution of reactants is due to metal-thiourea complex decomposition to form CuInS$_2$, and is attributed to indium sulphide being relatively volatile. Increasing the Cu/In precursor ratio proved to increase the anion/cation ratio in the CuInS$_2$ product. It also increased the crystallinity of the product, indicating that Cu-rich CuInS$_2$ crystals grow faster. Das et al. [46] reported that a stoichiometric product can be almost defect free. Increasing the Cu/In ratio above 0.8 gives increased defect densities, but they were much lower than in In-rich products.

The stoichiometry also affects whether an n-type or a p-type semiconductor is formed, depending on the most probable defects in Cu- and In-rich crystals, respectively. Cu$_{In}''$ and V$_{In}'''$ can make Cu-rich crystals p-type degenerate, in which the charge carrier concentration becomes so high that the electronic properties start to resemble that of a metal rather than a semiconductor [1]. This shows that intrinsic defects may have the potential for half-filling of the IB and doping of the n- and p-type emitters. In-rich crystals may become n-type degenerate as V$_S^{\cdot\cdot}$ and In$_{Cu}^{\cdot\cdot}$ introduce two donor levels each, but also V$_{Cu}'$ can form a compensating acceptor level. Anion vacancies are most strongly promoted in anion and Cu-deficient crystals according to Noufi et al. [64]. V$_{Cu}'$ easily forms in chalcopyrite CuInSe$_2$ and is responsible for p-type self-doping of stoichiometric CuInSe$_2$ [18]. Both stoichiometry and defect densities influence the band gap, which increases with decreasing Cu/In ratio, in addition to the conductivity and its type.

Stoichiometry between CuCl and InCl$_3$ as well as higher Cu/In ratios result in CuS impurities at a high temperature of 200 °C, while Cu/In ratios of 0.74 and 0.69 result in In$_2$S$_3$ byproduct [46]. Lee et al. [65] reported on the influence of the Cu/In ratio on formation of CuInSe$_2$ in En with elemental Se precursor, and found that no byproduct was formed at ratios up to 1.4, but Se impurities were found from a stoichiometric reaction

mixture. While stoichiometric mixtures often are used for solvothermal syntheses with elemental sulfur or selenium precursors in En [56, 58, 66], an excess of Tu is used in syntheses in water and ethanol [8, 36, 46].

Peng et al. [67] investigated the effect of increasing reactant concentrations between 0.01 M and 0.1 M of copper(II) sulphate ($CuSO_4$) and $InCl_3$ with an excess of thioacetamide (C_2H_5NS) in ethanol at 160 °C for 12 h with stirring. All these concentrations provided a pure chalcopyrite film, but the Cu/In ratio in the $CuInS_2$ product increased with increasing concentration. The substrate was only partly covered at 0.01 M, and at 0.03 M a ca. 1 μm thin film of interconnected nanoplates covered the substrate. At 0.05 M, these smooth nanoplates built up $2 - 3$ μm spheres above the network covering the substrate, and the film thickness approached 8 μm. The arrangement of microspheres on the substrate and nanoplates in each sphere became denser and the film thickness increased above 8 μm as the concentration increased to 0, 1 M.

Chang and Ting [58] found that increasing concentration of an elemental Se precursor from 0.00625 M to 0.05 M in stoichiometric mixtures with $CuCl_2 \cdot 2H_2O$ and $InCl_3$ in En at 200 °C decrease the formation of byproducts. It is concluded that the byproducts are intermediate products, and the reaction become more complete as the reaction rate increases with increasing reactant concentrations. The formation of nanorods in the En solvent decreases with increasing concentration as rapid nucleation at high concentrations form more irregular particles, while fewer nuclei have more time to grow at low concentrations [1].

There seems to be a trend that increasing temperature gives increasing crystallinity and less byproduct for different synthetic routes [35, 36, 65], also for the mechanism presented in Section 2.4.2. Feng et al. [36] also reported increased crystal sizes of 12.4 nm at 150 °C and 26.4 nm at 180 °C from the reaction between CuCl, $InCl_3 \cdot 4H_2O$ and Tu in ethanol for 6 h. The diameters of particles also increased from $380 - 510$ nm to $400 - 650$ nm. Furthermore, Peng et al. [67] suggested that film thickness also can increase with increasing temperature. Chang and Ting [58] reported on changes in morphology of $CuInSe_2$ from particles at 150 °C, plates at 180 °C and spheres at 200 °C in En, and attribute these changes to differences in reaction rates. In the mechanism presented, $CuInSe_2$ crystals form through diffusion within a solid solution of intermediate compounds of CuS and In_2Se_3, in which $CuInSe_2$ precipitates of low dimensions are formed faster than those of higher dimensions. Increased reaction rate with increasing temperature thus allows formation of plates and spheres rather than rods.

As with increase in temperature, increasing the reaction time allows a more complete reaction to occur, and a minimum time is required to prevent the occurrence of byproducts of intermediate compounds [1]. Feng et al. [36] reported on the formation of CuS byproduct in ethanol at 150 °C with a reaction time of 2 h and 4 h, but not 6 h. These experiments also show increased crystallinity with increased reaction time. The crystal sizes also increase with increasing reaction time as they get more time to grow after nucleation. $CuInS_2$ quantum dots of 6.6 nm and 8.7 nm have been achieved with a reaction time of 2 h and 4 h, respectively. Also the size of polycrystalline particles increases with this increase in reaction time, and their surface can change from rough to smooth. Yang and Chen [66] reported that nanorod growth in En is first initiated after recrystallization and their diameter and lengths as well as yield increase with increasing reaction time.

3   Experimental

3.1   Hydrothermal Synthesis

The first experimental objective was to develop a synthesis producing pure chalcopyrite $CuGaS_2$, taking the synthesis in an aqueous solution conducted by Hu et al. [8] and previous development reported by Sortland [1] as a basis. The experimental procedures were thus similar to those reported by Sortland [1], but some deviations from the synthesis by Hu et al. [8] were made. The $CuGaS_2$ precursors in all syntheses were $GaCl_3$ (Sigma-Aldrich, 99.99%, anhydrous beads, -10 mesh), CuCl (Sigma-Aldrich, $\geq$99.99%, anhydrous beads) and Tu (Sigma-Aldrich, $\geq$99.0%). $GaCl_3$ and CuCl were treated and stored in dry and inert Ar atmosphere in a M. Braun UNIlab glove box for several reasons [1]. Anhydrous CuCl and $GaCl_3$ are hygroscopic [42, 68] and absorption of water from a moist atmosphere introduces water of crystallization. This alters the formula unit and thus the molar mass so that the stoichiometry of reactants can not be controlled by accurate weighing of the solids. The CuCl as delivered from Sigma-Aldrich had a tint of olive green color, indicating that its surface was partially oxidized to Cu(OH)Cl, as described in Section 2.4, and storing in a glove box minimized further oxidation. Furthermore, the $GaCl_3$ was observed to agglomerate slightly from absorption of moisture during storage, and in air it liquefies by moisture absorption according to Equation (2.2) in Section 2.4 and fumes from HCl evolution.

   CuCl and $GaCl_3$ were stored in glass vials with plastic lids. As a precaution for CuCl being sensitive to light [69], the glass vial with CuCl was also wrapped in aluminium foil. Similar containment, with an additional Parafilm® wrapping, was used for transportation of these reactants from the glove box to the fume hood where they were dissolved added to water. CuCl and $GaCl_3$ were exposed to air for some seconds during addition to the solution, but this is in accordance with Sortland [1] not considered detrimental to the synthesis. This is because the stoichiometry was determined at the weighing of CuCl and $GaCl_3$, so formation of water of crystallization was not crucial after that. Furthermore, oxidation of CuCl was negligible during a short exposure to air when added to the solution, in accordance to Section 2.4.

   CuCl, $GaCl_3$ and Tu were weighed out according to Table 3.1 to the desired stoichiometry and concentrations after dissolution in water to a total volume of solution given by the fill factor in Table 3.2 and the autoclave volume [1]. A Sartorius BP121S digital analytical balance was used to weigh CuCl and $GaCl_3$ in the glove box, and Tu was weighed on a Sartorius TE214S analytical balance. The pH of the reaction solutions were adjusted by addition of HCl (VWR International Ltd., 37%, pro. analysi) and some syntheses utilized 1-pentanethiol (Sigma-Alrdich, 98%) as a complexing agent. According to Sortland [1], a low pH is necessary to prevent GaO(OH) precipitation, and complexing is used to stabilize copper ions from CuS and digenite precipitation. Table 3.2 summarize the HCl and 1-pentanethiol concentrations, autoclave volume, fill factor, heating time and temperature for each synthesis. The possibility of oxidation by oxygen in the air inside the autoclave was investigated in synthesis 1a by bubbling nitrogen into the reaction solution. In synthesis 1b, a copper foil (Alfa Aesar, 99.9%, annealed) was introduced into the reaction solution, and the Tu reagent was replaced by Sodium thiosulphate pentahydrate ($NaS_2O_3 \cdot 5H_2O$) (Sigma-Aldrich, $\geq$99.5%) as S precursor in

Table 3.1: Masses of CuCl, GaCl$_3$ and Tu reactants, their stoichiometry and dopant concentrations. The stoichiometry relation Cu:Ga:S is given as the actual concentrations of the Cu, Ga and S precursors in the reaction solution, assuming complete dissolution. *Sodium thiosulphate pentahydrate was used as S precursor instead of Tu in synthesis 1c.

Synthesis	m_{CuCl} [g]	$m_{\mathrm{GaCl_3}}$ [g]	m_{Tu} [g]	Cu:Ga:S [M:M:M]	$C_{\mathrm{NiCl_2}}$ [M]	$C_{\mathrm{FeCl_3}}$ [M]
1a	0.2976	0.5286	0.9133	0.030:0.030:0.120	0	0
1b	0.2967	0.5287	0.9135	0.030:0.030:0.120	0	0
1c	0.2966	0.5281	2.9785*	0.030:0.030:0.120	0	0
2a	1.2077	2.1480	3.7153	0.122:0.122:0.488	0	0
2b	3.3565	5.9677	10.3203	0.319:0.319:1.276	0	0
2c	0.3156	0.5616	0.9705	0.030:0.030:0.120	0	0
3a	0.2978	0.5280	0.9131	0.030:0.030:0.120	0	0
3b	0.2976	0.5276	0.9129	0.029:0.029:0.117	0	0
3c	2.1780	3.8739	6.6986	0.220:0.220:0.880	0	0
4a	0.2969	0.5286	0.9135	0.030:0.030:0.120	0	0
4b	0.2596	0.4620	0.7995	0.030:0.030:0.120	0	0
4c	0.2966	0.5287	0.2210	0.030:0.030:0.029	0	0
5a	0.2606	0.4628	0.7992	0.030:0.030:0.120	0	0
5b	0.2045	0.3622	0.6267	0.030:0.030:0.120	0	0
5c	0.2607	0.4621	0.7995	0.030:0.030:0.120	0	0
6a	0.2609	0.4627	0.7998	0.030:0.030:0.120	0	0
6b	2.4629	4.3809	7.5759	0.319:0.319:0.319	0	0
6c	0.5198	0.9250	1.5986	0.060:0.060:0.240	0	0
7a	1.5479	2.7524	4.7597	0.319:0.319:1.276	0	0
7b	1.5476	2.7528	4.7598	0.319:0.319:1.276	0	0
7c	0.1907	0.3381	0.5850	0.060:0.060:0.240	0	0
7d	0.5100	0.9092	1.5708	0.060:0.060:0.240	0	0
8a	2.9689	5.2806	9.1306	0.319:0.319:1.276	0	0
Ni8	1.6432	2.9212	5.0509	0.319:0.319:1.276	0.040	0
Ni16	1.6425	2.9216	5.0506	0.319:0.319:1.276	0.020	0
Fe8	1.6420	2.9214	5.0504	0.319:0.319:1.276	0	0.040
Fe16	1.6421	2.9216	5.0501	0.319:0.319:1.276	0	0.020

synthesis 1c as it is also a reducing agent.

Synthesis 7a is used as basis for syntheses Ni8, Ni16, Fe8 and Fe16, but without a substrate. The label of the doped syntheses reflects wether NiCl$_2$ or FeCl$_3$ is added, and the number represent the stoichiometry of the limiting CuGaS$_2$ precursor of CuCl and GaCl$_3$ to the dopant precursor. The dopant stoichiometry is also represented by the concentrations of NiCl$_2$ or FeCl$_3$ in Table 3.1 compared to the limiting Cu and Ga precursors. The NiCl$_2$ and FeCl$_3$ precursors were prepared as standardized solutions of nickel(II) chloride hexahydrate (NiCl$_2 \cdot$6H$_2$O) (MERCK, puriss, >97%) and iron(III) chloride hexahydrate (FeCl$_3 \cdot$6H$_2$O) (Sigma-Aldrich, puriss, >99%) in deionized water, respectively. During standardization, the solutions were heated in a Lab Star 1200/4

Table 3.2: Concentrations of HCl and 1-pentanethiol, volume, fill factor, heating temperature and time for each synthesis.

Synthesis	C_{HCl} [M]	$C_{\text{1-pentanethiol}}$ [M]	Volume [ml]	Fill factor	Temperature [°C]	Time [h]
1a	0.316	0	125	80%	180	12
1b	0.316	0	125	80%	180	12
1c	0.316	0	125	80%	180	12
2a	0.316	0	125	80%	180	12
2b	0.316	0	125	85%	180	12
2c	0.316	0	125	85%	180	12
3a	0.501	0	125	80%	180	12
3b	0.308	0	125	82%	180	1.75
3c	0.316	0	125	80%	180	12
4a	0.316	0.240	125	80%	180	12
4b	0.316	0	125	70%	250	12
4c	0.316	0	125	80%	180	12
5a	0.271	0.240	125	70%	250	20
5b	0.316	0	98	70%	250	20
5c	0.271	0.240	125	70%	250	5
6a	0.316	0.240	125	70%	250	30
6b	0.317	0	98	80%	180	30
6c	0.316	0.480	125	70%	250	30
7a	0	0	116	42%	250	30
7b	0	2.551	118	42%	250	30
7c	0.317	0.481	45	70%	250	30
7d	0.316	0.480	123	70%	250	30
8a	0	0	117	80%	250	30
Ni8	0	0	125	42%	250	30
Ni16	0	0	125	42%	250	30
Fe8	0	0	125	42%	250	30
Ni16	0	0	125	42%	250	30

chamber furnace at a rate of 50 °C/h to 100 °C and held at this temperature for 3 h before further heating at 200 °C/h to 700 °C for $NiCl_2$ and 800 °C for $FeCl_3$. After 6 h, the oxides obtained were cooled at 200 °C/h to 400 °C. A MITTLER TOLEDO AE260 DeltaRange analytical balance was used for weighing the crucibles before and after addition of the solutions and after heat treatment. The $NiCl_2$ solution was standardized to 0.6381 ± 0.0004 M and the $FeCl_3$ concentration was found to be 0.6387 ± 0.0004 M. The desired concentration in the syntheses was obtained through the volume of the standardized solution extracted by a pipette.

125 ml autoclaves of the model 4748 Large Capacity Bomb from Parr Instrument Company [70], depicted in Figure 3.1(a) were used in all syntheses except 7c. This synthesis utilized the 45 ml autoclave 4744 General Purpose Acid Digestion Vessel depicted in Figure 3.1(b), also from Parr Instrument Company. The Teflon cup goes into the steel

container to the left in Figures 3.1(a) and (b), with the lid and rupture disks on top, and the autoclave is sealed by screwing on the steel lid to the right and carefully tighten the screws on top of the 125 ml autoclaves with a hex key to prevent lifting of the Teflon lid during heating and pressure build-up. Both autoclave models are designed to operate at temperatures up to 250 °C [70]. The pressure limitation of the 125 ml autoclaves is 132 bar and 125 bar for the 45 ml autoclave. Due to deformation of the Teflon cup and its lid during the syntheses, each lid was only used with one cup to avoid pressure drop, leakage of gas and exposure of the stainless steel to the corrosive reaction solution. Since the autoclaves must withstand a high pressure build-up during heating, they have a simple design which does not allow for in-situ measurements for analysis of the reactions during synthesis [1]. Thus, information about the reactions occurring during synthesis is deduced from ex-situ analysis of the products in studies of hydrothermal syntheses.

(a)   (b)

Figure 3.1: Pictures of 125 ml (a) (adapted from Sortland [1]) and 45 ml (b) autoclaves. For reference, the steel container widths are 8 cm (a) and 5 cm (b), respectively.

In some syntheses, a quarter of a 2 inch Si(100) wafer was mounted vertically or horizontally above the precipitate forming in the bottom of the Teflon cups with substrate holders depicted in Figure 3.2 for film growth. Synthesis 5b and 6b used a large vertical substrate holder depicted to the left in Figure 3.2, which reduce the volume by 27 ml. In synthesis 7a, a substrate was mounted horizontally supported by two small vertical substrate holders, each on top of a cylindrical support in synthesis 7a, and two prismatic supports in were used in syntheses 7b. A small vertical substrate holder was used in synthesis 7d and a silica glass slide was used as substrate mounted on a large horizontal substrate holder in synthesis 8a.

Figure 3.2: Pictures of substrate holders including from left to right: Large vertical, large horizontal and small vertical substrate holders, cylindrical and prismatic supports.

The sealed autoclave was heated in a TERMAKS SERIES TS8000 drying cabinet to the temperature given in Table 3.2, which requires about 40 min for heating from room temperature to $160 - 180\,°C$. The only exceptions are synthesis 4b and 5c, in which a Binder FP 53 drying oven was used, and this oven required over 2 h for reaching $250\,°C$. The reaction time in Table 3.2 is reckoned from when a steady temperature was reached. Syntheses 5b and 5c was held at $195\,°C$ for about 1.8 h before heating was continued to $250\,°C$. Due to the built up pressure the autoclaves were not opened before cooling to room temperature, and similarly to Sortland [1] they generally cooled inside the heating cabinet until the air temperature in the cabinet was approaching room temperature before the autoclaves were taken out for complete cooling. The exception from such cooling is synthesis 3b, in which the autoclave was removed from the heating cabinet as the heating time for the syntheses in Table 3.2 was reached.

The obtained products were filtered with S&S 589² white ribbon ashless filter papers. A filter paper was placed in a Büchner funnel mounted on a Büchner flask connected to a water jet pump. After filtration, the products were dried on the filter paper in a Binder VD23 vacuum oven fitted with a Vacuubrand PC510 diaphragm pump at $60\,°C$ for 4 h under 10 mbar air pressure. Finally the as-obtained products were weighed and transferred to a glass vial with plastic lid for storage for later analyses.

3.2 X-ray Diffraction

All products were investigated for secondary phases and approximate purity of CuGaS2 by powder diffraction in a Bruker D8Focus X-ray Diffractometer using Cu Kα1 and Kα2 radiation with wavelengths of 1.5406 Å and 1.54439 Å respectively, with an weighted average of 1.54186 Å. Using a 0.06 mm slit for the incoming X-ray, the samples were scanned in a 2θ range of $15 - 70°$ with an increment of $0.04°$ over 2.5 s. These parameters were set in the XRD Wizard software from Bruker AXS and XRD Commander was used

to operate the diffractometer and to acquire the diffractograms.

Due to the small amounts of the products obtained, a thin layer of powder was distributed on a Si single-crystal that does not contribute to the background signal. The powder was dispersed in ethanol to achieve adhesion and uniform coverage of the wafer. Substrates used for film growth were mounted in an appropriate substrate holder by using putty and leveled to the sample holder height with a glass slide. The diffractograms were analyzed for different phases in version 15 of the EVA software from Bruker, using the diffractogram database of the International Center for Diffraction Data found in the software ICDD DDview+ 4.4.0.5 using PDF-4+ 2009 RDB 4.0905. Topas 4.2, also from Bruker AXS, was used perform Rietveld analyses on the diffractograms. This analysis fit parameters including unit cell dimensions and crystallite sizes as well as the composition of different phases to a diffractogram. Approximate product compositions from this analysis is used together with the product mass to calculate an approximate yield as shown in Appendix A.1.

3.3 SEM and EDS

The same samples were used for SEM and EDS. These were prepared by transferring agglomerated flakes of different colors obtained after synthesis, or powders if no flakes were obtained, onto carbon tape fastened to aluminium stubs for morphology analysis. The products were also dispersed in ethanol by stirring at 700 rpm to obtain a clear dispersion of particles for EDS analysis. The dispersions were dripped onto the parts of the stubs not covered by carbon tape and let dry. Substrates were cleaved and fastened to sample holders with carbon tape. A dedicated cross-section sample holder giving a 90° tilt angle were used for cross-section analysis of a cleaved edge. The secondary electron detector in a Hitachi S-5500 in-lens scanning (transmission) electron microscope (S(T)EM) was used to study the product morphologies. The beam current was set to $7\,\mu A$ and the accelerating voltage to $2\,kV$. EDS analysis was conducted in a Hitachi TM3000 tabletop SEM fitted with Bruker Quantax 70 EDS system, using an excitation voltage of $15\,kV$. A dedicated EDS spacer was used to adjust the height of the sample holder and thus the working distance to $8-9\,mm$. Elemental mapping is used to assess contamination elements and quantification within a selected circular area is compared to phases identified by XRD analysis to determine the morphologies formed by the different crystals.

The EDS detector measures the intensity of X-rays with different energies, of which some are characteristic to specific elements. The electron beam focused on the sample in the SEM can remove electrons in low-energy electron shells near the core of an element provided a sufficiently high excitation voltage is used to generate the electron beam. A characteristic X-ray photon is generated as an electron in an electron shell of higher energy relaxes to the vacant state [71]. The electron shells relate to the principal quantum number of orbitals and increase in energy in the sequence of letters in the alphabet starting with K. A sufficiently high excitation voltage is generally $1.5-2$ times the voltage related to the highest energy of the characteristic X-rays to be analyzed [1]. This critical excitation voltage is highest for Ga in $CuGaS_2$, and compared to its value of $10.367\,kV$, the excitation voltage used is near the lower limit of what is considered sufficient, but a higher excitation voltage was not available in the SEM.

3.4 Photoluminescence and Absorption Spectroscopy

The products Ni8, Ni16, Fe8 and Fe16 with dopant addition and product 7a were subject to photoluminescence spectroscopy (PL), in order to investigate IB formation by doping. The PL measurement setup used equipment from Horiba Jobin Yvon IBH, and included a FluoroCube photon-counting spectrometer consisting of a sample cube labeled 3 in Figure 3.3 with entrance and exit ports. Polarizers and filters could be placed at both entrance and exit ports and the exit port included a collection lens. The excitation source (1) was a A 5000XeF Sub-micro-second Xenon Flashlamp, emitting flashes of $0.1 - 0.8$ µs duration with $5 - 150$ mJ pulse energy covering the UV, visible and near infrared (NIR) wavelength ranges. A 5000M monochromator (2) with 1 nm wavelength resolution, selected the desired wavelength for excitation. A similar monochromator (4) at the exit port scanned the wavelengths detected by the photomultiplier tube detector TBX-04 (5), working in the range of $300 - 850$ nm wavelengths. Version 2.1 of the Datastation software, also from Horiba Jobin Yvon IBH, was used to operate the PL setup and obtain the spectra. Different excitation wavelengths were attempted, including 410 nm for luminescence from recombinations across the band gap, and 514 nm to investigate luminescence originating within the band gap due to IB formation. The excitation wavelengths must be sufficiently low to give excitation of electrons across a band gap, and luminescence of the sample occur as excited electrons are relaxed to a low energy band or state through radiative recombination explained in Section 2.1.
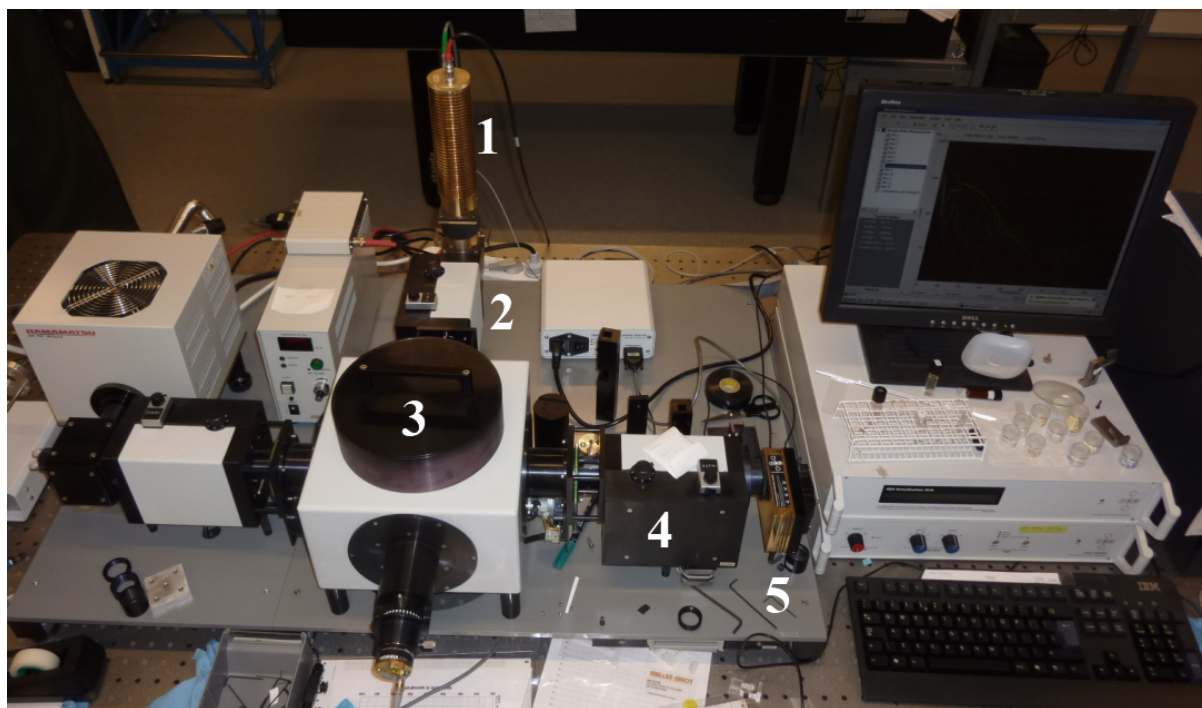
Figure 3.3: Picture of PL equipment including excitation source (1), monochromators (2, 4), sample cube (3) and detector (5).

Ultraviolet-visible (UV-Vis) absorption spectroscopy aided the determination of excitation wavelengths. Absorption spectroscopy can also reveal whether the products with dopant addition attain improved absorption, which according to Section 2.1 is a purpose

of introducing IB materials in solar cells. Samples were prepared by dispersing powders in ethanol in a VWR™ULTRASONIC CLEANER for 5 min, and these were transferred to cuvettes. As the dispersions settle at different rates and the different products have different particle sizes, the dispersions were not suitable for comparison of absorption coefficients. A SHIMADZU UV-1601PC UV-visible spectrophotometer recorded the absorbance spectrum between $200 - 1000$ nm wavelengths by comparing the known intensity of a light beam incident to the cuvette to that measured on the other side. The absorbance (A) is then calculated as the logarithm to the ratio of the incident beam intensity (i_0) to the intensity of the outgoing beam (i) according to Equation (3.1) [32].

$$A = \log \frac{i_0}{i} \tag{3.1}$$

The spectra of the analyzed products were obtained in the software package UV Probe, also from SHIMADZU, through comparison of the spectrum for the product dispersion to that of a reference sample of pure ethanol.

4 Results and Discussion

4.1 Purity and Yield

The first experimental goal is to find a hydrothermal synthesis producing pure $CuGaS_2$. Reproducing the synthesis reported by Hu et al. [8] is the selected strategy, and previous development of the synthesis reported by Sortland [1], specifically synthesis 4a, is used as a basis for refinement. For clarity, this synthesis is referred to as 4a[1] in this work. Even though Hu et al. [8] did not use additives directly, they introduced HCl to dissolve elemental Ga. In this work, the $GaCl_3$ reactant is instead added directly to the reaction solution and HCl is added to adjust pH. Furthermore, the high fill factor of 95% they used presents a danger of bursting the rupture disks in the autoclaves used in this work due to the high pressure achieved at 160 °C with such a high fill factor, which can be envisaged from Figure 2.10 in Section 2.4. A longer heating time than the 5 h used by Hu et al. [8] was also selected as a heating time of 12 h is suggested by Sortland [1].

Other deviations that may affect the results are the volume of the autoclaves used as it affects the amount of air in the autoclave and possibly the extent of inhomogeneities in the solution. In this work, 150 ml and 45 ml autoclaves with different geometries are used, while Hu et al. [8] used 50 ml autoclaves. Some of these differences may be related to several difficulties encountered in the pursuit of a synthesis that produce pure $CuGaS_2$ from CuCl, $GaCl_3$ and Tu in an aqueous solution, and the work presented here show part of the development towards this goal.

Table 4.1 summarizes this development in terms of compositions and yields of the different products from hydrothermal syntheses. In this table, m is the total product mass, x is the molar fraction calculated from the diffractogram for each product with the Topas software and yields are reproduced from calculations given in Appendix A.1. The calculations for marked syntheses in Table 4.1 show larger amounts of elements in the product than the precursors, and the inaccuracy of these calculations relate to the inaccuracy of the composition analyses and the varying composition of digenite, for which $Cu_1.8S$ is used in Appendix A.1. The term product relates to the total amount of all phases obtained from a synthesis after filtration, not only $CuGaS_2$. Since product 1c contained some impurity phases not common for any other products and did not contain $CuGaS_2$, its composition was not calculated and the corresponding cells are left empty. Furthermore, syntheses 7d and 8a are excluded from this analysis as they used reaction parameters from syntheses 6c and 6b, respectively, with introduction of a substrate holder as they were only intended for film growth.

Table 4.1: Mass (m) of as-obtained product and approximate composition and yield of $CuGaS_2$. *Yield too high for mass balance.

Product	m [g]	x_{CuGaS_2}	x_{CuS}	$x_{Cu_{2-\delta}S}$	$x_{GaO(OH)}$	x_{NiS_2}	x_{FeS_2}	Yield
1a	0.4346	86%	11%	3%	0%	0%	0%	67%
1b	0.3821	84%	13%	3%	0%	0%	0%	59%
1c	0.7515							
2a	2.1339	86%	12%	2%	0%	0%	0%	82%
2b	5.9532	87%	8%	4%	0%	0%	0%	82%
2c	0.3252	80%	21%	0%	0%	0%	0%	46%
3a	0.2856	77%	23%	0%	0%	0%	0%	42%
3b	0.1818	56%	5%	39%	0%	0%	0%	20%
3c	4.2786	92%	5%	3%	0%	0%	0%	94%*
4a	0.3709	92%	1%	7%	0%	0%	0%	59%
4b	0.4179	97%	3%	0%	0%	0%	0%	79%
4c	0.3528	41%	15%	18%	26%	0%	0%	67%
5a	0.4027	96%	0%	4%	0%	0%	0%	75%
5b	0.2385	78%	0%	19%	3%	0%	0%	49%
5c	0.3641	89%	0%	8%	3%	0%	0%	65%
6a	0.3200	84%	0%	16%	0%	0%	0%	54%
6b	3.4362	81%	4%	15%	0%	0%	0%	61%
6c	0.8316	100%	0%	0%	0%	0%	0%	80%
7a	2.8860	99%	0%	1%	0%	0%	0%	93%
7b	2.1959	97%	0%	3%	0%	0%	0%	70%
7c	0.2929	93%	0%	5%	2%	0%	0%	73%
Ni8	3.3624	96%	0%	0%	0%	4%	0%	100%
Ni16	3.3239	96%	0%	4%	0%	0%	0%	99%*
Fe8	3.3462	86%	0%	10%	0%	0%	4%	92%*
Fe16	3.3144	87%	7%	0%	0%	0%	6%	94%*

4.1.1 Oxidation of Cu^+

After the synthesis development reported by Sortland [1], about 15 mol% CuS remained as a secondary phase as determined from a scan of synthesis 4a[1] with parameters given in Section 3.2, providing improved intensities and composition accuracy compared to the scans reported by Sortland [1]. This was mainly achieved by optimization of HCl concentration and fill factor. Variation of temperature between 160 °C and 180 °C, reaction time between 5 h and 20 h and an excess of $GaCl_3$ of 0.06 M compared to a CuCl concentration of 0.030 M did not affect this product purity. The first syntheses in this work aimed to prevent oxidation of Cu^+ to Cu^{2+} necessary to form the CuS precipitate. One strategy was to investigate if the oxygen in the air above the reaction solution could cause the oxidation. This was motivated by the observation reported by Sortland [1] that increased fill factor resulted in reduced amounts of CuS impurity. Thus, nitrogen was bubbled through the reaction solution until the Teflon cup lid was put on so that it also would replace the air in the Teflon cup.

The diffractogram of product 1a is presented in Figure 4.1, with overlay of peak positions and relative intensities for the identified phases. The fit between the red lines with peaks in the diffractogram in terms of 2θ values and similarity between relative peak intensities and relative heights of the red lines show that the $CuGaS_2$ product is obtained. However, additional peaks in the diffractogram indicate CuS and digenite impurities. A variety of peak positions are found for the digenite phase in different products. According to Section 2.2, digenite slowly transforms to a metastable α-$Cu_{2-\delta}S$ phase as it is cooled below 73 °C after the syntheses, so that it may be present in two polymorphs in the products. Furthermore, it is an off-stoichiometric phase for which distortions of the crystal structure varies with composition, and the lattice parameters are tuned in the EVA software to match peak positions of known digenite phases to diffractograms.

The precipitate deposited along the Teflon cup wall and bottom in synthesis 1a, with additional powder in the bottom depending on the amounts of product formed, like in all syntheses producing $CuGaS_2$. The precipitate vary in color between red and black, in which the red color indicate Ga-rich $CuGaS_2$, while the black color originate from Cu-rich $CuGaS_2$ and the copper sulphides according to Section 2.2. The deposits showing this off-stoichiometry were typically, but not exclusively, red towards the Teflon cup and black towards the solution, indicating that Ga-rich $CuGaS_2$ precipitate before Cu-rich $CuGaS_2$. This might be related to dissolution of CuCl as it dissolves during heating, so the concentration of Cu^+ ions is initially much smaller than that of Ga^{3+} ions. However, Cu^+ ions are not in excess towards the end of the synthesis due to precipitation of copper sulphide impurities and neither of the cations are depleted from the solution in several syntheses providing this inhomogeneity, but Cu-rich $CuGaS_2$ is expected to be the preferred off-stoichiometry close to the borders between the stability regions of $CuGaS_2$ and CuS or Cu_2S in the stability diagrams in Figure 2.6. This is also shown in the phase diagram in Figure 2.7 in Section 2.2 as copper sulphide impurities become stable at increased Cu contents to the left of the dark $CuGaS_2$ single-phase region.

Figure 4.2 shows the result of the composition calculations in Topas on the diffractogram of product 1a in Figure 4.1. In this figure, the blue curve is the experimental diffractogram and the red curve is calculated based on curve fitting through Rietveld analysis given the crystal structures of $CuGaS_2$, CuS and digenite identified in the EVA software. The lower grey curve represents the fitting mismatch as the difference between the experimental and the calculated curve. The calculated compositions are not intended to be precisely accurate, but an accuracy of a few percent is expected at the high intensities usually obtained in the diffractograms, and a R-factor below approximately 5% is obtained for all Rietveld analyses. Although increased 2θ ranges are commonly employed for composition analyses, it does not provide more information regarding secondary phases and only two minor peaks originating from $CuGaS_2$ extend above the background for 2θ values between $70 - 100°$. However, as the calculations are based on comparisons of the areas beneath peaks originating from different crystals, this might lead to a slight underestimation of the $CuGaS_2$ purities, which contribute to the expected inaccuracy. In this respect the output compositions are only used as guidelines to assess the purity of the products and improvement of the synthesis. The mismatch curve in Figure 4.2 is representative for most syntheses, including the positive mismatch at the center of $CuGaS_2$ peaks with negative mismatch at both sides. Such mismatch relates to variations in crystallite sizes within each product, as the largest crystallites are responsible for the

sharp tip of the peaks while smaller crystallites give peak broadening. Calculated average crystallite sizes are in the nanometer scale, and this is further discussed in Section 4.3. Regarding composition analysis of the products, theses mismatch areas are to varying extents balanced out. Another common mismatch is seen at 2θ angles near $27°$, and the origin of the intensity rise in this region is discussed in Section 4.1.10.

The calculations presented in Figure 4.2 suggests a purity of about 86 mol% as reported in Table 4.1 for synthesis 1a, with impurities of ca. 11 mol% CuS and 3 mol% digenite. Together with the mass of the obtained product of 0.4346 g, this purity indicate a yield of about 67% related to the introduced amount of CuCl or $GaCl_3$ as limiting reactant. The purity and yield is thus comparable to that of synthesis 4a[1] reported by Sortland [1] of 85 mol% with a 15 mol% CuS impurity giving 68% yield. Removing oxygen does not significantly prevent oxidation of Cu^+ and formation of CuS, although the digenite impurity formed at the expense of CuS have lower contain Cu ions of lower oxidation states. Nevertheless, oxygen is not the oxidizing agent and air can be used in the synthesis.

Another strategy to prevent formation of CuS was to introduce elemental copper in synthesis 1b in order to reduce Cu^{2+} back to Cu^+ according to Equation (4.1).

$$Cu + Cu^{2+} \rightarrow 2Cu^+ \tag{4.1}$$

The diffractogram of product 1b is presented in Figure 4.1, and identification of the CuS phase along with digenite shows that also this strategy failed to prevent Cu^+ oxidation. The peak at $43°$ shows a disproportionately high intensity compared to the recorded peaks for CuS, shown as blue lines in Figure 4.1. This can relate to preferred orientation of the CuS crystallites so that Bragg reflection from the atomic planes giving this peak occur more frequently in the sample than in a sample with completely random crystal orientations. An additional peak at a 2θ angle just above $43°$ indicates minute quantities of an additional impurity phase that could not be identified. Such a minor impurity is not expected to significantly influence the purity calculated to 84 mol%, with 13 mol% CuS and 3 mol% digenite impurities similar to product 1a, while synthesis 4a[1] reported by Sortland [1] did not produce digenite. However, the similar CuS impurity contents in synthesis 1b and 4a[1] shows that the extent the reaction in Equation (4.1) is not significant and the reaction in Equation (4.1) is thus not spontaneous. Instead, the Cu foil showed sign of corrosion as a passivating layer was seen in the areas of the foil not covered by deposits. The yield of 59% is slightly reduced from that of syntheses 4a[1] and 1a.

According to Section 2.4.4, thiosulphate ($S_2O_3^{2-}$) is a reducing agent that has been utilized for deposition of sulphides, and it was selected as sulphide precursor instead of Tu in synthesis 1c in order to investigate whether it could reduce Cu^{2+} to prevent CuS formation. The reaction mechanisms of such depositions are not understood [47], but it is suggested that thiosulphate decomposes to elemental S that is reduced to S^{2-} by unreacted thiosulphate. The diffractogram of product 1c in Figure 4.3 shows that thiosulphate decompose to elemental S, but even though sulphide ions are formed as indicated by CuS precipitation, large amounts of S remain unreacted. Furthermore only divalent Cu ions precipitate, showing that oxidation of Cu^+ is in fact promoted in this synthesis. Contrary to the common observation in Section 2.4.4, thiosulphate is unable to reduce Cu^{2+}. Instead, elemental S might take part in oxidation of Cu^+, in which case Cu^+
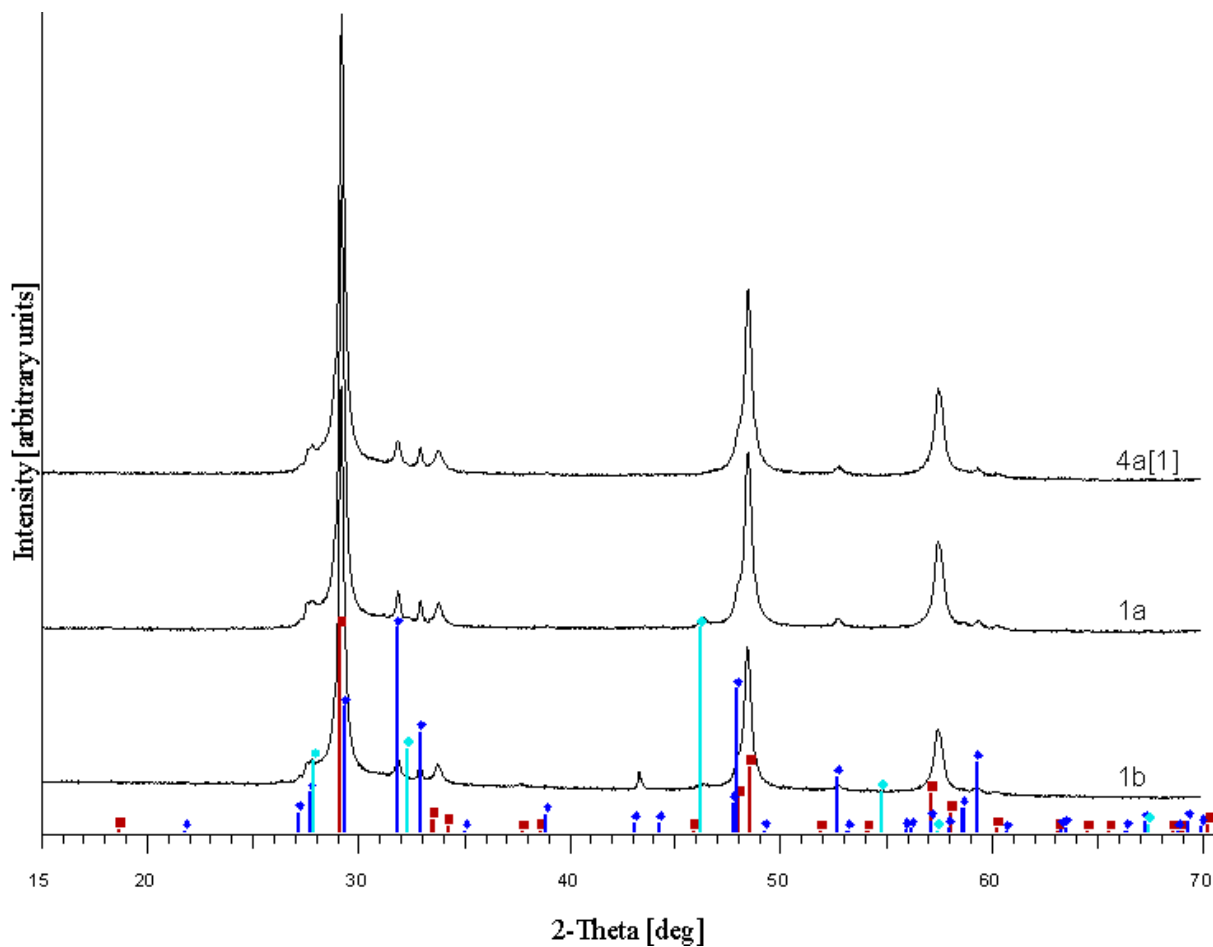
Figure 4.1: Diffractograms of products 4a[1], 1a and 1b with overlay of peaks for known phases: ■ $CuGaS_2$, ◆ CuS, ◈ $Cu_{2-\delta}S$.
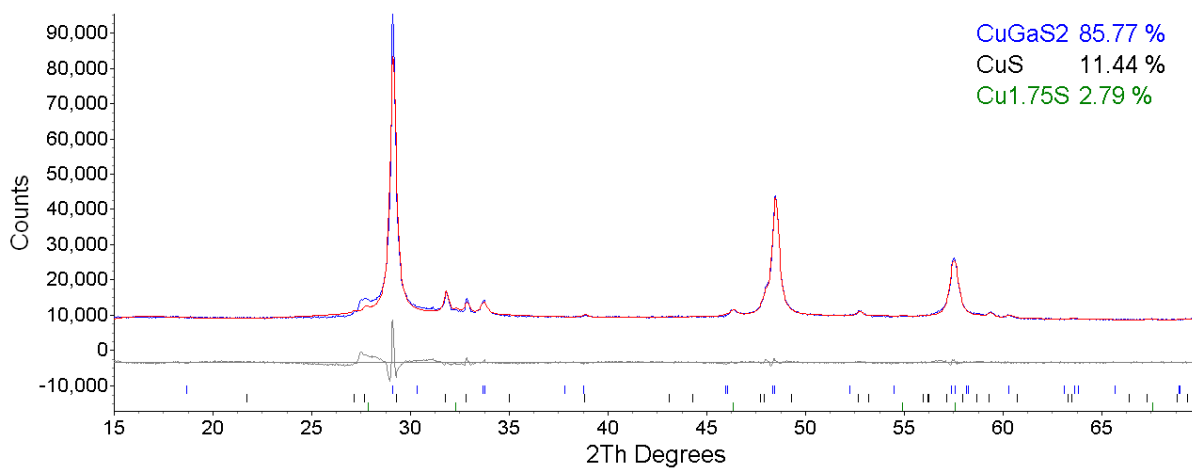

Figure 4.2: Output of Rietveld calculations on the diffractogram for product 1a. The blue curve is the diffractogram to which the Topas software fit the red curve and the grey curve shows the mismatch.

ions rather than thiosulphate reduce S to form the CuS precipitate. A phase of gallium oxide (Ga_2O_3) incorporating sulfur trioxide (SO_3) is a candidate impurity based on the remaining peaks in the diffractogram, possibly with a slightly compressed lattice as the misalignment of peaks to higher 2θ angles indicate a slightly smaller unit cell compared to the peaks for the known $(Ga_2O_3)_3(SO_3)_4 \cdot (H_2O)_9$ phase.
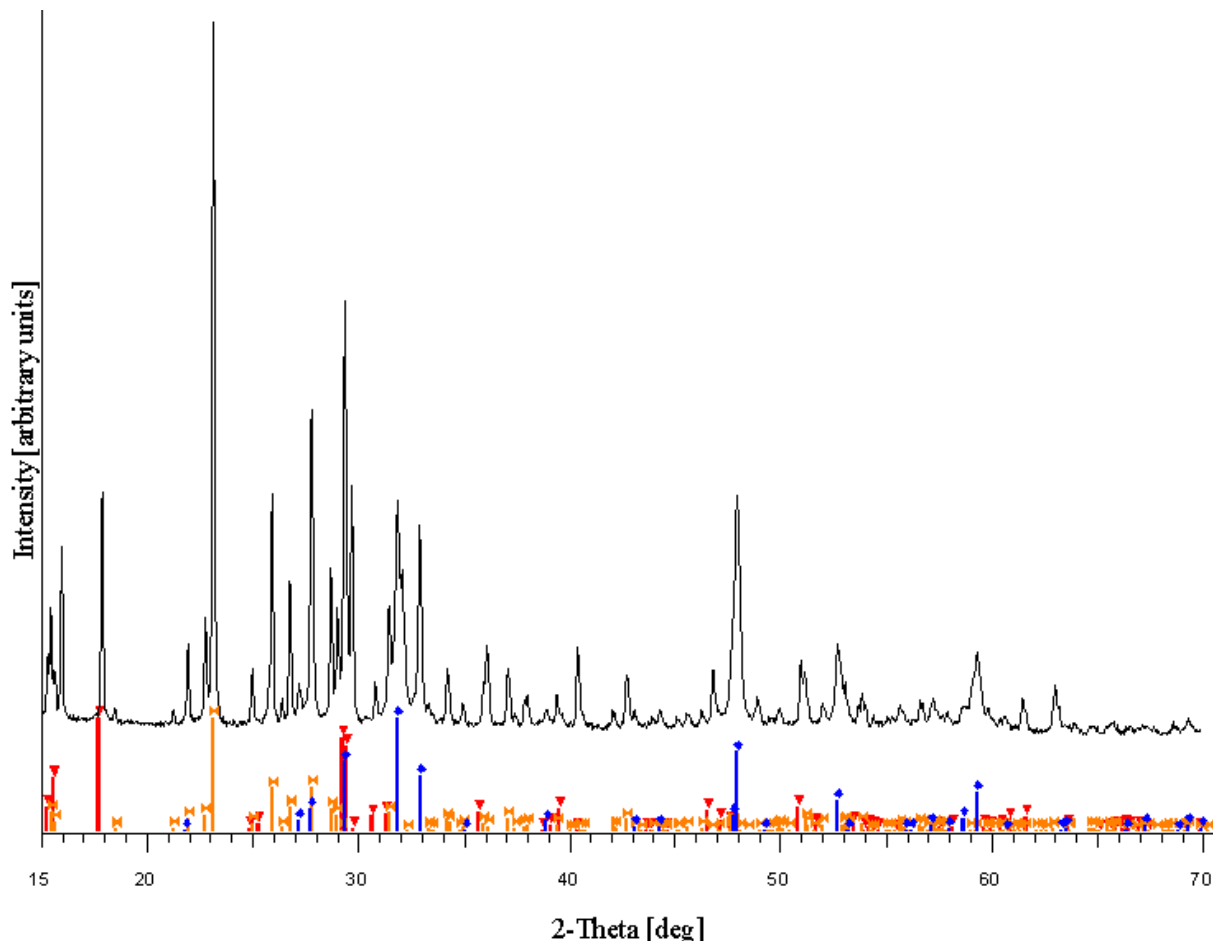

Figure 4.3: Diffractogram of product 1c with overlay of peaks for known phases: ⋈ S, ◆ CuS, ▼ $(Ga_2O_3)_3(SO_3)_4 \cdot (H_2O)_9$.

4.1.2 Heating Time

In synthesis 3b, the autoclave was removed from the heating cabinet for cooling after 1.75 h to investigate the reaction course. The concentrations and fill factor of this synthesis is slightly different than that of synthesis 4a[1], but these differences are considered insignificant based on the results of larger variations of these parameters in syntheses 2a and 2c. The diffractogram for product 3b shown in Figure 4.4 shows a relatively large impurity of 39 mol% digenite ($Cu_{2-\delta}S$) in addition to 5 mol% CuS, resulting in a low $CuGaS_2$ purity of 56 mol%. The yield is further reduced to 20% by the small amounts of product formed, which indicate that the synthesis was stopped during the particle growth and before precipitation reached equilibrium. The large digenite impurity compared to syntheses 4a[1], 1a and 1b with 12 h heating time shows that $Cu_{2-\delta}S$ is consumed during

the synthesis. Sortland [1] reported that also 5 h heating can be sufficient to prevent the digenite impurity. Thus, digenite is an intermediate phase for $CuGaS_2$ formation, like Cu_2S in the reaction mechanism in ethanol in Section 2.4.2. The difference is however the valency of copper in the intermediate copper sulphide as Feng et al. [36] report CuS and In_2S_3 to be intermediate products for formation of $CuInS_2$. This results in oxidation to form elemental S upon reduction of Cu^{2+} in Equation (2.13) in the proposed mechanism. However, as S is not identified in products containing $CuGaS_2$ in this work, reduction of Cu^{2+} does not occur, and the CuS impurity results. Furthermore, Ga_2S_3 is soluble in water and can not be an intermediate product. Formation of $CuGaS_2$ from the intermediate product similar to the proposed mechanism in Equations (2.12)–(2.13) in Section 2.4.2 is constructed in Equations (4.2).

$$Cu_{2-\delta}S + (2 - 2\delta)Ga^{3+} + (3 - 3\delta)S^{2-} \rightarrow (2 - 2\delta)CuGaS_2 + \delta CuS \qquad (4.2)$$
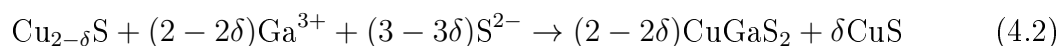
Even though this reaction may account for CuS impurities up to 20% as 0.2 is the highest value of δ for which $Cu_{2-\delta}S$ is stable, decomposition of $Cu_{2-\delta}S$ to yield CuS is possible without production of $CuGaS_2$. The remaining Cu^{2+}-poor $Cu_{2-\delta}S$ can then take up additional Cu^{2+} ions. According to the binary phase diagram for the Cu-S system in

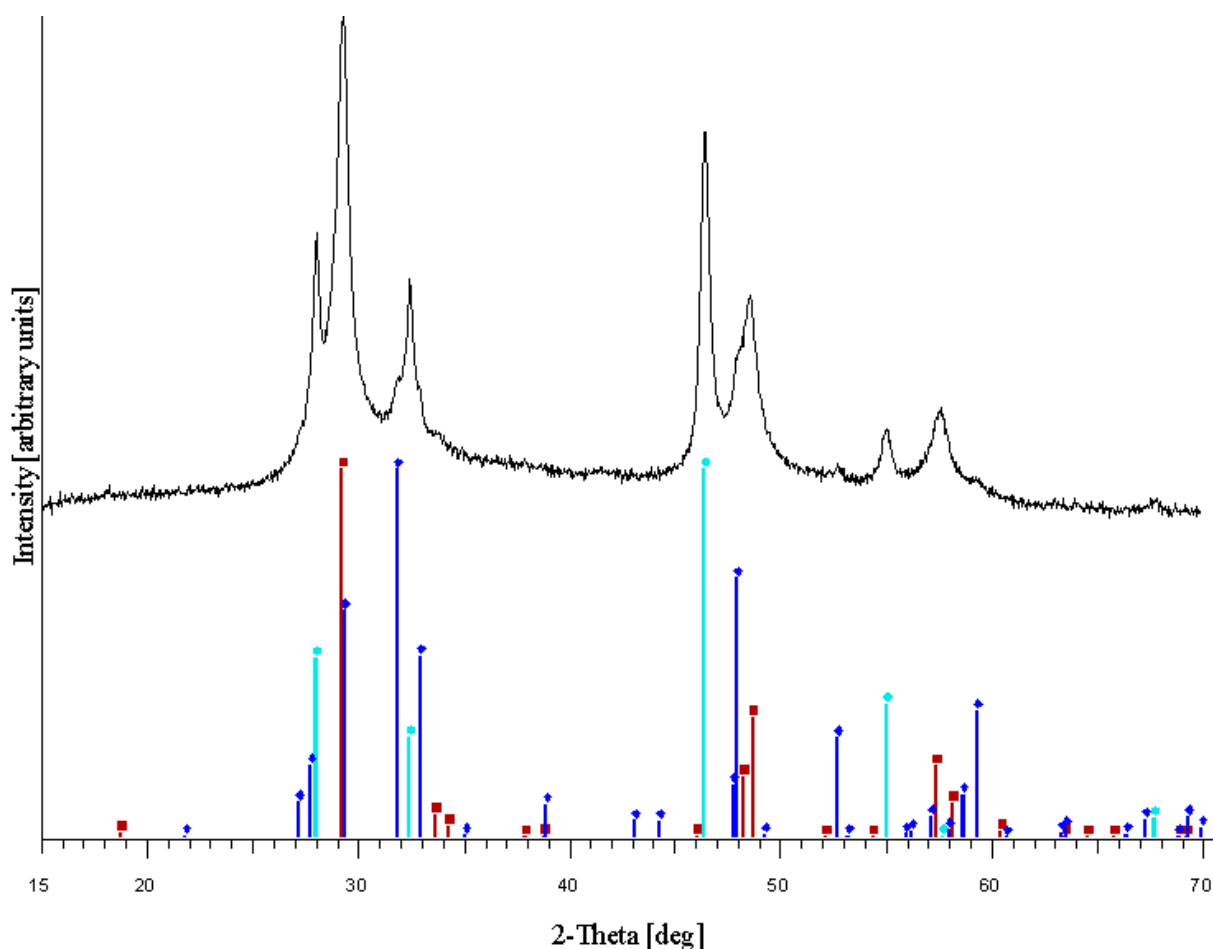
Figure 4.4: Diffractogram of product 3b with overlay of peaks for known phases: $\blacksquare$ $CuGaS_2$, $\blacklozenge$ CuS, $\bullet$ $Cu_{2-\delta}S$.

Figure 2.5 in Section 2.2, $Cu_{2-\delta}S$ is stable at 180 °C for $0.1 \leq \delta \leq 0.2$. At higher S contents, a two-phase region with CuS is stable at the synthesis temperature, which according to diffractogram 3b in Figure 4.4 is obtained in this product. The stability region of $Cu_{2-\delta}S$ borders towards a two-phase region with high-chalcocite Cu_2S at 33 at.%. Formation of Cu_2S instead of $Cu_{2-\delta}S$ as the intermediate phase may prevent the CuS impurity. According to the stability diagrams calculated by Bailey et al. [21] and Tablero and Fuertes Marrón [6] in Figure 2.6 in Section 2.2, this might be achieved at a reduced chemical potential of S^{2-}, which suggest a slower Tu decomposition and lower equilibrium concentrations of S^{2-} to be favorable.

4.1.3 Thiourea Stoichiometry

The effect of reducing the Tu concentration was investigated as formation of digenite instead of Cu_2S as the intermediate phase and the CuS impurity may according to the Cu-S phase diagram in Figure 2.5 in Section 2.2 relate to a too high S content, at which phases with increasing content of divalent copper ions become stable. Cu_2S is the desired intermediate phase for the $CuGaS_2$ synthesis as it does not contain Cu^{2+} ions forming the CuS impurity. In this respect, a Tu concentration of 0.029 M was used in synthesis 4c. The diffractogram of the obtained product in Figure 4.5 shows large amounts of 15 mol% CuS and 18 mol% digenite impurities. Even though the Tu concentration is reduced to the stoichiometric amount for Cu_2S precipitation and thus below the stoichiometric amount for $CuGaS_2$ formation, CuS and digenite make up the copper sulphide impurities and not Cu_2S. The high digenite content after 12 h heating time may be due to reduced rate of Tu decomposition by the reduced concentration, although this also requires slow consumption by Ga incorporation to form $CuGaS_2$ and the reduction in Tu concentration is also expected to alter the state of the reaction solution through reduced extent of decomposition and thus less acidification of the solution.

Although the Tu concentration of 0.029 M is below the stoichiometric concentration for $CuGaS_2$ precipitation, the calculations shown in Table A.2 in Appendix A.1 show that roughly 6% of the supplied Tu molecules do not contribute to precipitation of sulphides remained in the solution. A large part of the Cu and Ga ions remain unreacted due to the deficiency of S^{2-}. The formation of $GaO(OH)$ relates to a too high pH as explained in Section 2.4.2 and Sortland [1]. This is due to the reduced Tu concentration, as the contribution from Tu decomposition was not sufficient to make $GaO(OH)$ soluble during the synthesis with a HCl concentration of 0.316 M.
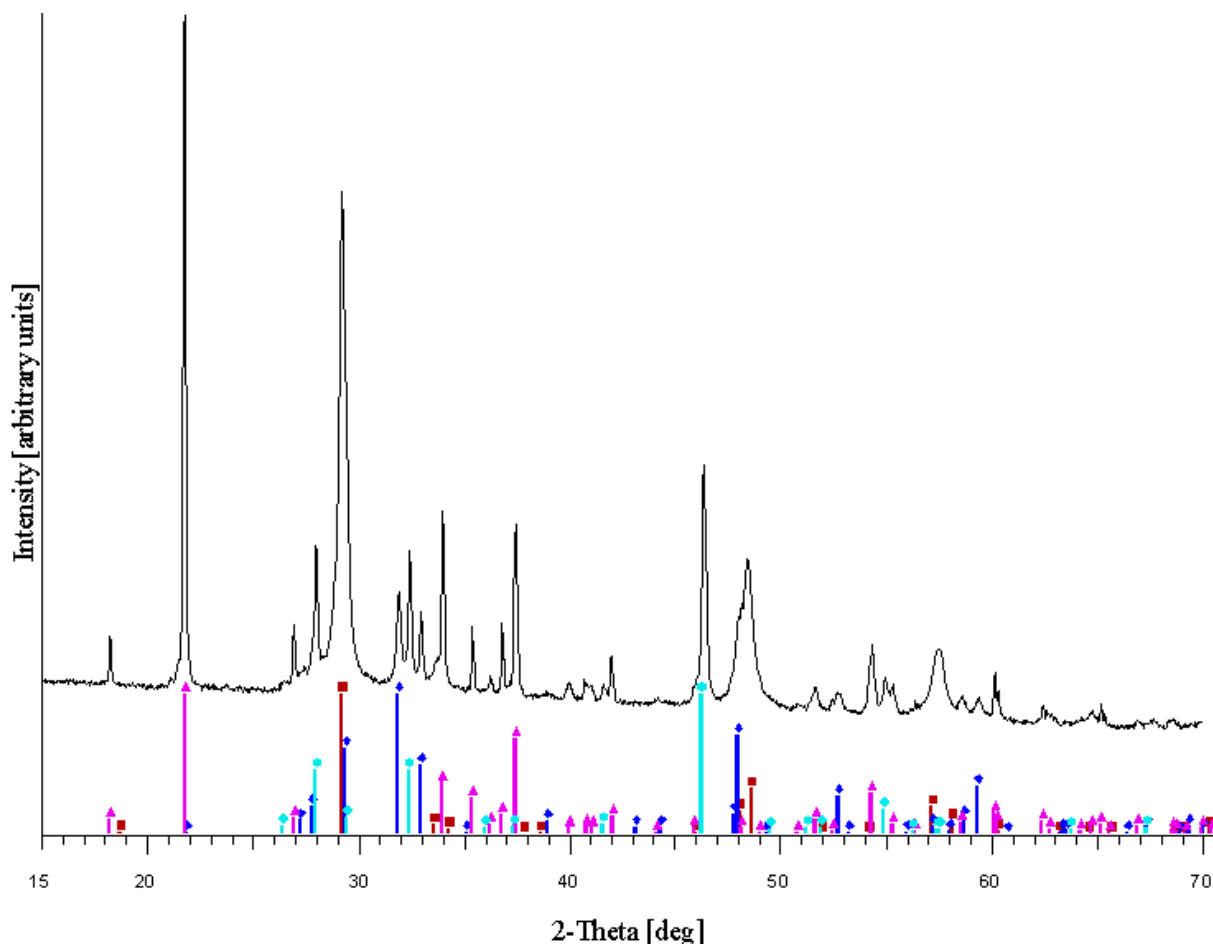
Figure 4.5: Diffractogram of product 4c with overlay of peaks for known phases: ▣ $CuGaS_2$, ◈ CuS, ◉ $Cu_{2-\delta}S$, ▲ GaO(OH).

4.1.4 HCl Concentration

The effect of HCl concentration on the synthesis was investigated by Sortland [1]. A slight increase in pH above 0.5 with 0.316 M HCl in synthesis 4a[1] yielded an additional impurity of gallium hydroxyoxide (GaO(OH)), and a very low pH resulted in low purity due to formation of $Cu_{2-\delta}S$, but the sensitivity towards increasing HCl concentration was not investigated. Thus, synthesis 3a employed a slightly increased HCl concentration of 0.501 M compared to synthesis 4a[1]. The diffractogram in Figure 4.6 shows a 23 mol% CuS impurity, giving relatively low $CuGaS_2$ purity of 77 mol% and 42% yield. As this represents a marked reduction in $CuGaS_2$ purity, the synthesis is confirmed to be sensitive also to increasing HCl concentration.
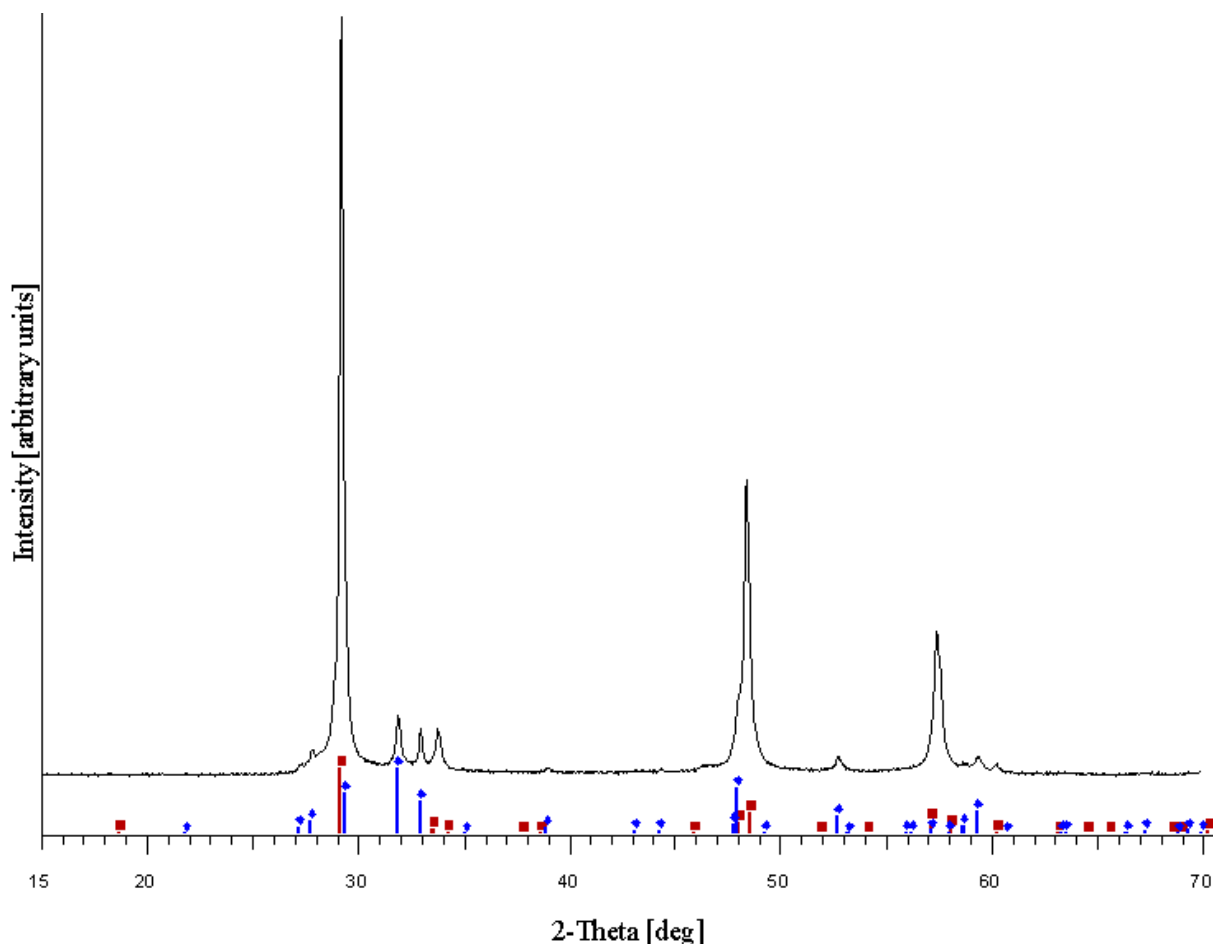
Figure 4.6: Diffractogram of product 3a with overlay of peaks for known phases: ◉ CuGaS$_2$, ◉ CuS.

4.1.5 Fill Factor

Synthesis 2c employed an increased fill factor of 85% to be able to investigate the increase in concentrations at this fill factor in synthesis 2b. A higher fill factor was not considered safe as water expands by 13% upon heating to 180 °C so that the autoclave becomes completely filled for fill factors above 88% in which case the pressure may suddenly rise above the design limit of the autoclaves as explained in Section 2.4. However, since a gas phase is retained at a fill factor of 85%, the pressure is not changed from the saturation pressure of water of 10 bar [72] according to Figure 2.10 in Section 2.4 providing the equilibria for H$_2$S evolution limit its partial pressure to a significantly lower value. The diffractogram in Figure 4.7 shows an impurity of CuS, and composition calculations indicate that it amounts to 21%, so that the CuGaS$_2$ purity is reduced to 79% compared synthesis 4a[1] with a fill factor of 80%. A similar alteration of fill factor at a lower HCl concentration of 0.10 M reported by Sortland [1] provided an additional impurity phase of digenite, so formation of this phase is prevented at a fill factor of 85% by optimization of pH in synthesis 2c. However, the lower purity of synthesis 2c along with its low yield of 46% compared to synthesis 4a[1] shows that a fill factor of 80% is beneficial for the purity in accordance with the observation by Sortland [1] that this fill factor is near some

44

optimum based on syntheses using 0.10 M HCl.
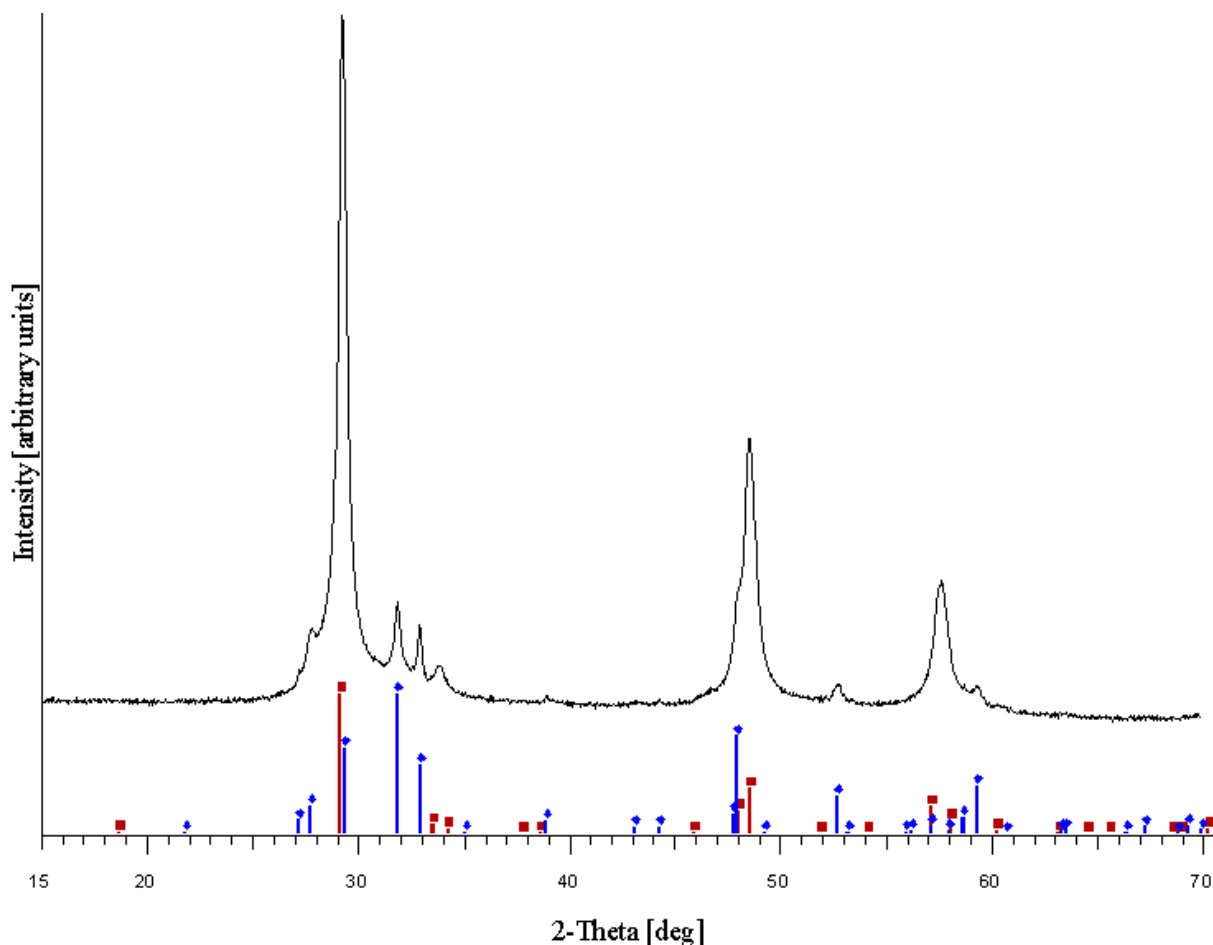
Figure 4.7: Diffractogram of product 2c with overlay of peaks for known phases: ■ CuGaS$_2$, ◆ CuS.

4.1.6 Reactant Concentrations

In order to assimilate the hydrothermal synthesis by Hu et al. [8] as closely as possible with the autoclaves used in this work, the concentrations of CuCl and GaCl$_3$ were increased to 0.319 M with two times excess of Tu in synthesis 2a, and a fill factor of 85% was used as discussed in Section 4.1.5. Provided the increased Tu concentration did not increase the partial pressure of H$_2$S significantly due to shifting equilibria, as explained in Section 2.4.2, the pressure in synthesis 2b was not changed from the saturation pressure of water. Although Hu et al. [8] used a temperature of 160°, the temperature of 180° was kept after synthesis 4a[1] as previous investigations by Sortland [1] show that such a temperature variation has no influence on the product composition.

In synthesis 2b, a yellow deposit was obtained along the Teflon cup wall, but the amount of this stoichiometric CuGaS$_2$ was minute compared to the brown and black precipitate at the bottom. As such a yellow product was not observed in synthesis 2c, this was achieved through increasing the concentrations. Figure 4.8 shows the diffractogram of the obtained product, and Rietveld analysis indicates a significantly decreased CuS

45

impurity of 8 mol% compared to 21 mol% in synthesis 2c. In spite of an additional digenite impurity of 4 mol%, the increased reactant concentrations in synthesis 2b provided a profound increase in purity of 87 mol% $CuGaS_2$ with 82% yield. The difference in concentrations have a large effect on the crystallite sizes discussed in Section 4.3, as the $CuGaS_2$ peak widths are greatly increased in the diffractogram of product 2b in Figure 4.8 compared to those in the diffractogram of product 2c in Figure 4.7 in Section 4.1.5. The increase in concentrations between synthesis 2b and 2c gives nearly a doubling of the yield to 82% and Cu^+ ions are nearly depleted form the solution according to calculations shown in Table A.2 in Appendix A.1, possibly because the initial conditions are further from equilibrium at increased concentrations, giving increased reaction rates for Tu decomposition and precipitation.
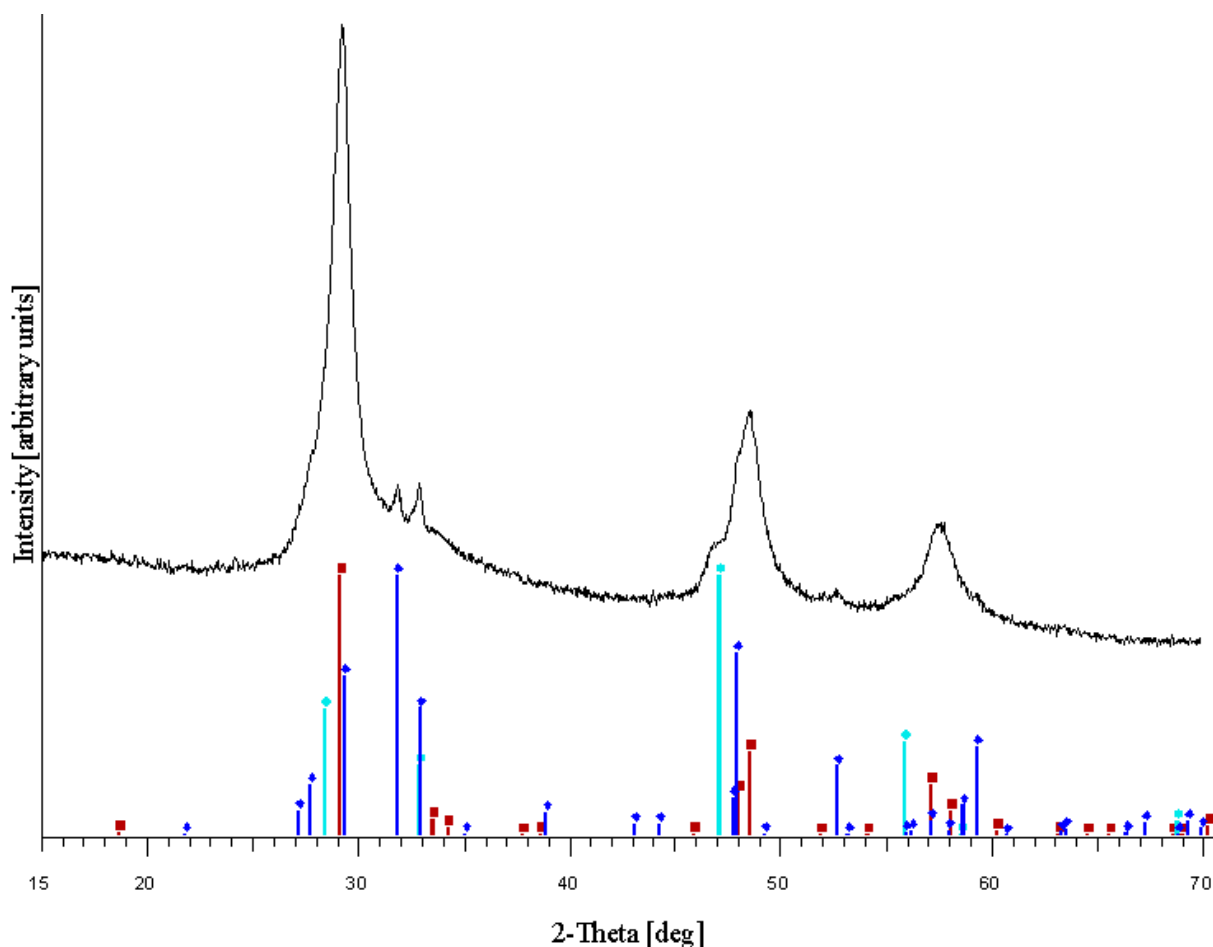
Figure 4.8: Diffractogram of product 2b with overlay of peaks for known phases: ■ $CuGaS_2$, ◆ CuS, ◆ $Cu_{2-\delta}S$.

Syntheses 2a and 3c aimed to investigate the effect of increasing concentration at a fill factor of 80% due to the higher purity obtained with this fill factor compared to 85%, and these syntheses are compared to synthesis 4a[1] in Figure 4.9. This comparison also shows peak broadening from syntheses 2a and 3c with increased reactant concentrations compared to 4a[1], supporting the trend of decreasing crystallite sizes with increasing concentrations discussed in Section 4.3.5. Calculated compositions indicate an increas-

ing purity up to 94 mol% as the cation concentrations are increased to 0.220 M. This is consistent with the increased purity of synthesis 2b with 0.319 M cation concentrations compared to synthesis 2c. However, the purity of 86 mol% in synthesis 2a using, 0.122 M CuCl and GaCl$_3$, is similar to that of synthesis 4a[1]. However, product 2a contained a 2 mol% digenite impurity in addition of 12 mol% CuS, as shown in Figure 4.10(a). Such small amounts of digenite also occurred in products 3c and 2b with higher cation concentrations of 0.220 M and 0.319 M, respectively, while the CuS impurity was reduced to 5 mol% in synthesis 3c, giving a CuGaS$_2$ purity of about 92 mol%. Such a trend of increasing purity with increasing reactant concentrations is also observed by Chang and Ting [58] for a solvothermal synthesis with elemental Se precursor described in Section 2.4.5. Figure 4.10(b) show that also the yield increases with increasing reactant concentrations. The yield in synthesis 3c approached 94%, although this is an overestimation due to a negative value for the percentage of Cu$^+$ ions remaining in the solution, as shown in Table A.2 in Appendix A.1. This trend correspond to the increasing yield from 46% for synthesis 2c using 0.030 M to 82% in synthesis 2b with 0.319 M cation concentrations with a fill factor of 85%, although the yields obtained at 80% fill is much higher, partially due to the increased purities.

The stability diagram in Figure 2.6(b) in Section 2.2 is used together with chemical potentials of Cu$^+$ and Ga^{3+} calculated in Appendix A.2 from initial concentrations using Debye-Hückel theory presented in Section 2.4.1, to assess the stability of CuGaS$_2$ and sulphide impurities in different syntheses through plotting of chemical potentials like in Figure 4.11. The Debye-Hückel calculations assume CuCl to be completely dissolved at the start of CuGaS$_2$ formation and that there is no complex formation, although Tu is thought to stabilize Cu$^+$ according to Section 2.4.2. The formation energies of CuGaS$_2$ and the competing phases in the stability diagram apply for formation from elemental Cu, Ga and S solids, corresponding to the standard state of these elements. This is represented for CuGaS$_2$ in Equation (4.3), for which the free energy of formation ($\Delta_f G$) is used to construct the stability diagram.

$$\text{Cu (s)} + \text{Ga (s)} + 2\text{S (s)} \rightarrow \text{CuGaS}_2 \text{ (s)} \tag{4.3}$$

However, the elements are dissolved as ions in an aqueous solution in hydrothermal syntheses, and since formation of an intermediate digenite phase in the reaction course does not affect the CuGaS$_2$ stability, Equation (4.4) can be used for CuGaS$_2$ production. This reaction is a sum of the reaction in Equation (4.3) and formation of Cu$^+$, Ga^{3+} and S^{2-} ions in aqueous solutions from Cu, Ga and S elemental solids, respectively. Since the chemical potentials of the elements in their standard states are defined to be zero and deviations in temperature and pressure are neglected for solids in the stability diagram [6], the free energy of formation of the ions equals their chemical potential. Thus, the free energy of the reaction in Equation (4.4) is given by equation (4.5). Similar equations can also be constructed for the competing phases in the stability diagram.

$$\text{Cu}^+ \text{ (aq)} + \text{Ga}^{3+} \text{ (aq)} + 2\text{S}^{2-} \text{ (aq)} \rightarrow \text{CuGaS}_2 \text{ (s)} \tag{4.4}$$
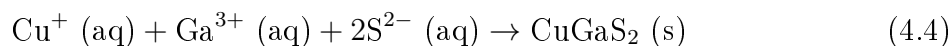
$$\Delta G = \Delta_f G_{\text{CuGaS}_2} - \mu_{\text{Cu}^+} - \mu_{\text{Ga}^{3+}} - 2\mu_{\text{S}^{2-}} \tag{4.5}$$

Lines in the stability diagram relate to the formation energies of different phases through the equilibrium chemical potentials of their constituent elements. The chemical potentials of Cu$^+$ and Ga^{3+} represent shifts from those for the corresponding elemental solids
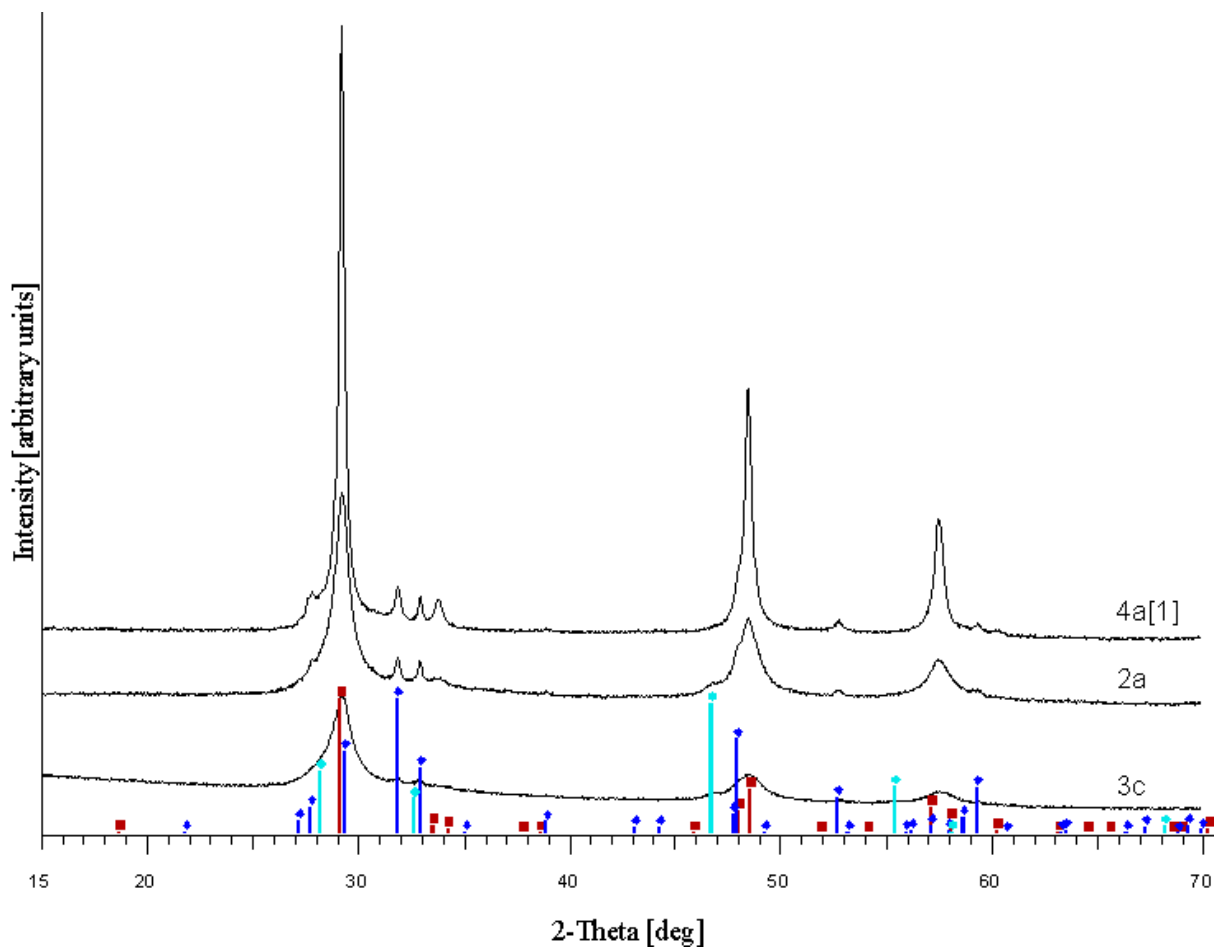
Figure 4.9: Diffractogram of product produced with varying reactant concentrations at 180 °C: 4a[1] (0.030 M), 2a (0.120 M and 3c (0.220 M). Including peaks for known phases: ▣ $CuGaS_2$, ◈ CuS, ◉ $Cu_{2-\delta}S$.
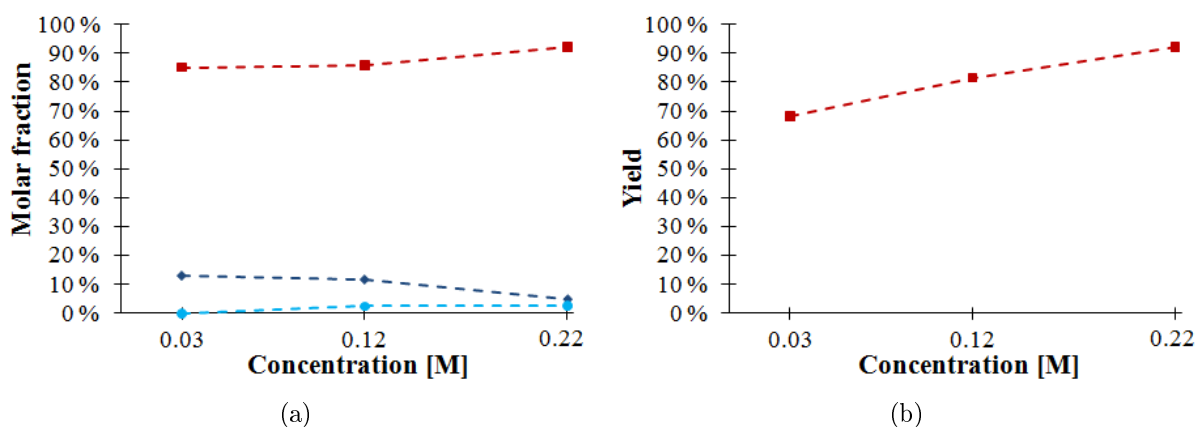

Figure 4.10: Product compositions (a) and yields (b) for syntheses with varying reactant concentrations. – ▪ – $CuGaS_2$, – ◆ – CuS, – ● – $Cu_{2-\delta}S$.
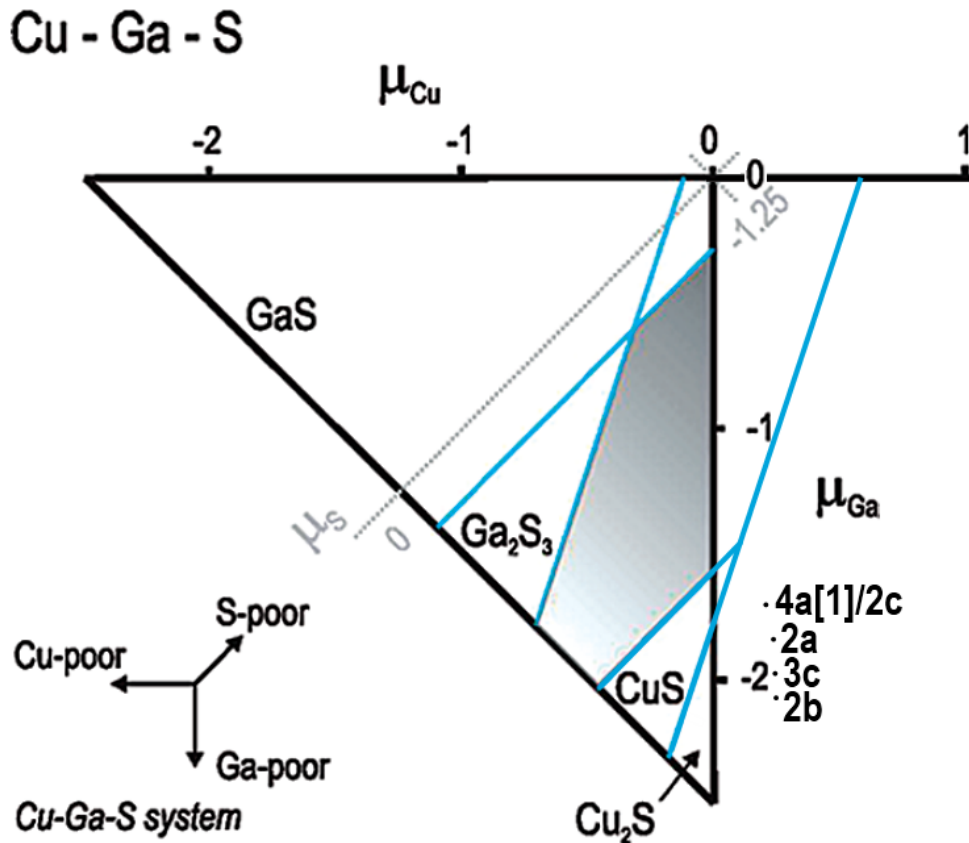
48

Figure 4.11: Stability diagram adapted from Tablero and Fuertes Marrón [6] modified with extrapolations and points for initial chemical potentials calculated for syntheses with varying concentrations at 180 °C: 4a[1] and 2c (0.030 M), 2a (0.122 M), 3c (0.220 M) and 2b (0.319 M).

at the origin. These chemical potentials are plotted for the initial conditions in synthesis 4a[1], 2a, 3c and 2b in Figure 4.11 to estimate the stability of the produced phase formed and assess changes in the synthesis that may prevent formation of the copper sulphide impurities. The chemical potential of S^{2-} is not required to plot the syntheses, and may vary throughout the synthesis as it is formed by slow decomposition of Tu and consumed by precipitation of sulphides and H_2S evolution, but it is assumed to eventually stabilize at equilibrium. Thus, a low S^{2-} concentration is selected for the calculations in which case it does not contribute to the ionic strength and thus does not affect the chemical potentials of Cu^+ and Ga^{3+}. The simplifications in these calculations give inaccurate results, and contradict the trend of increasing purity with increasing reactant concentrations. The increase in chemical potential of Cu^+ with increasing concentration is insignificant to the reduction in the chemical potential of Ga^{3+} in this respect, giving increasing distance from the $CuGaS_2$ single-phase region for the points for syntheses 4a[1], 2a and 3c with increasing reactant concentrations in the stability diagram in Figure 4.11. Formation of copper sulphides is expected to be favored with increasing distance into the stability regions of CuS and Cu_2S as this represent increasing chemical potentials above the equilibrium potentials for precipitation. Thus, reduced purity is expected from increasing reactant concentrations, which is opposite of the observed trend for these syntheses.

Both divalent and monovalent copper sulphides are stable at the calculated chemical potentials, correlating to the formation of CuS and the off-sotichiometric digenite impurity in synthesis 2a and 3c. Even though digenite is assumed stable at these chemical potentials, it may not appear as an impurity as it reacts further to form the more stable $CuGaS_2$ phase and the calculations do not contradict the absence of digenite in products 4a[1] and 2c with 0.030 M cation concentrations. The larger amount of CuS than digenite in syntheses 2a and 3c may relate to the increased distance from the stability border represented by the formation energy of divalent compared to monovalent copper sulphides, and copper-thiourea complex formation may reduce the chemical potential of copper ions towards the stability region of CuS. A similar comparison of synthesis 2c and 2b with 0.030 M and 0.319 M CuCl and $GaCl_3$ shows the same trend at an increased fill factor of 85%. The difference in purity between these syntheses compared to the difference in chemical potentials is much less than the difference in purity between syntheses 4a[1], 2a and 3c with a fill factor of 80%, as product 2c is 79% pure and product 2b is 87% pure. The Debye-Hückel calculations can not account for the influence of fill factor, as seen from the reduced purity of product 2c compared to 4a[1] while the same chemical potentials are calculated for these syntheses.

For the hydrothermal synthesis presented here, the borders at zero chemical potential of the stability diagrams in Figure 2.6 in Section 2.2 are not representative as elemental Cu is not formed even though Cu^+ has a positive standard free energy of formation [44], indicating that the reaction system does not provide spontaneous reactions for reduction of Cu^+ to Cu. Thus, the stability region of copper sulphides extends to positive chemical potentials of copper, and the border of the stability region of Cu_2S representing the formation energy in Figure 4.11 is extrapolated from Figure 2.6(b) in Section 2.2. The stability diagrams does not include the digenite intermediate phase, although the stability region of this phase is between the Cu_2S and CuS phases like in the phase diagram in Figure 2.5 in Section 2.2.

Increasing the reactant concentration also acidifies the solution during the synthesis as decomposition of Tu in Equation (2.7)is an acidic reaction. The Tu concentrations in syntheses 2a, 3c and 2b are higher than the HCl concentration, in which case the pH decreases during the synthesis as Tu decomposes. The sensitivity of the synthesis to pH is demonstrated in Section 4.1.4 and by Sortland [1], and acidification during the syntheses reduces the reaction rate of Tu decomposition according to Section 2.4.2. However, increased Tu concentrations increases the reaction rate of decomposition as the initial state is removed from equilibrium. Thus, a greater extent of decomposition is reached before the reverse reaction achieves the same rate at equilibrium. However, for this effect to be significant, the equilibrium concentrations can not be minute compared to the initial concentrations. The percentages of unreacted Cu^+ and Ga^{3+} ions of at least 20% for syntheses 4a[1] and 2c, seen in Table A.2 in Appendix A.1, show that the final concentrations are not insignificant compared to the initial concentrations in these syntheses. This explains the increased yields with increasing concentrations seen in Figure 4.10(b). Synthesis 3c produced a yellow solution after filtration, but no deposits of stoichiometric $CuGaS_2$ was observed in the product. The water was evaporated from this filtrate and XRD analysis showed large amount of ammonium chloride (NH_4Cl). This suggest that Tu also decomposes according to Equation (2.9) in the acidic reaction solution, but no tiocyanates were detected.

4.1.7 Complexing Agent

Due to the insufficient stability of copper-thiourea complexes demonstrated by the formation of copper sulphide impurities, a stronger complexing agent was sought for. Although ethylenediamine (En) has proven to yield pure and stoichiometric products at low fill factors [58], it is used as the solvent in the syntheses reported in Section 2.4.5 and thus compromises the goal of developing an environmentally friendly synthesis minimizing the use of organic solvents and also the economical benefits of using water as the solvent is lost. In the search for another complexing agent, also the possibility of introducing other impurities into the synthesis was considered and 1-pentanethiol was attempted as it does not introduce new elements into the synthesis and show strong complexing abilities [62]. Cu^{2+} ions may have coordination numbers of six in octahedral coordination, while Cu^+ predominantly form square planar complexes with coordination number four according to Section 2.4.4. To ensure sufficient 1-pentanethiol for formation of the most stable copper complexes, an excess of eight times the CuCl concentration was selected as also complexing of Cu^{2+} ions is desired to stabilize them from precipitation to form CuS. Although 1-pentanethiol is insoluble in water at room temperature, its influence on the synthesis indicate that it is dissolved above 180 °C.Using 1-pentanethiol makes syntheses solvothermal rather than hydrothermal as defined in Section 2.4, even though it is diluted in deionized water.

Adding 1-pentanethiol to a synthesis equivalent to 4a[1] did not improve the purity as seen from the diffractogram in Figure 4.12. However, digenite is the dominant impurity in this synthesis instead of CuS in synthesis 4a[1], and the minute peaks corresponding to CuS relates to a very small content of 1 mol%. Addition of 1-pentanethiol increased the purity from 85 mol% in synthesis 4a[1] to 92 mol%. However, a comparably small amount of product formed in synthesis 4a, giving a reduced yield of 59% compared to that of 68% for synthesis 4a[1] in spite of the increased purity. This is expected as the cations are stabilized in complexes in the solution, allowing a larger amount of Cu^+ and Ga^{3+} ions to remain in the solution at equilibrium.

Digenite is identified as an intermediate phase in Section 4.1.2, and since it is not formed in synthesis 4a[1] and the chemical potentials of copper ions are reduced from those in synthesis 4a[1] by complexing, it may not be a thermodynamically favored impurity in synthesis 4a. In that case, a longer reaction time is expected to allow complete consumption of this phase to produce a higher yield and even higher purity. Since digenite contain some Cu^{2+} ions that do not take part in the $CuGaS_2$ product, further consumption of digenite may release Cu^{2+} ions that can increase the CuS impurity content. The occurrence of digenite in product 4a correspond to decreased reaction rates as the concentration of free cations in the solution is drastically reduced as a consequence of formation of stable 1-pentanethiol complexes, and decomposition of complexes can become rate determining. Stabilization of Cu^+ and Cu^{2+} ions reduce the reaction rate of digenite formation, relating to the small amounts of product formed. Furthermore, the significant amount of digenite in product 4a suggest a low rate of incorporation of Ga into digenite to form $CuGaS_2$, which is reduced by stabilization of Ga^{3+}. Furthermore, Cu^+ ions are stabilized from oxidation and complexing of Cu^{2+} also counteract CuS precipitation both in terms of reduced rate of reaction and reduced concentration and chemical potential of Cu^{2+}, so that the equilibrium condition provide a lower content

of CuS precipitate in the multiphase region within the copper sulphide stability regions in the phase diagrams in Figure 2.6.
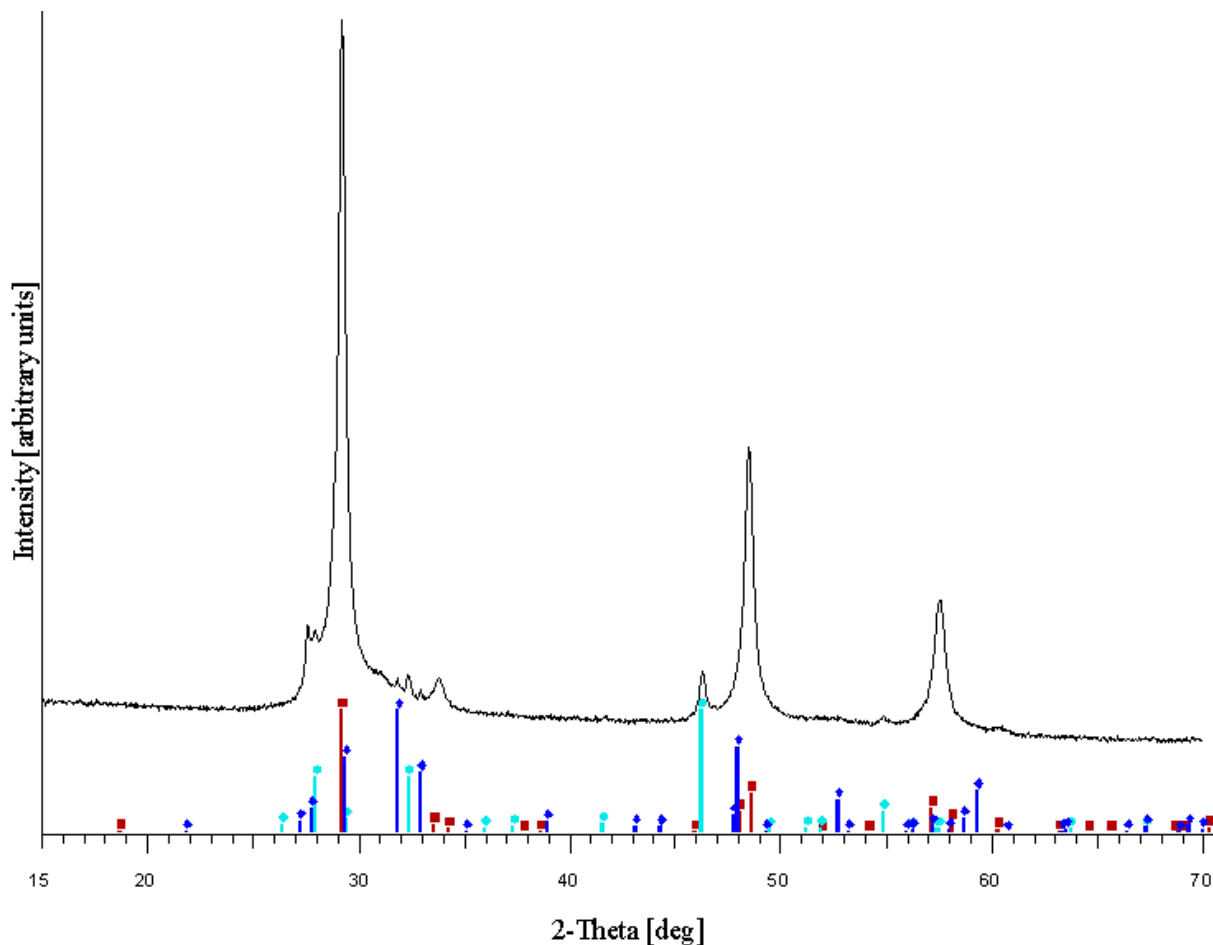
Figure 4.12: Diffractogram of product 4a with overlay of peaks for known phases: ■ $CuGaS_2$, ◆ CuS, ● $Cu_{2-\delta}S$.

4.1.8 Pressure

As explained in the introduction to this section, the high pressure used by Hu et al. [8] to produce pure and stoichiometric $CuGaS_2$ can not be reproduced in the autoclaves used in this work. The fill factor is for safety reasons kept low enough to avoid complete filling of the autoclaves after thermal expansion of the solution during heating to the reaction temperature. An alternative method to controllably increase the pressure is to heat the solution above 200 °C, as the vapor pressure of water start to increase significantly at this temperature according to Figure 2.10 in Section 2.4. The maximum design temperature for the autoclaves of 250 °C was selected as Figure 2.10 estimate the vapor pressure of water to still be below half of the pressure limit of the autoclaves at this temperature. However H_2S evolution from the acidic sulphide-containing solution may contribute to the pressure. The increased thermal expansion of water of 25% and 13% [72] during heating to 250 °C compared to 180 °C, respectively, requires the fill factor to be reduced from 80% to 70%. This variation in fill factor is expected to slightly influence the synthesis as

demonstrated at 180 °C in Section 4.1.5 and Sortland [1].

Synthesis 4b was based on synthesis 4a[1], with an increase in temperature to 250 °C and a reduced fill factor to 70%. The diffractogram in Figure 4.13 confirms the necessity of a high pressure in the hydrothermal synthesis of pure $CuGas_2$. The CuS impurity is reduced from 15 mol% in synthesis 4a[1] at 180 °C to 3 mol% at 250 °C. Although a temperature variation between 160 °C to 180 °C reported by Sortland [1] did not affect the product composition, other studies described in Section 2.4.5 have found a trend of increasing purity at increased temperatures up to 200 °C [35, 36, 65]. Part of this product, including particles dispersed in the solution, was stoichiometric as it showed a yellow color. Ideal calculations give a maximum partial pressure of H_2S of 18 bar if gaseous H_2S to accounts for all un-precipitated sulfur in this synthesis and a 25% expansion of water from room temperature to 250 °C [72]. As expected, H_2S evolution at low concentrations of Tu in this synthesis does not represent a safety risk due to increased pressure, but this calculation shows that increased pressure from H_2S evolution must be considered for increased concentrations. Dissolution of H_2S, keeps the H_2S partial pressure below the calculated maximum, although the partial pressure of H_2S may rise during the synthesis depending on the extent of Tu decomposition, which shifts the acid-base equilibria for H_2S formation as explained in Section 2.4.2
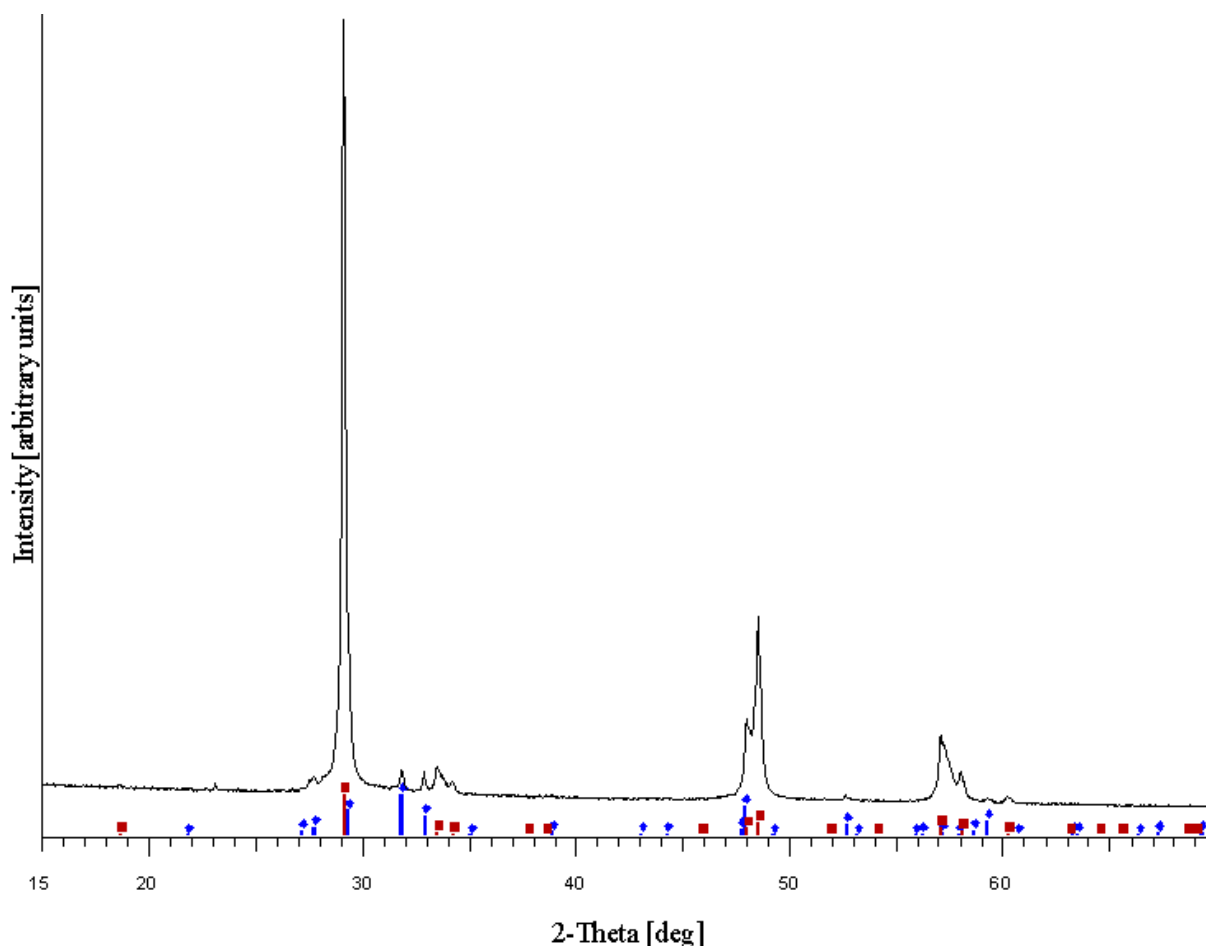

Figure 4.13: Diffractogram of product 4b with overlay of peaks for known phases: ■ $CuGaS_2$, ◆ CuS.

53

4.1.9 Heating Time with Complexing Agent

Both addition of 1-pentanethiol and increased temperature to 250 °C have proven to decrease the amount of CuS impurity, so a combination of these changes were attempted in synthesis 5a and 5c. Synthesis 5c was stopped after 5 h, while synthesis 5a used a heating time of 20 h to increase the extent of digenite consumption. The diffractograms in Figure 4.14 reveal that both syntheses prevent the formation of CuS, but the 8 mol% digenite content in product 5c is halved to 4 mol% by the increased reaction time in synthesis 5a, and the purity is increased from 89 mol% to 96 mol%. This suggests that at least synthesis 5c was stopped before $CuGaS_2$ formation was complete, which indicate reduced rates of digenite and $CuGaS_2$ formation with addition of 1-pentanethiol as discussed in Section 4.1.7. In addition to the increased temperature compared to synthesis 4a, also a slight increase in pH by reduction of the HCl concentration to 0.271 M in synthesis 5a and 5c contributed to an increased rate of Tu decomposition. This HCl concentration is sufficient for preventing GaO(OH) formation in synthesis 5a, but product 5c contain a 3 mol% GaO(OH) impurity due to insufficient acidification by incomplete Tu decomposition after 5 h. The increased yield of 75% obtained after 20 h heating in synthesis 5a compared to 65% obtained in synthesis 5c with a heating time of 5 h can be explained both by reduced
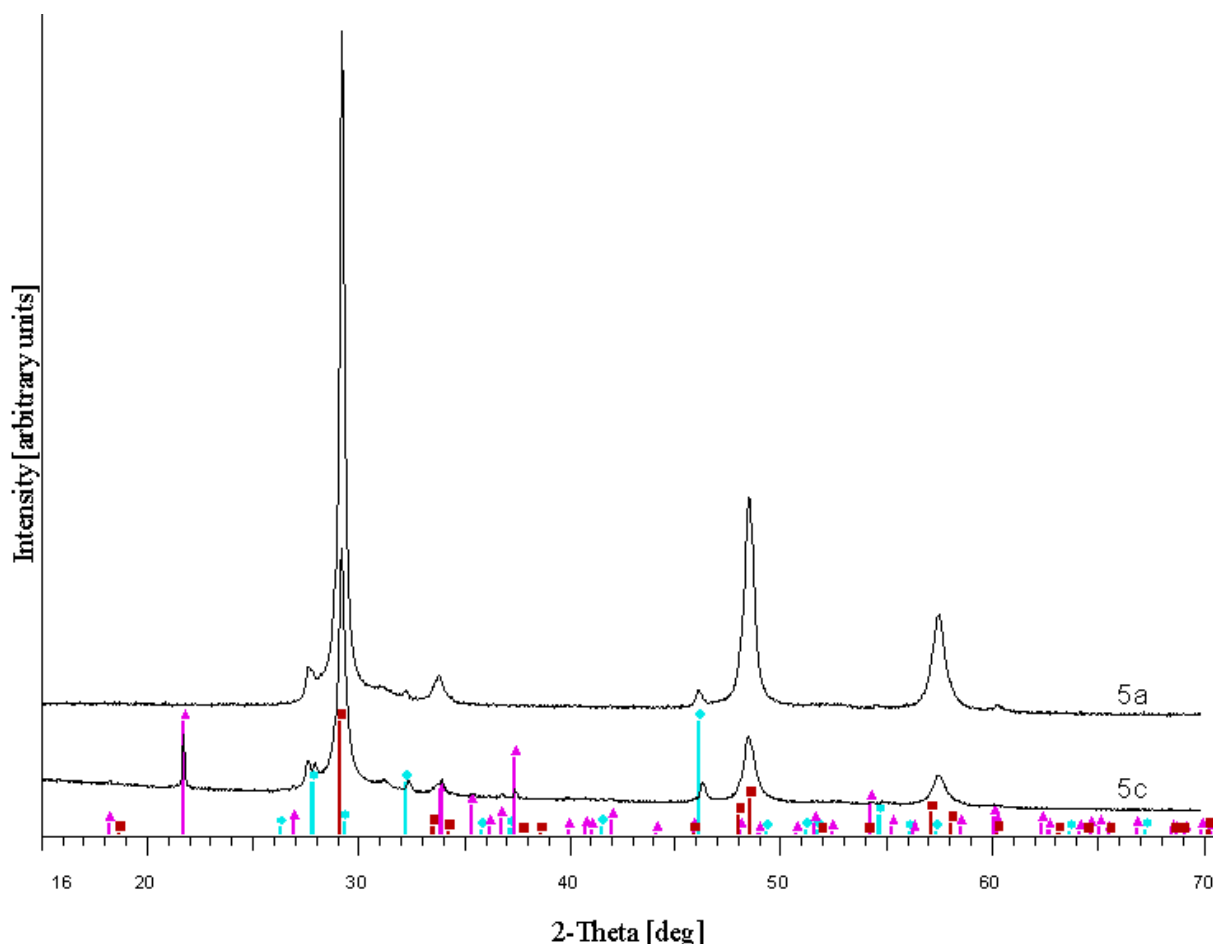
Figure 4.14: Diffractogram of products produced 1-pentanethiol with different heating times: 5c (5 h) and 5a (20 h. Peaks for known phases are included: ■ $CuGaS_2$, ◉ $Cu_{2-\delta}S$, ▲ GaO(OH).

reaction rates due to stabilization of the cations and incomplete Tu decomposition when 1-pentanethiol is used.

4.1.10 Reactant Concentrations at increased Pressure

In order to allow complete consumption of the digenite intermediate product, an increased reaction time of 30 h was utilized in synthesis 6a, but also the HCl concentration was restored to 0.316 M. The diffractogram of this product in Figure 4.15 shows a relatively high digenite content of 16 mol% in spite of the increased reaction time, giving a reduced purity of 84 mol% and yield of 54% compared to both syntheses 5a and 5c. No stoichiometric $CuGaS_2$ was observed in this product, but part of the precipitates in both synthesis 5a and 5c showed a yellow color.
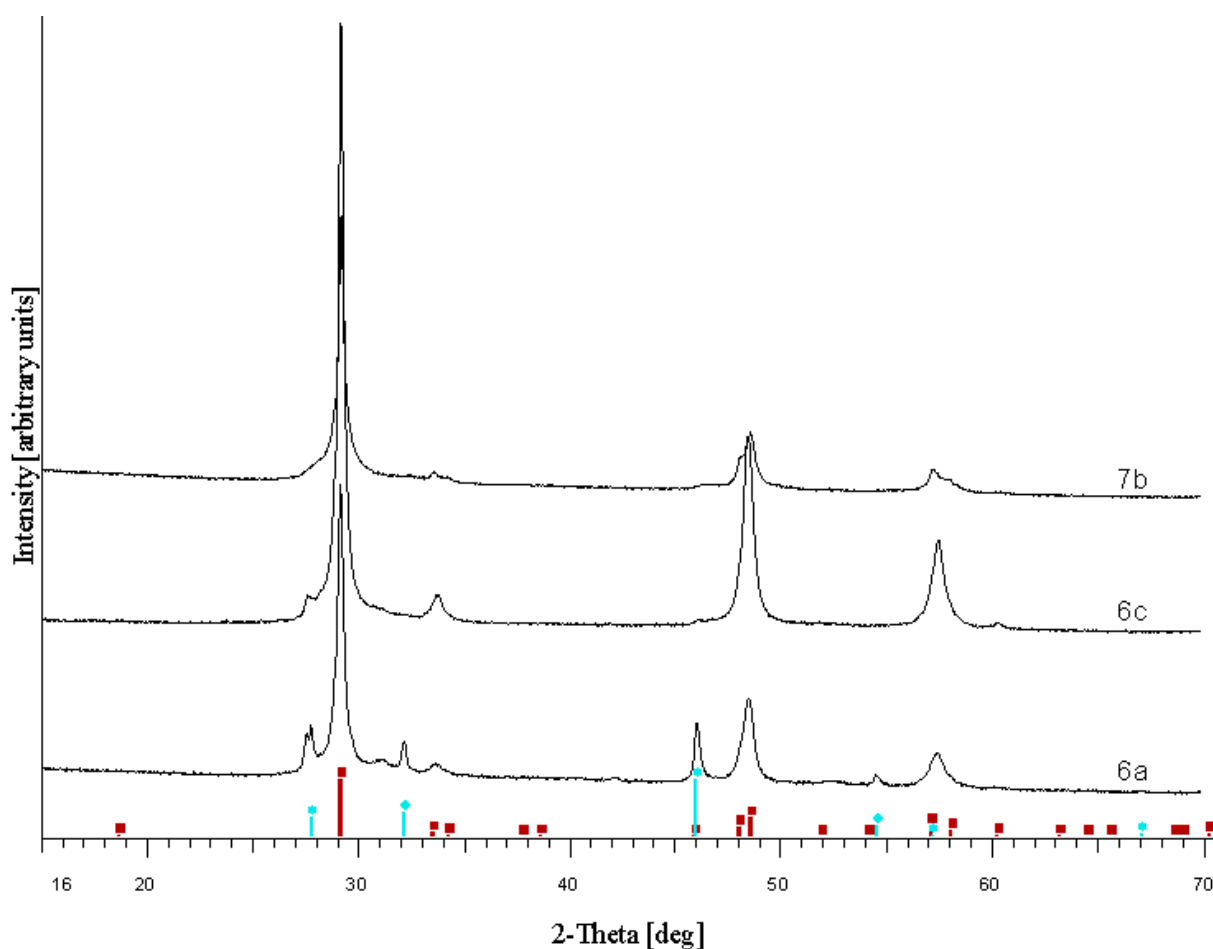
Figure 4.15: Diffractogram of products produced with varying reactant concentrations at 250 °C using 1-pentanethiol: 6a (0.03 M), 6c (0.06 M) and 7b (0.319 M). Including peaks for known phases: ■ $CuGaS_2$, ◉ $Cu_{2-\delta}S$.

Synthesis 6c utilized increased concentrations to 0.060 M CuCl and $GaCl_3$ in addition to a heating time of 30 h to increase the extent of reaction. Such a careful concentration increase give a maximum theoretical partial pressure of H_2S of 37 bar at the relatively high fill factor of 70%, if gaseous H_2S to account for all remains of the sulphide precursor.

Added to the saturation pressure of water of at least 65 bar according to Figure 2.10 in Section 2.4, this could theoretically provide a total pressure near the pressure limitation of the rupture disks. The diffractogram of product 6c shows a single phase of $CuGaS_2$ in Figure 4.15.

The diffractogram does however show a rise in intensity at a *2θ* angle of about 27.5° that is masked by peaks form CuS and digenite impurities in most other diffractograms. This can either be due to stacking faults in nanoscale crystallites, explained in Section 2.2, or it can be the strongest peak of another impurity phase. Product 6a shows a similar peak in addition to that of digenite, and also an unidentified artifact near 31°. In case the unidentified peak in the diffractogram of product 6c is due to stacking faults, synthesis 6c fulfills the first goal of developing an environmentally friendly synthesis producing pure $CuGaS_2$. Synthesis 6c also achieved the highest yield among syntheses using 1-pentane-thiol of 80%. However, the challenge remains to achieve a stoichiometric product that has a uniform electronic structure and band gap, which is desired for solar cell applications and photoluminescence (PL) measurements to characterize the electronic structure, and is discussed in Section 4.4.

At relatively high cation concentrations of 0.319 M in synthesis 7b, the fill factor was reduced to 42%, as pressure build-up from H_2S evolution at a theoretical maximum exceed the pressure limitation of the autoclaves. However, the maximum H_2S partial pressure of maximum 25 bar if all excess Tu would form H_2S gas in this synthesis is considered safe. Additionally, HCl was not added to synthesis 7b since the high concentration of acidic Tu of 1.276 M is more than sufficient for preventing GaO(OH) formation, and the concentration increase from synthesis 6a to 6c and 7b provide a reduction in pH of the reaction solution. The diffractogram of product 7b shows that this product also has a high purity, but the highest digenite peak at 46° is distinguishable, giving an impurity of maximum 3 mol% and a $CuGaS_2$ purity of 97 mol%.

The similarity in purity for product 6c and 7b in spite of the large concentration differences indicates that the concentration has less influence on the chemical potentials when 1-pentanethiol is utilized for its strong complexing abilities, in contrast to syntheses without 1-pentanethiol, although this is not supported by the decreased purity of product 6a. Contradictory to the trend of increasing yield with increasing reactant concentrations for syntheses 4a[1], 2a and 3c at 180 °C, synthesis 7b provided a lower yield of 70% compared to 80% for synthesis 6c. Furthermore, it can be seen from Table A.2 in Appendix A.1 that a higher yield is generally achieved in syntheses without 1-pentanethiol than in synthesis with 1-pentanethiol, which relates to reduced rates and extents of reaction due to formation of stable complexes. This is exemplified in Figure 4.16, in which the $CuGaS_2$ yields from syntheses with and without 1-pentanethiol with different reactant concentrations at 250 °C is plotted. This trend results from stabilization of ions in the solution due to formation of stable complexes, and suggests that precipitation is unable to completely shift the complex formation equilibria. Furthermore, complexing of the cations limits supersaturation of free ions and thus affect the rate of nucleation and growth according to Section 2.4.3. The comparatively low $CuGaS_2$ yield of synthesis 6a, as seen in Figure 4.16 is partly due to its lower purity. The width of the $CuGaS_2$ peaks increases from product 6a to 6c, and further to product 7b, which relates to a decrease in size of the smallest crystallites produced for syntheses with increasing reactant concentrations, as discussed in Section 4.3.9.
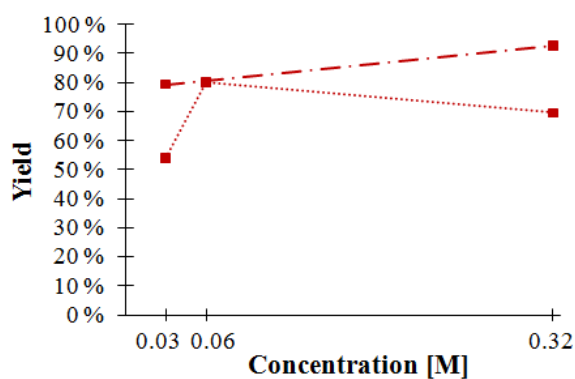
Figure 4.16: Yields of syntheses with and without 1-pentanethiol and varying reactant concentrations at 250 °C. ·····■····· Syntheses with 1-pentanethiol: 6a (0.030 M), 6c (0.060 M), 7b (0.319 M). — · ■ · Syntheses without 1-pentanethiol: 4b (0.030 M), 7a (0.319 M).

Synthesis 7a was similar to synthesis 7b, except that 1-pentanethiol was not added. A high purity is obtained from synthesis 7a and a only one small impurity peak assumedly corresponding to a digenite impurity of maximum 1 mol% can be distinguished in the diffractogram of product 7a in Figure 4.17, and a high yield of 93% is obtained. The high purity of product 7a shows that complexing by 1-pentanethiol is not necessary at 250 °C and reactant concentrations of 0.319 M CuCl and GaCl with 2 times Tu excess for $CuGaS_2$ precipitation. Like the comparisons of syntheses with increasing reactant concentrations with fill factors of 80% and 85% at 180 °C in Section 4.1.6 and to a limited extent syntheses using 1-pentanethiol presented in Figure 4.15, the increased reactant concentrations in synthesis 7a compared to 4b give peak broadening as seen from the diffractograms in Figure 4.17. Furthermore, no CuS impurity is formed in product 7a, which may be because HCl was not added to synthesis 7a and the fill factor was reduced, although the pressure is assumed to be determined from equilibria in both syntheses. The slightly higher purity of product 7a compared to product 4b with a 3 mol% CuS impurity is consistent with the trend of decreasing CuS impurity and increasing $CuGaS_2$ purity with increasing reactant concentrations at 180 °C discussed in Section 4.1.6. Synthesis 7a provided a higher purity and yield than synthesis 2b with a higher fill factor of 85% although low enough for the pressure to be determined from evaporation and dissolution equilibria at 180 °C. This relates to the difference in pressure, changes in chemical potentials at the increased temperature of 250 °C and possibly excessive acidification by HCl addition in synthesis 2b.
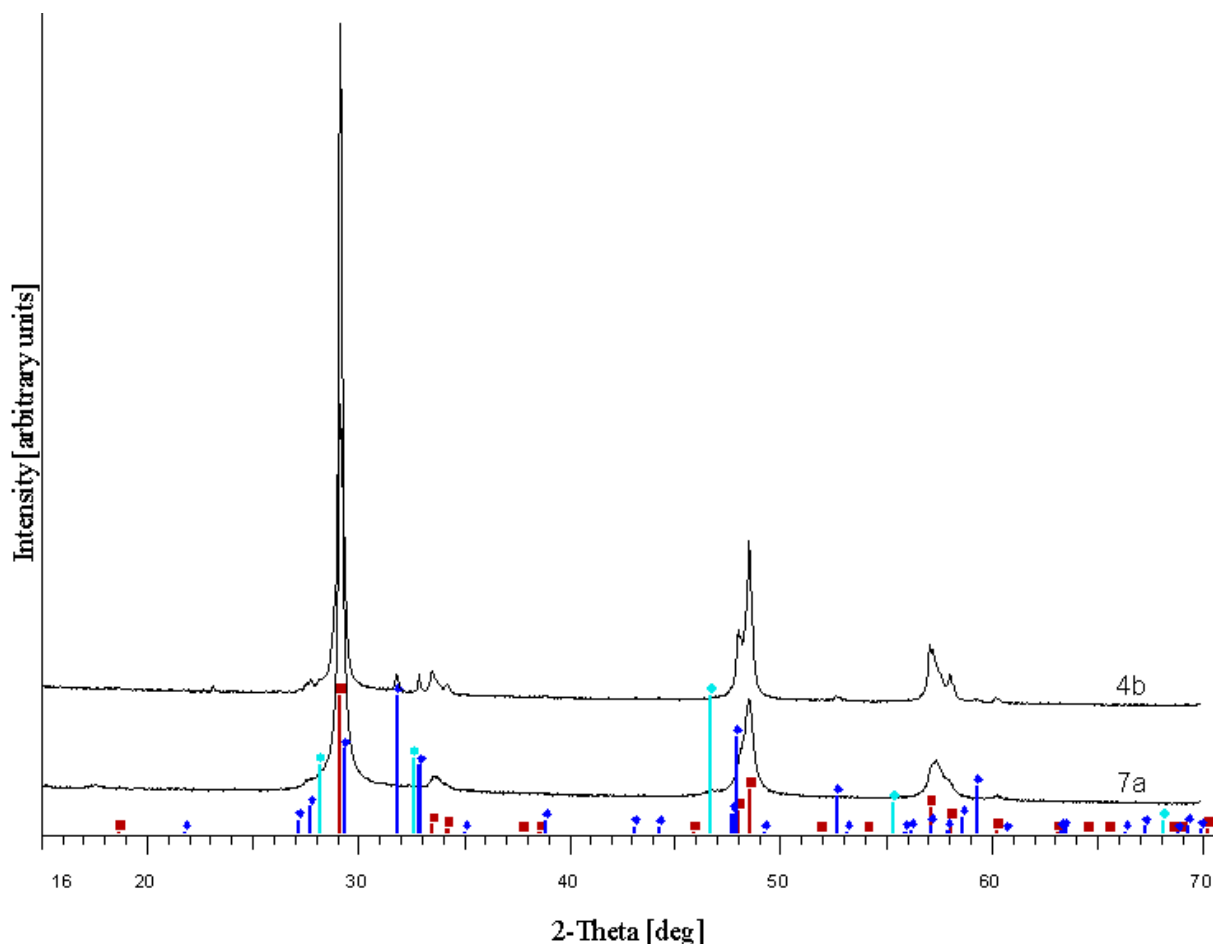
Figure 4.17: Diffractogram of products produced with varying reactant concentrations at 250 °C: 4b (0.03 M), and 7a (0.319 M). Including peaks for known phases: ■ $CuGaS_2$, ◆ CuS, ◆ $Cu_{2-\delta}S$.

The calculated chemical potentials plotted in the stability diagram in Figure 4.18 do not contradict the change from CuS in product 4b to digenite in product 7a as the impurity phase, as formation of a completely monovalent copper sulphide similar to digenite is more favored in synthesis 7a compared to 4b, although the calculations suggest that both CuS and monovalent copper sulphide could form in both syntheses. However, the increased distance from the $CuGaS_2$ single phase region for synthesis 7a compared to synthesis 4b in the stability diagram in Figure 4.18 does not correlate to the increased purity observed at the increased cation concentrations of 0.319 M in synthesis 7a. Such a deviation is discussed for syntheses with increasing reactant concentrations at 180 °C in Section 4.1.6. Comparing the chemical potentials at 250 °C shown in Figure 4.18 with those for syntheses 4a[1] and 2b in Figure 4.11 in Section 4.1.6 shows that the chemical potentials (μ_{Cu} and μ_{Ga}) are reduced with increasing temperature, which is due to the reduced relative permittivity of water at 250 °C, as seen in Table A.4 in Appendix A.2. This shifts the calculated chemical potentials towards the $CuGaS_2$ single-phase region, and thus contributes to the increased purities obtained at 250 °C compared to 180 °C. Based on the thermodynamic calculations presented in Figure 4.18, the $CuGaS_2$ formed is expected to be Cu-rich as explained in Section 2.2 which also relate to the formation

58
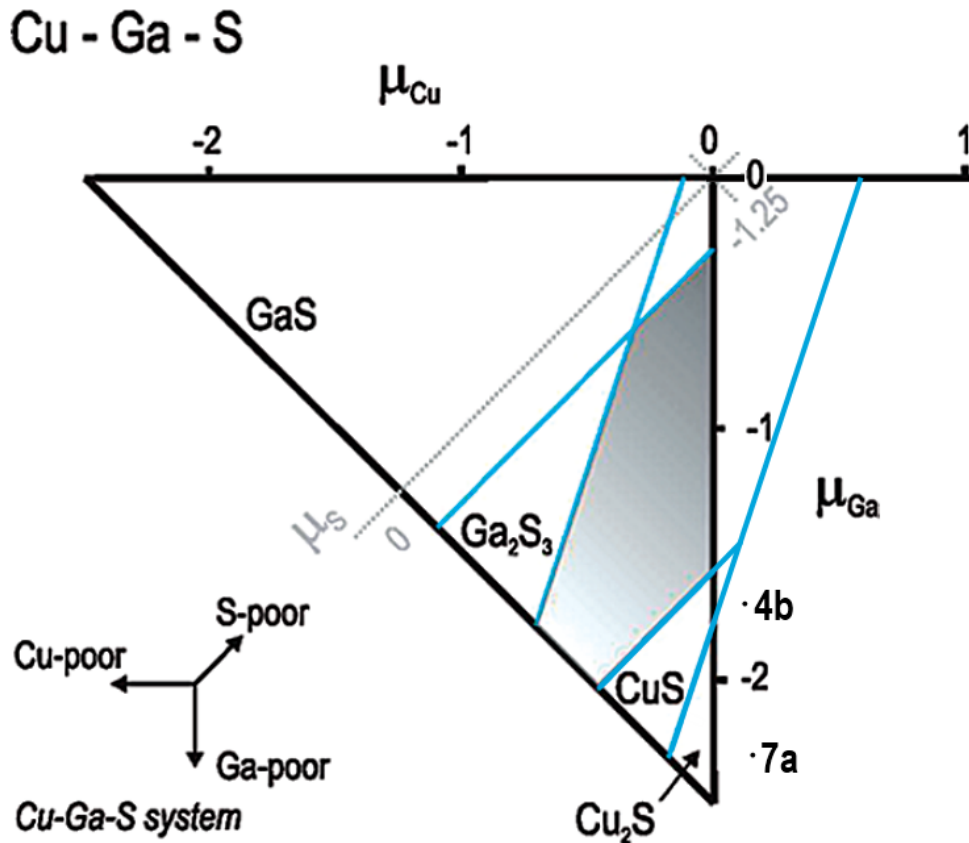
Figure 4.18: Stability diagram adapted from Tablero and Fuertes Marrón [6] modified with points for initial chemical potentials calculated for syntheses with varying concentrations at 250 °C: 4b (0.030 M), 7a (0.319 M).

of a copper sulphide impurity, and this contradicts the increased amounts of red, Ga-rich product formed in synthesis 7a.

Figure 4.19 summarizes the trends of improved purity upon variation of parameters that have proven important for the hydrothermal synthesis. These include increased pressure at 250 °C and stabilization by 1-pentanethiol. The diagram also illustrates the trend of increasing purity with increasing reactant concentrations, which is clear for all syntheses without 1-pentanethiol. Optimization of the fill factor to 80% at 180 °C is also demonstrated, although the pressure supposedly not significantly changed as it is determined by saturation equilibria for both fill factors. According to Sortland [1] and Section 4.1.4, pH adjustment through HCl addition is also important for improving the purity at low Tu concentrations.
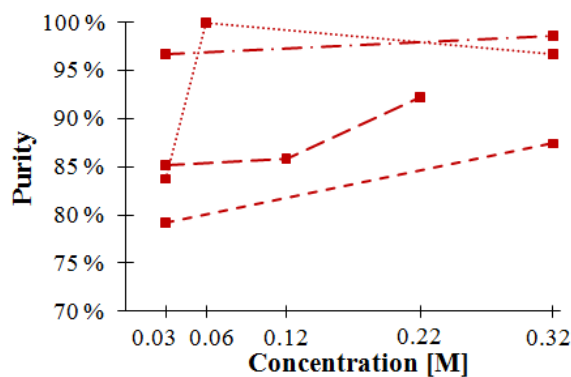
Figure 4.19: Puritiy improvements by variation of important parameters. – ◼ – Syntheses with 85% fill at 180 °C: 2c (0.030 M), 2b (0.319 M). — ◼ — Syntheses with 80% fill at 180 °C: 4a[1] (0.030 M), 2a (0.122 M), 3c (0.220 M). — · ◼ · Syntheses at 250 °C: 4b (0.030 M), 7a (0.319 M). ····◼···· Syntheses with 1-pentanethiol at 250 °C: 6a (0.030 M), 6c (0.060 M), 7b (0.319 M.

4.1.11   Volume

As the off-stoichiometry of all powder products may be due to inhomogeneities in the reaction solution, a smaller autoclave of 45 ml depicted in Figure 3.1(b) in Section 3.1 was used in synthesis 7c. Furthermore, this autoclave volume is similar to those used by Hu et al. [8] and Lu et al. [35] of 50 ml to obtain stoichiometric products. This synthesis was otherwise based on the parameters used in synthesis 6c, due to the high purity achieved.

This decrease in volume did not change the color of the product and thus, it proved unable to significantly increase the amount of stoichiometric product, which is further discussed in Section 4.3.10. The volume change does however influence the reaction conditions as seen by formation of digenite and GaO(OH) impurities in the diffractogram of product 7c shown in Figure 4.20 compared to the high purity of product 6c. The formation of 2 mol% GaO(OH) is particularly remarkable as the HCl and Tu concentrations were the same in syntheses 7c and 6c. This GaO(OH) impurity indicates that a higher HCl concentration is necessary to prevent GaO(OH) precipitation as the reaction volume is decreased. Additionally, the decrease in reactor volume accommodated a 5 mol% digenite impurity, resulting in a $CuGaS_2$ purity of 93%, and the yield of 73% is somewhat reduced compared to 80% in synthesis 6c. The intensity of the peak at a 2θ angle of 17° in the diffractogram in Figure 4.20 is significantly higher than what is expected for the GaO(OH) phase. Thus, there may be small quantities of another impurity phase having the highest peak at this 2θ angle, or GaO(OH) might show preferred orientation in the XRD sample. The relative height of this peak compared to the highest GaO(OH) peak indicates together with the low GaO(OH) content that the amount of an additional phase is not significant for the $CuGaS_2$ purity and yield.
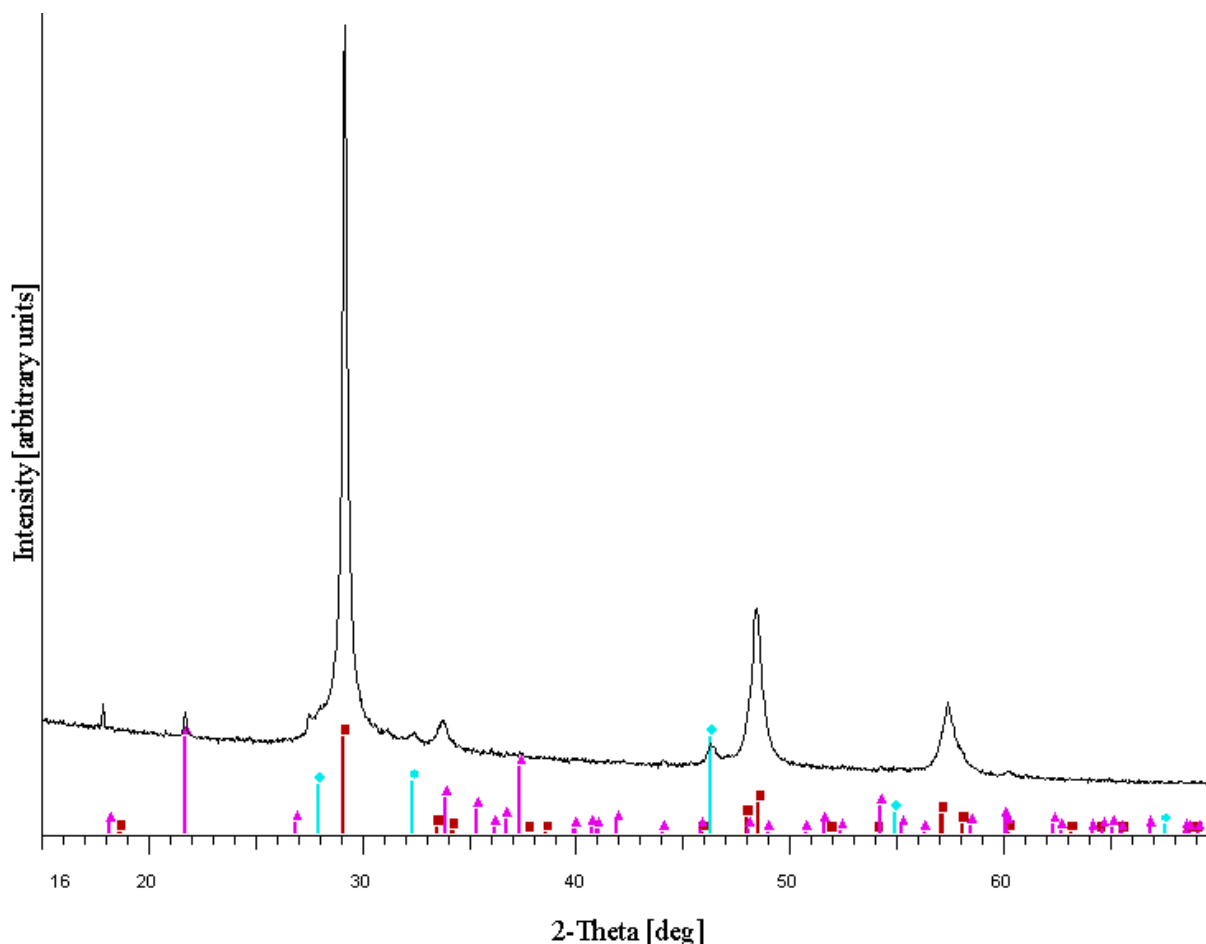
Figure 4.20: Diffractogram of product 7c with overlay of peaks for known phases: ■ CuGaS$_2$, ● Cu$_{2-\delta}$S ▲ GaO(OH).

4.1.12 Substrate

Several syntheses, particularly utilizing high concentrations, provided a yellow solution from dispersed stoichiometric CuGaS$_2$ crystals as well as yellow deposits on the Teflon cup wall above the precipitate at the bottom. This suggests that a stoichiometric film may also grow on a substrate held above the off-stoichiometric precipitates. A quarter of a Si(100) wafer is selected as substrate for film growth due to its similarity in crystal structure to CuGaS$_2$ as explained in Section 2.4.3, which promote epitaxial CuGaS$_2$ film growth as the precursors can be directly incorporated in the lattice on the Si surface.

In syntheses 5b, a Si substrate was positioned vertically near the surface of the solution in the large vertical substrate holder shown in Figure 3.2 in Section 3.1. The reaction parameters were unchanged from synthesis 4b, with low CuCl and GaCl$_3$ concentrations of 0.030 M and 250 °C. Introducing a substrate holder reduced the free volume in the Teflon cup to 98 ml and a comparison between the diffractograms of synthesis 4b and 5b in Figure 4.21 demonstrates the sensitivity of the synthesis to the reaction volume and the geometrical change caused by the substrate holder. The CuS impurity is prevented at the reduced volume in synthesis 5b, but instead it has a large digenite impurity of 19 mol% and 3 mol% GaO(OH), leaving a CuGaS$_2$ purity of 78 mol% in 49% yield. Formation

of GaO(OH) and increased amount of the digenite impurity can relate to the decrease in volume as discussed in Section 4.1.11. Additionally, the geometrical changes may contribute to the increased extent of inhomogeneities for instance at corners, as suggested by agglomerates showing the dark blue color of digenite in product 5b. Since 5 h is sufficient for consuming the digenite intermediate product in a synthesis equivalent to 4b at 180 °C as reported by Sortland [1], the consumption of digenite to form $CuGaS_2$ in synthesis 5b has supposedly come to a halt after 20 h, making the digenite impurity a stable byproduct. Such a decrease in the purity of the precipitate as a substrate and substrate holder is introduced is also found for synthesis 7d, which used the same reaction parameters as synthesis 6c.
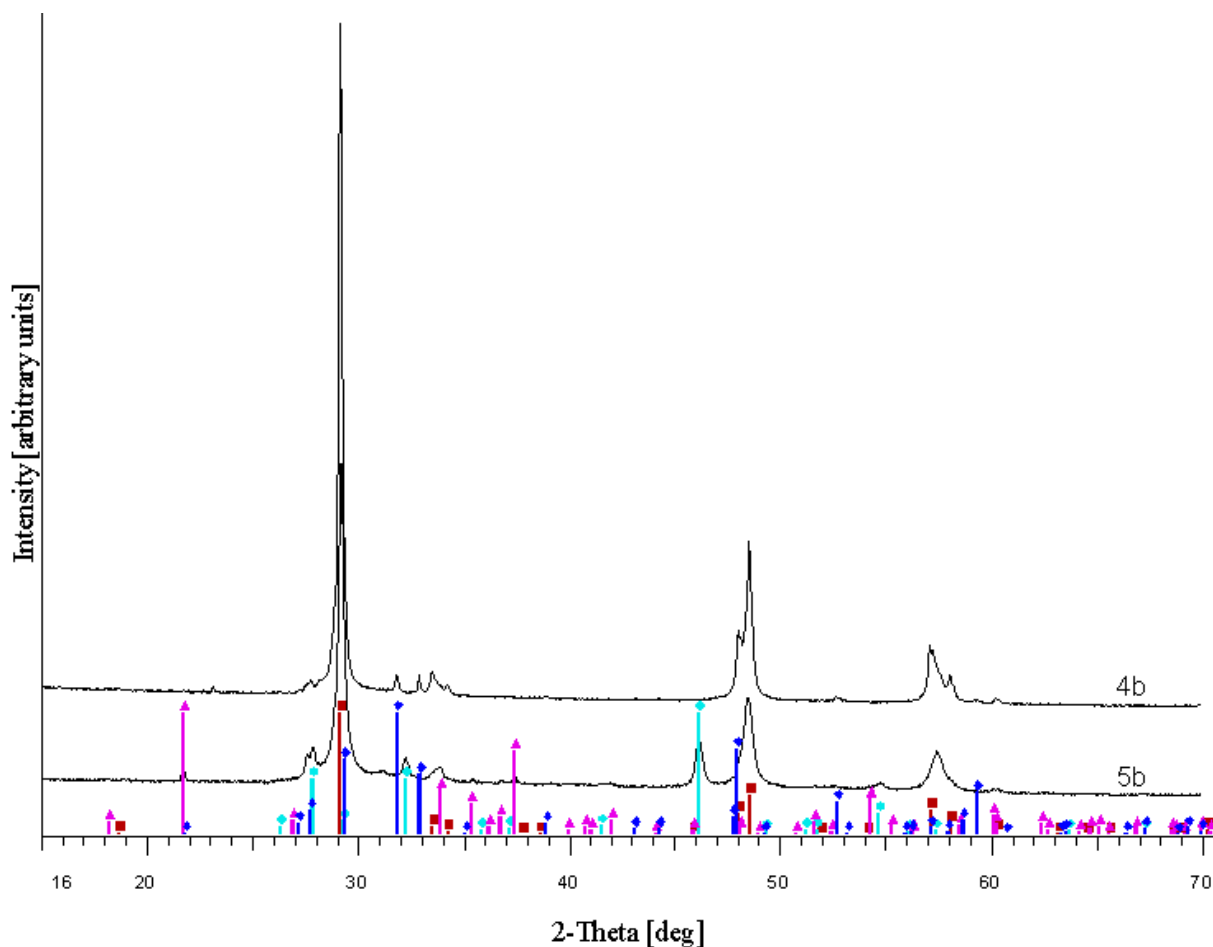
Figure 4.21: Diffractogram of product 4b produced with a reactor volume of 125 ml without substrate holder and product 5b produced with a volume of 98 ml due to a substrate holder. Peaks for known phases are included: ▣ $CuGaS_2$, ⬡ $Cu_{2-\delta}S$, ▲ GaO(OH).

No film was obtained after 20 h in synthesis 5b, and deposits of black, Cu-rich and red, Ga-rich $CuGaS_2$ could be washed away. The diffractogram of this substrate, labeled 5b(s) in Figure 4.22, shows no $CuGaS_2$ peaks, and all peaks that could be identified originate from the substrate, which is seen by a comparison with the diffractogram of a clean Si(100) substrate labeled Si(s) in Figure 4.22. This substrate gave a very intense peaks at 2θ angles below 70°, which is why the 2θ range is limited to just over 66° in

Figure 4.22. Additionally, no $CuGaS_2$ film was formed in synthesis 7d, as seen from the diffractogram of product 7d(s) in Figure 4.22. The substrate was mounted vertically in the small vertical substrate holder shown in Figure 3.2 in Section 3.1 in this synthesis, which was otherwise similar to synthesis 6c. This suggests that the reactant concentrations of 0.03 M in synthesis 5b and 0.06 M in synthesis 7d is too low for film formation.
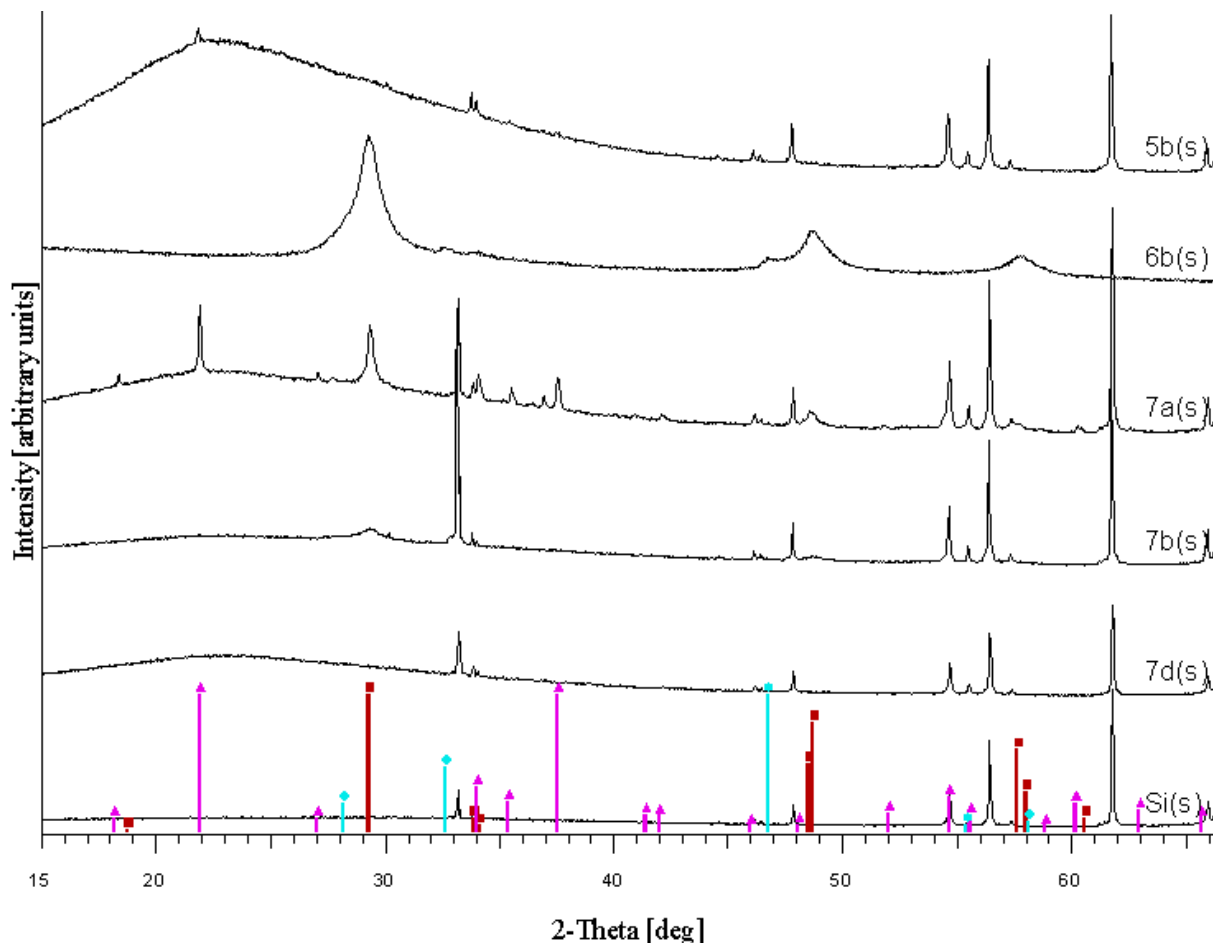
Figure 4.22: Diffractogram of products grown on substrates: 5b(s), 6b(s), 7a(s) and 7b(s), which compares to the clean Si(100) substrate Si(s). Including peaks for known phases: ■ $CuGaS_2$, ● $Cu_{2-\delta}S$, ▲ GaO(OH).

The low reactant concentrations used in synthesis 5b provided a clear solution, and high concentrations of 0.319 M CuCl and $GaCl_3$ with a four times higher Tu concentration was attempted in synthesis 6b with the hypothesis that film growth is promoted from a solution providing dispersed particles, and a dispersion of stoichiometric particles was observed at 0.319 M reactant concentrations at 180 °C in synthesis 2b. A thick yellow dispersion was reproduced in synthesis 6b with a slightly reduced fill factor to 80% and increased heating time of 30 h to promote film growth, and the substrate was covered by yellow, stoichiometric $CuGaS_2$. The diffractogram of this layer in Figure 4.22 shows complete coverage of the substrate as the peaks of Si(s) are not shown. Product 6b(s) does however contain a digenite impurity of 7 mol%. The powder obtained by filtration of only the dispersion gave a nearly identical diffractogram to that product 6b(s) and

a comparison with the diffractogram of the precipitate at the bottom of the Teflon cup shown in Figure 4.23 reveals a significantly higher $CuGaS_2$ purity of 93 mol% in the dispersion and on the substrate, as product 6b contained 4 mol% CuS and 15 mol% digenite. The large vertical substrate holder was also used in synthesis 6b, so the increased $CuGaS_2$ purity of 81 mol% and yield of 61% compared to product 5b is solely due to the increased reactant concentrations. Synthesis 8a used the same reaction parameters as synthesis 6b, except that HCl addition was omitted and a silica glass slide was used as substrate, since Peng et al. [67] were able to form $CuInS_2$ films on somewhat similar substrates of fluorine-doped tin oxide-coated conductive glass and a TiO_2 film. The silica glass substrate was mounted horizontally on the large horizontal substrate holder depicted in Figure 3.2 in Section 3.1 to limit particle deposits on the side facing downwards, but almost no film or deposits formed on the substrate as it remained transparent nearly all over even though a thick yellow dispersion was formed like in synthesis 6b.
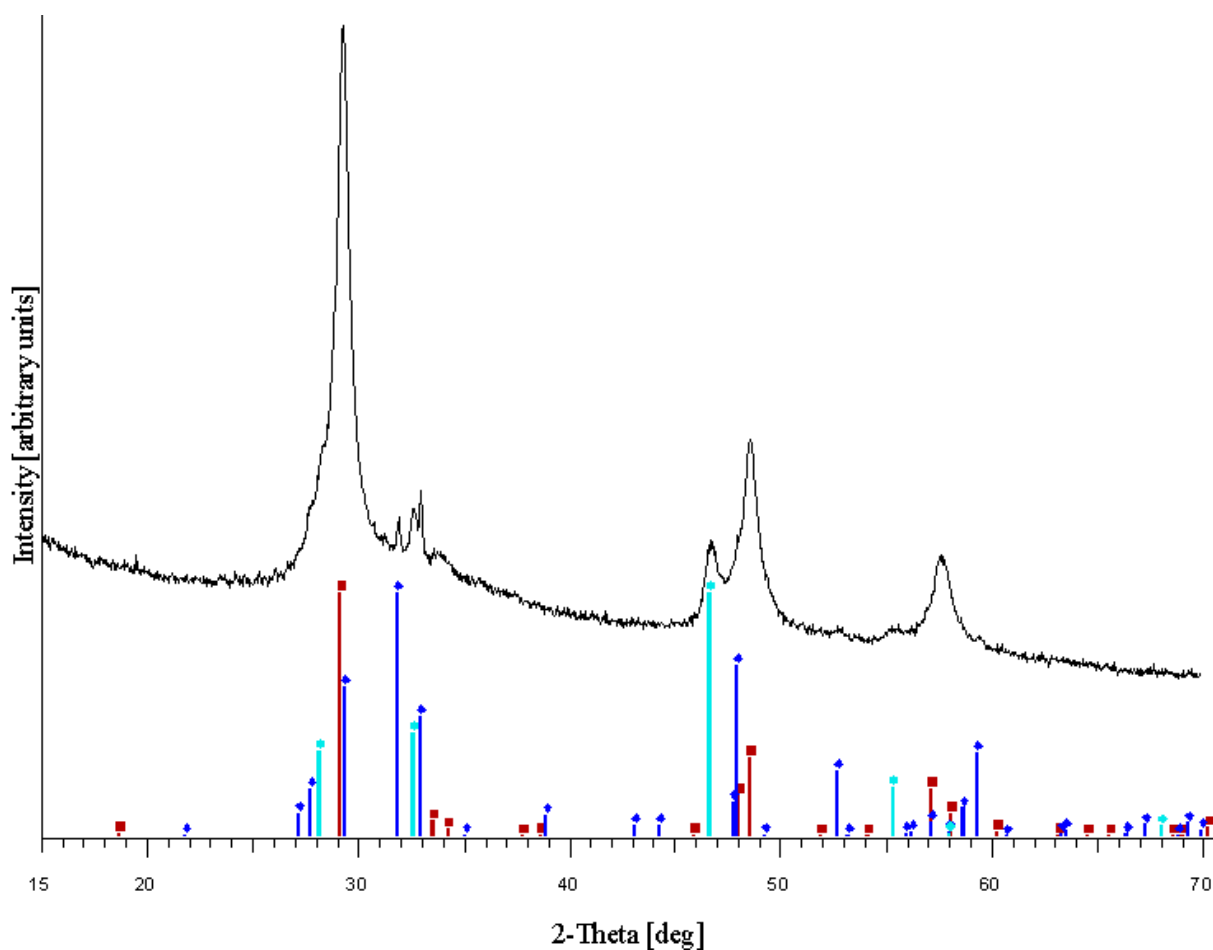
Figure 4.23: Diffractogram of the precipitate from synthesis 6b with overlay of peaks for known phases: ▣ $CuGaS_2$, ◈ CuS, ◉ $Cu_{2-\delta}S$.

A substrate was mounted horizontally supported by two small vertical substrate holders, each on top of a cylindrical support in synthesis 7a, and two prismatic supports in syntheses 7b, with the goal of obtaining increased purities compared to 6b(s) by increasing the pressure in synthesis 7a and also stabilize cations by complex formation in synthesis

7b. The changes proved detrimental to the stoichiometry, and only parts of the particles in the thick, orange dispersion produced in both syntheses 7a and 7b contained stoichiometric $CuGaS_2$. The high reactant concentrations in these syntheses provided some $CuGaS_2$ on the substrates, as seen from the diffractograms in Figure 4.22. While product 7a(s) was a partial coverage of red, Ga-rich deposits, product 7b(s) had a more uniform red coloration of the substrate as a film was formed, which due to the low thickness of $CuGaS_2$ in this film relates to the low $CuGaS_2$ peaks in the diffractogram. No impurity peaks in addition to the substrate is distinguishable in the diffractogram of product 7b(s), but product 7a(s) show a large amount of GaO(OH) based on the relative peak heights compare to the $CuGaS_2$ peaks.

4.1.13   Fe and Ni doping

Syntheses 6c, 7a and 7b have provided products of high purity, and synthesis 7a was selected for investigating doping with Fe and Ni since it does not use 1-pentanethiol. These dopants were selected since they are found to have sufficient solubility in $CuGaS_2$ and may form an IB at concentrations between 6.25% and 25% substitution as explained in detail in Section 2.3. $NiCl_2$ and $FeCl_3$ are the selected dopant precursors as the chlorides are soluble in water and they provide the desired valencies of the metal ions Ni^{2+} and Fe^{3+}. The $CuGaS_2$ single-phase region in Figure 2.6(b) in Section 2.2 is not completely diminished by competing NiS and NiS_2 phases containing divalent Ni, even at the highest Ni^{2+} chemical potential of zero, at which elemental Ni become stable. However, oxidation during the synthesis might form other competing nickel sulphides as have been proven for oxidation of Cu^+ described in Section 4.1.1. Fe^{3+} ions provided by dissolution of $FeCl_3$ have the desired valency for preferential Fe_{Ga} substitution according to Section 2.3, as such substitution is calculated by Tablero and Fuertes Marrón [6] to provide a IB position more optimal for IBSC applications than Fe_{Cu} and mixed substitution according to Section 2.3. A concentration of 0.040 M $NiCl_2$ and $FeCl_3$ precursors was selected as a start for syntheses Ni8 and Fe8, respectively, as 12.5% substitution is found sufficient for IB formation in $CuGa_{7/8}Fe_{1/8}S_2$ and increased dopant concentrations favor precipitation of competing nickel of iron sulphides.

   Introducing such small concentrations of $NiCl_2$ or $FeCl_3$ does not change the chemical potentials of Cu^+ and Ga^{3+} significantly from synthesis 7a, and all syntheses with dopants are in the same region of the stability diagram in Figure 4.24 as synthesis 7a in Figure 4.18. In Figure 4.24, Debye-Hückel calculations in Table A.5 in Appendix A.2 is used to calculate the Ni^{2+} and Fe^{3+} chemical potentials for the syntheses assuming that these ions do not take part in complex formation. Equilibrium is assumed for the redox reactions necessary to from NiS_2 or FeS_2 from S^{2-} and Ni^{2+} or Fe^{3+} ions so that the chemical potentials for syntheses with dopant addition in Table A.5 can be compared to the free energy of formation of NiS_2 or FeS_2 in stability diagrams. Based on the formation energies, the minimum sulphide chemical potential for NiS_2 and FeS_2 precipitation is calculated and the corresponding green lines are added to the stability diagram in Figure 4.24. Even though this chemical potential in synthesis Ni8 is calculated to be slightly below the limit for NiS_2 formation, this competing phase is observed in the diffractogram of product Ni8 in Figure 4.25. Sulphide precipitation during the synthesis and complexing by Tu might reduced chemical potentials sufficiently to make NiS_2 a stable competing phase, but this
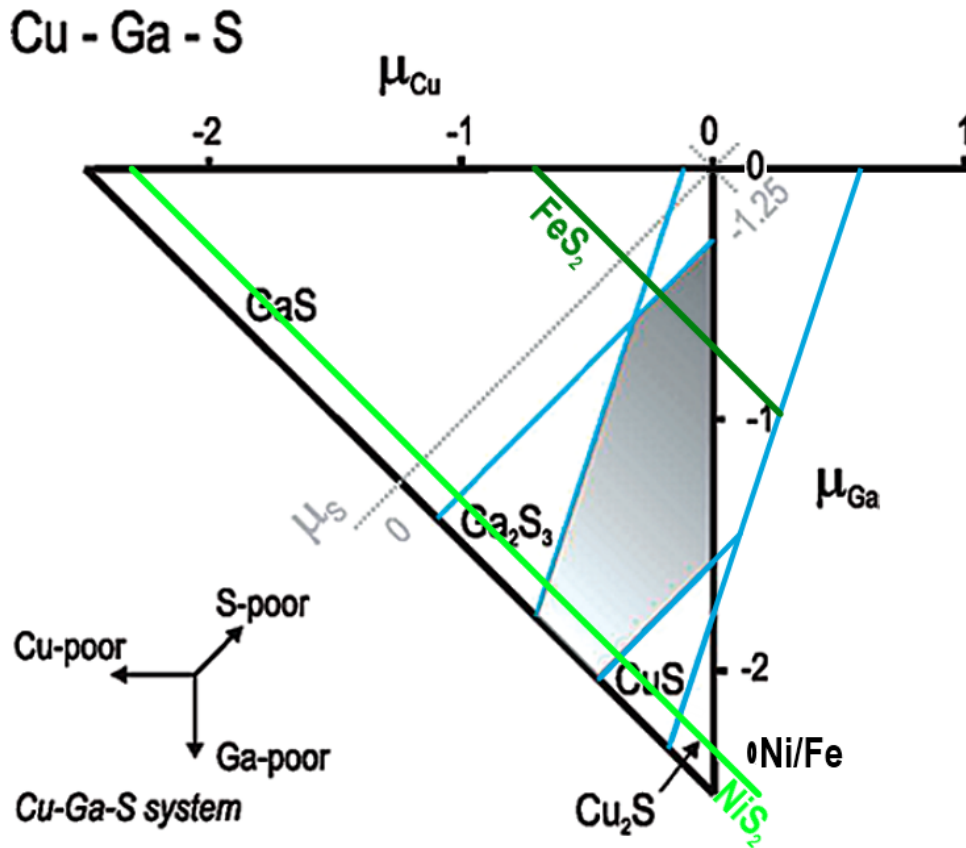
Figure 4.24: Stability diagram adapted from Tablero and Fuertes Marrón [6] modified with the stability of NiS_2 and FeS_2 in addition to chemical potentials calculated for syntheses with Ni or Fe dopants: Ni8, Ni16, Fe8 and Fe16.

deviation can also relate to the inaccuracy of the calculations. This analysis of the NiS_2 stability is also valid for synthesis Ni16, as the calculated chemical potentials are not significantly changed. The amount of 4 mol% NiS_2 in product Ni8 reduces the maximum doping concentration to 8% of the $CuGaS_2$ amount, which is the ratio of the amount of substance of $Ni_{Cu/Ga}$ to that of $CuGaS_2$ in Table A.3 in Appendix A.1. No copper sulphide impurities are produced and 100% yield of $CuGaS_2$ is achieved.

The NiS_2 impurity indicates limited incorporation of Ni in $CuGaS_2$ at the experimental conditions, and higher doping concentrations can not be achieved by increasing the concentration of the dopant precursor. Thus, the $NiCl_2$ concentration was reduced to 0.020 M in synthesis Ni16. Although this does not significantly change the chemical potential of Ni^{2+} according to the Debye-Hückel calculations in Appendix A.2, no NiS_2 impurity is observed in the diffractogram of product Ni16 in Figure 4.25, which leaves a maximum doping concentration of 6% Cu or Ga substitution. Instead, a 4 mol% digenite impurity is formed, although this may be too high as it represents larger amounts of copper ions in the product than what is supplied as shown in Table A.2 in Appendix A.1. This impurity indicates that relatively small amounts of $NiCl_2$ also may influence the formation of $CuGaS_2$, for instance through increased ionic strength as explained in Section 2.4.1, and that the high $CuGaS_2$ purity produced by synthesis 7a is sensitive to relatively small variations. Like for synthesis Ni8, the calculated $CuGaS_2$ yield of 99% in synthesis Ni16 is some percent too high as it represent an overconsumption of

Figure 4.25: Diffractograms of products produced with different $CuGaS_2$:Ni stoichiometries: Ni8 (8:1) and Ni16 (16:1). Including peaks for known phases: ■ $CuGaS_2$, ◆ CuS, ◆ $Cu_{2-\delta}S$, ▤ NiS_2.

the supplied Cu^+ and Ga^{3+} ions.

Addition of 0.040 M $FeCl_3$ to a synthesis similar to 7a resulted in an additional FeS_2 impurity, seen from the diffractogram of synthesis Fe8 in Figure 4.26, which amounts to 4 mol%, and the maximum doping concentration is limited to 8% Cu or Ga substitution. Rietveld alanysis also give a 10 mol% digenite impurity, although the calculations in Table A.3 in Appendix A.2 suggests a lower molar fraction as this give a higher Cu content in the product than the CuCl precursor. The calculated $CuGaS_2$ yield of 92% is also high in view of the product purity of 86 mol%. Like for formation of NiS_2 in synthesis Ni8, S^{2-} ions are oxidized to S^-, but formation of FeS_2 also requires reduction of the supplied Fe^{3+}, and the redox reaction in Equation (4.6) may account for half the amount of S^{2-} oxidation.

$$Fe^{3+} + S^{2-} \rightarrow Fe^{2+} + S^- \tag{4.6}$$

Fe^{2+} is a more stable oxidation state of Fe than Fe^{3+} in aqueous solutions [73], which may favor reduction to Fe^{2+} in the reaction solution. Doping by Fe^{2+} at Cu and/or Ga sites rather than Fe^{3+} which preferentially substitute Ga according to Section 2.3 is thus possible. In this case, Fe_{Cu} can contribute to IB formation and give an IB structure

less optimal compared to the preferred IB position for IBSC applications from solely Fe_{Ga} substitution as explained in Sections 2.1 and 2.3. However an additional oxidation reaction is required to make an spontaneous redox reaction in order to reduce all the supplied Fe^{3+} ions, and there are no signs of increased Cu^{+} oxidation in synthesis Ni8. Product Fe16 contained a 7 mol% CuS impurity not observed in other syntheses with dopant addition or synthesis 7a, in which digenite is the copper sulphide impurity. The diffractogram of product Fe16 in Figure 4.26 also show a FeS_2 impurity which amounts to less than 6 mol%, as it is limited by the supply of $FeCl_3$, so $CuGaS_2$ can only contain very small amounts of Fe in this product. The 93% yield is high compared to the $CuGaS_2$ purity of 87%, and this supports the trend of a higher or equally high yield from all syntheses with dopant addition compared to synthesis 7a.

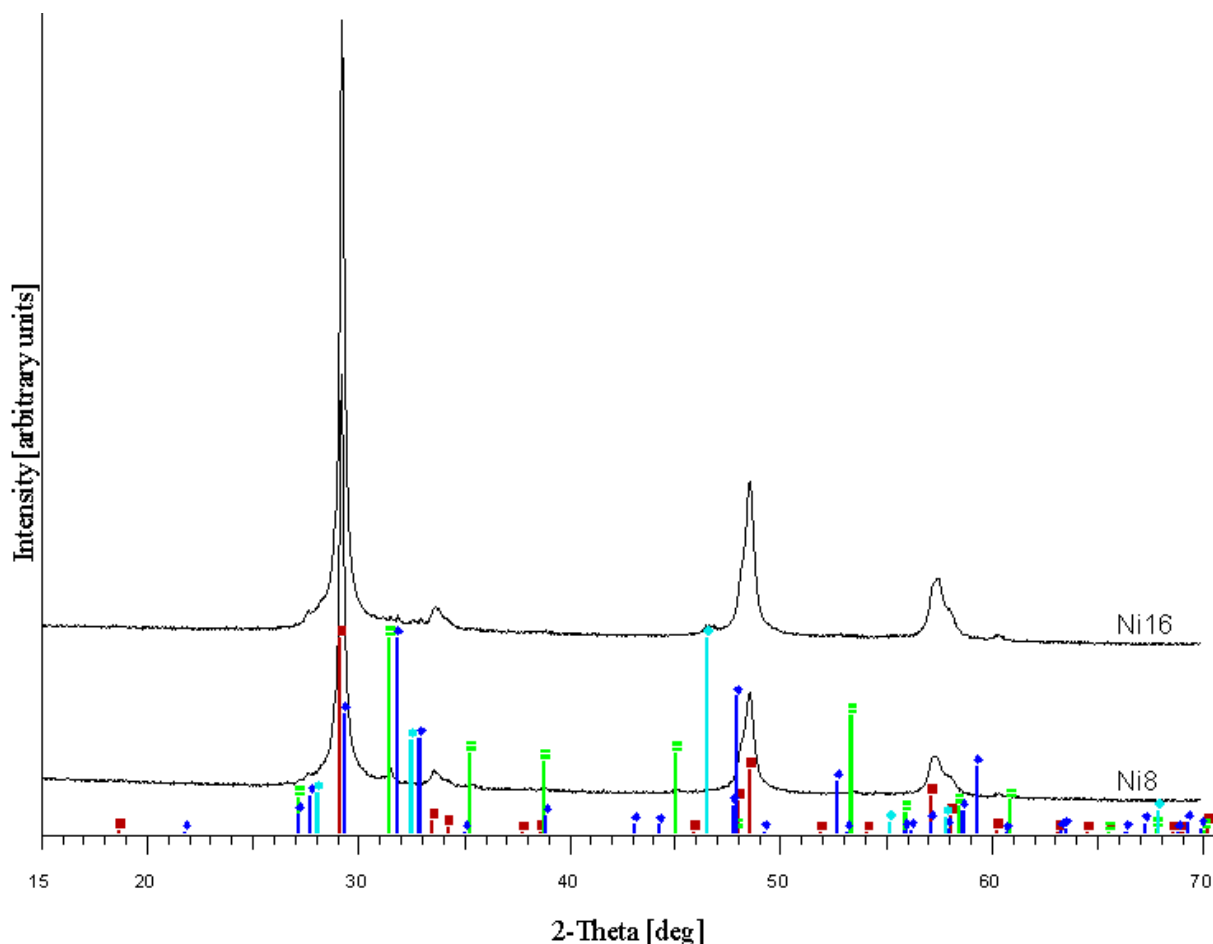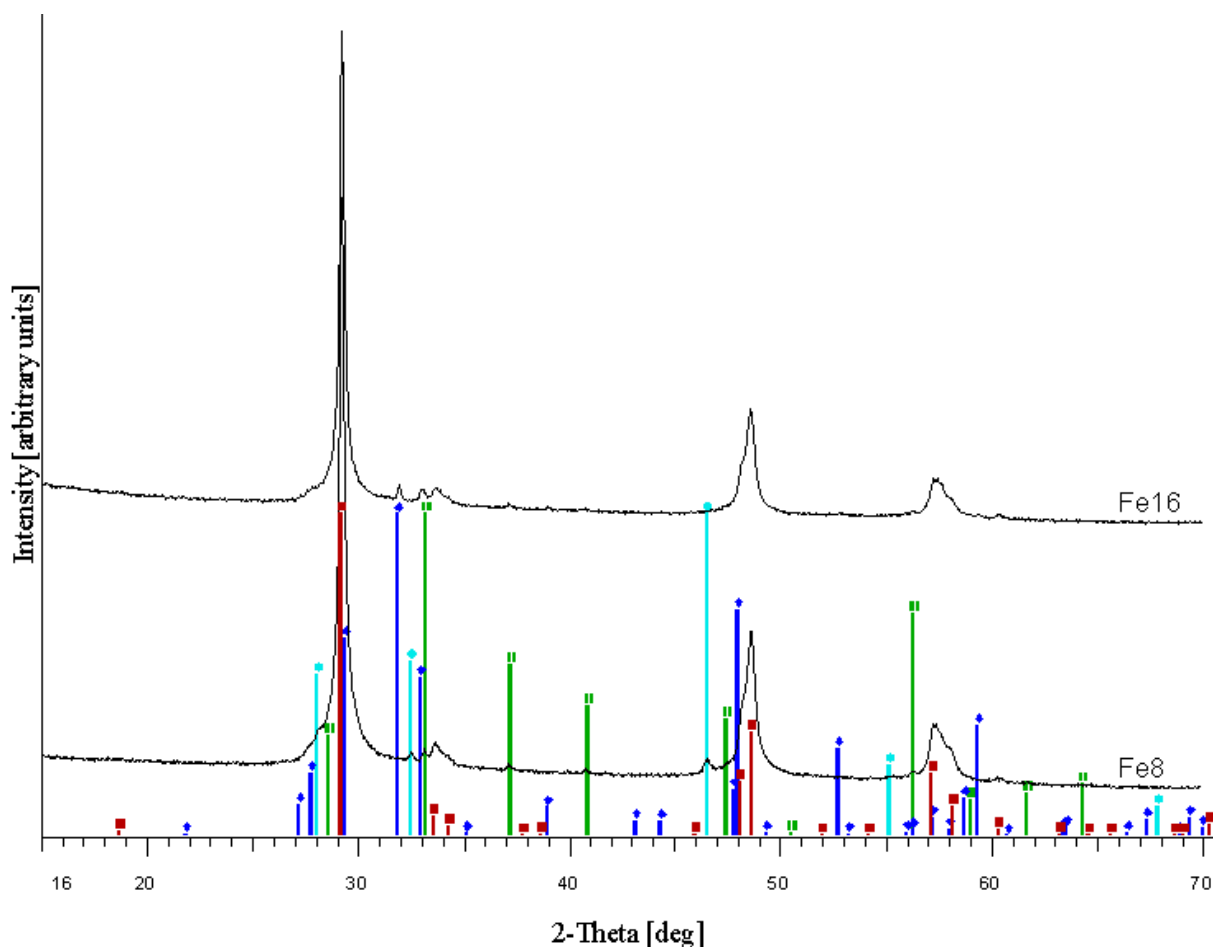Figure 4.26: Diffractograms of products produced with different $CuGaS_2$:Fe stoichiometries: Fe8 (8:1) and Fe16 (16:1). Including peaks for known phases: ■ $CuGaS_2$, ◆ CuS, ◆ $Cu_{2-\delta}S$, ⦿ FeS_2.

The Rietveld analysis also calculated lattice parameters from the diffractograms, and these are expected to change with doping concentration as presented for $CuGaS_2$:Fe in Section 2.3. The calculated $CuGaS_2$ lattice parameters for products Ni8, Ni16, Fe8 and Fe16 are compared to the undoped reference product 7a in Figure 4.27, and the points for syntheses with Fe doping also compares to the trend of the Fe_{Ga} substitution reported

by DiGiuseppe et al. [28] in Figure 4.27. The points for products with dopant addition use the maximum dopant to $CuGaS_2$ stoichiometry for which all supplied dopant ions in excess of the NiS_2 and FeS_2 impurities are incorporated into $CuGaS_2$.
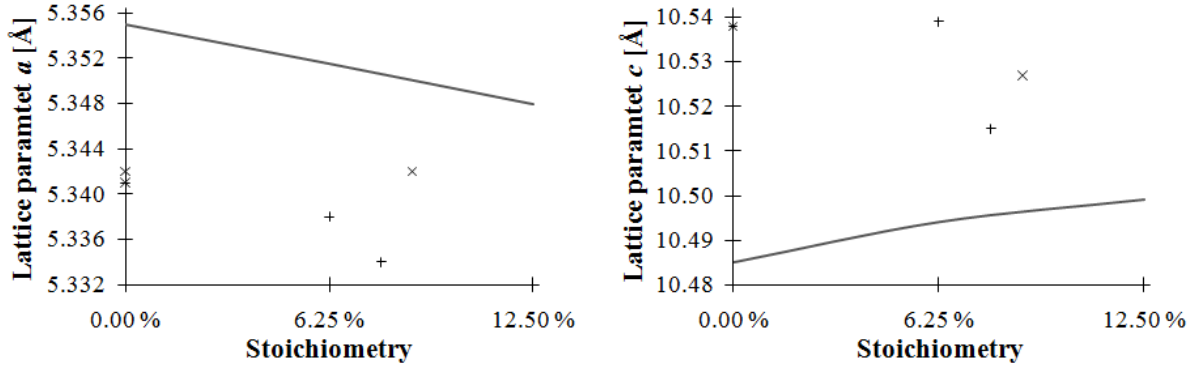
Figure 4.27: Lattice parameters a (a) and c (b) of $CuGaS_2$ modifications produced from different stoichiometries of dopants: ✳ undoped $CuGaS_2$ from synthesis 7a, + $CuGaS_2$:Ni, ✕ $CuGaS_2$:Fe and ——— $CuGaS_2$:Fe parameters determined by DiGiuseppe et al. [28].

All points for products with Fe doping show a shorter lattice parameter a and a longer lattice parameter c than what DiGiuseppe et al. [28] found for their polycrystalline samples with Fe_{Ga} substitution. This can relate to lattice strain in the nanoscale crystallites obtained in the hydrothermal syntheses. Furthermore, the relatively small variation in a and the decrease in c is not consistent with the trend found by DiGiuseppe et al. [28], which also can be related to different extents of lattice strain between products. However, the accuracy of this analysis is uncertain partly due to the range of composition in the off-stoichiometric products, which can alter the lattice parameters according to Section 2.2, as well as the actual dopant concentrations in products with dopant addition. The small difference in a and identical c values for product 7a and Fe16 does however support the observation that $CuGaS_2$ in Fe16 is not doped to a significant extent. Also Fe_{Cu} substitution is a possibility as this does not significantly alter the unit cell of the similar chalcopyrite $CuInSe_2$ according to Section 2.3. Products with Ni addition show a trend of decreasing a and c lattice parameters, which give a decreasing unit cell volume. This might be explained from comparing ionic radii of Ni to Ga or Cu depending on site of substitution. The ionic radius of trivalent Ni of 60 pm is slightly shorter than that of trivalent Ga of 62 pm [44], so that lattice distortions around Ni_{Ga} substitutions allow a decrease in the unit cell volume. The ionic radius of divalent Cu is larger than that of divalent Ni, and if this relation to also holds for the monovalent ions, a decreasing unit cell volume contradicts Ni_{Cu} substitution.

Doping of $CuGaS_2$ to form an IB can be expected to change the product color as one of the additional band gaps introduced by the IB can be in the visible spectrum with wavelengths ranging from $400 - 700$ nm [74]. This is because the $CuGaS_2$ band gap of 2.46 eV relates to a photon wavelength of 504 nm towards the blue part of the visible spectrum according to (2.1) in Section 2.1, and unless the IB is close to the middle of the band gap for which the corresponding photon wavelength is 1008 μm, the largest of the band gaps involving the IB (E_H) can absorb visible light. The products with Fe

addition showed a green coloration corresponding to Fe doping, but this is also observed for $CuGaS_2$ with Fe and Ni impurities below the limit for IB formation as described in Section 2.3. Products with Ni addition does not show such a coloration compared to undoped $CuGaS_2$ in product 7a. These observations suggest that $CuGaS_2$ might not be doped at all, and this is revealed by EDS analyses in Section 4.2.

4.2 Characterization of Particles

Commonly observed particles are studied regarding morphology by SEM and the constituent phases are identified by EDS. All EDS spectra show peaks corresponding to the common contaminants C and Al. The thickness of several particles is so small that the emission volume for characteristic X-rays extend below the particles and into the carbon tape or aluminum stub below. For this reason, C and Al are commonly detected on and around the particles by mapping, although their signals are weaker on particles than around them. However, since these elements are not included in the syntheses, they can be excluded from mapping and quantification analyses to determine which phases constitute the different particles. Al contamination can also originate from the specimen chamber walls of the SEM used for EDS analyses, and detection of such diffuse signals can give a small peak of Al signal from an area above a carbon tape, or a small C peak above an area of the Al stub away from the carbon tape. The latter is the case for the spectrum of an agglomerate in product Ni16 in Figure 4.28, which is representative for all $CuGaS_2$ particles, even in products with dopants. The C peak above a carbon tape and Al peak from the sample stub surface, respectively, are high in the spectrums. This is because areas outside the particles are included in mapping for identifying contamination signals that are not confined to the particles, but it also relates to the emission depth.

O contamination can be detected in absorbed moisture and surface oxidation of for instance the Al stubs. EDS analysis can not detect H in moisture. The reason for this is that H has no electrons in electron shell L or higher energy shells, so that there are no electrons that can relax to the K-shell and emit characteristic X-rays after ionization. The O signal is omitted in EDS mapping unless it is confined to the particle studied. The energy range in the spectrums is narrowed to 3 kV as it covers all or most of the peaks for all elements and the density of peaks in this range make them difficult to distinguish at larger energy ranges. Quantification of peaks is not accurate for the EDS analyses since the particles generally do not have a flat and dense surface [1], and this gives varying compositions up to several percent depending on the area of a particle selected for quantification.
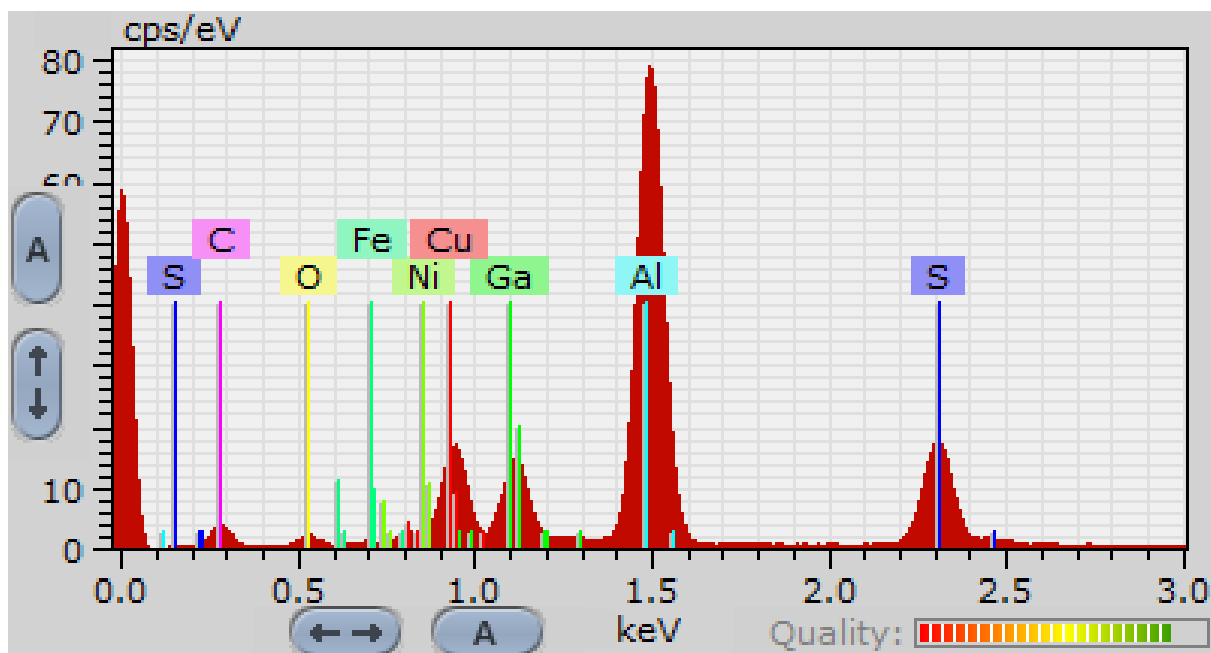
Figure 4.28: EDS spectrum representative for CuGaS$_2$ particles.

CuGaS$_2$ particles of products with Ni and Fe addition show a similar spectrum to those of CuGaS$_2$ particles in syntheses without dopants, with no significant Fe or Ni signal. Thus, the analyzed particles are not doped to a desirable concentration, although very small dopant concentrations may not be detected. Also quantification give negligible Fe and Ni contents of less than 1 mol%. This indicates that the Ni or Fe ions are more stable in the aqueous solution than in CuGaS$_2$. However, the opposite case in which Fe and Ni incorporation in CuGaS$_2$ from the aqueous solution is very favorable could give a high dopant concentration in the first CuGaS$_2$ particles to form, and fast depletion of Fe or Ni ions in the solution leaves that the majority of the product undoped, but this does not correspond well with the formation of NiS$_2$ and FeS$_2$ impurities.

4.2.1 CuGaS$_2$ Particles

The precipitates show a range of different particle morphologies, and those identified to CuGaS$_2$ are labeled in the SEM image of product 3b in Figure 4.29. Spheres, cylindrical rods, roses and irregular particles have also been reported by Sortland [1]. Such large variations in particle morphologies indicate complex growth conditions and may also relate to inhomogeneities in the reaction solution and the CuGaS$_2$ product. According to Section 2.4.3, CuGaS$_2$ is not predicted to form rods as no chelating or self-organizing complexing agent is used. Varying extents of irregularities of the spherical, cylindrical and rose-like shapes give ranges of irregular particles that more or less assimilate these ideal shapes, while the morphology of other irregular particles can not be related to any of the other particle shapes. The appearance and sizes of particles presented in this section is further discussed for each product in Section 4.3.

71
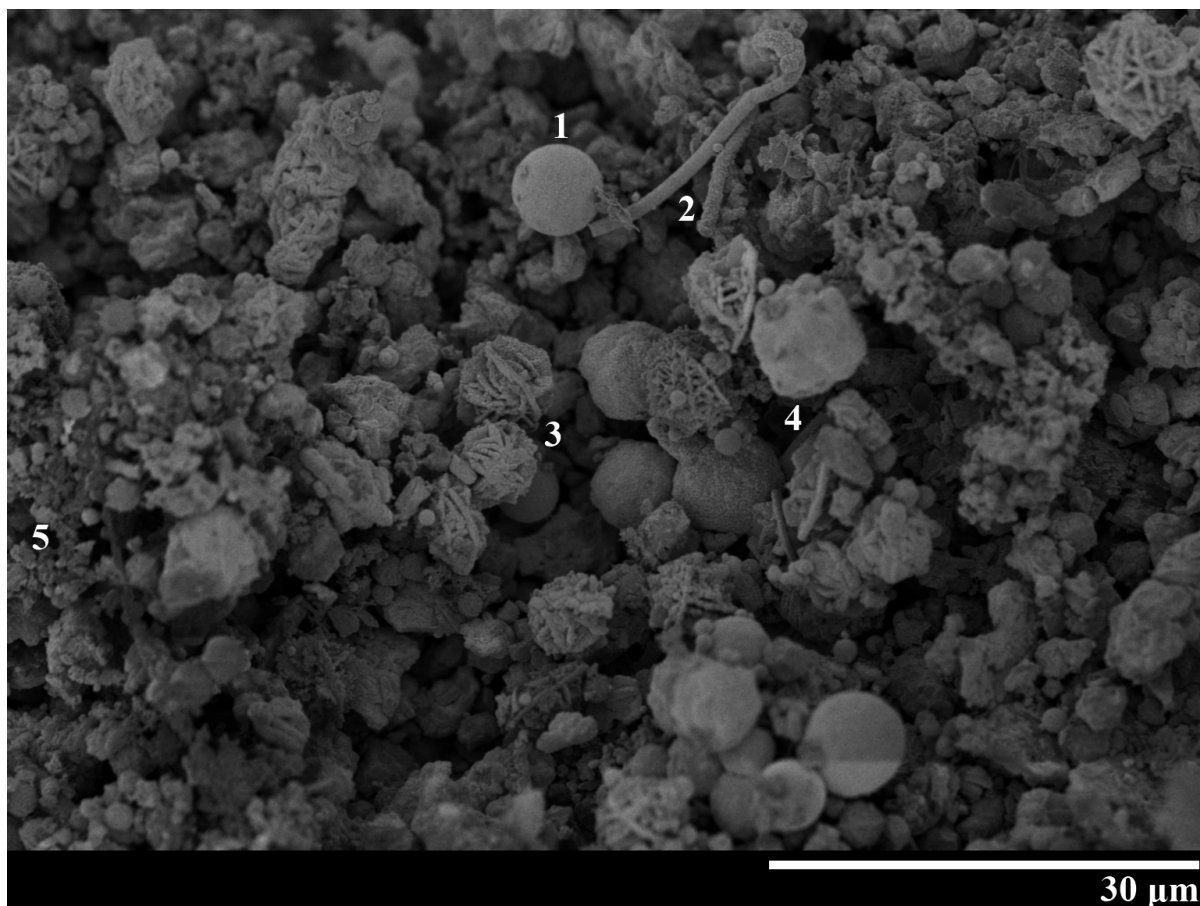
Figure 4.29: SEM image of product 3b showing spheres (1), cylindrical rods (2), roses (3), irregular particles (4) and network structures (5).

A common irregularity of spherical particles is a network of intergrown spheres depicted in Figure 4.30(a), which supposedly form by heterogeneous nucleation onto existing spheres. Completely spherical particles like the one labeled in Figure 4.29 require homogeneous nucleation in the bulk solution as their growth are not hindered in any directions by a surface. The spheres can consist of a core and a shell as shown in Figure 4.30(b) or only a shell, giving hollow spheres like in Figure 4.30(c). Sortland [1] suggested that hollow spheres may form by nucleation and growth onto bubbles from H_2S evolution or boiling of water as such bubbles may remain stable in the solution at elevated pressures.

The core of the sphere in Figure 4.30(b) is made up by different crystallites than the shell, although this is not always the case. Thus, different broken spheres in Figure 4.31 was analyzed for composition by EDS mapping and quantification in order to investigate whether the core could be the digenite intermediate product onto which a $CuGaS_2$ shell is grown. This analysis reveals that the core may indeed be the digenite phase as quantification of Cu and S peaks in a spectrum obtained from the indent of the sphere in Figure 4.31(b) relate to the stoichiometry $Cu_{1.9}S$ of digenite, while quantification of the sphere surface relate to $CuGaS_2$. EDS mapping in Figure 4.31(d) reveals the difference in composition between the surface and the core by the strengthened Cu signal and weakened Ga signal from the indent of this sphere. Product 3a containing this sphere was not found to contain digenite by XRD analysis in Figure 4.6, but digenite can be present in

small quantities in such spheres without being detected in the XRD spectrum. The core of the sphere to the left in Figure 4.31 is CuGaS$_2$ as determined from quantification and show by the unchanged Cu and Ga signal intensities between the shell and core in the EDS map in Figure 4.31(c).
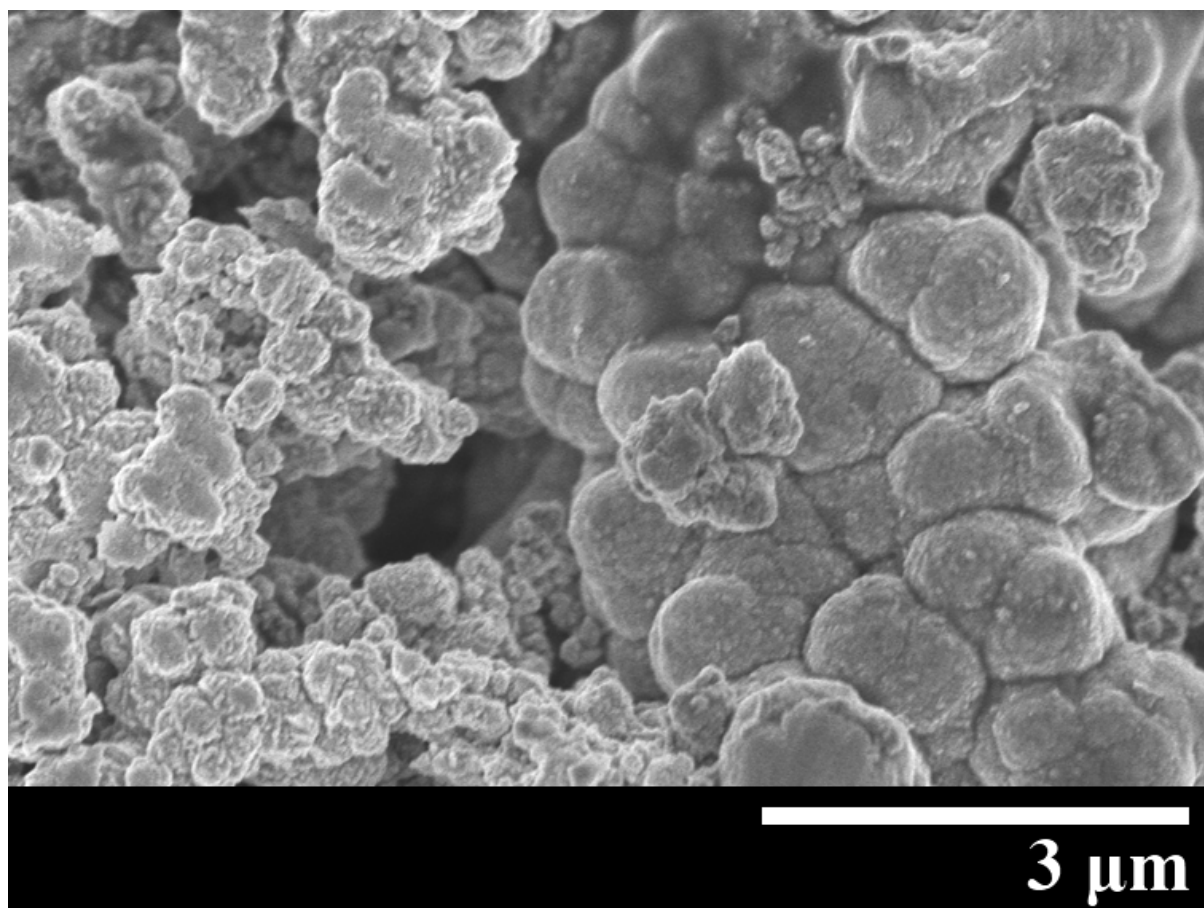
(a)
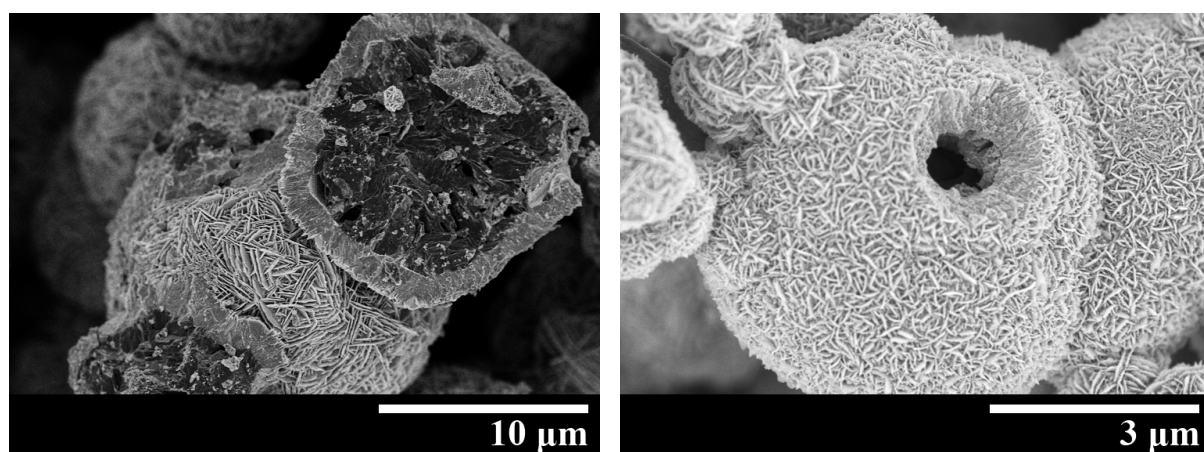
(b)

(c)

Figure 4.30: SEM images of intergrown spheres in product 6b (a), a sphere with inner core in product 1b (b) and a hollow sphere in product 5c (c).

(a)　　　　　　　　　　　　(b)

(c)　　　　　　　　　　　　(d)
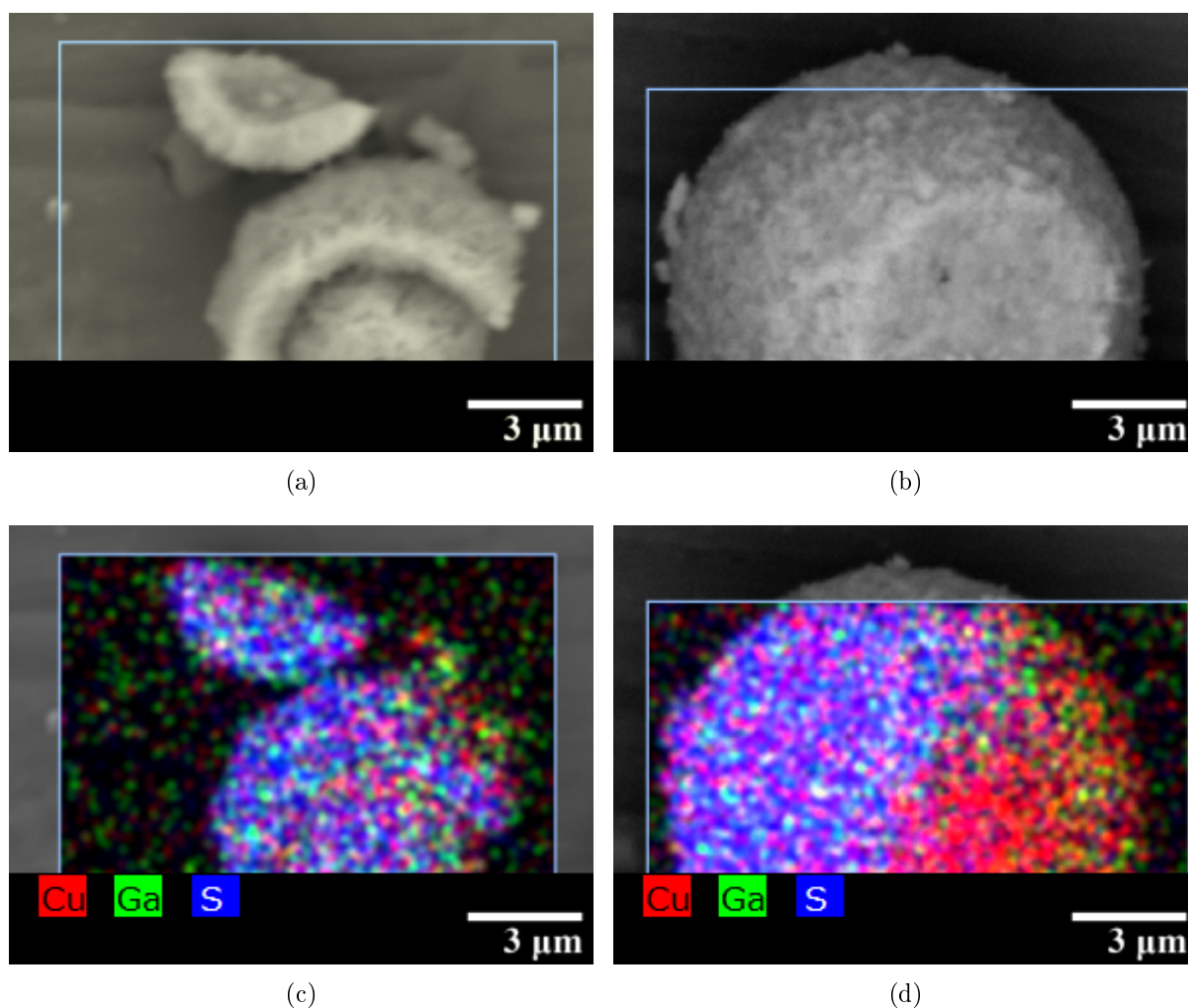
Figure 4.31: SEM images and EDS mapping of a broken sphere with inner core from product 1b to the left and from product 3a to the right.

Roses are made up from plates growing in different directions, usually from a base plate which in Figure 4.29 gives roses a hexagonal shape. These hexagonal plates correspond with the hexagonal crystal structure of CuS [75], and Sortland [1] suggested that such sulphides may form the rose skeleton of plates onto which $CuGaS_2$ nucleates and grows. Additionally, Li et al. [75] and Thongtem et al. [76] have produced similar CuS plate structures in solvothermal syntheses. This also explains the hierarchical growth of roses shown for nanoplate crystallites in Figure 4.32(b), in which $CuGaS_2$ crystallites form a surface morphology of each plate and their sizes determine the plate thickness. EDS analyses of roses with thin and thick plates in product 4c give further support to this suggestion. Quantification of the base plate in the thin rose depicted in Figure 4.32(a) gives a composition of 29 at.% Cu, 22 at.% Ga and 33 at.% S, while quantification of plates in a rose in product 6a with the thickness of plates resembling that of the labeled roses in Figure 4.29 show a lower Cu content of 26 at.% Cu, 24 at.% Ga and 50 at.% S.

74
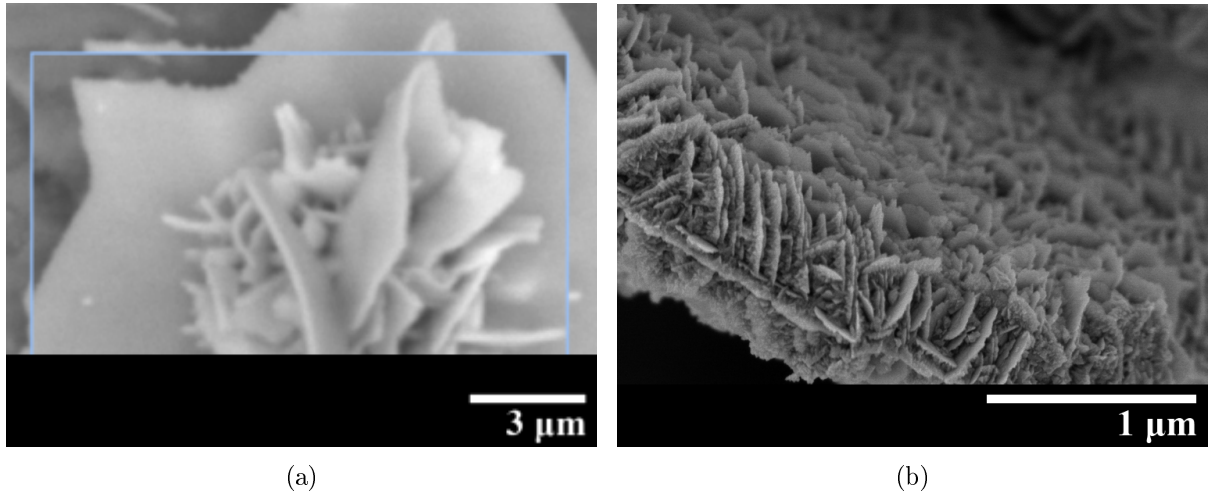
Figure 4.32: SEM image of a rose with thin plates (a) in product 4c and hierarchical hierarchical growth of rose plates (b) in product 2c.

The surface of the different $CuGaS_2$ particles can be made up from a variety of crystallite shapes summarized as nanoplates, nanopyramids and nanospheres in Figure 4.34 with varying extents of irregularities reaching completely irregular crystallites. The high specific surface area of nanoplates and the unfaceted surface of nanospheres suggest these crystallites to grow far from equilibrium even though Tu decompose slowly. Network structures are agglomerates of more or less separate crystallites as depicted in Figure 4.33 and differ from intergrown spheres in that the spheres are polycrystalline, which is seen by acknowledging that all crystallites depicted in Figure 4.34 are on the surface of spheres. Polycrystalline particles form through heterogeneous nucleation onto existing crystallites and aggregation of the small crystallites according to Section 2.4.3, while network structures solely form through homogeneous nucleation, which is promoted by a higher free energy of nucleation and supposedly form further from equilibrium.

The network structure in Figure 4.33(a) includes nanoplates also depicted on a sphere in Figure 4.34(a), onto which small pyramids grow on one of the sides. Preferential growth on one side of a nanoplate is not expected as the crystallographic planes on the parallel surfaces are the same due to the tetragonal crystal structure of $CuGaS_2$, but early features created on one side may serve as nucleation sites that promote further growth on that side compared to the smooth side [1]. Varying extents of growth of such pyramids give a range of irregularities between nanoplates and nanopyramids depicted in Figure 4.34(c), which also shows that these nanopyramids can align along a plane or be randomly oriented.

Figure 4.34(a) also show how nanoplates are grown together in a cross-section of a spherical shell. In roses, nanoplates on the edge of the larger plates tend to align along the plane of the larger plates as depicted in Figure 4.32(b), and additional nanoplates grow in specific directions from this plane. Nanoplates on spheres can align as in Figure 4.34(b), which also show that the nanoplates can be slightly curved and smooth on both sides, similar to the $CuInS_2$ nanoplates Peng et al. [67] synthesized in ethanol as described in Section 2.4.2. The planar nanoplates with features on one side most commonly occurring in the products presented in this work, have also been found by Feng et al. [36] in $CuInS_2$

products. Nanospheres depicted in a mixture of nanoplates on the surface of a sphere in product 2a are small compared to nanoplates and nanopyramids. The crystallites show varying extents of irregularities, usually as a combination between these ideal morphologies. For instance, poorly defined nanoplates can be seen as a combination of nanoplates and the typical irregularity of a rough surface, shown on a sphere in product 3c in Figure 4.34(e).

Das et al. [46] found that only In-rich $CuInS_2$ form nanoplate crystallites, whereas Cu-rich particles show an irregular surface similar to the rough surface in Figure 4.34(e), which may suggest that nanoplates occurring in this work only consist of Ga-rich $CuGaS_2$. EDS analysis of particles in product 1b shows a slightly increased Ga content in a cylindrical rod with nanoplate surface of 23 at.% Cu, 23 at.% Ga and 54 at.% S compared to a network structure of irregular crystallites represented in Figure 4.33(b), with composition 26 at.% Cu, 25 at.% and 49 at.% S. However, the composition of the cylindrical sphere relate to stoichiometric rather than Ga-rich $CuGaS_2$ and the differences in compositions between these crystallite morphologies are smaller than the expected inaccuracy of the EDS analysis. Additionally, the network structure in the red, Ga-rich part of product 2c in Figure 4.33(a) contains nanoplates while only irregular crystallites are seen Figure 4.33(b), showing the brown part of this product containing Cu-rich $CuGaS_2$.

(a)   (b)
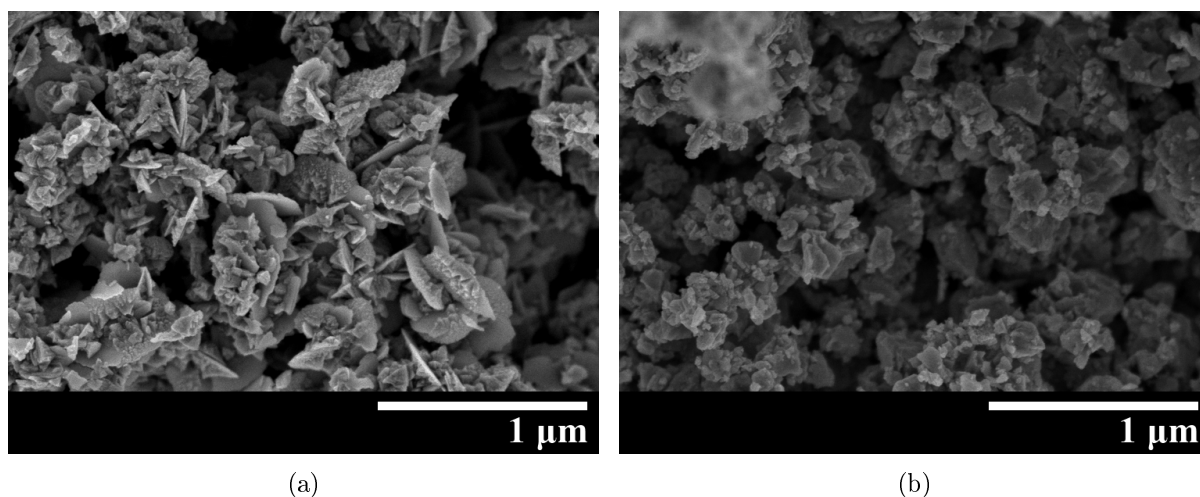
Figure 4.33: SEM images of network structures in the red, Ga-rich part (a) in product 2c and the brown part (b) containing Cu-rich $CuGaS_2$.
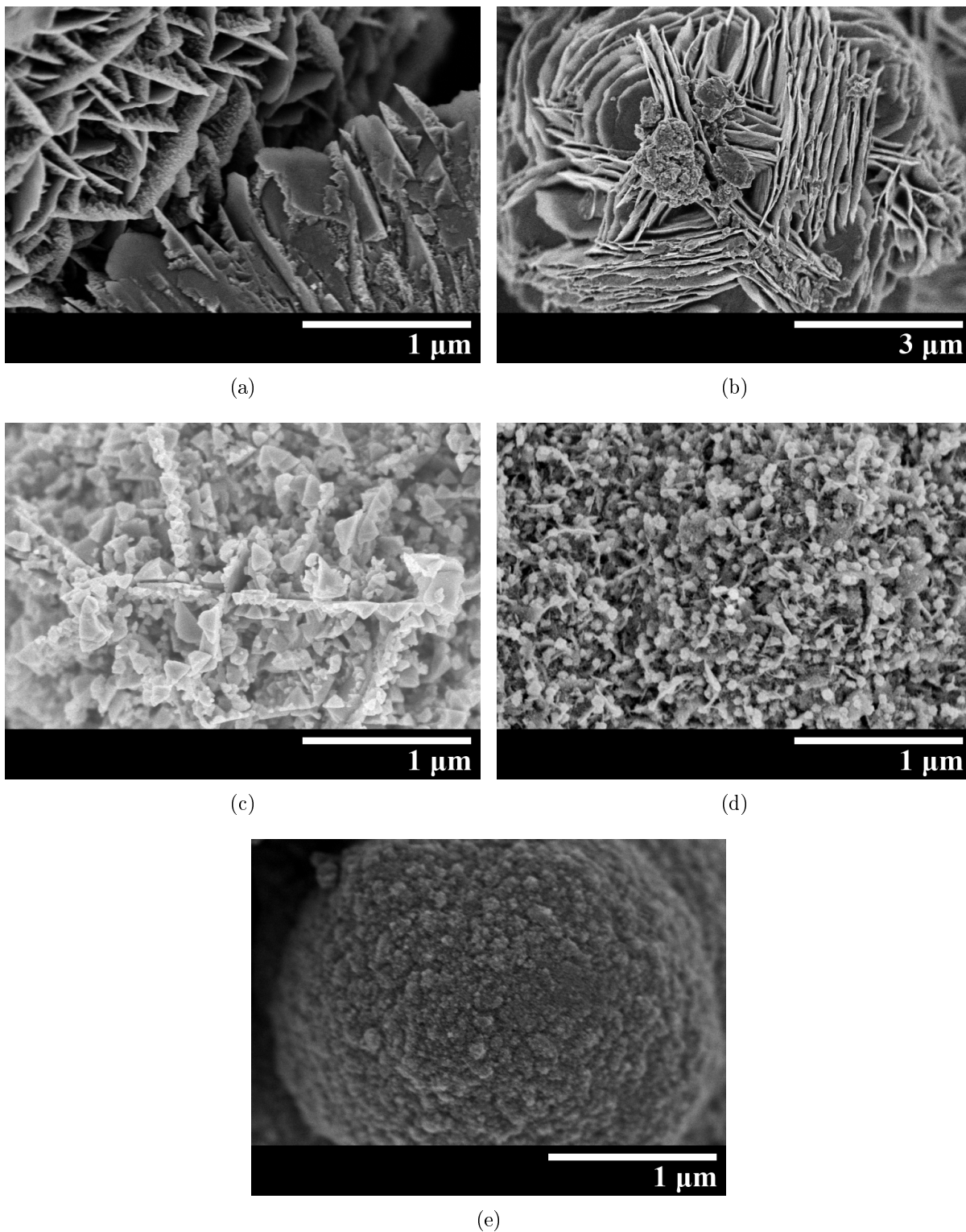
Figure 4.34: SEM images of different CuGaS$_2$ crystallites on spheres: Nanoplates with pyramids (a), which also can be smooth and aligned (b), nanopyramids (c), nanospheres (d) and irregular crystallites forming a rough surface (e).

4.2.2 Impurity Particles

The intermediate product digenite was apparent as a dark blue powder in product 5b. Digenite particles show a range of different morphologies from intergrown plates to irregular crystals, depicted in Figure 4.35. Although these particle morphologies are different from the common $CuGaS_2$ particles and crystallites, irregular crystals similar to the digenite particle depicted in Figure 4.36(b) have also been identified as $CuGaS_2$, e.g. in products 1b and 2c. The spectrum in Figure 4.36(a) shows only a very weak Ga signal, and as the Ga and O signals show the same strength outside the particle as on it, neither of these elements are part of the particle. Nevertheless, Ga is included along with Cu and S in EDS mapping shown in Figure 4.36(c) since it was present in product 5b. Quantification of Cu and S peaks from the particle in Figure 4.36 gives a composition of 65 at.% Cu and 34 at.% S, which relate to the empirical formula $Cu_{1.8}S$ of digenite.
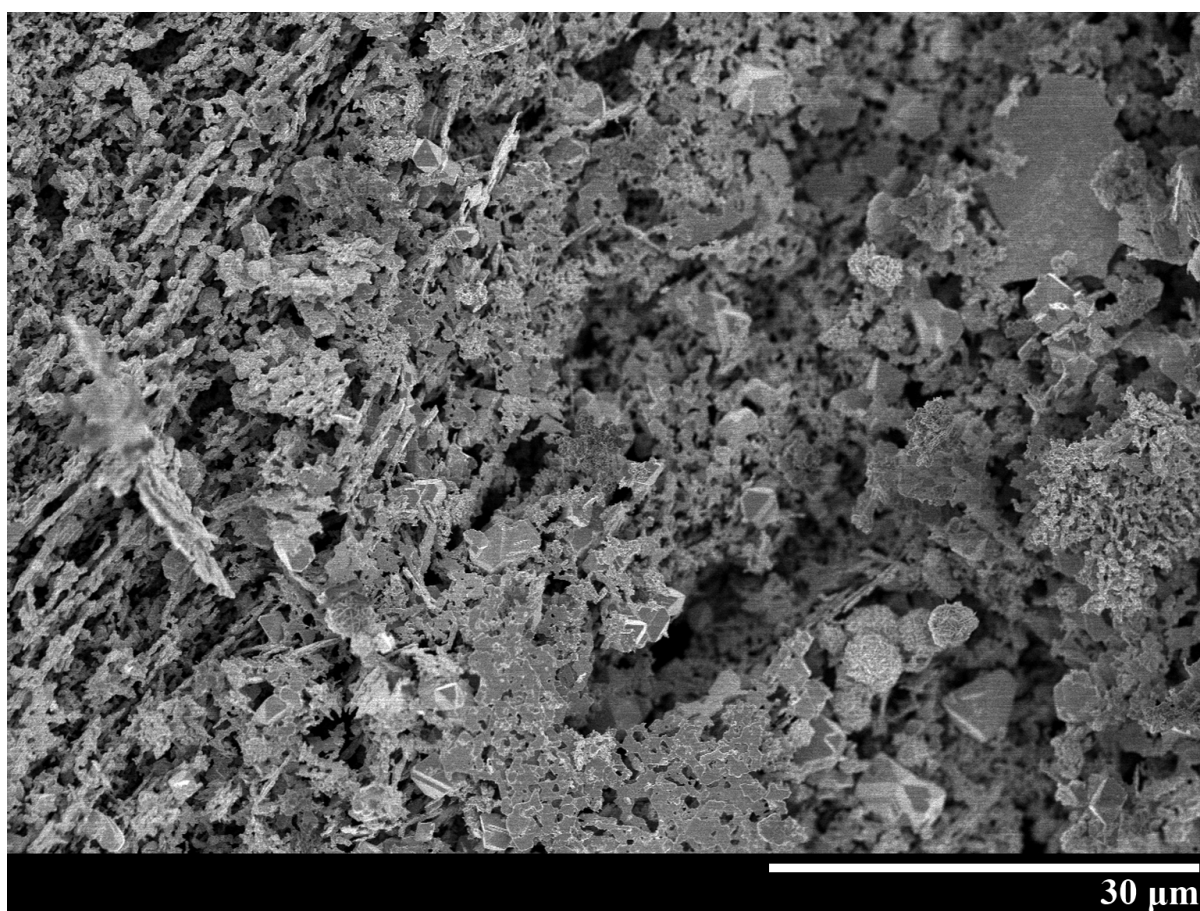
Figure 4.35: SEM image of a dark blue part of product 5b containing digenite.
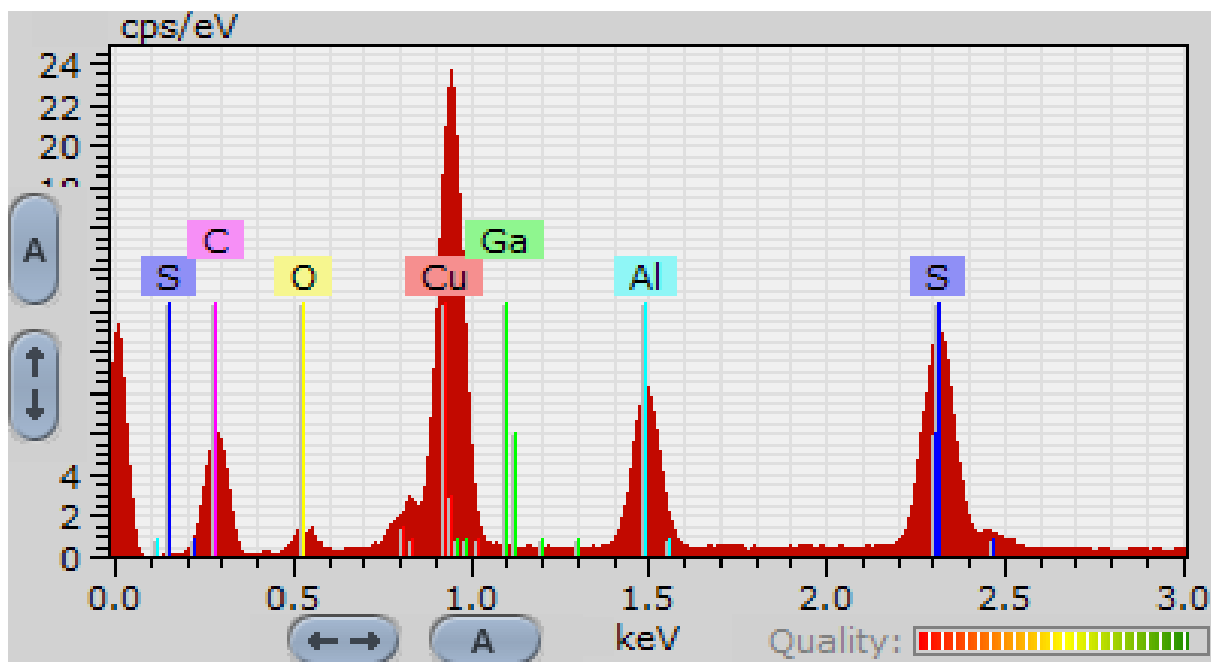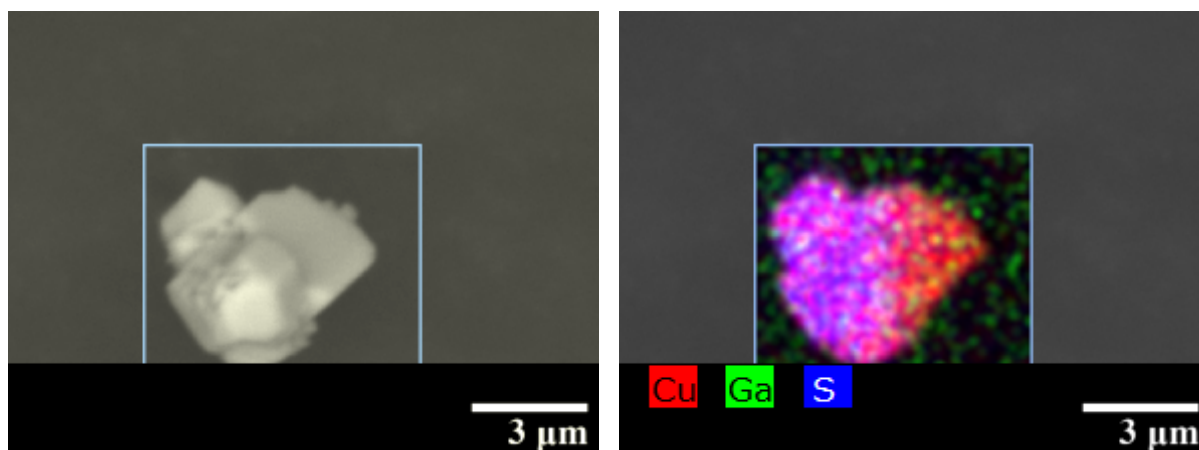
Figure 4.36: EDS spectrum (a), SEM image (b) and EDS mapping (c) of a digenite particle in product 5b.

CuS was identified in a spherical particle depicted in Figure 4.37(b) in product 2a. The weak and diffuse Ga signal in the EDS map in Figure 4.37(c) and the low amount of 6 at.% Ga calculated by quantification of Cu, Ga and S peaks in the EDS spectrum in Figure 4.37(a) indicate that this sphere is not a CuGaS$_2$ particle. It is however identified as the CuS phase from equal amounts of 47 at.% Cu and S. The SEM image in Figure 4.37(d) shows irregular particles in product 2a consisting of hexagonal crystallite plates similar to the CuS crystallites synthesized by Li et al. [75]. Such crystallites have also been found to make up spherical particles in synthesis 1c.
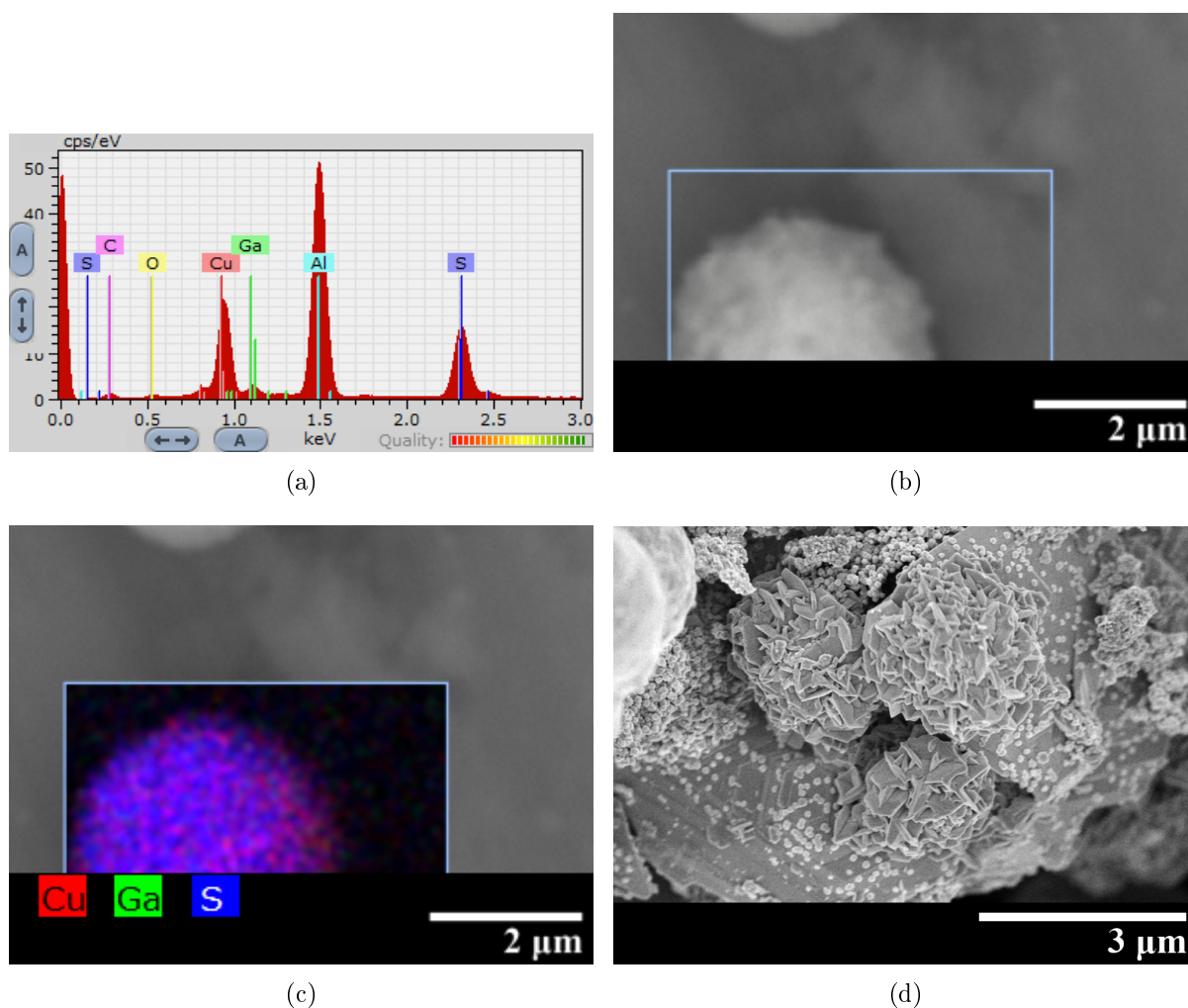
Figure 4.37: EDS spectrum (a), SEM image (b) and EDS mapping (c) of a CuS particle along with a SEM image of CuS crystallites (d) in product 2a.

Figure 4.38(b) shows rod crystallites in product 5c, and such a rod is identified by EDS mapping in Figure 4.38(c). The O signal is included in EDS mapping and quantification of this particle because it, like the Ga signal, is significantly stronger on the particle than in the background, while Cu and S signals are equally weak all over the mapped area. The EDS spectrum in Figure 4.38(a) show a relatively strong O and Ga signal along with low intensities for Cu and S, also indicating that O is part of the particle along with Ga. Additionaly, Sortland [1] found these rods to ideally have a rhombohedral cross-section, corresponding to the orthorhombic crystal structure of GaO(OH) [20].
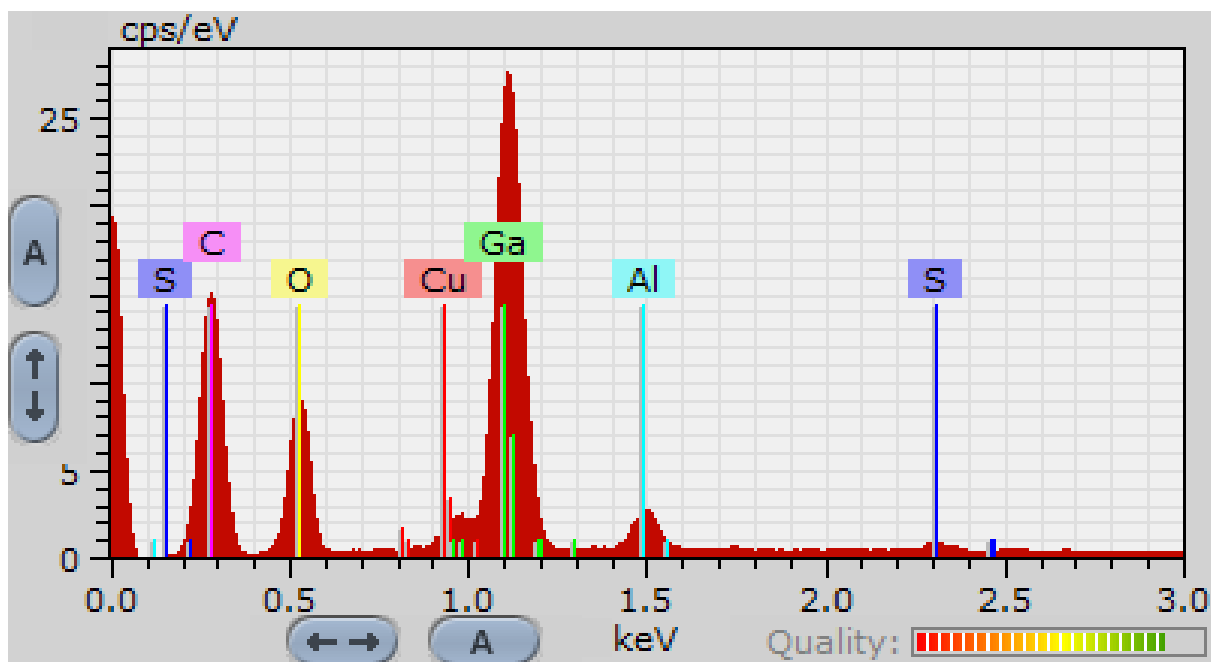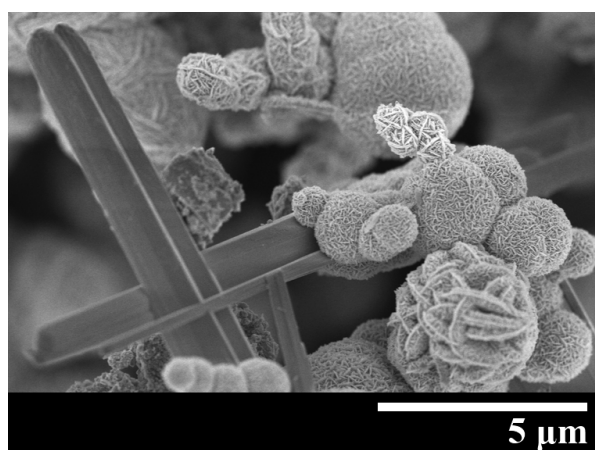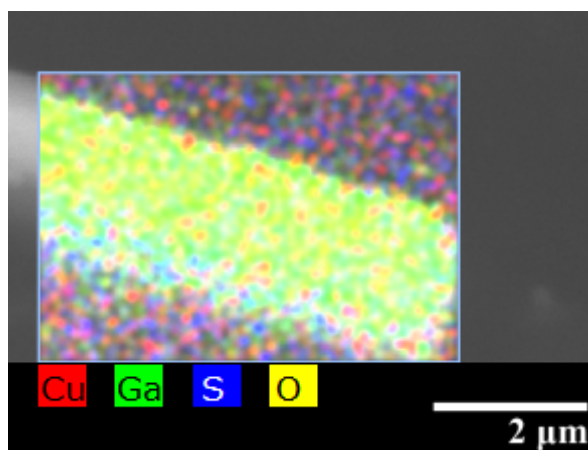
Figure 4.38: EDS spectrum (a), SEM image (b) and EDS mapping (c) of GaO(OH) rods in product 5c.

Synthesis 1c used sodium thiosulphate pentahydrate as S precursor instead of Tu, and this yielded no $CuGaS_2$ product as discussed in Section 4.1.1, but instead CuS, S and $(Ga_2O_3)_3(SO_3)_4 \cdot (H_2O)_9$ impurities. The morphologies of these phases are summarized in the SEM image of product 1c in Figure 4.39, in which hexagonal plates of CuS are recognized. The $(Ga_2O_3)_3(SO_3)_4 \cdot (H_2O)_9$ impurity have been identified in a prismatic crystal of which EDS mapping shown in Figure 4.40(b) reveals that it contains Ga, O and S. This EDS mapping reveals that the peaks for C and Al are background signals in the spectrum in Figure 4.40(a). Quantification gives a ratio O:Ga:S of 10.5:1.4:1, while the ratio of atoms in the formula unit $(Ga_2O_3)_3(SO_3)_4 \cdot (H_2O)_9$ is 7.5:1.5:1. The O signal have a contribution from absorbed moisture or other contamination sources, as seen in

81

EDS spectra of particles not containing O, and this can explain the increased O content from quantification compared to the formula unit from the phase determined by XRD.
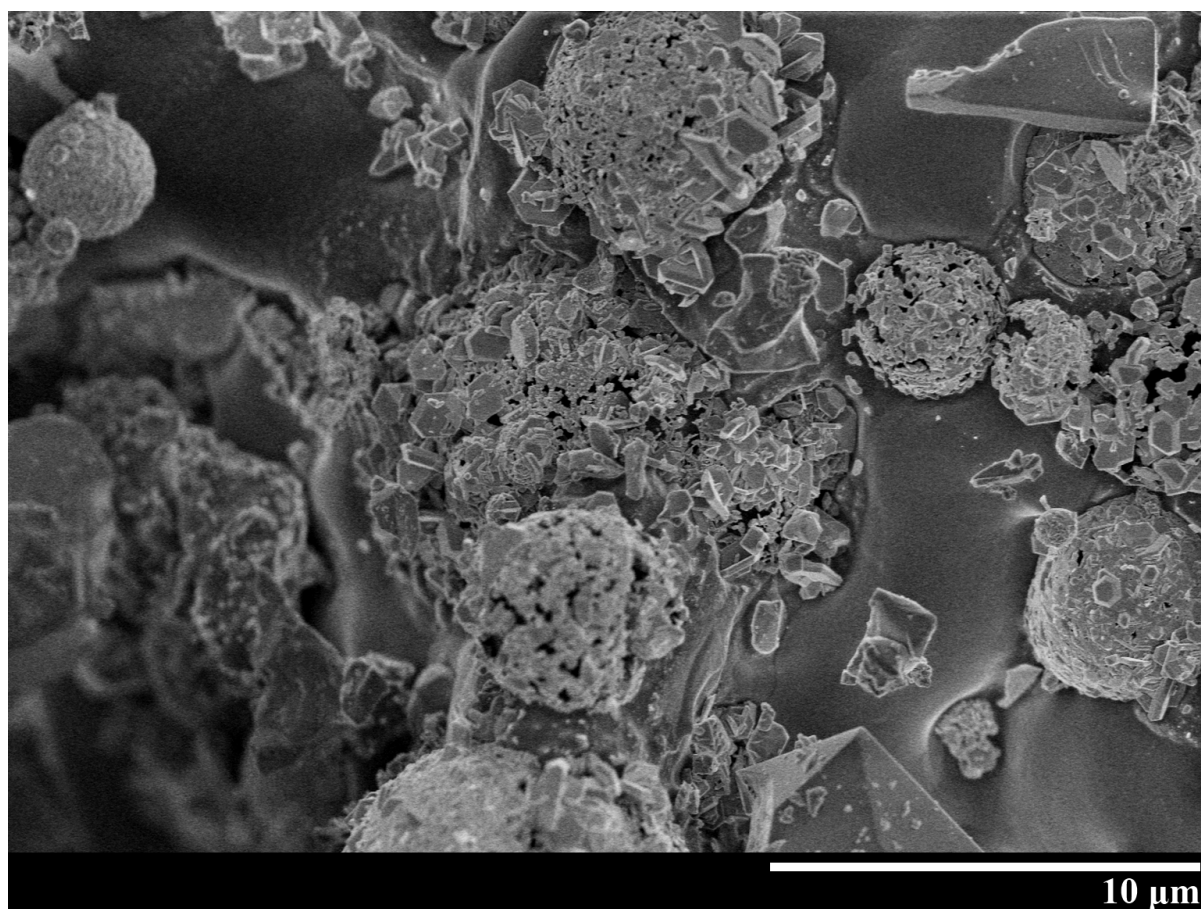
Figure 4.39: SEM image of product 1c.

(a)

(b)
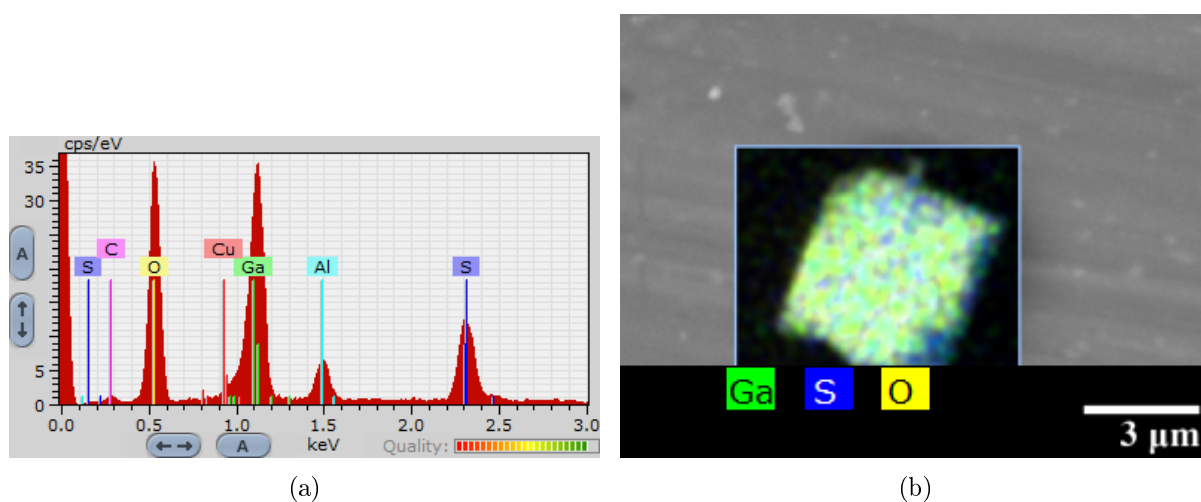
Figure 4.40: EDS spectrum (a), and EDS mapping (b) of a $(Ga_2O_3)_3(SO_3)_4 \cdot (H_2O)_9$ particle in product 1c.

The smooth mass filling between the crystals in Figure 4.39 developed a pattern seen on the particle subject to EDS mapping in Figure 4.41(b) upon magnification. The Al and C signals in the EDS spectrum in Figure 4.41(a) are excluded as background signals in EDS mapping, and Figure 4.41(b) reveal that the particle is a pure S phase.

| (a) | (b) |
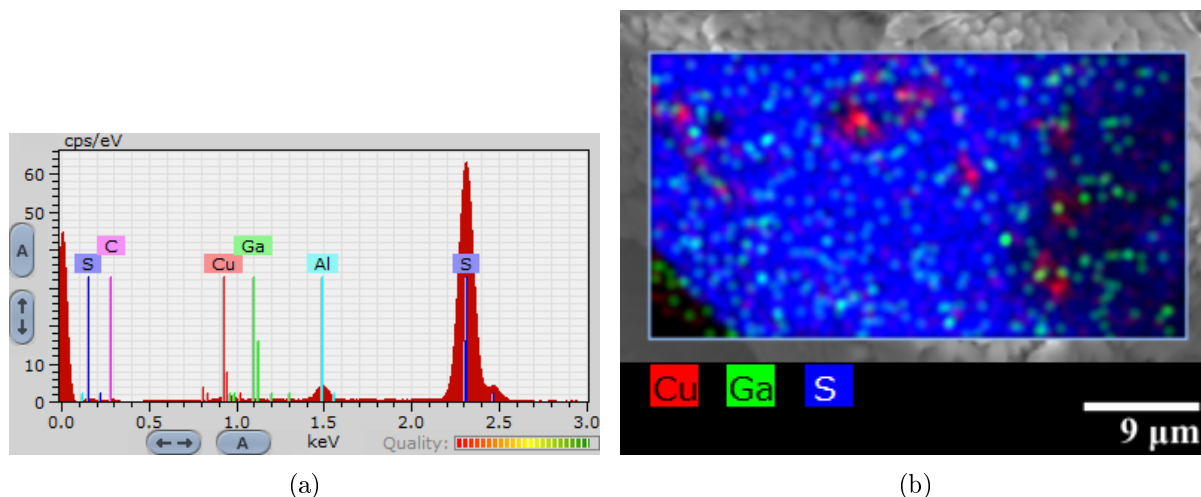
Figure 4.41: EDS spectrum (a), and EDS mapping (b) of a S particle in product 1c.

The NiS_2 impurity in product Ni8 was found in an agglomerate of hexagonal plates and rods depicted in figure 4.42(a). The spectrum in Figure 4.42(b) shows a minor Ga peak and no Cu signal is distinguishable, while O, C and Al are excluded as contaminations. Mapping of Cu, Ga and S signals shown in Figure 4.42(c) reveal that both the Cu and Ga signals show a similar intensity outside and on the agglomerate, which indicate that they are not present in significant amounts in the agglomerate. The agglomerate does however contain S and Ni, as the corresponding characteristic X-rays are intensified from it as shown in Figure 4.42(d). Quantification of the Ni and S correspond well with the empirical formula NiS_2, which is the compound identified by XRD in Section 4.1.13.

A similar analysis of the EDS spectrum and maps in Figure 4.43 identifies the spherical particle of prismatic crystallites in Figure 4.43(a) to contain Fe and S. EDS quantification of this particle give a Fe:S stoichiometry of 1:1.96, which represent some off-stoichiometry compared to the FeS_2 phase identified by XRD in Section 4.1.13. NiS_2 and FeS_2 has the same crystal structure according to Section 2.2, but still they form different crystallite shapes. The prismatic FeS_2 crystallites are supposedly grown closer to equilibrium compared to the rods and plates of NiS_2 based on their regular shape exposing low index planes of the pyrite structure as explained in Section 2.4.3. Furthermore, the larger size of FeS_2 crystallites compared to NiS_2 indicates a lower ratio of nucleation rate to growth rate for FeS_2.
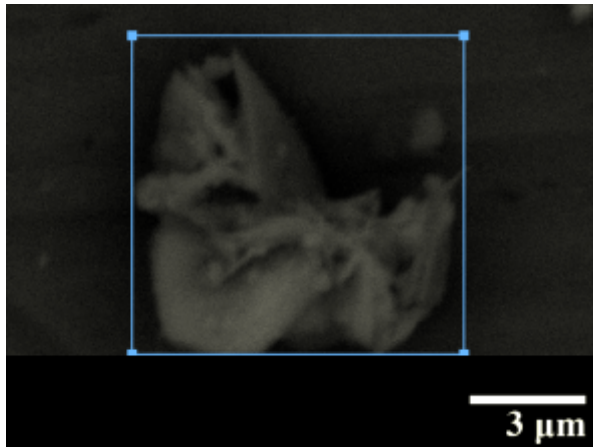
(a)
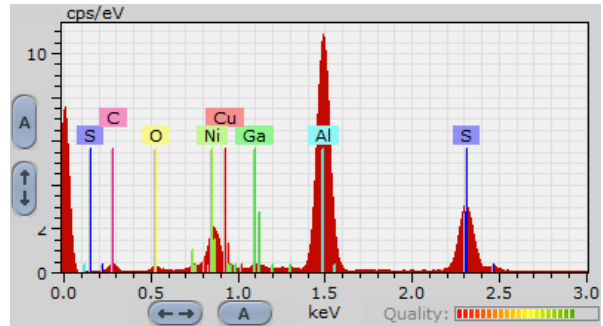
(b)
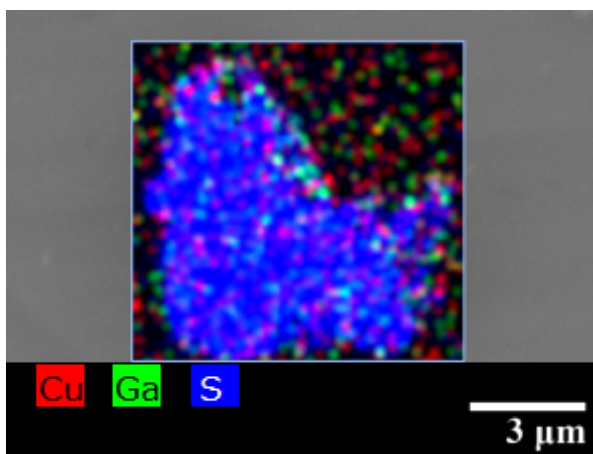
(c)
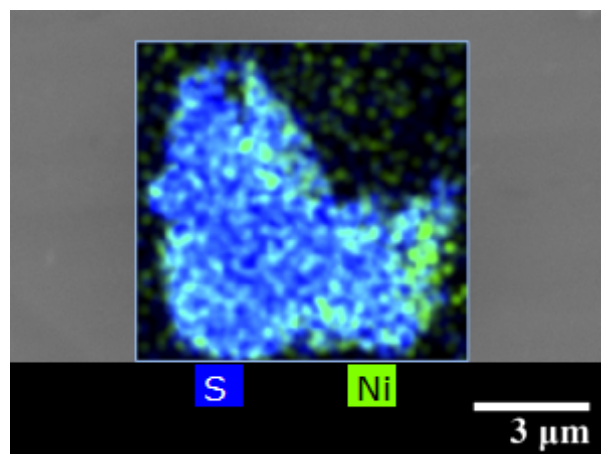
(d)

Figure 4.42: SEM image (a) and EDS spectrum (b) in addition to mapping of Cu, Ga and S (c) and Ni and S signals (d) of a NiS_2 agglomerate in product Ni8.

(a)

(b)

(c)

(d)
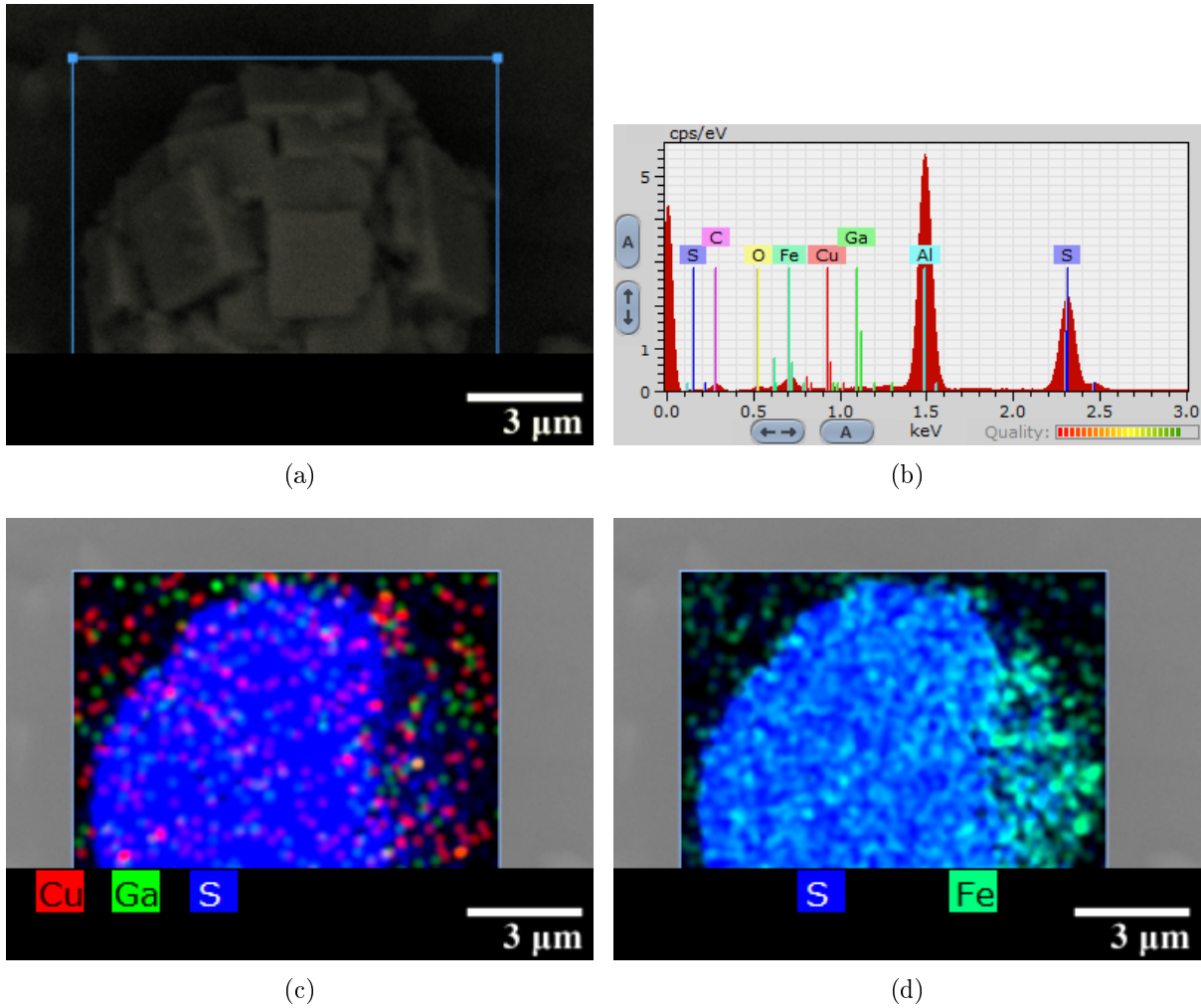
Figure 4.43: SEM image (a) and EDS spectrum (b) in addition to mapping of Cu, Ga and S (c) and Fe and S signals (d) of a FeS_2 particle in product Fe8.

4.3 Morphology

Variations in abundance of different particles, particle sizes and morphology variations for specific particles by changes in synthesis parameters are investigated by SEM. Also inhomogeneities within products, described in detail in Sortland [1], are revealed by morphology variations in addition to the color of the $CuGaS_2$ products. As densification and heat treatment of the obtained powders are required to obtain a dense material, preferably a $CuGaS_2$ single crystal for minimizing non-radiative recombination losses in IBSCs described in Section 2.1, small and densely packed particles are the preferred morphology of precipitates. However, film growth can potentially give the desired density and crystallinity without further treatment, and it can limit the material costs like for the present thin-film CIGS solar cells.

Variations in intensity from different $CuGaS_2$ particles in the SEM images presented in this section reveals limited conductivity giving edge charging, which typically make particles with a nanoplate surface brighter than particles with other surface morphologies. Average crystallite sizes calculated in the Topas software from the $CuGaS_2$ peak widths in

85

diffractograms presented in Section 4.1 are also used to assess nucleation and growth of the products. The calculated crystallite sizes are below 30 nm, which is significantly shorter than characteristic lengths of the nanoplates and nanopyramids presented in Figure 4.34 in Section 4.2.1. This relates to the large size distribution of crystallites as also the smallest crystallites like those nucleating on nanoplates are included for the calculations as discussed in Section 4.1.1. The crystallite shapes also make the calculated crystal sizes incomparable to dimensions in SEM images, particularly for nanoplates. Synthesis 1c is not included in this section as it did not produce $CuGaS_2$ at all, and syntheses 7d and 8a are excluded as they are similar to syntheses 6c and 6b, respectively, but with a substrate onto which no $CuGaS_2$ product was formed as discussed in Section 4.1.12.

Syntheses 4a[1], 1a and 1b used the same synthesis parameters and produced approximately the same product compositions, so substituting air with nitrogen in synthesis 1a and adding a Cu foil to synthesis 1b did not alter the synthesis significantly. These products are compared in Figure 4.44 for both black and brown precipitates, although product 1b was almost exclusively black. The brown color represent a mixture of red, Ga-rich $CuGaS_2$ and black, Cu-rich product. Product 1b also contained a minute amount of red precipitate indicating almost entirely Ga-rich $CuGaS_2$. This product consisted nearly exclusively of the network structure of nanoplates similar to that presented in Figure 4.33(a) in Section 4.2.1. The comparison in Figure 4.44 shows marked differences in the morphology between products 4a[1], 1a and 1b. Particularly, the extent of irregularities and particle sizes vary greatly between the products, and this reveals how sensitive the morphology is to the hydrothermal conditions. Particle sizes are represented by the diameters of spheres, which are in the range $4-11$ μm for the Cu-rich part of product 4a[1], $6-9$ μm in product 1a and $6-16$ μm in product 1b. The crystallite sizes determined from the diffractograms in Figure 4.1 in Section 4.1.1 is however near 18 nm for all these products. Spheres and roses, along with related irregular particles with the characteristic nanoplate surface structure, are most abundant in all three products and spheres are more abundant in the Cu-rich product than the brown precipitate containing Ga-rich $CuGaS_2$. Product 1b also contained red precipitate of entirely Ga-rich $CuGaS_2$.
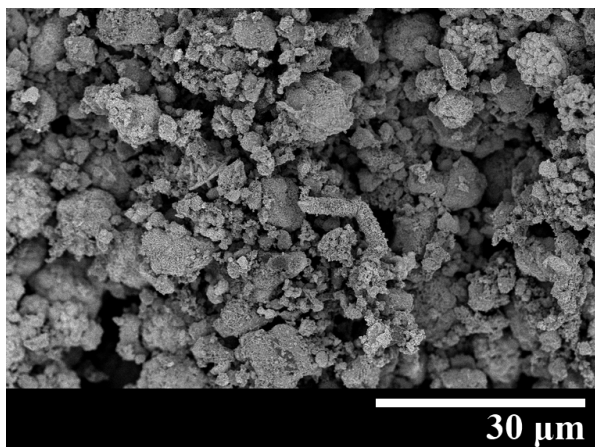
(a) 4a[1]; Ga-rich
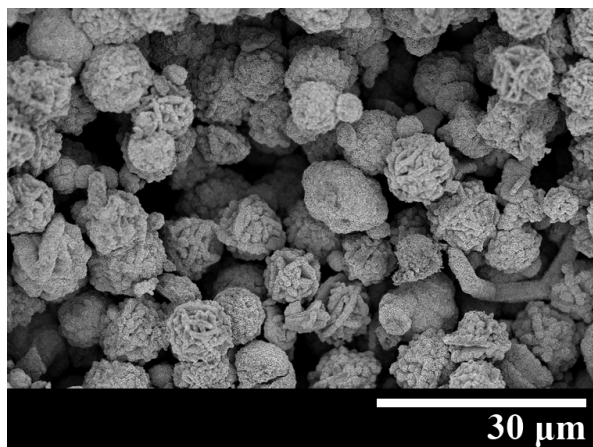
(b) 4a[1]; Cu-rich
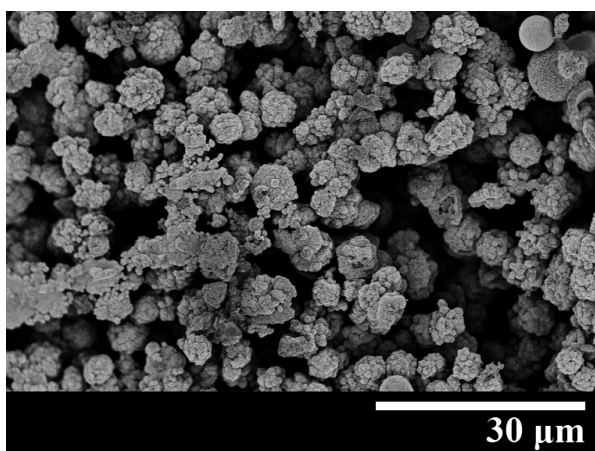
(c) 1a; Ga-rich
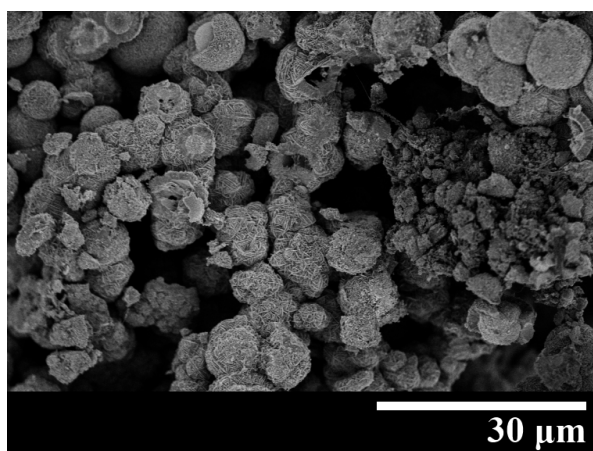
(d) 1a; Cu-rich
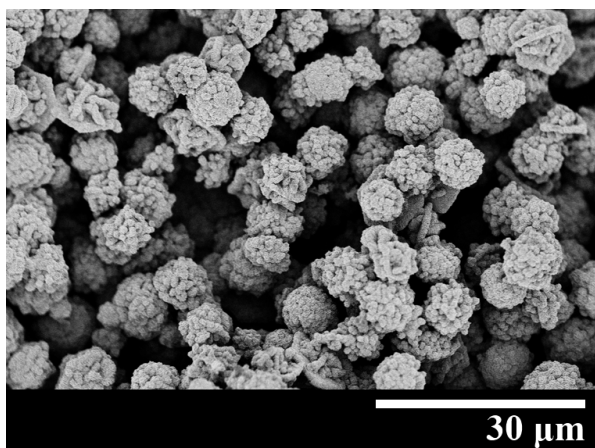
(e) 1b; Ga-rich
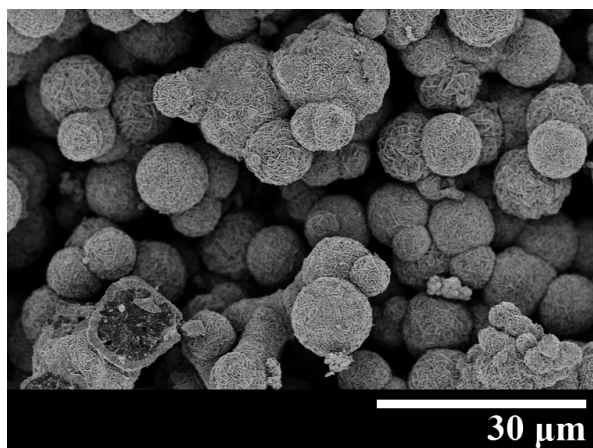
(f) 1b; Cu-rich

Figure 4.44: SEM images of products 4a[1] (adapted from Sortland [1]), 1a and 1b. The brown (partly Ga-rich) precipitates are arranged to the left and black (Cu-rich) precipitates to the right.

4.3.1 Heating Time

Although synthesis 3b did not use quite the same concentrations and fill factor as P4a, 1a and 1b, which is seen from Tables 3.1 and 3.2 in Section 3.1, the large reduction in reaction time from 12 h to 1.75 h is expected to influence the morphology to a far greater extent. The SEM image in 4.45 shows extensive inhomogeneities of spheres and roses, and particularly the spheres show large size variations of $0.5 - 8$ µm, which indicates that the precipitation was stopped before nucleation had come to a halt. The many small particles present in such a nucleation period explain the broad peaks reported for the XRD analysis in Section 4.1.2, indicating an average crystallite size of 6 nm. In comparison, the roses are far more developed and their smaller size variations suggest the onset of ageing. As roses have a higher Cu content according to EDS measurements as discussed in Section 4.2.1, this relate to the observation by Das et al. [46] that Cu rich $CuInS_2$ show increased growth rate and suggests that this is also the case for Cu rich $CuGaS_2$. The development of roses might also be related the proposal in Section 4.2.1 and Sortland [1] that a copper sulphide form the characteristic structure of ideally hexagonal plates in the roses, on which $CuGaS_2$ nanoplates grow onto, so that a faster growth rate of this copper sulphide may explain the greater development of roses. X-ray diffraction of this product revealed large amounts of $Cu_{2-\delta}S$ in this product, according to Section 4.1.2, but only particles identified to contain $CuGaS_2$ are observed
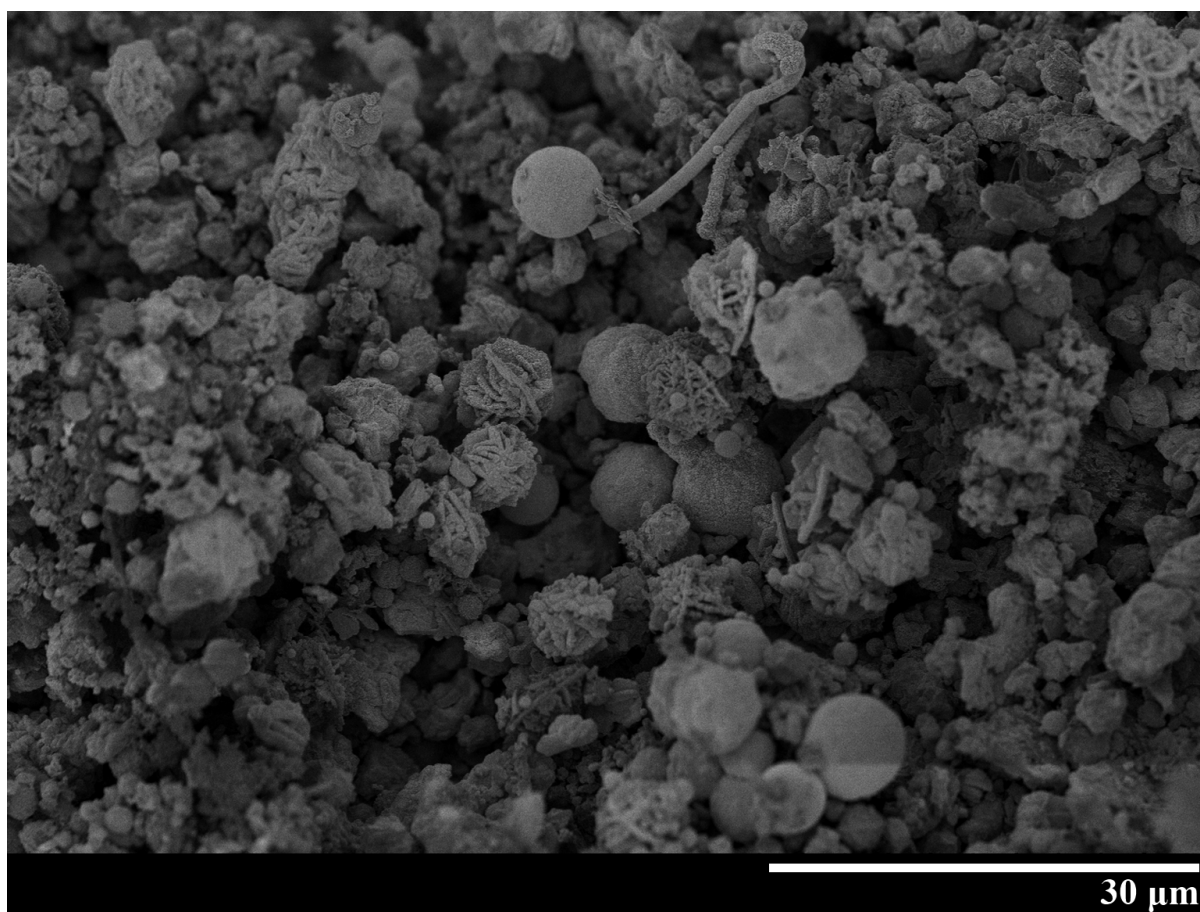
Figure 4.45: SEM image of the black (Cu-rich) product 3b.

by SEM. As an intermediate phase, $Cu_{2-\delta}S$ can take up Ga^{3+} and S^{2-} from the solution to grow $CuGaS_2$ nanoplates as proposed in Equation (4.2) in Section 4.1.2. This explains why pure $Cu_{2-\delta}S$ particles are not observed, but digenite may instead be present inside roses and spheres as discussed in Section 4.2.1.

4.3.2 Thiourea Stoichiometry

Synthesis 4c reduced the concentration of Tu in synthesis 4a[1] below the stoichiometric amount, resulting in large amounts of GaO(OH) and digenite impurities in addition to the CuS impurity also reported for 4a[1]. The black, Cu-rich product show white spots and GaO(OH) rods are relatively abundant as seen in the SEM image in Figure 4.46. Although product 4c contains roses, their abundance is greatly reduced from that of the Cu-rich part of product 4a[1] produced with two times Tu excess for $CuGaS_2$ precipitation, and is depicted in Figure 4.44(b). The intergrown spherical and irregular $CuGaS_2$ particles in product 4c are greatly reduced by limiting the S^{2-} supply as sphere diameters are less than 2 µm, while the diameters of spherical particles in product 4a[1] are in the range $4 - 11$ µm. The nanoplate surface structure found in product 4a[1] is lost as the Tu concentration is reduced from 0.120 M in synthesis 4a[1] to 0.029 M in synthesis 4c, in which the $CuGaS_2$ particles show a rough surfaces structure like that in Figure 4.34(e) in Section 4.2.1. However, the average crystallite size of 16 nm calculated from the
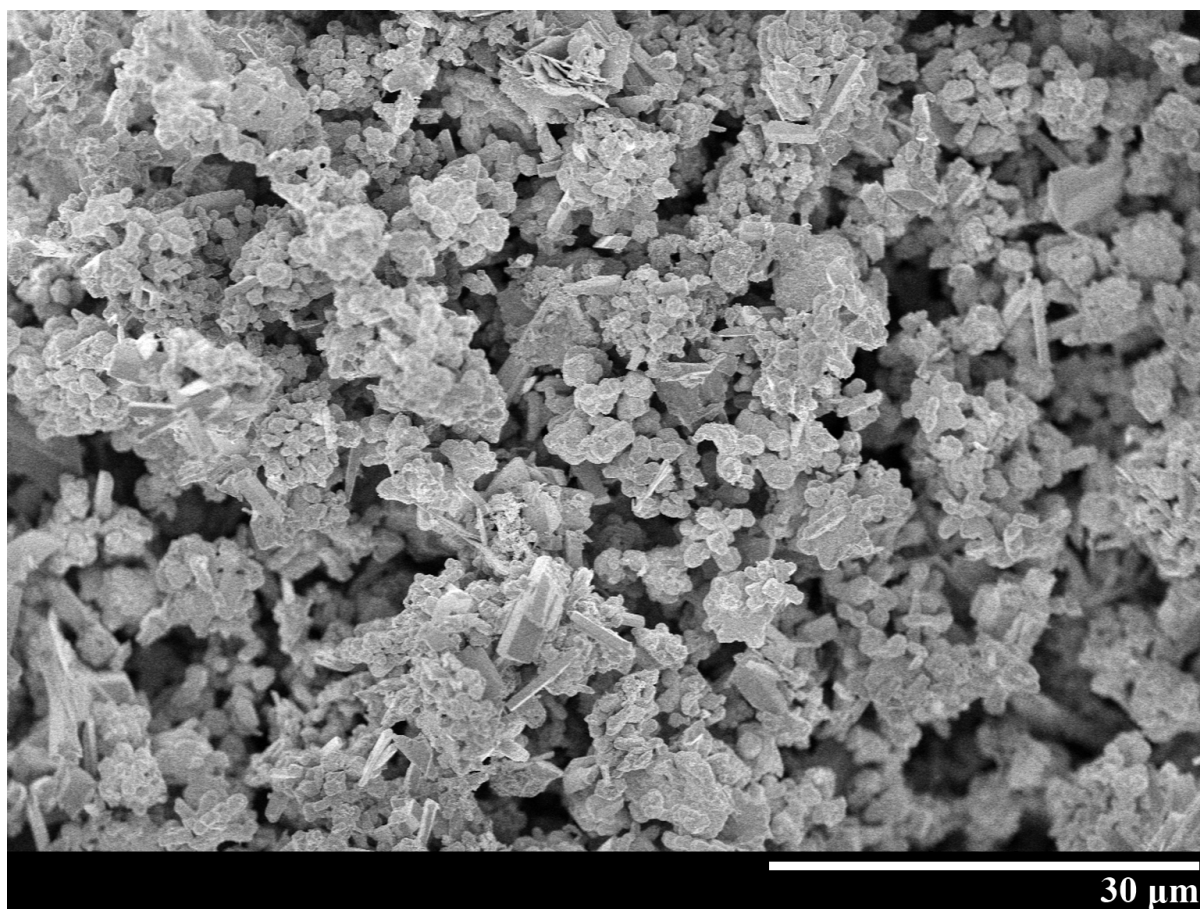
Figure 4.46: SEM image of the black (Cu-rich) product 4c.

diffractogram in Figure 4.5 are similar to those in products 4a[1], 1a and 1b.

4.3.3   HCl Concentration

The sensitivity of the synthesis to the HCl concentration is demonstrated by a comparison of the morphology in Figures 4.47(a) and the SEM images of product 4a[1] in Figures 4.44(a) and (b). Being all black, product 3a shows more similarities with the black precipitate of product 4a[1] in Figure 4.44(b) than the brown precipitate. Among the similarities is the extent of irregularities with a large variation of the sizes of irregular particles. The spheres observed in Figure 4.47(a) are comparatively large, approaching 13 μm. Neither roses or similar irregular particles are present in synthesis 3a, with its slightly increased HCl concentration of 0.501 M compared to 0.316 M in synthesis 4a[1]. Also, the surface structure of a spheres in Figure 4.47(b) represents a gradual transition from the nanoplate surface structure in product 4a[1] to a smoother surface seen on the intergrown spheres in Figure 4.30(a), through growth on both sides of the nanoplates. Furthermore, the calculated average crystallite size of 29 nm form the diffractogram in Figure 4.6 in Section 4.1.4 represent a significant increase, which may relate to the decreased rate of Tu decomposition with decreasing pH and thus decreased supersaturation and rate of nucleation compared to the growth rate.

(a)   (b)
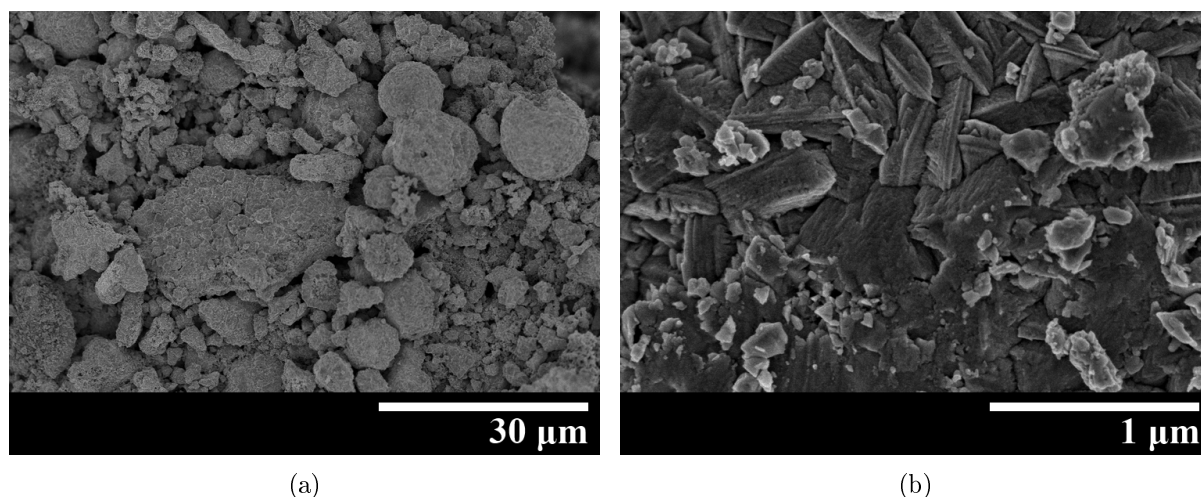
Figure 4.47: SEM image of the black (Cu-rich) product 3a (a) and a sphere with characteristic nanoplate irregularity (b).

4.3.4   Fill Factor

Increasing the fill factor at a HCl concentration of 0.316 M show a different trend than that for 0.10 M reported by Sortland [1]. The morphology change at 0.316 M HCl is seen by comparing SEM images of product 2c in Figure 4.48 to those of product 4a[1] in Figures 4.44(a) and (b). While spheres become more abundant with increasing fill factor for syntheses using 0.10 M HCl [1], rods and network structures become increasingly abundant at 0.31631 M HCl. The size of intergrown spheres observed in the Cu-rich part of product 2c is somewhat reduced to $3-8$ μm compared to product 4a[1], while the average crystallite size of 10 nm calculated from the diffractogram in Figure 4.7 in

Section 4.1.5 show a reduction from 18 nm in product 4a[1]. This may however also be affected by the increased content of Ga-rich $CuGaS_2$ in product 2c as its color variation ranged from red to brown, if pure Ga-rich $CuGaS_2$ favor network structures as discussed in Section 4.2.1. Figure 4.48(b) shows a transition between the network structure and rods, although the crystallite shapes are changed from irregular to nanoplates in rods, which is seen in the magnification in Figure 4.48(d). The Ga-rich precipitate also contains characteristic particles magnified in Figure 4.48(c) with a hemisphere grown out of a plate.

(a) 2c; Ga-rich

(b) 2c; Cu-rich

(c)

(d)
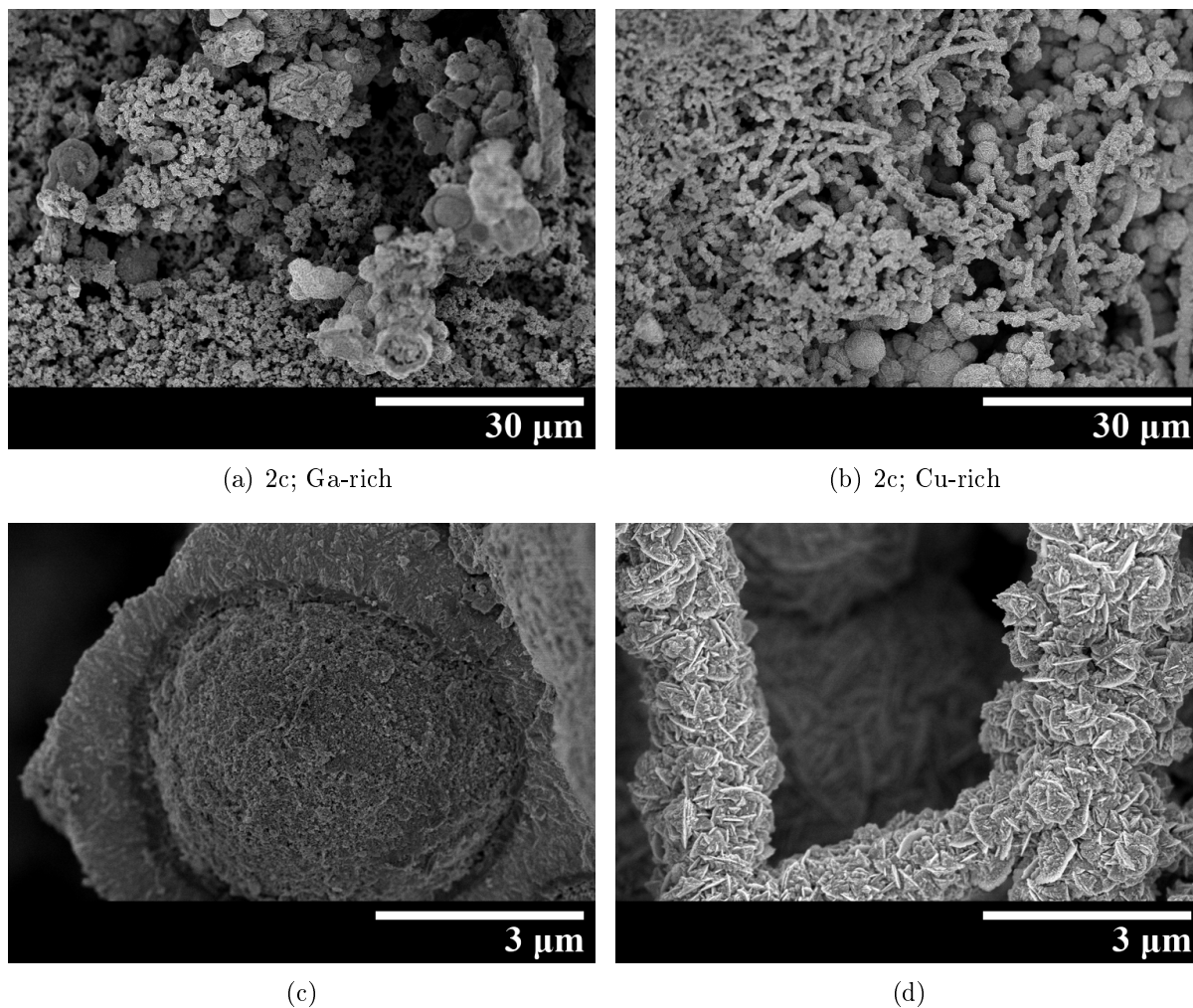
Figure 4.48: SEM images of the red (Ga-rich) part of product 2c including characteristic particles (c), and the brown (partly Cu-rich) part containing rods (d).

4.3.5 Reactant Concentrations

Compared to product 2c, depicted in Figures 4.48(a) and (b), the SEM image of product 2b in Figure 4.49 shows the effect of an over tenfold increase in concentrations. This concentration increase also results in changes in the off-stoichiometry of $CuGaS_2$. A large part of product 2c was Ga-rich as seen from its red and brown color, while the majority of brown powder in product 2b showed a less extent of Ga-rich $CuGaS_2$. A large part of product 2b show a network structure with the similar grainy crystallites found in the brown, partly Cu-rich precipitate of product 2c shown in Figure 4.33(b) in Section 4.2.1. The large plates shown in Figure 4.50(a) also have a porous structure of submicron crystallites. The small crystals in these structures are the cause of the broad peaks in the diffractogram of product 2b shown in Figure 4.8 in Section 4.1.6, and their average size is calculated to 5 nm. The increased reactant concentrations in product 2b gives increased rate of Tu decomposition and increased supersaturation, which according to Section 2.4.3 increases the rate of nucleation compared to the growth rate. This results in smaller crystallites, and an increased rate of homogeneous nucleation can explain the increasing abundance of network structures compared to polycrystalline particles with increasing reactant concentrations. Although product 2b also contains polycrystalline spheres with diameters of $0.3 - 2$ μm, these are smaller than the polycrystalline rods and $2 - 8$ μm spheres in product 2c.
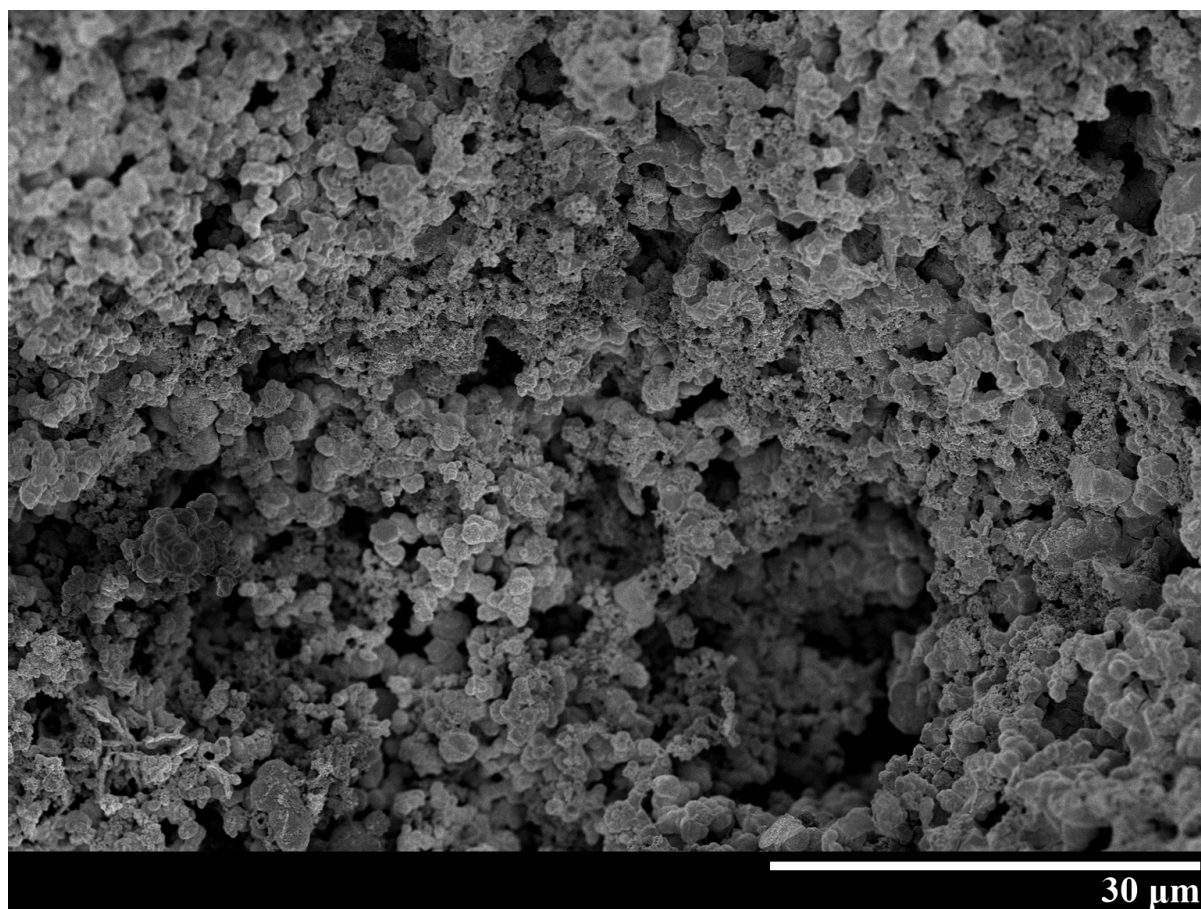
Figure 4.49: SEM image of the brown (Ga- and Cu-rich) product 2b.

(a)   (b)
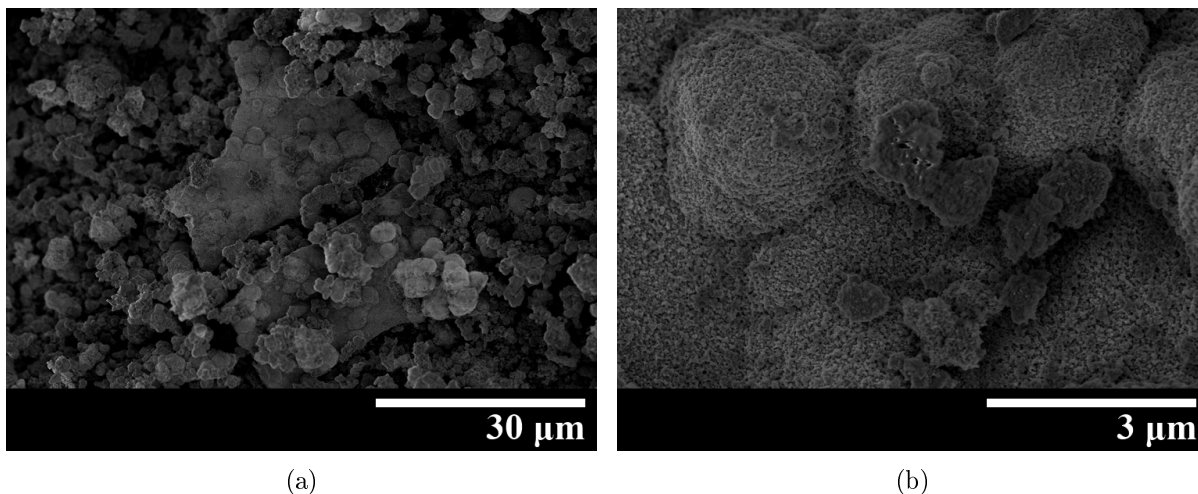
Figure 4.50: SEM images of plates (a) and their nanostructure (b) in product 2b.

Syntheses 2a and 3c aimed to investigate the effect of increasing concentration at a fill factor of 80% due to the higher purity obtained with this fill factor compared to 85% according to Section 4.1, and these products are compared to product 4a[1] in Figure 4.9. This comparison demonstrates the change in morphology upon changing cation concentrations from 0.030 M in synthesis 4a[1] to 0.122 M in 2a and 0.220 M in 3c, with four times higher Tu concentrations. Product 2a was the most Cu-rich product as it appears all black, the highest concentration used in synthesis 3c showed the highest content of Ga-rich $CuGaS_2$ as part of this product is red and the rest is a brown mixture of Cu- and Ga-rich $CuGaS_2$. The lowest concentrations in synthesis 4a[1] gave an intermediate stoichiometry as part of this product is brown and part is black.

The SEM images of these products in Figure 4.51 show decreasing particle sizes from syntheses with increasing reactant concentrations as the Cu-rich part of product 4a[1] show particle sizes of $4 - 10$ μm, product 2a contains $0.5 - 4$ μm spheres and the spheres in the Cu-rich part of product 3c show a further decrease in diameters to $0.6 - 3$ μm. The decrease in particle sizes with increasing reactant concentrations is due to increased supersaturation giving increased rate and extent of nucleation so that a smaller part of the reactants are available for particle growth. This alos explains the trend of decreasing crystallite sizes calculated to 18 nm from the diffractogram of product 4a[1], 6 nm in product 2a and 4 nm in product 3c. The increased abundance of network structures in product 3c shows together with product 2b a trend of increasing abundance of networks structures with increasing reactant concentrations. However, a comparison of product 2a and 4a[1] suggests that changes in concentrations below 0.122 M is not significant in this respect.

At increased concentrations, the nanoplate surface structure common in product 4a[1] is in some spheres of product 2a mixed with nanospheres as shown in Figure 4.34(d) in Section 4.2.1, while most of the spheres and rods show a somewhat porous alteration of the irregular surface represented in Figure 4.34(e). This irregular surface is also abundant in product 3c, along with poorly defined nanoplates on spheres. The network structures of product 2a and 3c exclusively contain irregular crystallites, which are shown in in Figure 4.33(b) in Section 4.2.1.

93
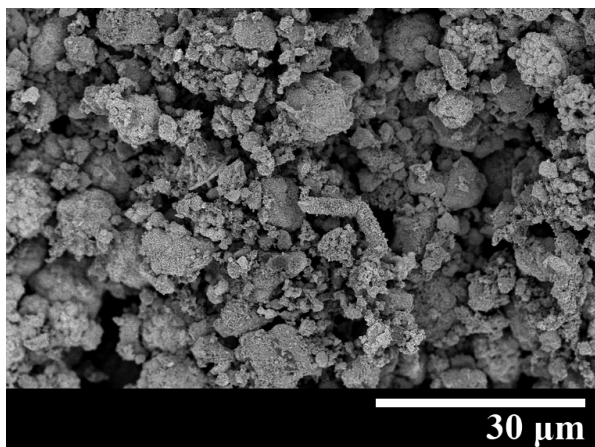
(a) 4a[1]; Ga-rich
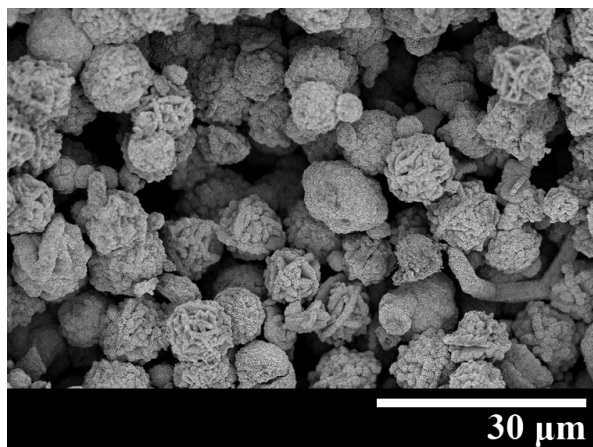
(b) 4a[1]; Cu-rich
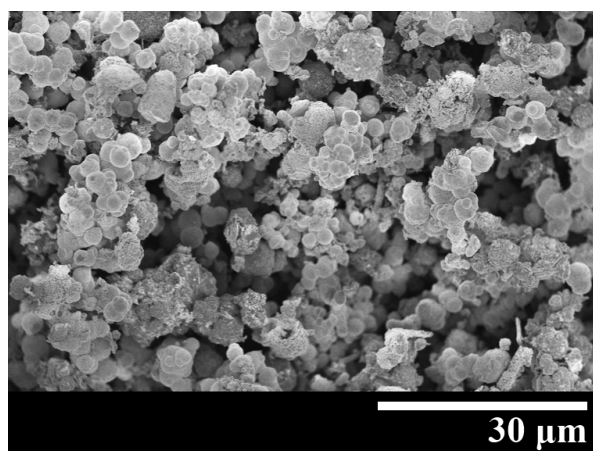
(c) 2a; Cu-rich
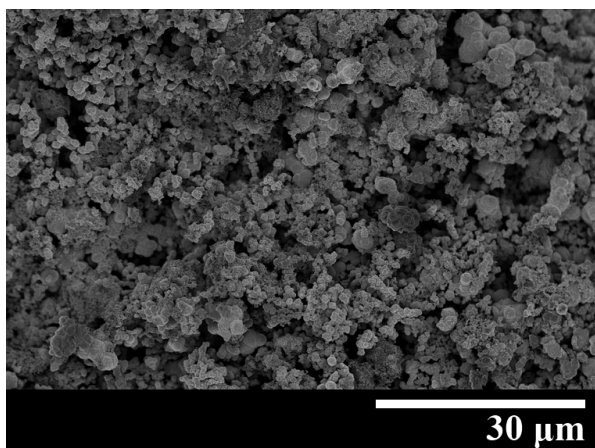
(d) 3c; Ga-rich
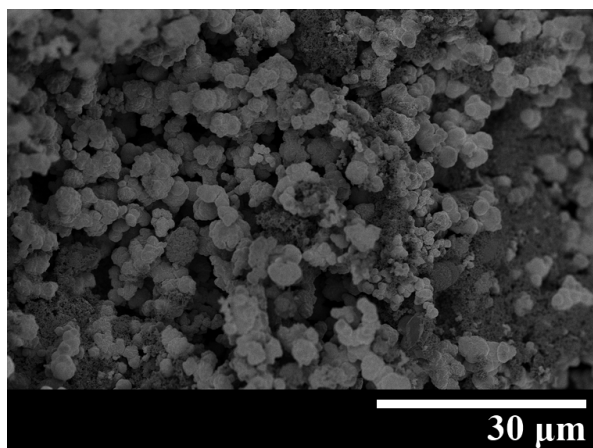
(e) 3c; Cu-rich

Figure 4.51: SEM images of Ga- and Cu-rich parts of products produced with different reactant concentrations: 4a[1] (0.030 M), 2a (0.122 M) and 3c (0.220 M).

94

4.3.6 Complexing Agent

Adding 1-pentanethiol in a similar synthesis to 4a[1] produce a more uniform stoichiometry as a dark brown part of product 4a only differ from the black, Cu-rich part by a minor contribution of red color from Ga-rich $CuGaS_2$, which compares to the more reddish brown part of product 4a[1]. This also gives a more uniform distribution of predominately agglomerated spheres in the Cu-rich part of product 4a depicted in Figure 4.52(b) and large irregular particles built up from smaller intergrown particles depicted in Figure 4.52(a) in the Ga-rich part. This increased uniformity may relate to the stable concentration of free cations in solution due to the equilibrium of complex formation in contrast to the gradual depletion of free cations as these are consumed in syntheses without formation of stable complexes. The diameters of spheres in the Cu-rich part of $1-9$ μm compared to $4-11$ μm in product 4a[1] and the decreased average crystallite size calculated from the diffractogram of product 4a of 11 nm is not expected since complex formation significantly reduce the concentration of free cations in the solution, which according to Section 2.4.3 would reduce the rate of nucleation and leave more of the reactants available for particle growth.

Nearly all particles in product 4a have a typical nanoplate surface, including the characteristic cone-shaped core of a broken spheres to the bottom left of Figure 4.52(b). Such cores have the smallest nanoplates observed, which may be explained by a relatively short time of exposure to the reactants in solution for growth of $CuGaS_2$ nanoplates fromon possibly a digenite core. Also the nanoplates appear much larger in the Ga-rich part than the Cu-rich part of product 4a. Part of the particles in the Ga-rich product have nanoplates similar to those shown in Figure 4.34(b) in Section 4.2.1, but in addition be aligned and have a smooth surface, they are also somewhat curved.

(a) 4a; Ga-rich   (b) 4a; Cu-rich
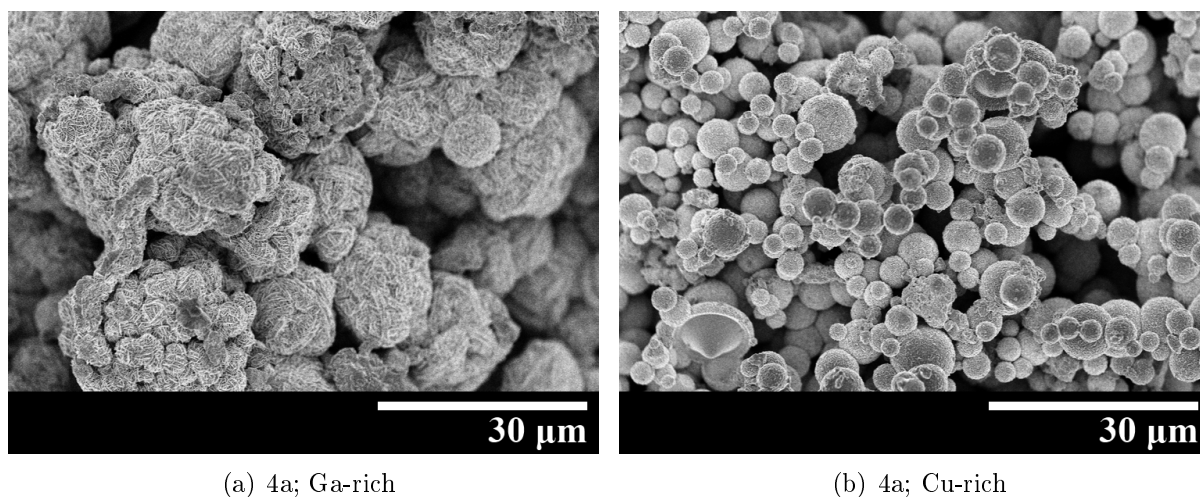
Figure 4.52: SEM images of brown (partly Ga-rich) and black (Cu-rich) parts of product 4a.

4.3.7 Pressure

The increased pressure at 250 °C of at least 65 bar according to Figure 2.10 in Section 2.4 provides some stoichiometric product seen from a partly yellow deposit along the Teflon cup wall and the filtrate showed a strong yellow color from dispersed particles of stoichiometric $CuGaS_2$ small enough to penetrate the filter paper. Stoichiometric $CuGaS_2$ was also mixed into the precipitate, giving an orange color to the part containing Ga-rich $CuGaS_2$ and a darker orange color to the most Cu-rich part of product 4b. The SEM image in Figure 4.53(a) reveals a GaO(OH) rod although this impurity is not sufficiently abundant to give peaks in the diffractogram in Figure 4.13 in Section 4.1.8. The average crystallite size of 30 nm calculated from this diffractogram is the largest among all products in this work, and this is consistent with the observation by Feng et al. [36] that crystal sizes increases with temperature as described in Section 2.4.5. The SEM images of product 4b show increased amount of network structures and reduced particle sizes represented by $2 - 8$ μm spheres compared to $4 - 11$ μm spheres in product 4a[1], depicted in Figure 4.44(a) and (b).

The increase in temperature from 180 °C in synthesis 4a[1] to 250 °C in synthesis 4b gives increased rate of reactions and particle growth, leaving more time for ageing of product 4b compared to 4a[1], although both products show large variations of particle sizes and shapes. Spheres are among the most abundant particles in product 4b shown in Figure 4.53 compared to roses and irregular particles in product 4a[1] depicted in Figures 4.44(a) and (b). Also, a larger amount of particles have grown into one another at the increased pressure in product 4b compared to 4a[1], giving a denser arrangement of particles. The surface structure of particles is completely changed form nanoplates in product 4a[1] to denser pyramidal crystallites in product 4b. Assumedly, the necessary change in fill factor from 80% in synthesis 4a[1] to 70% at 250 °C in synthesis 4b contributed to the changes in morphology in accordance to Section 4.3.4 and Sortland [1].

(a) 4b; Ga-rich
(b) 4b; Cu-rich
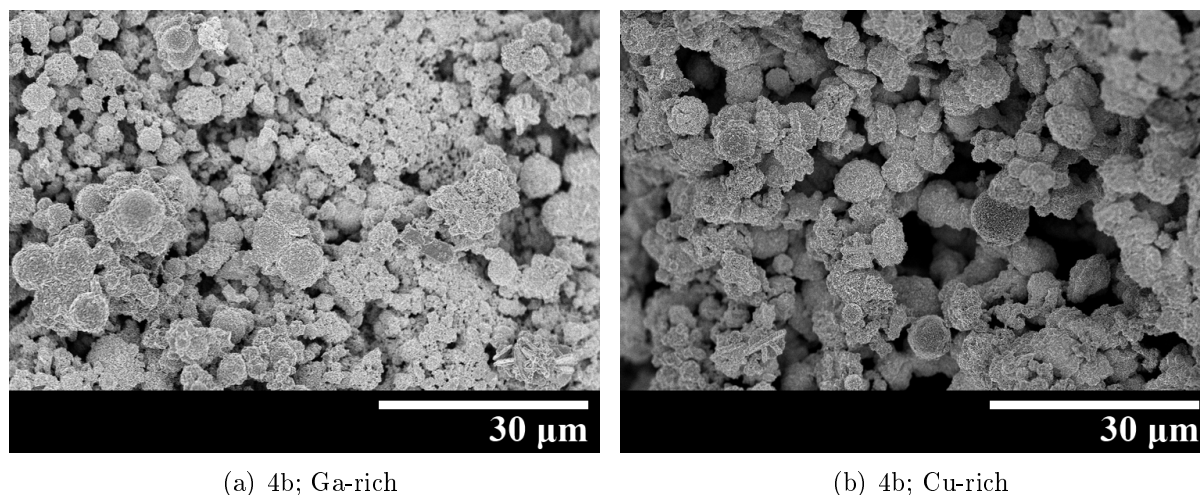
Figure 4.53: SEM images of orange (partly Ga-rich) and dark orange (partly Cu-rich) parts of product 4b.

4.3.8 Heating Time with Complexing Agent

Comparing products 5a and 5c in Figure 4.54 shows the effect of reaction time on syntheses using 1-pentanethiol as complexing agent at 250 °C. The reduced HCl concentration of 0.271 M combined with incomplete Tu decomposition after a reaction time of 5 h in synthesis 5c produced GaO(OH) rods, predominantly in the red, Ga-rich part depicted in Figure 4.54(a). The digenite impurity is not revealed in separate particles in either of these products. Increased reaction time to 20 h in synthesis 5a proved beneficial to the CuGaS$_2$ stoichiometry in addition to the purity, as no black, Cu-rich CuGaS$_2$ was observed in product 5a. Instead, part of this product showed a light orange color from mixing of stoichiometric CuGaS$_2$ with the more abundant Ga-rich product. A similar light brown precipitate was also produced after 30 h with 0.316 M HCl in synthesis 6a and is depicted in Figure 4.55 in Section 4.3.9.

The increased average crystallite sizes of 13 nm in product 5c compared to 19 nm in product 5a suggests synthesis 5c to be stopped during particle growth. Furthermore,

(a) 5c; Ga-rich

(b) 5c; Cu-rich

(c) 5a; Ga-rich

(d) 5a; stoichiometric
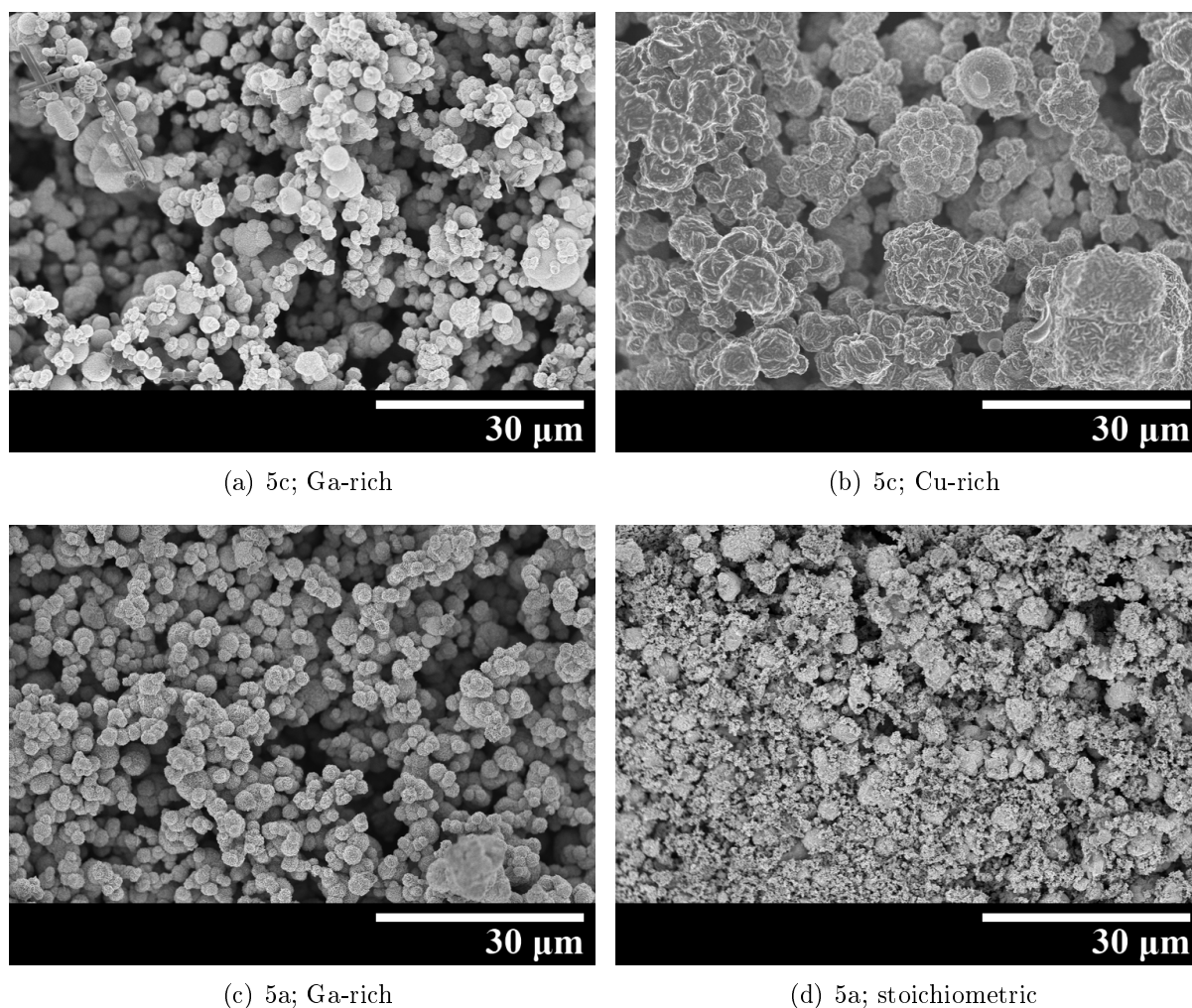
Figure 4.54: SEM images of different stoichiometries of products produced with 1-pentanethiol and different reaction times: 5c (5 h) and 5a (20 h).

the sphere diameters in product 5c show a wider distribution of $0.7 - 7\ \mu m$ than the $1 - 6\ \mu m$ spheres in product 5a. However, the trend reported by Feng et al. [36] of increasing particle sizes as the time for particle growth increases, is not observed for products 5c and 5a. The trend of narrowing particle size distributions with increasing reaction time may relate to prolonged nucleation due to slow Tu decomposition, for which small nuclei are formed until Tu decomposition comes to a halt, rather than ageing explained in Section 2.4.3. Even though slow decomposition limits inhomogeneities in the S^{2-} concentration and thus the sizes of nucleus formed, variations in the time available for particle growth is supposedly more important for the particle size distribution in the hydrothermal syntheses presented in this work. Additionally, the spheres in the black, Cu-rich part of both product 5c are grown into irregular shapes while the spheres in the red, Ga-rich parts are to a larger extent separate.

The spheres in red, Ga-rich parts of products 5a and 5c show a surface of nanoplates. These nanoplates are smaller in product 5c than in product 5a and pyramids are grown from some of these nanoplates in product 5a, like in Figure 4.33(a) in Section 4.2.1. The nanoplates on the surface of particles in the Cu-rich part of both products 5c are mostly smooth like in Figure 4.34(b), but not aligned to the same extent. The part of product 5a containing stoichiometric $CuGaS_2$ consists exclusively of dense pyramidal or irregular crystallites, of which some pyramidal crystallites arrange along a plane as depicted in Figure 4.34(c) in Section 4.2.1. This comparison indicates that the crystallite morphologies show large differences with product stoichiometry along with reaction time through nucleation, particle growth and possibly ageing.

4.3.9 Reactant Concentrations at increased Pressure

An increased reaction time of 30 h and increased HCl concentration of 0.316 M compared to syntheses 5a and 5c produced a light brown precipitate in product 6a depicted in Figure 4.55. The color suggest that only a part of the precipitate was stoichiometric, and that also Ga- and Cu-rich $CuGaS_2$ was present. A large variation of sizes and shapes of particles is shown in Figure 4.55, which relates to the variation of stoichiometry giving different particle morphologies. One dominant morphology is a network structure of densely packed nanoplate crystallites contrasting to the pyramidal and irregular crystallites in the network structure of the stoichiometric part of product 5a depicted in Figure 4.54(d). Also large irregular particles of nanoplates and characteristic sheets with the same nanostructure of plates with pyramids and plates grown out of them as the nanoplates depicted in 4.33(a) are observed in the partly stoichiometric precipitate in product 6a.

Further increasing the reaction time from 20 h in synthesis 5a to 30 h in synthesis 6a did not increase the crystallite sizes when also the HCl concentration was increased from 0.271 M to 0.316 M, as the average crystallite size was calculated to 16 nm in product 6a. However, synthesis 6a supports the trend of narrowing sphere size distributions in the Ga-rich precipitates with increasing reaction time as it is reduced from $0.7 - 7\ \mu m$ in product 5c and $1 - 6\ \mu m$ in product 5a depicted in Figure 4.54 in Section 4.3.8 to $2 - 4\ \}7\mu m$ in Figure 4.56(a). However, the intergrown spheres in the Cu-rich precipitate shows a wider size distribution with increasing reaction time as their dimensions are $1 - 14\ \mu m$ in product 6a depicted in Figure 4.56(b), and $1 - 9\ \mu m$ in product 5c. As in

product 5c, spheres in the Ga-rich part in Figure 4.56(a) are to a larger extent separate than the intergrown spheres in the Cu-rich part of product 6a depicted in Figure 4.56(b), and the nanoplates on the surface of particles in the Cu-rich part are mostly smooth like in Figure 4.34(b), but not aligned to the same extent.
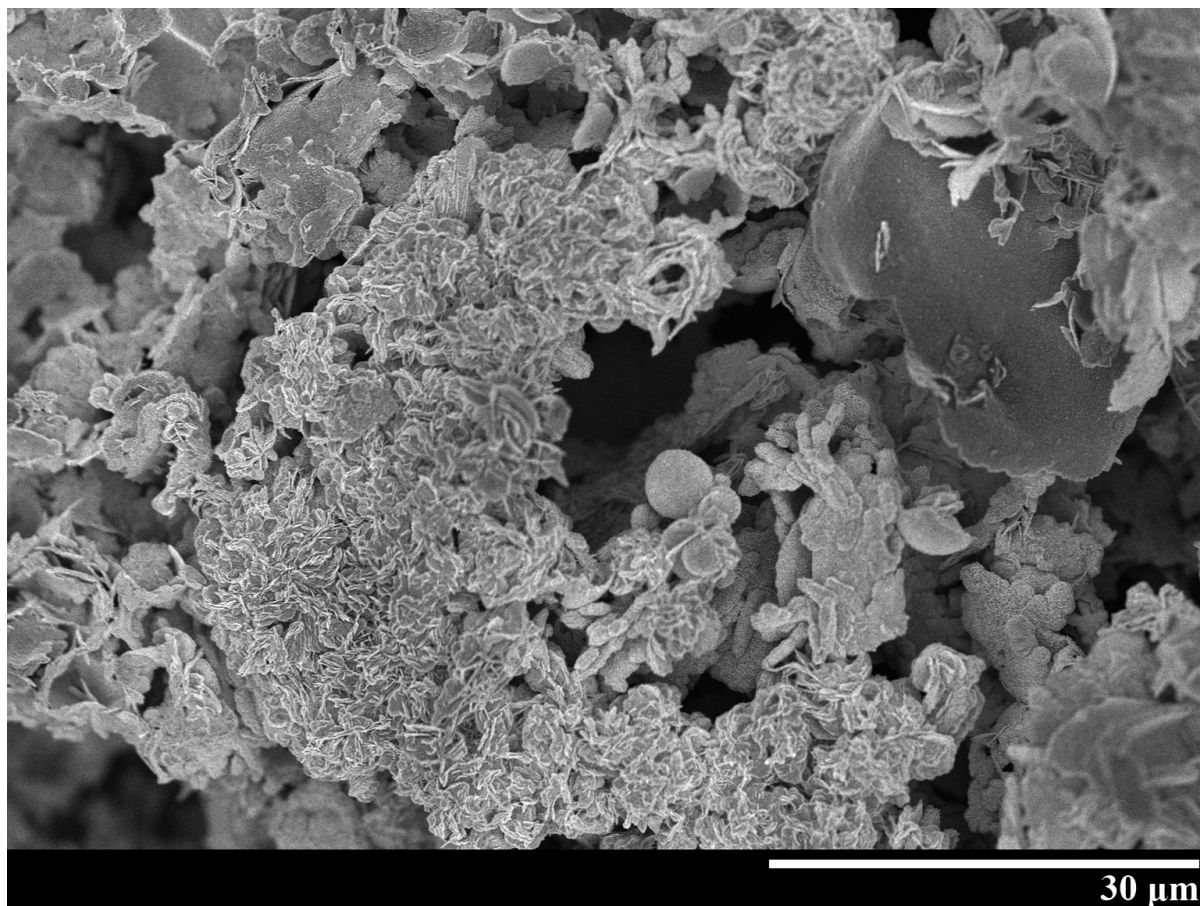
Figure 4.55: SEM image the light brown (partly stoichiometric) part of product 6a.

Compared to synthesis 4a, synthesis 6a utilized a higher temperature of 250 °C compared to 180 °C and over doubled the reaction time to 30 h from 12 h in synthesis 4a. In the Cu-rich precipitates, these changes provided increased particle sizes of $1 - 14$ µm in product 6a compared to $1 - 9$ µm in product 4a as seen from Figure 4.52 in Section 4.3.6. The $2 - 4$ µm spheres in the Ga-rich part of product 6a is however smaller than the irregular particles in the Cu-rich parts of product 4a, reaching 18 µm across. The average particle size calculated from the diffractograms of these products is increased form 12 nm to 16 nm by the increased temperature and reaction time, giving increased growth rates and extent of reaction. Additionally, spheres are to a larger extent grown into one another in the Cu-rich part of product 6a shown in Figure 4.56(b), and this morphology is also abundant in the Ga-rich part in Figure 4.56(a) instead of the irregular particles with smaller spherical and irregular shapes on the surface in product 4a. Somewhat smooth, partly aligned nanoplates depicted in Figure 4.34(b) in Section 4.2.1 are seen on the particle surfaces in the Cu-rich precipitate in product 6a, while the nanoplates in the Ga-rich as well as the stoichiometric precipitate have grown pyramids on one side as

99

depicted in Figure 4.34(a) in Section 4.2.1. These nanoplate structures are also found in product 4a, but in products of opposite off-stoichiometry, and the presence of nanoplates in Cu-rich products indicates that this crystallite morphology is not exclusive for Ga-rich $CuGaS_2$ as discussed in Section 4.2.1.

The pure product obtained by doubling the concentrations of reactants and 1-pentane-thiol from a cation concentration of 0.030 M in synthesis 6a to 0.060 M with four times higher Tu concentrations and eight times higher 1-pentanethiol concentrations had no ob-servable yellow, stoichiometric precipitate. The black, Cu-rich part of product 6c shown in Figure 4.56(d) show a similar morphology of intergrown spheres with a nanoplate sur-face structure as product 6a in Figure 4.56(b). The increased extent of ageing and the increased rates of nucleation and growth accompanying the increase in reactant concen-trations resulted in larger spheres of $5 - 15\ \mu m$ in the Cu-rich precipitate compared to those of $1 - 14\ \mu m$ in product 6a. The nanoplates in the Cu-rich part of product 6c also had increased growth of pyramids and a lower degree of alignment compared to those in prod. However, the spheres in the red, Ga-rich part of product 6c show a greater size variation of $1 - 7\ \mu m$ compared to $2 - 4\ \mu m$ in product 6a, and these spheres are not at all grown into one another in product 6c. These changes in morphology are relatively small, and also the average crystallite sizes are similar, as it is calculated to 17 nm from the diffractogram of product 6c in Figure 4.15 in Section 4.1.10.

While no stoichiometric precipitate was observed in either of product 6a or 6c, a small part of product 7b had an orange color. Along with observations of spheres with both nanopyramidal crystallites aligned along a plane and nanoplates, presented in Figure 4.34(c) and (a) in Section 4.2.1, this indicate that product 7b contained some stoichiomet-ric $CuGaS_2$ along with red, Ga-rich $CuGaS_2$. A significantly larger amount this product was Ga-rich compared to 6a and 6c, giving a reddish variation of brown as the dominant color of this product, which also reveal formation of Cu-rich $CuGaS_2$. This brown part show the same morphology as the orange agglomerate depicted in Figure 4.56(e), sup-posedly due to the large amounts of Ga-rich product in both parts. Color variations of deposited product along the height of the Teflon cup wall from yellow near the top to black near the bottom and red in between in synthesis 7d, which was similar to synthesis 6c and introduced a substrate for investigation of film growth, suggests the possibility that fill factor influence the stoichiometry.

The relatively large increase in reaction concentrations in synthesis 7b to 0.319 M compared to 6a and 6c makes network structures abundant due to increased supersat-uration giving higher nucleation rates compared to growth rates like the concentration increase in syntheses without 1-pentanethiol discussed in Section 4.3.5 and explained in Section 2.4.3. The concentration increase does not influence the average size due to com-plexing of the cations for which supersaturation of free ions in the solution and thus the nucleation rate is not significantly increased, as the average crystallite size is calculated to 15 nm from the diffractogram for product 7b in Figure 4.15 in Section 4.1.10. Product 7b also shows similar intergrown spheres to those in products 6a and 6c, but with a rough surface structure as shown in shown in Figure 4.34(e). Furthermore, their sizes of up to $3\ \mu m$ and abundance are greatly reduced.
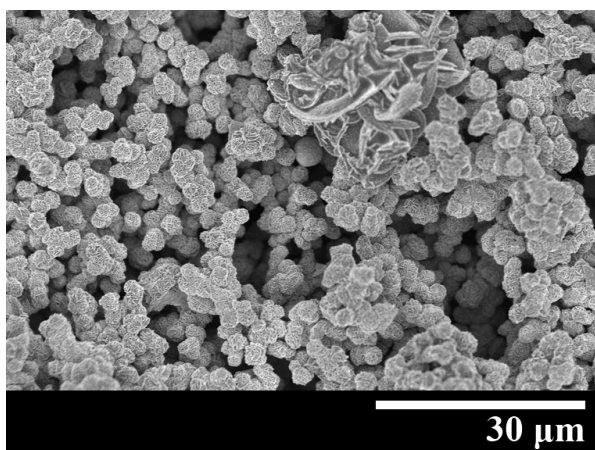
(a) 6a; Ga-rich
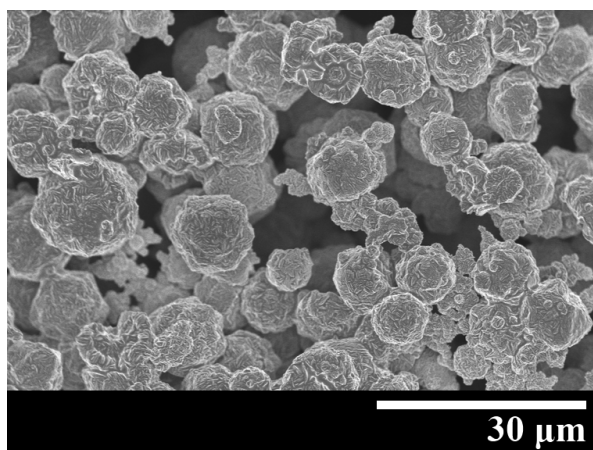
(b) 6a; Cu-rich
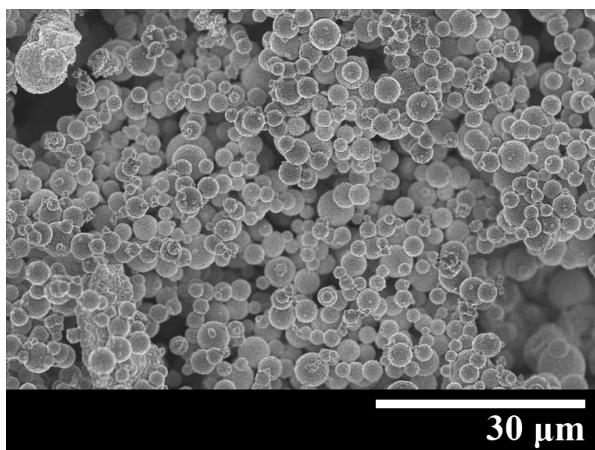
(c) 6c; Ga-rich
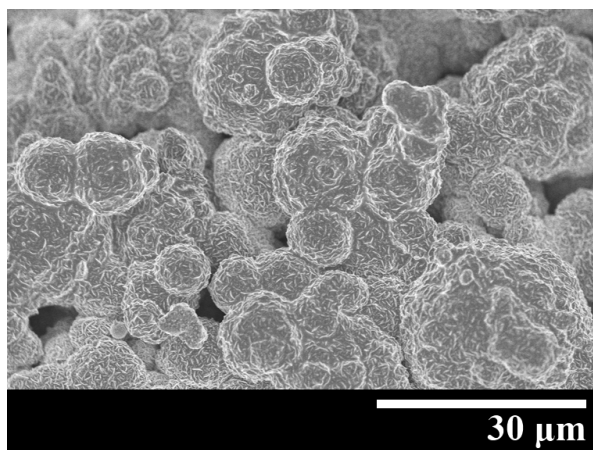
(d) 6c; Cu-rich
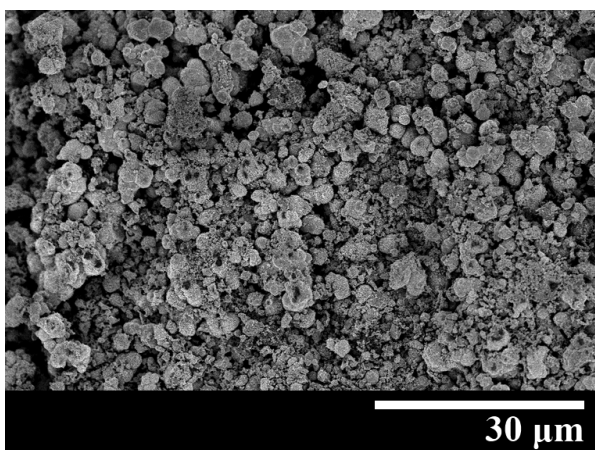
(e) 7b; Ga-rich

Figure 4.56: SEM images of reddish (Ga-rich) and black (Cu-rich) parts of products produced at 250 °C with 1-pentanethiol and different reactant concentrations: 6a (0.030 M), 6c (0.060 M) and 7b (0.319 M).

Synthesis 7a, which was similar to 7b without 1-pentanethiol, produced a similar stoichiometry as the powder obtained in synthesis 7a showed the same color variations as product 7b. However, the morphology of the orange and brown parts of product 7a depicted in Figure 4.57 are different. The orange part containing stoichiometric $CuGaS_2$ predominately shows a densely agglomerated networks structure of irregular crystallites along with up to 3 µm spheres. Such irregularities of nanopyramidal crystallites are also present in the network structure of the brown part. This Ga-rich precipitate also contain $1-4$ µm intergrown spheres with nanoplate crystallites with varying extent of irregularities. These morphology characteristics are similar to those of product 7b, although the agglomerate of product 7b is more densely packed than the brown part of product 7a. Thus, the morphology is not significantly influenced by use of 1-pentanethiol at high cation reactant concentrations, which is also supported by similar average crystal sizes, which is calculated to 18 nm for product 7a.

Compared to product 4b depicted in Figure 4.53 in Section 4.3.7 with reactant concentrations of 0.030 M, product 7a in Figure 4.57 shows increased amounts of network structures and smaller particles, which compares to spheres of $2-8$ µm in product 4b, which relate to the increased concentration in product 7a. Also the average crystallite size is reduced from 30 nm to 18 nm by the concentration increase. The significantly increase in crystallite sizes from product 2b, with an average crystallite size of 5 nm, is explained by increased Tu decomposition and thus growth rates due to the temperature increase from 180 °C to 250 °C, combined with an increased heating time from 12 h to 30 h allowing prolonged ageing in synthesis 7a. Additionally, the increased reaction time of 30 h in synthesis 7a compared to 12 h in synthesis 4b contributes to decrease the size differences through ageing as reported by Sortland [1] and explained in Section 2.4.3. The changes in concentration and fill factor between these syntheses also alters the crystallite morphologies from predominately nanopyramidal crystallites in product 4b.

(a) 7a; Ga-rich

(b) 7a; stoichiometric
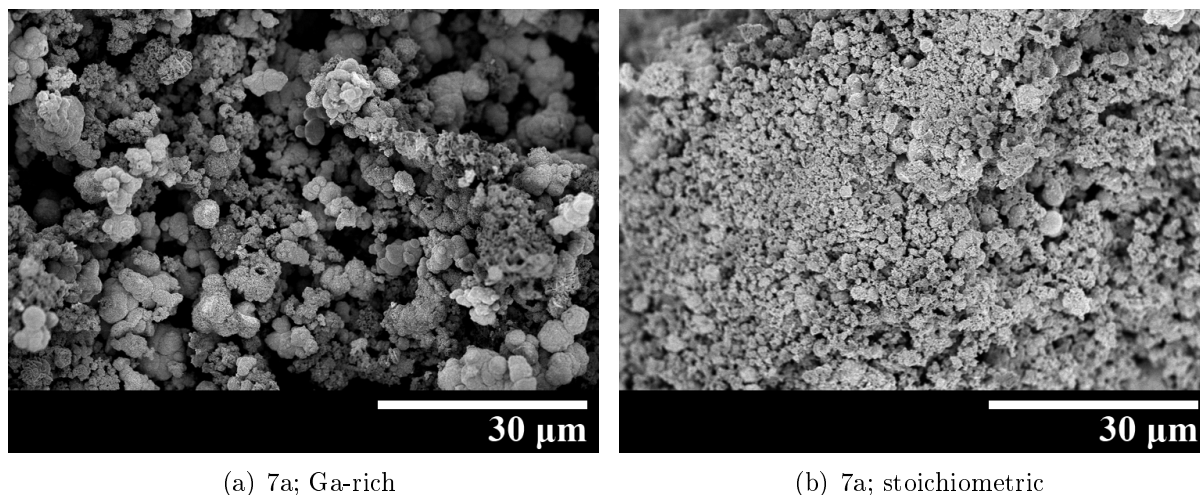
Figure 4.57: SEM images of brown (partly Ga-rich) and orange (partly stoichiometric) parts of product 7a.

4.3.10 Volume

An attempt to improve stoichiometry of the highly pure product 6c was conducted in synthesis 7c by using a smaller autoclave of 45 ml depicted in Figure 3.1(b) in Section 3.1, which compares to 125 ml autoclaves used in all other syntheses. This decrease in volume did not change the color of the product and thus, it proved unable to significantly increase the amount of stoichiometric $CuGaS_2$. Possibly, the reactor volume of 45 ml is large enough to accommodate a similar extent of inhomogeneities as the 125 ml autoclaves, or the product inhomogeneities may be due to changing reaction conditions during the course of reaction as discussed in Section 4.1.1. For instance, formation of Cu-rich product in the beginning will deplete Cu^+ ions in the solution faster than Ga^{3+}, so that Ga-rich $CuGaS_2$ forms towards the end, or vice versa.

Spherical particles are predominant in product 7c in Figure 4.58, like in product 6c depicted in Figures 4.56(c) and (d) in Section 4.3.9. However, the nanoplate crystallites in product 6c are changed towards nanopyramidal crystallites with this volume decrease, although the average crystallite size of 18 nm is similar to that of product 6c of 17 nm. In addition to this, the sizes of intergrown spheres of $1 - 6$ µm in the Cu-rich part and $2 - 6$ µm in the Ga-rich part of product 7c reveal that the Ga-rich and Cu-rich parts of product 7c has more similar morphologies than those of product 6c, and this might indicate more uniform growth conditions at the reduced reactor volume in synthesis 7c. The particle sizes are reduced from $5 - 15$ µm in the Cu-rich part of product 6c along with decreased extent of intergrowth of the spheres. The volume reduction gives increased extent of intergrowth of the spheres in the Ga-rich part and the majority of the spheres are larger, but within a similar range to that in product 6c, which is $1 - 7$ µm.

(a) 7c; Ga-rich   (b) 7c; Cu-rich
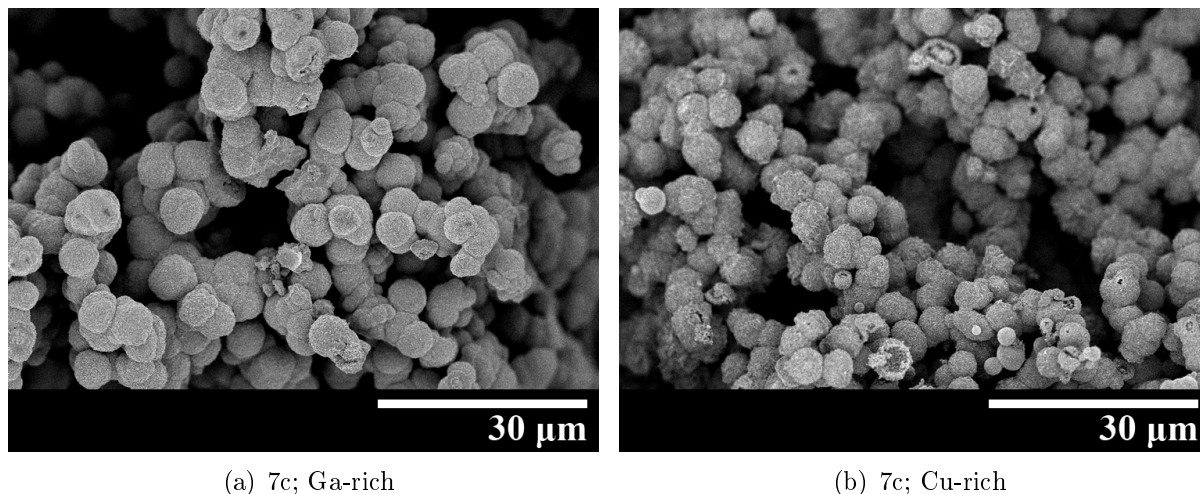
Figure 4.58: SEM images of red (Ga-rich) and black (Cu-rich) parts of product 7c.

4.3.11 Substrate

Synthesis 5b, which is similar to synthesis 4b, but with increased reaction time from 12 h to 20 h and reduced volume to 98 ml as it sought to grow a $CuGaS_2$ film on a Si(100) substrate mounted vertically in a large vertical substrate holder depicted in Figure 3.2 in Section 3.1. In contrast to synthesis 4b, no stoichiometric $CuGaS_2$ was achieved in synthesis 5b and the substrate was only partly covered in red and black precipitates. The changes in geometry and volume due to the substrate holder seem to have increased the extent of inhomogeneities, as the powder product 5b contained white agglomerates of GaO(OH) rods and dark blue digenite depicted in Figure 4.35 in Section 4.2.2. However, Ga- and Cu-rich $CuGaS_2$ are not produced separately, but in a brown mixture depicted in Figure 4.59(a). The dominant morphology of product 5b is intergrown spheres common for both the Ga- and Cu-rich parts of product 4b shown in Figure 4.53 in Section 4.3.7, and the sphere diameters of $1 - 6$ μm in product 5b are comparable to those of $2 - 8$ μm in product 4b. The diffractograms in Figure 4.21 in Section 4.1.12 show reduced average crystallite size of 18 nm in product 5b compared to 30 nm in 4b. The networks structure in the Ga-rich part of product 4b depicted in Figure 4.53(a) is not reproduced in product 5b. The surface of the spheres consists mainly of nanoplates, but also nanospheres are present in product 5b. Characteristic hollow rods depicted in Figure 4.59(b) are formed by growth of pyramidal crystallites onto orthormobic GaO(OH) rods, which later have dissolved due to acidification from Tu decomposition. Also pyramidal crystallites aligned along a plane were formed in product 5b.
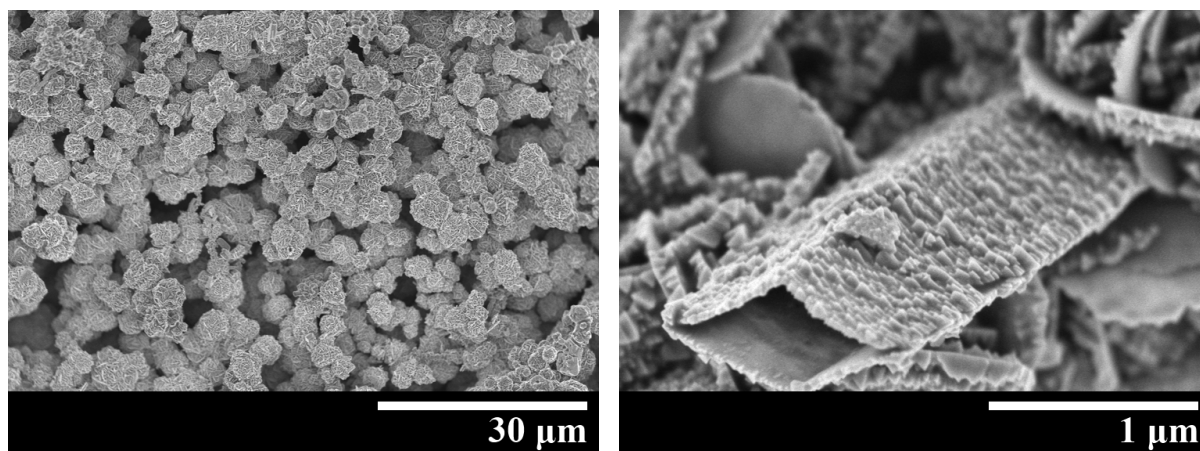
Figure 4.59: SEM image of the brown (Ga- and Cu-rich) product 5b (a) and a hollow rod (b).

A tenfold increase in reactant concentrations in synthesis 6b provided the same dominant morphology of intergrown spheres in both the red, Ga-rich part and the brown mixture containing Cu-rich $CuGaS_2$, as seen in Figure 4.60. The significantly increased reaction rates and extent of nucleation give much smaller intergrown spheres with diameters of $0.4 - 2$ μm compared to synthesis 5b. This morphology and the concentration increase correlate with reduced average crystallite size of 7 nm in product 6b. The same concentrations of 0.319 M CuCl and $GaCl_3$ at 280 °C in synthesis 2b provided a similar average size of 5 nm crystallites, although at a shorter reaction time of 12 h compared

to 30 h in synthesis 6b and with increased fill factor of 85% compared to 80% without substrate holder. Also synthesis 3c using cation concentrations of 0.220 M with a reaction time of 12 h produced equally small crystallites. The comparable sizes of intergrown spheres to those of $0.3 - 3$ µm in product 2b and $0.6 - 3$ µm in product 3c, indicates that the particles did not grow in spite of increased growth time in synthesis 6b as the reactants were depleted from a small extent of growth of the many nuclei formed during nucleation. It may also suggest that dissolution of small particles and growth of larger particles through ageing is a very slow process, possibly due to the low solubility of $CuGaS_2$ according to Section 2.4.3. However, the network structure in product 2b and 3c of even smaller particles is not present in product 6b.

(a) 6b; Ga-rich   (b) 6b; Cu-rich
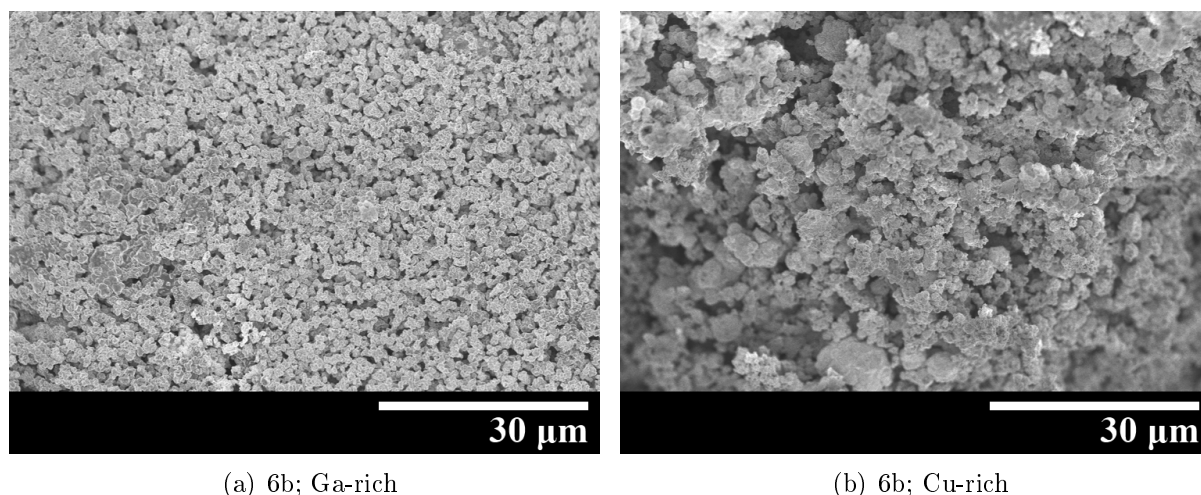
Figure 4.60: SEM images of red (Ga-rich) and brown (partly Cu-rich) parts of product 6b.

The high concentration in synthesis 6b provided a thick orange dispersion and yellow deposits along the Teflon cup wall like in syntheses 2b and 3c, along with a yellow deposit on the Si substrate labeled product 6b(s). Figure 4.61(a) shows a lot of particles on the substrate, ranging from sheets to a partly covering cracked layer of islands with agglomerated intergrown spheres similar to that in the Cu-rich precipitate in product 6b on top, and also digenite particles presented in Figure 4.35 in Section 4.2.2 were recognized. The surface structure of the islands assimilates that of the intergrown spheres depicted in Figure 4.30(a) in Section 4.2.1 and such an island were identified as $CuGaS_2$ by EDS analysis. A representative cross-section SEM image in Figure 4.61(b) show the particles on top of a bright layer with some cracks and voids. This bright layer in the image is supposedly a deformed zone of the Si wafer formed during cleavage to create the SEM sample, as only background signals corresponding to Cu, Ga and S was observed for cross-section EDS mapping of such a layer compared to the particles on top, while a comparatively strong Si signal originated from it. Furthermore, only the substrate was recognized by XRD analysis after removal of the particles in an ultrasonic bath, and only parts of the layer of islands remained adherent to the substrate. Their partly coverage and island shape indicate an island growth mode and thus limited wetting of $CuGaS_2$ onto the Si(100) substrate according to Section 2.4.3.

105

(a)	(b)
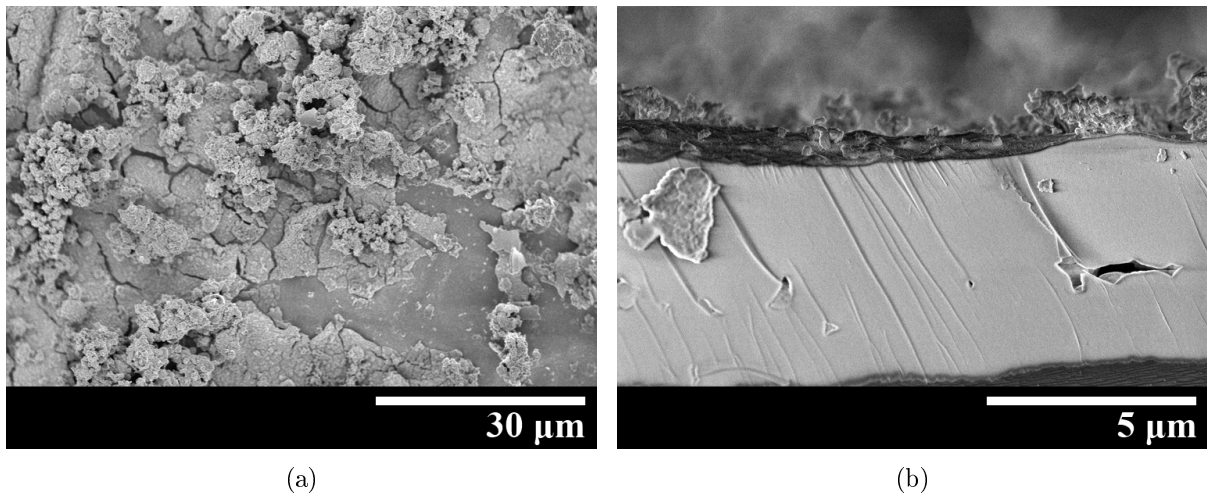
Figure 4.61: Top view (a) and cross-section (b) SEM images of product 6b(s).

The deposit in product 7a(s) from the orange dispersion obtained in the synthesis varies in color from red to orange and only covers part of the substrate. Its morphology, depicted in Figure 4.62(a) is similar to that of the orange precipitate of product 7a depicted in Figure 4.57(b), showing predominately a dense network structure along with some spherical particles. However, the $CuGaS_2$ peaks in the diffractogram shown in Figure 4.22 is thinner than those of product 6b(s), which indicates larger crystal sizes contrasting to the smaller particle sizes. The GaO(OH) phase identified by XRD for product 7a(s) is not observed as the characteristic rods identified in Section 4.2.2. A horizontal orientation of the substrate was selected to achieve film growth on the (100) atomic plane of Si at the polished side of the wafers facing down, and limit deposits of particles. Figure 4.62(b) reveals however that no film is formed. The deposits formed on the unpolished side of the wafer facing upwards, since gravity makes particles settle on this side, although the substrate fell off the supports during both syntheses 7a and 7b. Additionally, parts of the Si wafer appear etched by the acidic reaction solution.

(a)	(b)
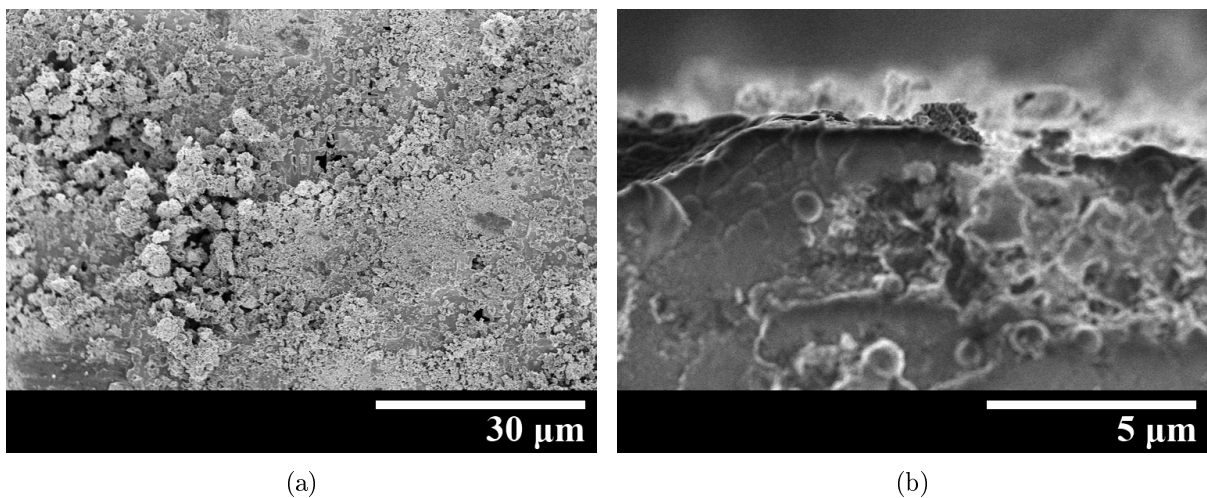
Figure 4.62: Top view (a) and cross-section (b) SEM images of product 7a(s).

Figure 4.63 shows that a completely covering film is obtained by addition of 1-pentane-thiol in synthesis 7b, and the red coloration of the substrate indicate that it is Ga-rich like product 7a(s). The bright color of the film surface in Figure 4.63 is due to edge charging of nanoplate crystallites, which also Peng et al. [67] grew on FTO conductive glass in a solvothermal synthesis of $CuInS_2$. The film of brighter color than the Si wafer does not compare to the bright layer observed in the substrate of product 6b(s) in Figure 4.61(b). Stabilization of cations by 1-pentanethiol in synthesis 7b proved necessary to prevent rapid homogeneous nucleation forming particles rather than a film on the substrate, although homogeneously nucleated particles could be washed off the substrate also in this synthesis. The film thickness shown in Figure 4.63(b) is not uniform, partly because the film grew on the unpolished side of the Si wafer. As a film was not formed on the polished side, the wetting of $CuGaS_2$ on Si is not sufficient for epitaxial growth, possibly due to lattice mismatch according to Section 2.4.3, and nucleation is favored at corners and other active sites for heterogeneous nucleation. Island growth is however a possible growth mode like for product 6bs, for which islands have coalesced to form a completely covering film in synthesis 7b. Figures 4.63(a) and (b) also show rod-shaped particles even though GaO(OH) was not detected by XRD as seen in the diffractogram in Figure 4.22 in Section 4.1.12. EDS mapping indicate that these particles do not contain $CuGaS_2$, as the Cu, Ga and S signals are weakened over the particles. Variations in the Si signal is however expected to depend on the inhomogene film thickness as it varies below 1 µm so that the Si substrate is included in the excitation volume to varying extents across the surface. The particles could not be identified by EDS, probably due the varying Si contamination signal from the substrate, which can mask a Si signal from the particles.

(a)   (b)
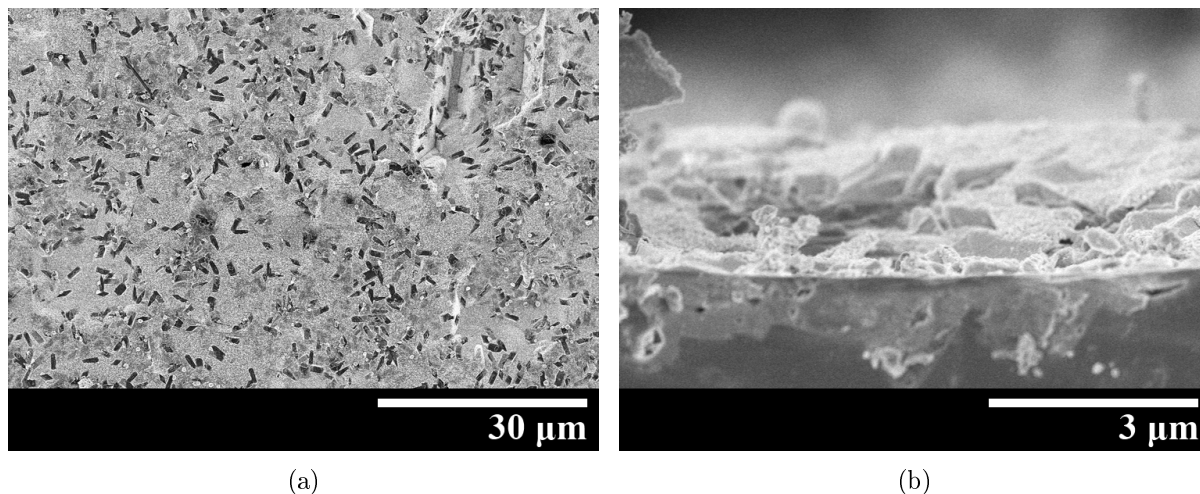
Figure 4.63: Top view (a) and cross-section (b) SEM images of product 7b(s).

4.3.12 Fe and Ni doping

The morphologies of syntheses similar to 7a with $NiCl_2$ addition, although without a substrate holder, are depicted in Figure 4.64. Addition of 0.020 M $NiCl_2$ in synthesis Ni16 produce a mainly reddish brown, Ga-rich precipitate depicted in Figure 4.64(c), with some orange agglomerates in which stoichiometric $CuGaS_2$ contribute with yellow coloration. Like for all products with dopant addition, the product colors does not reveal any significant changes in stoichiometry for the majority of the precipitate, but the amounts of orange precipitate in product Ni8 was not sufficient to make a SEM sample and such agglomerates were not produced in syntheses Fe16 and Fe8. The orange agglomerate containing stoichiometric $CuGaS_2$ in product Ni16, depicted in Figure 4.64(b), shows a more uniform network structure of crystallites that to a larger degree are separated from one another compared to those in product 7a depicted in Figure 4.57(b), and they are not at all aggregated into spheres. The network structures in these products contain similar irregular and pyramidal crystals.

(a) Ni16; Ga-rich

(b) Ni16; stoichiometric

(c) Ni8; Ga-rich
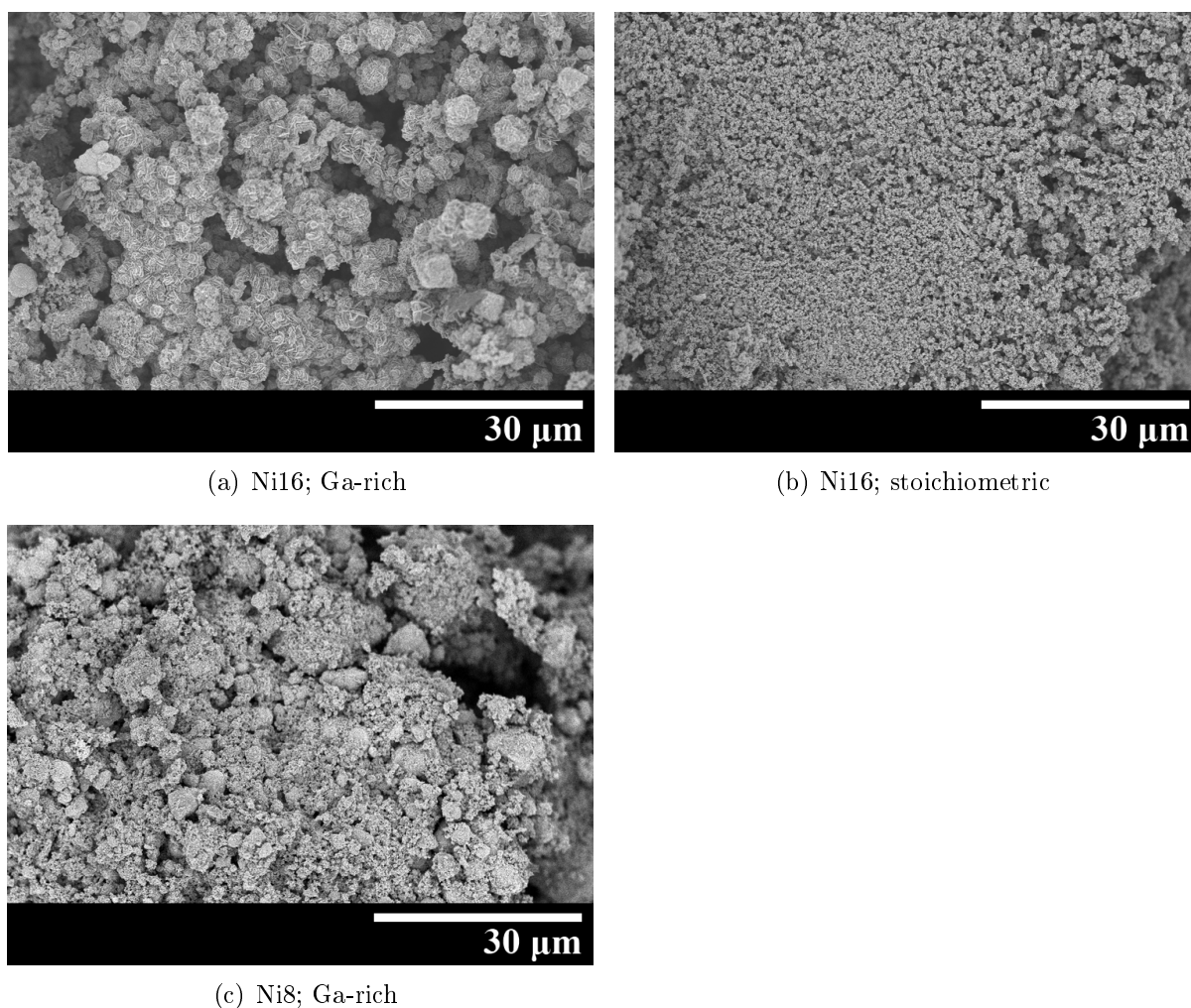
Figure 4.64: SEM images of brown (partly Ga-rich) and orange (partly stoichiometric) parts of products produced with varying $NiCl_2$ concentrations: Ni16 (0.040 M) and Ni8 (0.020 M).

A comparison of the mostly Ga-rich brown precipitates in products 7a, Ni16 and Ni8 reveals an increasing density of particles with increasing $NiCl_2$ addition. Increasing $NiCl_2$ concentration also give a transition from intergrown spheres up to 3 μm in product 7a to irregular particles up to 13 μm across in product Ni8 with 0.040 M $NiCl_2$. Product Ni16 show an intermediate stage of bulky irregular particles. These particles contain nanoplate crystallites several times larger than those making up the network structure in the Ga-rich precipitates. The smaller nanoplate crystallites relate to the broadened $CuGaS_2$ peaks in the diffractogram of product Ni16 giving a slightly increased average crystallite size of 20 nm compared to Ni8 in Figure 4.25 in Section 4.1.13 with 17 nm average crystallite size and that of product 7a in Figure 4.17 in Section 4.1.10 with average crystallite sizes of 18 nm, both containing mainly irregular pyramidal crystallites. The larger nanoplate crystallites in the irregular particles in product Ni16 contributes to the increased peak height with a narrow upper part for product Ni16.

Addition of 0.020 M $FeCl_3$ in syntheses Fe16 and 0.040 M $FeCl_3$ in Fe8 did not significantly change the product stoichiometry from that in product 7a, as a brown mixture of Ga- and Cu-rich $CuGaS_2$ dominated both products Fe8 and Fe16. However, a green coloration of these products could be observed as discussed in Section 4.1.13. These syntheses also produced the same dominant morphologies of intergrown spheres and network structures as the brown, Ga-rich precipitate in product 7a, depicted in Figure 4.57(a). Product Fe16 depicted in Figure 4.65(a) stand out in this comparison as a denser agglomerate, while the morphology of product Fe8 closely resembles that of product 7a. As the addition of dopant ions can alter the chemical potentials and the product composition as discussed in Section 4.1.13, it can also alter the product morphologies. However, the comparison of products 7a, Fe16 and Fe8 indicate that the ions introduced by dopant addition may not be the main contributor to differences in morphology for syntheses with doping. The differences may instead relate to the high sensitivity of the morphology to the growth conditions, which also relates to the extensive morphology variations within the products. A notable characteristic of product Fe8 is the large sizes of irregular aggregates compared to those formed in product 7a from intergrown spheres, which show diameters up to 3 μm in both products 7a and Fe8. Nanoplate crystallites are typical for the intergrown spheres in these products, while those in product Fe16 show a rough surface like that depicted in Figure 4.34(e) in Section 4.2.1, while the irregular and pyramidal crystallites are common for the network structures in products 7a, Fe16 and Fe8 alike. The average crystallite size calculated from the diffractograms of these products are slightly reduced to 13 nm in product Fe8 compared to 18 nm calculated for syntheses Fe16 and 7a.

(a) Fe16   (b) Fe8
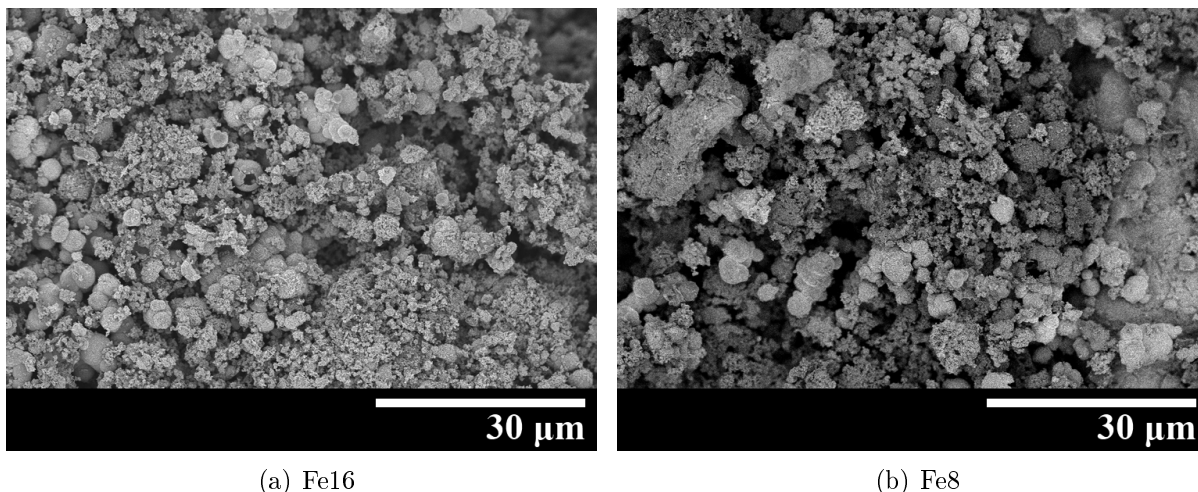
Figure 4.65: SEM images of brown (Ga- and Cu-rich) products produced with varying FeCl$_3$ concentrations: Fe16 (0.020 M) and Fe8 (0.040 M).

4.4 Photoluminescence

Products with dopant addition and product 7a was subject to photoluminescence spectroscopy in order to characterize the electronic structure and particularly IB formation. Different excitation wavelengths, including 410 nm for luminescence from recombinations across the band gap, and 514 nm to investigate luminescence originating within the band gap due to IB formation, was attempted. No luminescence of the powders could be obtained for wavelengths up to 850 nm, either at room temperature or in liquid nitrogen. Photoluminescence relies on radiative recombinations following electron excitations, so non-radiative recombination in the samples is detrimental to the luminescence. The Ga- and Cu-rich off-stoichiometries in the brown precipitates in these products have high defect densities according to Section 2.1, which can make non-radiative recombination through trapping dominant, in which case luminescence is not expected. In this respect, also the stoichiometric deposit in product 6b(s) on a Si substrate as well as a yellow powder obtained from the yellow dispersion obtained in synthesis 6b was analyzed. However, no luminescence could be obtained from these samples, which may indicate too high defect densities also in this yellow precipitate.

The large range of particle sizes in these products, seen in Figures 4.61, 4.57, 4.64 and 4.65 in Section 4.3, extend below the wavelength of 504 nm relating to the CuGaS$_2$ band gap. Thus the particles are expected to scatter the light that is interesting for measurements of the band gap and IB formation. As light is scattered away from the detector in the spectrophotometer, absorption spectroscopy can not distinguish it from absorption in the sample. However, band gap absorption is expected to show a distinct absorption edge relating to the band edges, while scattering is identified as positive absorbance measured for all wavelengths corresponding to energies below the CuGaS$_2$ band gap in the absorbance spectrum of yellow, stoichiometric particles from the dispersion obtained in synthesis 6b, as shown in Figure 4.66(a). Furthermore, the spectra in Figure 4.66 show no band gap absorption edge near 504 nm corresponding to the band gap of CuGaS$_2$, and products with dopant addition, represented by the off-sotichiometric product Fe8 in Fig-

ure 4.66(b), give no distinguishable absorbance peak at longer wavelengths. Absorption within the band gap is however not expected as $CuGaS_2$ is not doped in any products. Films are desirable for PL measurements due to scattering by particles in powders and dispersions, but no luminescence was measured from the Ga-rich film in product 7b(s) depicted in Figure 4.63.

(a)

(b)
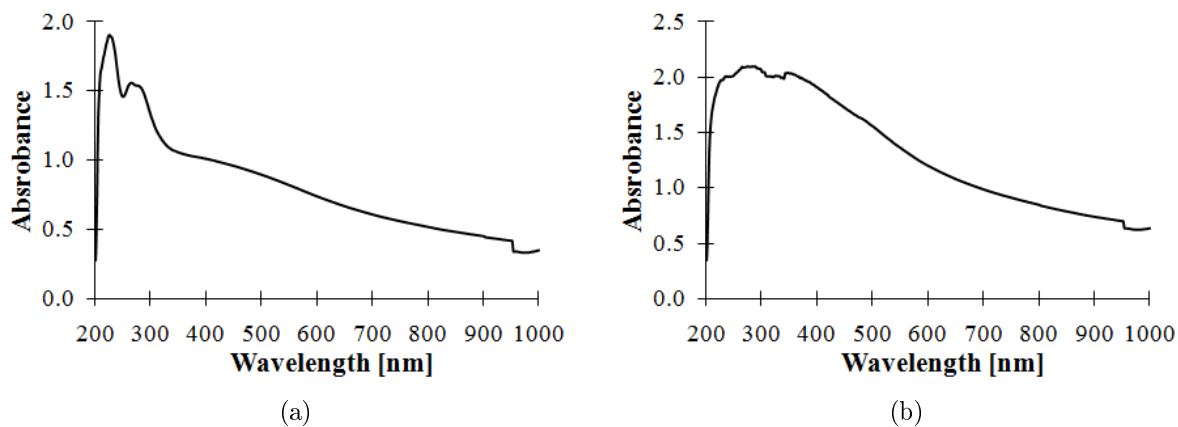
Figure 4.66: Absorbance spectra of yellow (stoichiometric) dispersion from synthesis 6b and product Fe8 with dopant addition.

5 Conclusion

Different hydro- and solvothermal syntheses producing $CuGaS_2$ of high purity from CuCl and $GaCl_3$ have been developed. The most important parameters include pH through HCl addition and reactant concentrations, complexing by 1-pentanethiol, reaction time, temperature and the related saturation pressure for fill factors that retain a gas phase. At low reactant concentrations of 0.030 M CuCl and $GaCl_3$ with four times higher Tu concentration, the synthesis is sensitive to the HCl concentration at an initial pH near 0.5. However, increasing the Tu concentration can provide the necessary acidification to prevent GaO(OH) formation, and this can give high purity products at a lower final pH. H_2S evolution from the acidic reaction solution is a competing reaction to precipitation of sulphides following the slow Tu decomposition.

A secondary phase of digenite is identified as an intermediate product due to its formation in syntheses with short reaction times of 1.75 h without 1-pentanethiol and 12 h with this complexing agent. This phase also appears as a stable impurity at increased heating times, which is supported by stability calculations using Debye-Hückel theory for syntheses without 1-pentanethiol. The high chemical potential of Cu^+ ions in aqueous solutions also gives a CuS impurity. This impurity is formed through oxidation of Cu^+ in the acidic reaction solution. Dissolved oxygen has been excluded as the oxidizing agent.

Addition of a strong complexing agent like 1-pentanethiol stabilizes the Cu^+ and Ga^{3+} cations and reduces CuS and digenite impurities at prolonged reaction times of 30 h, as the rate of incorporation of Ga^{3+} into the digenite intermediate product is reduced. Combined with a temperature of 250 °C, giving increased saturation pressure of water and increased reaction rates, products of high purity are obtained at CuCl and $GaCl_3$ concentrations of 0.060 M and 0.319 M with four times higher Tu concentration. The yields of 80% and 70%, respectively, differ from the trend of increasing yields with increasing reactant concentrations found for syntheses without 1-pentanethiol that is expected as the initial concentrations is removed from the equilibrium condition. Additionally, increasing reactant concentrations give increasing product purity in syntheses without 1-pentanethiol, although stability calculations using Debye-Hückel theory suggest the opposite trend. A hydrothermal synthesis using 0.319 M CuCl and $GaCl_3$ and four times higher Tu concentration produced a high purity product with 93% yield.

This hydrothermal synthesis providing $CuGaS_2$ of high purity was selected for Ni and Fe doping by addition of $NiCl_2$ and $FeCl_3$, respectively. These dopants formed NiS_2 and FeS_2 impurities through oxidation of S^{2-} and reduction of Fe^{3+}. EDS analyses revealed no significant doping of $CuGaS_2$, and thus an IB is not expected to have formed. Additionally, the sensitivity of the hydrothermal synthesis is demonstrated by these syntheses as the CuS and digenite contents are changed with relatively small variations of 0.020 M and 0.040 M dopant precursors. The synthesis is also sensitive to the autoclave volume and geometry as a autoclave with reduced volume of 45 ml significantly reduced the purity compared to the a high purity product obtained in a 125 ml autoclave, and introducing substrate holders for for film growth decrease the purity of powder precipitates.

All precipitates show inhomogeneities regarding $CuGaS_2$ stoichiometry and morphology. This relates to changing reaction conditions as Tu decomposition acidifies the solution during the synthesis, while Cu^+ and Ga^{3+} are consumed at different rates to form Cu-rich and Ga-rich precipitates. Yellow, stoichiometric $CuGaS_2$ have been deposited on

Si substrate from a dispersion obtained in syntheses with high reactant concentrations approaching 0.319 M CuCl and GaCl$_3$, and a Ga-rich film was grown with 1-pentanethiol. Off-stoichiometries and related defects may be the reason why the products showed no photoluminescence. The products were neither suited for absorption spectroscopy due to scattering of a wide range of wavelengths.

Inhomogeneities are also demonstrated by the variety of CuGaS$_2$ crystallite and particle morphologies summarized in Section 4.2.1. Common crystallite shapes of nanoplates, nanopyramids and nanospheres with varying extents of inhomogeneities indicate non-equilibrium growth conditions. Either of these crystallite shapes can form open network structures, roses, rods, spheres and irregular particles, of which spheres can have a core and shell structure or be hollow. The morphology is sensitive to the growth conditions and show large variations within the products, particularly between precipitates of different stoichiometry. However, increasing reactant concentrations tend to give increased abundance of network structures and reduced particle sizes due to increased rates of nucleation.

The quality of the products is not satisfactory for solar cell applications in terms of stoichiometry and the high purity requirements without further processing. Further synthesis development is necessary to obtain doping as well as higher quality products, possibly by further increasing the pressure or explore complexing for film growth. The sensitivity of the hydrothermal synthesis for instance to the autoclave volume also suggests that the syntheses are not representative for large-scale industrial production, and further development is required to reduce the extents of product inhomogeneities and promote the robustness of the hydrothermal synthesis.

References

[1] Ø. S. Sortland. *Wet chemical synthesis of materials for intermediate band solar cells.* Department of Materials Technology, NTNU, Trondheim, 2010. Unpublished work.

[2] A. Martí, C.R. Stanley, and A. Luque. *Intermediate Band Solar Cells (IBSC) Using Nanotechnology* in T. Soga. *Nanostructured Materials for Solar Energy Conversion*, page 540. Elsevier B.V., Amsterdam, 1st edition, 2006. ISBN 978-0-444-52844-5.

[3] A. Martí, D. F. Marrón, and A. Luque. Evaluation of the efficiency potential of intermediate band solar cells based on thin-film chalcopyrite materials. *J. Appl. Phys.*, 103(7):073706/1–073706/6, 2008.

[4] W. Shockley and H. J. Queisser. Detailed balance limit of efficiency of *p-n* junction solar cells. *J. Appl. Phys.*, 32:510–519, 1961.

[5] A. Luque and A. Martí. The intermediate band solar cell: Progress toward the realization of an attractive concept. *Adv. Mater. (Weinheim, Ger.)*, 22(2):160–174, 2010.

[6] C. Tablero and D. Fuertes Marrón. Analysis of the electronic structure of modified $CuGaS_2$ with selected substitutional impurities: Prospects for intermediate-band thin-film solar cells based on Cu-containing chalcopyrites. *J. Phys. Chem. C*, 114 (6):2756–2763, 2010.

[7] C. J. Hibberd, E. Chassaing, W. Liu, D. B. Mitzi, D. Lincot, and A. N. Tiwari. Non-vacuum methods for formation of Cu(In, Ga)(Se, S)$_2$ thin film photovoltaic absorbers. *Prog. Photovolt: Res. Appl.*, 18:434–452, 2009.

[8] J. Hu, B. Deng, C. Wang, K. Tang, and Y. Qian. Hydrothermal preparation of $CuGaS_2$ crystallites with different morphologies. *Solid State Commun.*, 121(9-10): 493–496, 2002.

[9] P. A. Tipler and G. Mosca. *Physics for scientists and engineers*, page 998. W. H. Freeman and Company, New York, 5th edition, 2004. ISBN 0-7167-4389-2.

[10] SUNLab. URL http://sunlab.site.uottawa.ca/research.php?iact= hc&vpx=100&vpy=293&dur=1929&hovh=147&hovw=343&tx=218&ty=66&ei= KkPHTI2eM4iWOomdpP0B&oei=G0PHTPXDOZDrOYazlR8&esq=2&page=2&tbnh= 89&tbnw=207&start=26&ndsp=31&ved=1t:429,r:16,s:26. October 26, 2010.

[11] L. Cuadra, A. Martí, and A. Luque. Influence of the overlap between the absorption coefficients on the efficiency of the intermediate band solar cell. *Electron Devices, IEEE Transactions on*, 51(6):1002–1007, 2004.

[12] A. Luque. The confinement of light in solar cells. *Sol. Energy Mater.*, 23(2-4): 152–163, 1991.

[13] P. Palacios, I. Aguilera, P. Wahnón, and J. C. Conesa. Thermodynamics of the formation of Ti- and Cr-doped $CuGaS_2$ intermediate-band photovoltaic materials. *J. Phys. Chem. C*, 112(25):9525–9529, 2010.

[14] A. Luque, A. Martí, E. Antolín, and C. Tablero. Intermediate bands versus levels in non-radiative recombination. *Phys. B (Amsterdam, Neth.)*, 382(1-2):320–327, 2006.

[15] K.-H. Hellewege, M. Böhm, H. Landolt, and O. Madelung, editors. *Landolt-Börnstein: Numerical Data and Functional Relationships in Science and Technology*, group III, 17h, pages 34,37. Springer-Verlag, Heidelberg, 1985. ISBN 3-540-13507-3.

[16] S. C. Abrahams and J. L. Bernstein. Piezoelectric nonlinear optic $CuGaS_2$ and $CuInS_2$ crystal structure: Sublattice distortion in $A^I B^{III} C_2^{VI}$ and $A^{II} B^{IV} C_2^V$ type chalcopyrites. *J. Chem. Phys.*, 59(10):5415–5422, 1973.

[17] K. Momma and F. Izumi. VESTA: A three-dimensional visualization system for electronic and structural analysis. *J. Appl. Crystallogr.*, 41(3):653–658, 2008.

[18] S. B. Zhang, S.-H. Wei, A. Zunger, and H. Katayama-Yoshida. Defect physics of the $CuInSe_2$ chalcopyrite semiconductor. *Phys. Rev. B: Condens. Matter Mater. Phys.*, 57(16):9642–9656, 1998.

[19] V. Gurin. Nanoparticles of ternary semiconductors in colloids – Low-temperature formation and quantum size effects. *Colloids Surf., A*, 142(1):35–40, 1998.

[20] Y. Zhao, R. L. Frost, J. Yang, and W. N. Martens. Size and Morphology Control of Gallium Oxide Hydroxide GaO(OH), Nano- to Micro-Sized Particles by Soft-Chemistry Route without Surfactant. *J. Phys. Chem. C*, 2008.

[21] C. L. Bailey, L. Liborio, G. Mallia, S. Tomić, and N. M. Harrison. Defect physics of $CuGaS_2$. *Phys. Rev. B: Condens. Matter Mater. Phys.*, 81(20):205214/1–205214/8, 2010.

[22] Webmineral. Covellite Mineral Data. URL `http://webmineral.com/data/Covellite.shtml`. May 22, 2011.

[23] Webmineral. Digenite Mineral Data. URL `http://webmineral.com/data/Digenite.shtml`. May 22, 2011.

[24] G. Sick and K. Schwerdtfeger. A contribution to the Thermodynamics of High-Temperature Digenite $Cu_{2-y}S$. *Metall. Mater. Trans. B*, 15(4):736–739, 1984.

[25] D. J. Chakrabarti and D. E. Laughiln. The Cu-S (Copper-Sulfur) System. *Bull. Alloy Phase Diagrams*, 4(3):254–271, 1983.

[26] R. Wu, Y. F. Zheng, X. G. Zhang, Y. F. Sun, J. B. Xu, and J. K. Jian. Hydrothermal synthesis and crystal structure of pyrite. *J. Cryst. Growth*, 266(4):523–527, 2004.

[27] M. Kokta, J. Carruthers, M. Grasso, H. Kasper, and B Tell. Ternary phase relations in the vicinity of chalcopyrite copper gallium sulfide. *J. Electron. Mater.*, 5(1):69–89, 1976.

[28] M. DiGiuseppe, J. Steger, A. Wold, and E. Kostiner. Preparation and characterization of the system copper gallium iron sulfide ($CuGa_{1-x}Fe_xS_2$). *Inorg. Chem. (Washington, DC, U. S.)*, 13(8):1828–1831, 1974.

[29] J.-M. Raulot, C. Domain, and J.-F. Guillemoles. Fe-doped $CuInSe_2$: An *ab initio* study of magnetic defects in a photovoltaic material. *Phys. Rev. B Condens. Matter Mater. Phys.*, 71(3):035203/1–035203/12, 2005.

[30] H. J. Von Bardeleben, A. Goltzéné, C. Schwab, J. M. Friedt, and R. Poinsot. Stoichiometry of the ternary semiconductor $CuGaS_2$: ^{57}Fe as determined by Mössbauer spectroscopy. *J. Appl. Phys.*, 46(4):1736–1738, 1975.

[31] K. Tanaka, K. Ishii, S. Matsuda, Y. Hasegawa, and K. Sato. Optical characterization of deep levels in single crystals of copper gallium sulfide ($CuGaS_2$) grown by chemical vapor transport. *Jpn. J. Appl. Phys., Part 1*, 28(1):12–15, 1989.

[32] D. F. Shriver, P. W. Atkins, T. L. Overton, J. P. Rourke, M. T. Weller, and F. A. Armstrong. *Shriver & Atkins inorganic chemistry*, pages 174, 460, 466. W. H. Freeman and Company, New York, 4th edition, 2006. ISBN 0-19-926463-5.

[33] U. Kaufmann. Electronic structure of Ni^+ in I_B-III-VI_2 chalcopyrite semiconductors. *Phys. Rev. B: Condens. Matter Mater. Phys.*, 11(7):2478–2484, 1975.

[34] R. I. Walton. Subcritical solvothermal synthesis of condensed inorganic materials. *Chem. Soc. Rev.*, 31:230–238, 2002.

[35] Q. Lu, J. Hu, K. Tang, Y. Qian, G. Zhou, and X. Liu. Synthesis of nanocrystalline $CuMS_2$ (M = In or Ga) through a solvothermal process. *Inorg. Chem. (Washington, DC, U. S.)*, 39(7):1606–1607, 2000.

[36] J. Feng, J. Han, and X. Zhao. Synthesis of $CuInS_2$ quantum dots on TiO_2 porous films by solvothermal method for absorption layer of solar cells. *Prog. Org. Coat.*, 64(2-3):268–273, 2009.

[37] K. Byrappa and M. Yoshimura. *Handbook of hydrothermal technology - A technology for crystal growth and materials processing*, pages 3, 7. Noyes Publications / William Andrew Publishing, LLC, Norwich, NY, 2001. ISBN 978-0-8155-1445-9.

[38] P. M. Rørvik. *Synthesis of nanoparticles*, pages 6–7. Department of Materials Technology, NTNU, Trondheim, 2010. Unpublished work.

[39] B. Das, R. N. Roy, K. S. Pitzer, D. R. Gregory, and S. A. Kiefer. Thermodynamics of the $GaCl_3$-HCl-H_2O System at 25 °C. *J. Solution Chem.*, 29(3):289–297, 2000.

[40] Pastor, A. C. (Hughes Aircraft Co., USA). METHOD FOR PREPARING CUPRIC ION-FREE CUPROUS CHLORIDE. US Patent 4,582,579, April 15, 1986.

[41] C. Eisel and M. W. Tausch. Molecular hydrogen from hydrochloric acid and copper under UV light irradiation. *J. Photochem. Photobiol., A*, 128(1-3):151–154, 1999.

[42] C. Lampe-Önnerud, A. Hårsta, and U. Jansson. CVD of copper using CuCl as precursor. *J. Phys. IV France*, 02(C2):C2/881–C2/888, 1991.

[43] C. H. Hamann, A. Hamnett, and W. Vielstich. *Electrochemistry*, pages 32–33, 48–49, 41, 174–177. Wiley-VCH, Weinheim, 2nd edition, 2007. ISBN 978-3-527-31069-2.

[44] G. Aylward and T. Findlay. *SI Chemical Data*. John Wiley & Sons Australia, Ltd, Milton, 5th edition, 2002. ISBN 0-470-80044-5.

[45] M. Uematsu and E. U. Franck. Static Dielectric Constant of Water and Steam. *J. Phys. Chem. Ref. Data*, 9(4):1292–1306, 1980.

[46] K. Das, S. K. Panda, S. Gorai, P. Mishra, and S. Chaudhuri. Effect of Cu/In molar ratio on the microstructural and optical properties of microcrystalline $CuInS_2$ prepared by solvothermal route. *Mater. Res. Bull.*, 43(10):2742–2750, 2008.

[47] G. Hodes. *Mechanisms of Chemical Deposition* in *Chemical Solution Deposition Of Semiconductor Films*, chapter 3, pages 2–5, 32, 43–44. Marcel Dekker, Inc., New York, 2002. ISBN 978-0-203-90909-6.

[48] S. Gorai, D. Ganguli, and S. Chaudhuri. Synthesis of copper sulfides of varying morphologies and stoichiometries controlled by chelating and nonchelating solvents in a solvothermal process. *Cryst. Growth Des.*, 5(3):875–877, 2005.

[49] W. H. R. Shaw and D. G. Walker. The decomposition of thiourea in water solutions. *J. Am. Chem. Soc.*, 78:5769–72, 1956.

[50] Y. Jiang, Y. Wu, X. Mo, W. Yu, Y. Xie, and Y. Qian. Elemental solvothermal reaction to produce ternary semiconductor $CuInE_2$ (E = S, Se) nanorods. *Inorg. Chem. (Washington, DC, U. S.)*, 39(14):2964–2965, 2000.

[51] W. A. Tiller. *The science of crystallization: microscopic interfacial phenomena*, pages 338–339. Cambridge University Press, New York, 1991. ISBN 0-521-38827-9.

[52] J. Livage and D. Roux. *Specific Features of Nanoscale Growth* in C. Bréchignac, P. Houdy, M. Lahmani. *Nanomaterials and Nanochemistry*, pages 388–389, 392–393. Springer-Verlag Berlin Heidelberg, New York, 2007. ISBN 978-3-540-72992.

[53] G. Cao. *Nanostructures and Nanomaterials - Synthesis, Properties and Applications*, pages 24, 55–58. World Scientific, London, 2004. ISBN 978-1-86094-415-4.

[54] P. Becker, P. Seyfried, and H. Sigert. The Lattice Parameter of Highly Pure Silicon Single Crystals. *Z. Phys. B*, 48(1):17–21, 1982.

[55] V. T Livieri. *Controlled Synthesis of Nanoparticles in Microheterogeneous Systems*, pages 81–83. Springer US, Boston, MA, 2006. ISBN 978-0-387-26429-5.

[56] B. Li, Y. Xie, J. Huang, and Y. Qian. Synthesis by a solvothermal route and characterization of $CuInSe_2$ nanowhiskers and nanoparticles. *Adv. Mater. (Weinheim, Ger.)*, 11(17):1456–1459, 1999.

[57] Encyclopædia Britannica Online. Chelate. URL `http://search.eb.com/eb/article-9022756`. September 11, 2010.

[58] C.-H. Chang and J.-M. Ting. Phase, morphology, and dimension control of CIS powders prepared using a solvothermal process. *Thin Solid Films*, 517(14):4174–4178, 2009.

[59] W. Kurz and D. J. Fisher. *Fundamentals of solidification*, pages 34–37. Trans Tech Publications Inc, Totton, UK, 4th edition, 1998. ISBN 0-87849-804-4.

[60] C. Henry. *Size Effect on Structure and Morphology of Free or Supported Nanoparticles* in C. Bréchignac, P. Houdy, M. Lahmani. *Nanomaterials and Nanochemistry*, pages 8–9. Springer-Verlag Berlin Heidelberg, New York, 2007. ISBN 978-3-540-72992.

[61] N. N. Greenwood and A. Earnshaw. *Chemistry of the elements*. Pergamon Press, Oxford, 2nd edition, 1988. ISBN 0-7506-3365-4.

[62] L. M. Laglera and C. M. G. van den Berg. Copper complexation by thiol compounds in estuarine waters. *Mar. Chem.*, 82(1-2):71–89, 2003.

[63] I. M. Klotz, G. H. Czerlinski, and H. A. Fiess. A Mixed-valence Copper Complex with Thiol Compounds. *J. Am. Chem. Soc.*, 80(12):2920–2923, 1958.

[64] R. Noufi, R. Axton, C. Herrington, and S. K. Deb. Electronic properties versus composition of thin films of $CuInSe_2$. *Appl. Phys. Lett.*, 45(6):668–670, 1984.

[65] C.-H. Lee, C.-H. Wu, and C.-H. Lu. Microwave-assisted solvothermal synthesis of copper indium diselenide powders. *J. Am. Ceram. Soc.*, 93(7):1879–1883, 2010.

[66] Y.-H. Yang and Y.-T. Chen. Solvothermal preparation and spectroscopic characterization of copper indium diselenide nanorods. *J. Phys. Chem. B*, 110(35):17370–17374, 2006.

[67] S. Peng, F. Cheng, J. Liang, Z. Tao, and J. Chen. Facile solution-controlled growth of $CuInS_2$ thin films on FTO and TiO_2/FTO glass substrates for photovoltaic application. *J. Alloys Compd.*, 481(1-2):786–791, 2009.

[68] T. P. Chusova, L. N. Zelenina, Y. G. Stenin, Z. I. Semenova, and V. A. Titov. Thermodynamics of vaporization of gallium trichloride. *Russ. Chem. Bull.*, 56(7):1313–1317, 2007.

[69] Product No. 651745: Copper(I) chloride, Sigma-Aldrich Norway AS: Oslo, Norway, January 02, 2009.

[70] Parr Instrument Company. General Purpose Acid Digestion Bombs. URL `http://www.parrinst.com/default.cfm?Page_ID=209`. October 4, 2010.

[71] J. Hjelen. *Scanning elektron-mikroskopi*, pages 39–41,47,77. Metallurgisk institutt, NTH, Trondheim, 1989. Unpublished work.

[72] The Engineering ToolBox. Water - Thermal Properties. URL `http://www.engineeringtoolbox.com/water-thermal-properties-d_162.html`. December 3, 2010.

[73] Eduard Job Foundation for Thermo- and Matterdynamics. Table of chemical potentials. URL `http://www.job-stiftung.de/index.php?id=54,0,0,1,0,0`. June 19, 2011.

[74] Encyclopædia Britannica Online. Colour. URL `http://www.britannica.com/EBchecked/topic/126658/colour/21838/The-visible-spectrum`. June 2, 2011.

[75] F. Li, W. Bi, T. Kong, and Q. Qin. Large-scale synthesis of CuS hexaplates in mixed solvents using a solvothermal method. *Mater. Lett.*, 64(2):111–114, 2010.

[76] T. Thongtem, C. Pilapong, and S. Thongtem. Optical, photocatalytic properties of novel CuS nanoplate-based architectures synthesised by a solvothermal route. *Cryst. Res. Technol.*, 44(7):729–735, 2009.

[77] Product No. 450898: Gallium(III) chloride, Sigma-Aldrich Norway AS: Oslo, Norway, August 21, 2009.

[78] Product No. T8656: Thiourea, Sigma-Aldrich Norway AS: Oslo, Norway, October 15, 2010.

[79] Webmineral. Gallite Mineral Data. URL `http://webmineral.com/data/Gallite.shtml`. June 22, 2011.

[80] Webmineral. Tungsgallite Mineral Data. URL `http://webmineral.com/data/Tsumgallite.shtml`. June 22, 2011.

[81] Webmineral. Pyrite Mineral Data. URL `http://webmineral.com/data/Pyrite.shtml`. June 22, 2011.

[82] Webmineral. Vaesite Mineral Data. URL `http://webmineral.com/data/Vaesite.shtml`. June 22, 2011.

[83] J. G. Speight. *Lange's Handbook of Chemistry*, page 1.259. McGraw-Hill, New York, 16th edition, 2005. ISBN 0-07-143220-5.

A   Appendix

A.1   Calculation of Yields

The worksheet in Table A.1 show the formulas and molar masses used to calculate the yields of the different phases in the products. The digenite composition is assumed to be $Cu_{1.8}S$ in all products. Due to the length of the formulas, the spreadsheet is broken between column F and G into two subtables, of which the latter is the continuation of the rows in the upper table. The cells for input values are marked in Table A.1, and they are also emphasized in Table A.2. The input molar fractions are taken from the Topas calculations on the diffractograms. The ions represent precursors that do not precipitate, but remain in solution or form a gas like H_2S. The yield of a compound is the ratio of its amount to the amount of the limiting precursor for the elements in the compound, and such calculations are conducted for all compounds, not only $CuGaS_2$. Table A.2 shows the calculations for undoped products of which the composition could be calculated from the diffractogram in the Topas software, including product 4a[1] from Sortland [1]. The worksheet in Table A.1 is extended to include $FeCl_3$ and $NiCl_2$ precursors, FeS_2 and NiS_2 impurities and the remaining Fe or Ni ions available for doping of $CuGaS_2$ are shown in the columns labeled $Fe_{Ga/Cu}$ and $Ni_{Ga/Cu}$ in Table A.3. Since the atomic weights of Ga, Cu, Fe and Ni atoms are similar and the doping concentrations are limited to maximum $\frac{1}{8}$ and $\frac{1}{16}$, the molar mass of $CuGaS_2$ is assumed unchanged for products with dopant addition.

I

Table A.1: Formulas used in an Microsoft® Office Excel spreadsheet for calculating yields of syntheses (adapted with modifications from Sortland [1]).

	A	B	C	D	E	F
1		CuCl	$GaCl_3$	Thiourea	$CuGaS_2$	CuS
2	Molar mass [g/mol]	99	176.08	76.12	197.4	95.61
3	Reference	[69]	[77]	[78]	[79]	[22]
4						
5	**Product**	CuCl	$GaCl_3$	Thiourea	Product	$CuGaS_2$
6	Yield					=F9/MIN(B9;C9;D9/2)
7	Molar fraction					*Input*
8	Mass [g]	*Input*	*Input*	*Input*	*Input*	=F9*E2
9	Amount of substance [mol]	=B8/B2	=C8/C2	=D8/D2	=E8/(F7*E2+G7*F2+H7*G2+I7*H2)	=E9*F7

	G	H	I	J	K	L
1	$Cu_{1.8}S$	GaO(OH)	FeS_2	NiS_2		
2	146.45	100.05	119.98	122.82		
3	[23]	[80]	[81]	[82]		
4						
5	CuS	$Cu_{2-\delta}S$	GaO(OH)	Cu^+	Ga^{3+}	S^{2-}
6	=G9/MIN(B9;D9)	=H9/MIN(B9/9;D9/5)	=I9/C9	=J9/B9	=K9/C9	=L9/D9
7	*Input*	*Input*	*Input*	*Input*		
8	=G9*F2	=H9*G2	=I9*H2			
9	=E9*G7	=E9*H7	=E9*I7	=B9-(F9+G9+H9*1.8)	=C9-(F9+I9)	=D9-(F9*2+G9+H9*1.8)

Table A.2: Microsoft® Office Excel spreadsheet for calculation of yields of syntheses without dopants.

4a[1]	CuCl	GaCl$_3$	Thiourea	Product	CuGaS$_2$	CuS	Cu$_{2-\delta}$S	GaO(OH)	Cu$^+$	Ga^{3+}	S^{2-}
Yield					68.13 %	11.86 %	0.00 %	0.00 %	20.16 %	31.87 %	62.98 %
Molar fraction					85.14 %	14.86 %	0.00 %	0.00 %			
Mass [g]	0.2975	0.5279	0.9133	0.4373	0.4032	0.0341	0.0000	0.0000			
Amount of substance [mol]	0.0030	0.0030	0.0120	0.0024	0.0020	0.0004	0.0000	0.0000	0.0006	0.0010	0.0076

1a	CuCl	GaCl$_3$	Thiourea	Product	CuGaS$_2$	CuS	Cu$_{2-\delta}$S	GaO(OH)	Cu$^+$	Ga^{3+}	S^{2-}
Yield					67.34 %	8.92 %	4.05 %	0.00 %	19.78 %	32.66 %	63.50 %
Molar fraction					85.76 %	11.37 %	2.87 %	0.00 %			
Mass [g]	0.2976	0.5286	0.9133	0.4346	0.3991	0.0256	0.0099	0.0000			
Amount of substance [mol]	0.0030	0.0030	0.0120	0.0024	0.0020	0.0003	0.0001	0.0000	0.0006	0.0010	0.0076

1b	CuCl	GaCl$_3$	Thiourea	Product	CuGaS$_2$	CuS	Cu$_{2-\delta}$S	GaO(OH)	Cu$^+$	Ga^{3+}	S^{2-}
Yield					58.59 %	9.33 %	3.59 %	0.00 %	28.50 %	41.52 %	67.91 %
Molar fraction					83.81 %	13.34 %	2.85 %	0.00 %			
Mass [g]	0.2967	0.5287	0.9135	0.3821	0.3466	0.0267	0.0087	0.0000			
Amount of substance [mol]	0.0030	0.0030	0.0120	0.0021	0.0018	0.0003	0.0001	0.0000	0.0009	0.0012	0.0081

2a	CuCl	GaCl$_3$	Thiourea	Product	CuGaS$_2$	CuS	Cu$_{2-\delta}$S	GaO(OH)	Cu$^+$	Ga^{3+}	S^{2-}
Yield					81.51 %	11.07 %	4.22 %	0.00 %	3.20 %	28.48 %	55.90 %
Molar fraction					85.87 %	11.66 %	2.47 %	0.00 %			
Mass [g]	1.2077	2.4480	3.7153	2.1339	1.9629	0.1291	0.0419	0.0000			
Amount of substance [mol]	0.0122	0.0139	0.0488	0.0116	0.0099	0.0014	0.0003	0.0000	0.0004	0.0040	0.0273

2b	CuCl	GaCl$_3$	Thiourea	Product	CuGaS$_2$	CuS	Cu$_{2-\delta}$S	GaO(OH)	Cu$^+$	Ga^{3+}	S^{2-}
Yield					82.23 %	7.81 %	7.21 %	0.00 %	2.78 %	17.77 %	55.94 %
Molar fraction					87.43 %	8.31 %	4.26 %	0.00 %			
Mass [g]	3.3565	5.9677	10.3203	5.9532	5.5011	0.2532	0.1989	0.0000			
Amount of substance [mol]	0.0339	0.0339	0.1356	0.0319	0.0279	0.0026	0.0014	0.0000	0.0009	0.0060	0.0758

Table A.2: Microsoft® Office Excel spreadsheet for calculation of yields of syntheses without dopants (continued).

2c	CuCl	GaCl$_3$	Thiourea	Product	CuGaS$_2$	CuS	Cu$_{2-\delta}$S	GaO(OH)	Cu$^+$	Ga^{3+}	S^{2-}
Yield					45.84 %	12.06 %	0.00 %	0.00 %	42.10 %	54.19 %	74.06 %
Molar fraction					79.17 %	20.83 %	0.00 %	0.00 %			
Mass [g]	0.3156	0.5616	0.9705	0.3252	0.2884	0.0368	0.0000	0.0000			
Amount of substance [mol]	0.0032	0.0032	0.0127	0.0018	0.0015	0.0004	0.0000	0.0000	0.0013	0.0017	0.0094

3a	CuCl	GaCl$_3$	Thiourea	Product	CuGaS$_2$	CuS	Cu$_{2-\delta}$S	GaO(OH)	Cu$^+$	Ga^{3+}	S^{2-}
Yield					42.10 %	12.66 %	0.00 %	0.00 %	45.38 %	57.90 %	75.78 %
Molar fraction					76.83 %	23.17 %	0.00 %	0.00 %			
Mass [g]	0.2978	0.5280	0.9131	0.2856	0.2492	0.0364	0.0000	0.0000			
Amount of substance [mol]	0.0030	0.0030	0.0120	0.0016	0.0013	0.0004	0.0000	0.0000	0.0014	0.0017	0.0091

3b	CuCl	GaCl$_3$	Thiourea	Product	CuGaS$_2$	CuS	Cu$_{2-\delta}$S	GaO(OH)	Cu$^+$	Ga^{3+}	S^{2-}
Yield					19.65 %	1.71 %	24.81 %	0.00 %	53.90 %	80.35 %	86.30 %
Molar fraction					55.83 %	4.88 %	39.29 %	0.00 %			
Mass [g]	0.2976	0.5276	0.9129	0.1818	0.1162	0.0049	0.0607	0.0000			
Amount of substance [mol]	0.0030	0.0030	0.0120	0.0011	0.0006	0.0001	0.0004	0.0000	0.0016	0.0024	0.0103

3c	CuCl	GaCl$_3$	Thiourea	Product	CuGaS$_2$	CuS	Cu$_{2-\delta}$S	GaO(OH)	Cu$^+$	Ga^{3+}	S^{2-}
Yield					93.94 %	5.11 %	5.10 %	0.00 %	-4.10 %	6.06 %	51.04 %
Molar fraction					92.20 %	5.02 %	2.78 %	0.00 %			
Mass [g]	2.1792	3.8739	6.6986	4.2786	4.0798	0.1076	0.0913	0.0000			
Amount of substance [mol]	0.0220	0.0220	0.0880	0.0224	0.0207	0.0011	0.0006	0.0000	-0.0009	0.0013	0.0449

4a	CuCl	GaCl$_3$	Thiourea	Product	CuGaS$_2$	CuS	Cu$_{2-\delta}$S	GaO(OH)	Cu$^+$	Ga^{3+}	S^{2-}
Yield					58.86 %	0.94 %	8.09 %	0.00 %	32.11 %	41.20 %	69.22 %
Molar fraction					91.55 %	1.46 %	6.99 %	0.00 %			
Mass [g]	0.2969	0.5286	0.9135	0.3709	0.3485	0.0027	0.0197	0.0000			
Amount of substance [mol]	0.0030	0.0030	0.0120	0.0019	0.0018	0.0000	0.0001	0.0000	0.0010	0.0012	0.0083

Table A.2: Microsoft® Office Excel spreadsheet for calculation of yields of syntheses without dopants (continued).

4b	CuCl	GaCl$_3$	Thiourea	Product	CuGaS$_2$	CuS	Cu$_{2-\delta}$S	GaO(OH)	Cu$^+$	Ga^{3+}	S^{2-}
Yield					79.42 %	2.72 %	0.00 %	0.00 %	17.86 %	20.63 %	59.67 %
Molar fraction					96.69 %	3.31 %	0.00 %	0.00 %			
Mass [g]	0.2596	0.4620	0.7995	0.4179	0.4111	0.0068	0.0000	0.0000	0.0005	0.0005	
Amount of substance [mol]	0.0026	0.0026	0.0105	0.0022	0.0021	0.0001	0.0000	0.0000	0.0005	0.0005	0.0063

4c	CuCl	GaCl$_3$	Thiourea	Product	CuGaS$_2$	CuS	Cu$_{2-\delta}$S	GaO(OH)	Cu$^+$	Ga^{3+}	S^{2-}
Yield					67.14 %	12.41 %	25.74 %	21.04 %	29.70 %	46.50 %	5.70 %
Molar fraction					40.69 %	15.04 %	17.89 %	26.38 %			
Mass [g]	0.2966	0.5287	0.2210	0.3528	0.1924	0.0344	0.0628	0.0632	0.0009	0.0014	
Amount of substance [mol]	0.0030	0.0030	0.0029	0.0024	0.0010	0.0004	0.0004	0.0006	0.0009	0.0014	0.0002

5a	CuCl	GaCl$_3$	Thiourea	Product	CuGaS$_2$	CuS	Cu$_{2-\delta}$S	GaO(OH)	Cu$^+$	Ga^{3+}	S^{2-}
Yield					75.06 %	0.00 %	6.19 %	0.00 %	18.86 %	24.94 %	61.56 %
Molar fraction					95.61 %	0.00 %	4.39 %	0.00 %			
Mass [g]	0.2606	0.4628	0.7992	0.4027	0.3894	0.0000	0.0133	0.0000	0.0005	0.0007	
Amount of substance [mol]	0.0026	0.0026	0.0105	0.0021	0.0020	0.0000	0.0001	0.0000	0.0005	0.0007	0.0065

5b	CuCl	GaCl$_3$	Thiourea	Product	CuGaS$_2$	CuS	Cu$_{2-\delta}$S	GaO(OH)	Cu$^+$	Ga^{3+}	S^{2-}
Yield					49.06 %	0.00 %	21.14 %	1.82 %	30.00 %	49.12 %	72.54 %
Molar fraction					78.27 %	0.00 %	18.82 %	2.91 %			
Mass [g]	0.2045	0.3622	0.6267	0.2385	0.1992	0.0000	0.0355	0.0038	0.0006	0.0010	
Amount of substance [mol]	0.0021	0.0021	0.0082	0.0013	0.0010	0.0000	0.0002	0.0000	0.0006	0.0010	0.0060

5c	CuCl	GaCl$_3$	Thiourea	Product	CuGaS$_2$	CuS	Cu$_{2-\delta}$S	GaO(OH)	Cu$^+$	Ga^{3+}	S^{2-}
Yield					64.87 %	0.00 %	10.34 %	2.24 %	25.01 %	32.89 %	66.14 %
Molar fraction					89.02 %	0.00 %	7.91 %	3.07 %			
Mass [g]	0.2607	0.4621	0.7995	0.3641	0.3361	0.0000	0.0222	0.0059	0.0007	0.0009	
Amount of substance [mol]	0.0026	0.0026	0.0105	0.0019	0.0017	0.0000	0.0002	0.0001	0.0007	0.0009	0.0069

Table A.2: Microsoft® Office Excel spreadsheet for calculation of yields of syntheses without dopants (continued).

6a	CuCl	GaCl$_3$	Thiourea	Product	CuGaS$_2$	CuS	Cu$_{2-\delta}$S	GaO(OH)	Cu$^+$	Ga^{3+}	S^{2-}
Yield					53.92 %	0.00 %	18.80 %	0.00 %	27.43 %	46.08 %	70.41 %
Molar fraction					83.73 %	0.00 %	16.27 %	0.00 %			
Mass [g]	0.2609	0.4627	0.7998	0.3200	0.2797	0.0000	0.0403	0.0000	0.0007	0.0012	0.0074
Amount of substance [mol]	0.0026	0.0026	0.0105	0.0017	0.0014	0.0000	0.0003	0.0000			

6b	CuCl	GaCl$_3$	Thiourea	Product	CuGaS$_2$	CuS	Cu$_{2-\delta}$S	GaO(OH)	Cu$^+$	Ga^{3+}	S^{2-}
Yield					60.58 %	2.72 %	19.58 %	0.00 %	17.12 %	39.42 %	66.31 %
Molar fraction					81.66 %	3.67 %	14.66 %	0.00 %			
Mass [g]	2.4629	4.3809	7.5759	3.4362	2.9752	0.0648	0.3963	0.0000	0.0043	0.0098	0.0660
Amount of substance [mol]	0.0249	0.0249	0.0995	0.0185	0.0151	0.0007	0.0027	0.0000			

6c	CuCl	GaCl$_3$	Thiourea	Product	CuGaS$_2$	CuS	Cu$_{2-\delta}$S	GaO(OH)	Cu$^+$	Ga^{3+}	S^{2-}
Yield					80.24 %	0.00 %	0.00 %	0.00 %	19.76 %	19.81 %	59.88 %
Molar fraction					100.00 %	0.00 %	0.00 %	0.00 %			
Mass [g]	0.5198	0.9250	1.5986	0.8316	0.8316	0.0000	0.0000	0.0000	0.0010	0.0010	0.0126
Amount of substance [mol]	0.0053	0.0053	0.0210	0.0042	0.0042	0.0000	0.0000	0.0000			

7a	CuCl	GaCl$_3$	Thiourea	Product	CuGaS$_2$	CuS	Cu$_{2-\delta}$S	GaO(OH)	Cu$^+$	Ga^{3+}	S^{2-}
Yield					92.54 %	0.00 %	2.40 %	0.00 %	5.08 %	7.46 %	53.40 %
Molar fraction					98.58 %	0.00 %	1.42 %	0.00 %			
Mass [g]	1.5479	2.7524	4.7597	2.8860	2.8555	0.0000	0.0305	0.0000	0.0008	0.0012	0.0334
Amount of substance [mol]	0.0156	0.0156	0.0625	0.0147	0.0145	0.0000	0.0002	0.0000			

7b	CuCl	GaCl$_3$	Thiourea	Product	CuGaS$_2$	CuS	Cu$_{2-\delta}$S	GaO(OH)	Cu$^+$	Ga^{3+}	S^{2-}
Yield					69.43 %	0.00 %	4.21 %	0.00 %	26.36 %	30.58 %	64.70 %
Molar fraction					96.74 %	0.00 %	3.26 %	0.00 %			
Mass [g]	1.5476	2.7528	4.7598	2.1959	2.1423	0.0000	0.0536	0.0000	0.0041	0.0048	0.0405
Amount of substance [mol]	0.0156	0.0156	0.0625	0.0112	0.0109	0.0000	0.0004	0.0000			

Table A.2: Microsoft® Office Excel spreadsheet for calculation of yields of syntheses without dopants (continued).

7c	CuCl	GaCl$_3$	Thiourea	Product	CuGaS$_2$	CuS	Cu$_{2-\delta}$S	GaO(OH)	Cu$^+$	Ga^{3+}	S^{2-}
Yield					73.39 %	0.00 %	7.02 %	1.93 %	19.82 %	24.68 %	62.35 %
Molar fraction					92.62 %	0.00 %	4.94 %	2.44 %			
Mass [g]	0.1907	0.3381	0.5850	0.2929	0.2782	0.0000	0.0110	0.0037			
Amount of substance [mol]	0.0019	0.0019	0.0077	0.0015	0.0014	0.0000	0.0001	0.0000	0.0004	0.0005	0.0048

Table A.3: Microsoft® Office Excel spreadsheet for calculation of yields of syntheses with dopants.

Ni8	CuCl	GaCl$_3$	Thiourea	NiCl$_2$	Product	CuGaS$_2$	CuS	Cu$_{2-\delta}$S	NiS$_2$	Ni$_{Ga/Cu}$	Cu$^+$	Ga^{3+}	S^{2-}
Yield						99.76 %	0.00 %	0.00 %	37.43 %	62.57 %	0.29 %	0.24 %	47.78 %
Molar fraction						95.52 %	0.00 %	0.00 %	4.48 %				
Mass [g]	1.6432	2.9212	5.0509		3.3624	3.2671			0.0953				
Amount of substance [mol]	0.0166	0.0166	0.0664	0.0021	0.0173	0.0166	0.0000	0.0000	0.0008	0.0013	0.0000	0.0000	0.0317

Ni16	CuCl	GaCl$_3$	Thiourea	NiCl$_2$	Product	CuGaS$_2$	CuS	Cu$_{2-\delta}$S	NiS$_2$	Ni$_{Ga/Cu}$	Cu$^+$	Ga^{3+}	S^{2-}
Yield						98.80 %	0.00 %	6.53 %	0.00 %	100.00 %	-5.33 %	1.21 %	49.68 %
Molar fraction						96.46 %	0.00 %	3.54 %	0.00 %				
Mass [g]	1.6425	2.9216	5.0506		3.3239	3.2358		0.0881	0.0000				
Amount of substance [mol]	0.0166	0.0166	0.0664	0.0010	0.0170	0.0164	0.0000	0.0006	0.0000	0.0010	-0.0009	0.0002	0.0330

Fe8	CuCl	GaCl$_3$	Thiourea	FeCl$_3$	Product	CuGaS$_2$	CuS	Cu$_{2-\delta}$S	FeS$_2$	Fe$_{Ga/Cu}$	Cu$^+$	Ga^{3+}	S^{2-}
Yield						91.86 %	0.00 %	18.57 %	35.38 %	64.62 %	-10.43 %	8.17 %	49.28 %
Molar fraction						86.17 %	0.00 %	9.68 %	4.15 %				
Mass [g]	1.6420	2.9214	5.0504		3.3462	3.0075		0.2506	0.0901				
Amount of substance [mol]	0.0166	0.0166	0.0663	0.0021	0.0177	0.0152	0.0000	0.0017	0.0007	0.0013	-0.0017	0.0014	0.0327

Fe16	CuCl	GaCl$_3$	Thiourea	FeCl$_3$	Product	CuGaS$_2$	CuS	Cu$_{2-\delta}$S	FeS$_2$	Fe$_{Ga/Cu}$	Cu$^+$	Ga^{3+}	S^{2-}
Yield						93.46 %	7.76 %	0.00 %	105.69 %	-5.69 %	-1.22 %	6.57 %	48.03 %
Molar fraction						86.69 %	7.20 %	0.00 %	6.11 %				
Mass [g]	1.6421	2.9216	5.0501		3.3144	3.0602	0.1231	0.0000	0.1342				
Amount of substance [mol]	0.0166	0.0166	0.0663	0.0010	0.0179	0.0155	0.0013	0.0000	0.0011	-0.0001	-0.0002	0.0011	0.0319

A.2   Debye-Hückel Calculations

Debye-Hückel theory presented in Section 2.4.1 is used to calculate the Cu, Ga, Ni and Fe chemical potentials (μ) in the reaction solution from initial conditions of syntheses with different reactant concentrations and temperatures (T). Parameters and formulas used in the Microsoft® Office Excel spreadsheet are presented in Table A.4 and the calculations for syntheses with and without dopants are presented in Table A.5. Due to the length of the formulas, the spreadsheet is broken between column D and E into two subtables, of which the latter is the continuation of the rows in the upper table. The relative permittivity of water (ε_r) at 180 °C is approximated by the value for 175 °C and 10 bar reported by Uematsu and Franck [45], which is the saturation pressure of water at 180 °C [72], and at 250 °C the value for the saturation pressure of approximately 50 bar is used. Due to the pressure increase during heating, using the molar heat capacity at constant pressure (c_p) is also an approximation. Water expands by 13% upon heating from room temperature to 180 °C as expressed by Water expansion in Table A.4, which result in a dilution of the concentrations (C) used as input from Table 3.1 in Section 3.1. The S^{2-} concentration is set to zero since it is limited by sulphide precipitation, H_2S evolution and the slow and possibly incomplete Tu decomposition, so that is assumed not to contribute to the ionic strength (I). The remaining parameters in Table A.4 are the elementary charge (e), the vacuum permittivity (ε_0), the Boltzmann constant (k_B), the Avogadro constant (N_A), activity coefficient (γ), standard free energy of formation ($\Delta_f G^0$) and the charge number (z) of ions. The chemical potential of S^{2-} for syntheses Ni8, Ni16, Fe8 and Fe16 in Table A.5 represent the limit for NiS_2 or FeS_2 precipitation used to construct Figure 4.24, and is not intended as an estimate for the chemical potential of S^{2-} ions in the solution as this depends on Tu decomposition, precipitation of different sulphides and H_2S formation. Equilibrium is assumed for the redox reactions necessary to from NiS_2 or FeS_2 from S^{2-} and Ni^{2+} or Fe^{3+} ions so that the chemical potentials in syntheses with dopant addition can be compared to the free energy of formation of NiS_2 or FeS_2 in stability diagrams. The calculations of this limiting S^{2-} chemical potential along with the chemical potential of dopants in solution in Table A.4 is excluded for calculations on syntheses without dopant addition in Table A.5.

Table A.4: Formulas used in an Microsoft® Office Excel spreadsheet for Debye-Hückel calculations.

	A	B	C	D
1	Parameter	Value		Reference
2	e [C]	=1.602*10^(-19)		[44]
3	k_B [J/K]	=1.381*10^(-23)		[44]
4	N_A [mol^{-1}]	=6.022*10^23		[44]
5	ε_0 [C^{2}s^{2}kg^{-1}m^{-3}]	=8.854*10^(-12)		[44]
6	T [K]	=180+273.15	=250+273.15	
7	ε_r (175° C, 10 bar)	39	27	[45]
8	Water expansion	1.13	1.25	[72]
9				
10	Compound	$\Delta_f G^0$ [J/mol]	c_p [J/(molK)]	Reference
11	Cu$^+$	50000	-40.58	[73]
12	Ga^{3+}	-159000	330.54	[44]
13	Ni^{2+}	-45610	128.87	[73]
14	Fe^{3+}	-4600	315.89	[73]
15	NiS$_2$	-717230	82.45	[83]
16	FeS$_2$	-166940	-52.93	[73]
17				
18	**Synthesis**		I [M]	=0.5*(B20^2*C20+B21^2*C21+B22^2*C22+B23^2*C23+B24^2*C24+B25^2*C25)
19	Compound	z	C [M]	ln(γ)
20	Cu$^+$	1	=Input/C8	=-1*B20^2*B2^3*B4^(1/2)*(D18*1000/2)^(1/2)/(4*PI()*(C7*B5*B3*C6)^(3/2))
21	Ga^{3+}	3	=Input/C8	=-1*B21^2*B2^3*B4^(1/2)*(D18*1000/2)^(1/2)/(4*PI()*(C7*B5*B3*C6)^(3/2))
22	Ni^{2+}	2	=Input/C8	=-1*B22^2*B2^3*B4^(1/2)*(D18*1000/2)^(1/2)/(4*PI()*(C7*B5*B3*C6)^(3/2))
23	S^{2-}	-2	0	
24	H$^+$	1	=Input/C8	
25	Cl$^-$	-1	=C20+3*C21+C24	

Table A.4: Formulas used in an Microsoft® Office Excel spreadsheet for Debye-Hückel calculations (continues).

	E	F
	μ [J/mol]	μ [eV]
19		
20	=(B11+C11*(C6-298.15))+B3*B4*C6*(D20+LN(C20))	=E20/B2/B4
21	=(B12+C12*(C6-298.15))+B3*B4*C6*(D21+LN(C21))	=E21/B2/B4
22	=(B13+C13*(C6-298.15))+B3*B4*C6*(D22+LN(C22))	=E22/B2/B4
23	=(B15+C15*(C6-298.15))-E22)/2	=E23/B2/B4

Table A.5: Microsoft® Office Excel spreadsheet for Debye-Hückel calculations of syntheses with different reactant concentrations.

4a[1]		I [M]	0.466		
Compund	z	C [M]	$\ln(\gamma)$	μ [J/mol]	μ [eV]
Cu^+	1	0.027	-1.22	25445	0.26
Ga^{3+}	3	0.027	-10.98	-162812	-1.69
S^{2-}	-2	0.000			
H^+	1	0.280			
Cl^-	-1	0.386			

2a		I [M]	1.036		
Compund	z	C [M]	$\ln(\gamma)$	μ [J/mol]	μ [eV]
Cu^+	1	0.108	-1.82	28467	0.30
Ga^{3+}	3	0.108	-16.37	-177840	-1.84
S^{2-}	-2	0.000			
H^+	1	0.280			
Cl^-	-1	0.712			

3c		I [M]	1.643		
Compund	z	C [M]	$\ln(\gamma)$	μ [J/mol]	μ [eV]
Cu^+	1	0.195	-2.29	28911	0.30
Ga^{3+}	3	0.195	-20.62	-191625	-1.99
S^{2-}	-2	0.000			
H^+	1	0.280			
Cl^-	-1	1.059			

2b		I [M]	2.256		
Compund	z	C [M]	$\ln(\gamma)$	μ [J/mol]	μ [eV]
Cu^+	1	0.282	-2.68	28828	0.30
Ga^{3+}	3	0.282	-24.16	-203574	-2.11
S^{2-}	-2	0.000			
H^+	1	0.280			
Cl^-	-1	1.409			

4b		I [M]	0.421		
Compund	z	C [M]	$\ln(\gamma)$	μ [J/mol]	μ [eV]
Cu^+	1	0.024	-1.62	17584	0.18
Ga^{3+}	3	0.024	-14.60	-164387	-1.70
S^{2-}	-2	0.000			
H^+	1	0.253			
Cl^-	-1	0.349			

Table A.5: Microsoft® Office Excel spreadsheet for Debye-Hückel calculations of syntheses with different reactant concentrations (continued).

7a		I [M]	1.786		
Compund	z	C [M]	$\ln(\gamma)$	μ [J/mol]	μ [eV]
Cu^+	1	0.255	-3.34	20384	0.21
Ga^{3+}	3	0.255	-30.09	-221474	-2.30
S^{2-}	-2	0.000			
H^+	1	0.000			
Cl^-	-1	1.021			

Ni8		I [M]	1.882		
Compund	z	C [M]	$\ln(\gamma)$	μ [J/mol]	μ [eV]
Cu^+	1	0.255	-3.43	20000	0.21
Ga^{3+}	3	0.255	-30.88	-224942	-2.33
Ni^{2+}	2	0.032	-13.73	-91323	-0.95
S^{2-}	-2	0.000		-8746	-0.09
H^+	1	0.000			
Cl^-	-1	1.085			

Ni16		I [M]	1.835		
Compund	z	C [M]	$\ln(\gamma)$	μ [J/mol]	μ [eV]
Cu^+	1	0.255	-3.39	20189	0.21
Ga^{3+}	3	0.255	-30.49	-223223	-2.31
Ni^{2+}	2	0.016	-13.55	-93589	-0.97
S^{2-}	-2	0.000		-7613	-0.08
H^+	1	0.000			
Cl^-	-1	1.053			

Fe8		I [M]	1.978		
Compund	z	C [M]	$\ln(\gamma)$	μ [J/mol]	μ [eV]
Cu^+	1	0.255	-3.52	19622	0.20
Ga^{3+}	3	0.255	-31.66	-228316	-2.37
Fe^{3+}	3	0.032	-31.66	-86260	-0.89
S^{2-}	-2	0.000		-46295	-0.48
H^+	1	0.000			
Cl^-	-1	1.117			

Table A.5: Microsoft® Office Excel spreadsheet for Debye-Hückel calculations of syntheses with different reactant concentrations (continued).

Fe16		I [M]	1.882		
Compund	z	C [M]	$\ln(\gamma)$	μ [J/mol]	μ [eV]
Cu^+	1	0.255	-3.43	19998	0.21
Ga^{3+}	3	0.255	-30.88	-224936	-2.33
Fe^{3+}	3	0.016	-30.88	-85908	-0.89
S^{2-}	-2	0.000		-46470	-0.48
H^+	1	0.000			
Cl^-	-1	1.069			